

A Thesis for the Degree of Ph.D in Engineering

**Periodic/Aperiodic Separation Filter
for Control and Diagnosis**

February 2020

Graduate School of Science and Technology
Keio University

MURAMATSU, Hisayoshi

Acknowledgements

This dissertation is a summary of my research from April 2015 to February 2020 as a member of Katsura Laboratory, the Faculty of Science and Technology, Keio University. I would like to express my gratitude to the people who supported my doctoral research.

First of all, I am deeply grateful to my supervisor Professor Dr. Seiichiro Katsura, Department of System Design Engineering, Keio University. He has taught me to find my own research and proposals, and I have been able to tackle research based on my philosophy and interesting theme of the periodic/apperiodic separation filter for control and diagnosis. Moreover, he provided opportunities for journal submissions and presentations at conferences. I cannot imagine that I could find the theme and publish the studies without the kind help.

I would like to offer my special thanks to the members of my Ph. D. dissertation committee, Professor Dr. Hiromitsu Ohmori, Department of System Design Engineering, Keio University, Associate Professor Dr. Masahiro Yukawa, Department of Electronics and Electrical Engineering, Keio University, and Assistant Professor Dr. Masaki Inoue, Department of Applied Physics and Physico-Informatics, Keio University.

I would like to show my greatest appreciation for the professors: Professor Dr. Kouhei Ohnishi at Keio University, Professor Dr. Toshiyuki Murakami at Keio University, Associate Professor Dr. Takahiro Yakoh at Keio University, Professor Dr. Hiroaki Nishi at Keio University, Lecturer Dr. Hiroshi Yoshizawa at Tokyo Women's Medical University Hospital, Assistant Professor Dr. Takahiro Nozaki at Keio University, and Assistant Professor Dr. Yoshihiro Itaguchi at Shizuoka University, who always gave valuable comments at the research meetings.

I would like to thank Dr. Eiichi Saito, Dr. Kazumasa Miura, Dr. Satoshi Nishimura, and Mr. Masaki Takeya. Dr. Eiichi Saito taught me how to research and study in the field of control, and my research life is strongly inspired by his heart in research. Dr. Kazumasa Miura, Dr. Satohshi Nishimura, and Mr. Masaki Takeya kindly helped, discussed, and reviewed my research results. Their advice highly improved the reliability of my research. Without their precious support, it would not be possible to conduct the research.

Moreover, I would like to thank Mr. Yuta Kakimi, Mr. Xiao Feng, and Mr. Takahiro Ebato, who

gave interesting discussions. Also, I would like to thank Mr. Alexandre de Langlade, Mr. Yuki Inoue, Mr. Masahiro Komuta, Mr. Kazutaka Takemoto, Mr. Kohei Torikai, and Mr. Akihito Beppu, who have encouraged me. Let me appreciate everyone in Katsura Laboratory.

Finally, I would like to express my gratitude to my father Motoyasu Muramatsu, my mother Momoko Muramatsu, and my brothers Kohki Muramatsu and Fumitaka Muramatsu. Your kind and warm-hearted assistance have enabled me to research without any inconvenience, and I would like to thank you from my heart.

February 3rd, 2020

A handwritten signature in black ink, reading "Hisayoshi Muramatsu". The signature is written in a cursive style with a horizontal line underneath the name.

Contents

Acknowledgements	i
Contents	iii
List of Figures	vi
List of Tables	xi
1 Introduction	1
1.1 Background	1
1.1.1 Periodicity and Aperiodicity in Filters and Controls	1
1.1.2 Periodicity and Aperiodicity in Motion Controls	2
1.1.3 Periodicity and Aperiodicity in Disturbances	3
1.1.4 Periodicity and Aperiodicity in Industrial Inspection and Human Behavior	4
1.2 Motivation	5
1.2.1 Periodicity and Aperiodicity for Filters and Controls	5
1.2.2 Periodicity and Aperiodicity for Motion Controls	6
1.2.3 Periodicity and Aperiodicity for Disturbances	6
1.2.4 Periodicity and Aperiodicity for Industrial Inspection and Human Behavior	7
1.3 Chapter Organization	7
2 Periodic/Aperiodic Separation	9
2.1 Outline	9
2.2 Periodic/Aperiodic Separation Filter	9
2.2.1 Definitions for Periodic/Aperiodic State	9
2.2.2 Construction of Periodic/Aperiodic Separation Filter	11
2.2.3 Separation Examples	18
2.3 Frequency Estimation	23

2.3.1	Frequency Estimator	23
2.3.2	Adaptive Algorithm	27
2.3.3	Convergence of Adaptive Algorithm	30
2.3.4	Frequency-Estimation Examples	33
2.4	Summary	36
3	Periodic/Aperiodic State Control	37
3.1	Outline	37
3.2	Separated Periodic/Aperiodic State Feedback Control	38
3.2.1	Control System	38
3.2.2	Separated Stabilities	39
3.3	Periodic/Aperiodic Motion Control	49
3.3.1	Acceleration Control System	49
3.3.2	Six Periodic/Aperiodic Motion Controls	51
3.3.3	Experiments	57
3.4	Summary	66
4	Periodic/Aperiodic Disturbance Compensation	79
4.1	Outline	79
4.2	Periodic-Disturbance Compensation	80
4.2.1	Periodic-Disturbance Observer	80
4.2.2	Experiments	91
4.3	Aperiodic-Disturbance Compensation	93
4.3.1	Problem of Periodic-Disturbance Observer	93
4.3.2	Enhanced Periodic-Disturbance Observer	98
4.3.3	Experiments	107
4.4	Summary	108
5	Periodic/Aperiodic Diagnosis	111
5.1	Outline	111
5.2	Aperiodic Leak Detection	112
5.2.1	PASF-Based Haptic Leak Detection	112
5.2.2	Package Inspection Simulation	115
5.3	Periodic Proficiency Diagnosis	123
5.3.1	Proficiency Diagnosis for Motor Learning	123
5.3.2	PASF-Based Proficiency Diagnosis	126
5.4	Summary	129

6 Conclusions	135
References	138
Achievements	148

List of Figures

1-1	Chapters of this dissertation.	8
2-1	Conceptual diagram of the periodic/aperiodic states, lifted periodic/aperiodic states, PASF, and lifted PASF.	11
2-2	Block diagram of the general periodic/aperiodic separation filter.	13
2-3	Block diagram of the first-order periodic/aperiodic separation filter.	14
2-4	Bode diagrams of the extraction characteristics of the first-order PASF with variations in the separation frequency ρ . The fundamental frequency is $\omega_0 = 2\pi/\Pi T_s = 1$ rad/s.	15
2-5	Four convergence examples of the periodic state \hat{x}_p using the first-order PASF. The input signal is $\sin(4\pi t)$	16
2-6	Bode diagram of the interference transfer functions $[1 - F(z^{-1})]F(z^{-1})$. The fundamental frequency is $\omega_0 = 2\pi/\Pi T_s = 1$ rad/s.	18
2-7	Effects of the interference on the separation. The separation frequencies are $\rho = 1$ rad/s if $tT_s < 20$ s and $\rho = 0.01$ rad/s if $20 \text{ s} \leq tT_s$	19
2-8	Estimated periodic states \hat{x}_p of four separation examples using the first-order PASF with variations in the separation frequency ρ . The input signal is (2.33).	21
2-9	Separation example of the multiple sine waves in (2.36) using the first-order PASF.	22
2-10	Separation examples of the multiple sine waves in (2.36) using the classical filters.	24
2-11	Bode diagram of the band-pass filters with variations in g_b . The other parameters are $\hat{\omega}_0 = 100$ rad/s and $T_s = 0.1$ ms.	25
2-12	Bode diagram of the notch filters with variations in r . The other parameters are $\xi = -2 \cos(100T_s)$ and $T_s = 0.1$ ms.	26
2-13	Convergence of the notch filters with variations in the notch parameter r	26
2-14	Calculation flow of the frequency estimator.	27
2-15	Calculation flow of the adaptive notch filter.	31
2-16	Step frequency estimations for the frequency-varying sine wave in (2.91) with variations in r . The standard parameters are $\hat{\omega}_0(0) = 100$ rad/s, $\kappa = 10$, $\lambda = 0.999$, $\delta = 1000$, $g = 1000$ rad/s, $g_b = 1000$ rad/s, and $T_s = 0.1$ ms.	33

2-17	Step frequency estimations for the frequency-varying sine wave in (2.91) with variations in κ . The standard parameters are $\hat{\omega}_0(0) = 100$ rad/s, $r = 0.7$, $\lambda = 0.999$, $\delta = 1000$, $g = 1000$ rad/s, $g_b = 1000$ rad/s, and $T_s = 0.1$ ms.	33
2-18	Step frequency estimations for the frequency-varying sine wave in (2.91) with variations in λ . The standard parameters are $\hat{\omega}_0(0) = 100$ rad/s, $r = 0.7$, $\kappa = 10$, $\delta = 1000$, $g = 1000$ rad/s, $g_b = 1000$ rad/s, and $T_s = 0.1$ ms.	33
2-19	Step frequency estimations for the frequency-varying sine wave in (2.91) with variations in δ . The standard parameters are $\hat{\omega}_0(0) = 100$ rad/s, $r = 0.7$, $\kappa = 10$, $\lambda = 0.999$, $g = 1000$ rad/s, $g_b = 1000$ rad/s, and $T_s = 0.1$ ms.	34
2-20	Step frequency estimations for the frequency-varying sine wave in (2.91) with variations in g . The standard parameters are $\hat{\omega}_0(0) = 100$ rad/s, $r = 0.7$, $\kappa = 10$, $\lambda = 0.999$, $\delta = 1000$, $g_b = 1000$ rad/s, and $T_s = 0.1$ ms.	34
2-21	Step frequency estimations for the frequency-varying sine wave in (2.91) with variations in g_b . The standard parameters are $\hat{\omega}_0(0) = 100$ rad/s, $r = 0.7$, $\kappa = 10$, $\lambda = 0.999$, $\delta = 1000$, $g = 1000$ rad/s, and $T_s = 0.1$ ms.	34
2-22	Step frequency estimations for a periodic state including harmonics in (2.92). The other parameters are $\hat{\omega}_0(0) = 100$ rad/s, $r = 0.7$, $\kappa = 10$, $\lambda = 0.999$, $\delta = 1000$, and $T_s = 0.1$ ms.	35
3-1	Block diagram of the periodic/aperiodic state feedback control.	39
3-2	Block diagram of the ACS.	50
3-3	Block diagrams of the six periodic/aperiodic motion control systems.	52
3-4	Bode diagrams of the complementary sensitivity functions of the PVAF control system in (3.131). The other parameters are $M_n = 0.3$, $K_{tn} = 0.24$, $K_I = 6400$, $K_P = 240$, $K_F = 5$, $M_v = 0.1$, $D_v = 50$, $K_v = 800$, $\rho = 1$ rad/s, and $\Pi = 2\pi$ s.	58
3-5	Bode diagrams of the complementary sensitivity functions of the PFAV control system in (3.132). The other parameters are $M_n = 0.3$, $K_{tn} = 0.24$, $K_I = 6400$, $K_P = 240$, $K_F = 5$, $M_v = 0.1$, $D_v = 50$, $K_v = 800$, $\rho = 1$ rad/s, and $\Pi = 2\pi$ s.	59
3-6	Bode diagrams of the complementary sensitivity functions of the PVAI control system in (3.133). The other parameters are $M_n = 0.3$, $K_{tn} = 0.24$, $K_I = 6400$, $K_P = 240$, $K_F = 5$, $M_v = 0.1$, $D_v = 50$, $K_v = 800$, $\rho = 1$ rad/s, and $\Pi = 2\pi$ s.	60
3-7	Bode diagrams of the complementary sensitivity functions of the PIAV control system in (3.134). The other parameters are $M_n = 0.3$, $K_{tn} = 0.24$, $K_I = 6400$, $K_P = 240$, $K_F = 5$, $M_v = 0.1$, $D_v = 50$, $K_v = 800$, $\rho = 1$ rad/s, and $\Pi = 2\pi$ s.	61

3-8	Bode diagrams of the complementary sensitivity functions of the PFAI control system in (3.135). The other parameters are $M_n = 0.3$, $K_{tn} = 0.24$, $K_I = 6400$, $K_P = 240$, $K_F = 5$, $M_v = 0.1$, $D_v = 50$, $K_v = 800$, $\rho = 1$ rad/s, and $\Pi = 2\pi$ s.	62
3-9	Bode diagrams of the complementary sensitivity functions of the PIAF control system in (3.136). The other parameters are $M_n = 0.3$, $K_{tn} = 0.24$, $K_I = 6400$, $K_P = 240$, $K_F = 5$, $M_v = 0.1$, $D_v = 50$, $K_v = 800$, $\rho = 1$ rad/s, and $\Pi = 2\pi$ s.	63
3-10	Initial postures of the experimental manipulator.	65
3-11	Experimental position results of the PVAF control.	67
3-12	Experimental force results of the PVAF control.	68
3-13	Experimental position results of the PFAV control.	69
3-14	Experimental force results of the PFAV control.	70
3-15	Experimental angle results of the PVAI control.	71
3-16	Experimental torque results of the PVAI control.	72
3-17	Experimental position results of the PIAV control.	73
3-18	Experimental force results of the PIAV control.	74
3-19	Experimental position results of the PFAI control.	75
3-20	Experimental force results of the PFAI control.	76
3-21	Experimental position results of the PIAF control.	77
3-22	Experimental force results of the PIAF control.	78
4-1	Conceptual diagram of the periodic disturbance model.	80
4-2	Block diagrams of a DOB.	81
4-3	Bode diagrams of the sensitivity and complementary sensitivity functions of the PDOB without the low-pass filter $q_p(z^{-1})$ in (4.13). The parameters are $\omega_0 = 100$ rad/s, $\gamma = 0.5$, $g_p = 1000$ rad/s, and $T_s = 0.01$ ms.	83
4-4	Bode diagrams of the sensitivity and complementary sensitivity functions of the PDOB with the low-pass filter $q_p(z^{-1})$ in (4.13). The parameters are $\omega_0 = 100$ rad/s, $\gamma = 0.5$, $g_p = 1000$ rad/s, and $T_s = 0.01$ ms.	84
4-5	Block diagram of the PDOB.	85
4-6	Effect of the delay calculation in (4.15) on the frequency change of the sensitivity function $1 - Q_p(z^{-1})z^{-1}$ around the fundamental frequency, which is caused by the low-pass filter $q_p(z^{-1})$ in (4.13). The parameters are $\omega_0 = 100$ rad/s, $\gamma = 0.5$, $g_p = 1000$ rad/s, and $T_s = 0.01$ ms.	85
4-7	Bode diagrams of the sensitivity and complementary sensitivity functions of the PDOB with variations in the design parameter γ . The parameters are $\omega_0 = 100$ rad/s, $g_p = 1000$ rad/s, and $T_s = 0.01$ ms.	88

4-8	Fundamental-wave attenuation performance of the PDOB with variations in ω_0/g_p	89
4-9	Equivalent block diagram of the DOB structure in Fig. 4-2(a).	89
4-10	Comparative Bode diagrams of the PDOB and DOBs. The parameters for the PDOB are $\omega_0 = 100$ rad/s, $\gamma = 0.5$, $g_p = 1000$ rad/s, and $T_s = 0.01$ ms. The cutoff frequencies for DOB1 and DOB2 are 25 rad/s and 100 rad/s, respectively.	90
4-11	Results of the comparative experiments for the PDOB.	92
4-12	Discrete Fourier transform results of Fig. 4-11 between 20 s and 100 s.	94
4-13	Block diagrams of the enhanced PDOB.	98
4-14	Bode diagrams of the PDOB. The parameters are $\omega_0 = 100$ rad/s, $\gamma = 0.5$, $g_p = 1000$ rad/s, and $T_s = 0.01$ ms.	101
4-15	Bode diagrams of the DOB. The parameters are $g_a = 1000$ rad/s and $T_s = 0.01$ ms.	102
4-16	Bode diagrams of the enhanced PDOB. The parameters are $\omega_0 = 100$ rad/s, $\gamma = 0.5$, $g_p = 1000$ rad/s, $g_a = 1000$ rad/s, and $T_s = 0.01$ ms.	103
4-17	Enlarged view of the sensitivity functions of the PDOB, DOB, and enhanced PDOB in Figs. 4-14(a), 4-15(a), and 4-16(a).	104
4-18	Block diagram of the position control system using the enhanced PDOB.	106
4-19	Results of the comparative experiments for the enhanced PDOB.	109
4-20	Discrete Fourier transform results of Fig. 4-19 between 10 s and 100 s.	110
5-1	Overview of the PASF-based haptic leak detection.	114
5-2	Haptic leak detector using a linear motor.	115
5-3	Yank waveforms between 1988 s and 1996 s in Simulation 1.	116
5-4	Mean yank values in Simulation 1.	117
5-5	Yank waveforms between 1988 s and 1996 s in Simulation 2.	118
5-6	Yank waveforms between 1520 s and 1528 s in Simulation 3.	119
5-7	Mean yank values in Simulation 2.	120
5-8	Mean yank values in Simulation 3.	120
5-9	Comparison of the detection performance with and without the PASF using the ROC curve.	121
5-10	Accuracy index for threshold design.	122
5-11	Counter-clockwise logarithmic spiral trajectory for the motor learning experiment.	123
5-12	Angle, angular velocity, angular acceleration, and angular jerk waveforms of θ satisfying the minimum-angular-jerk in (5.23).	125
5-13	Experimental system.	126
5-14	Schedule of the drawing practice.	126
5-15	Twenty subjects' trial errors.	127

5-16	Twenty subjects' phase errors at the evaluation and practice phases. The error bars stand for SDs, and the symbols ***, **, *, and n.s. stand for the statistic results: $p < 0.001$, $p < 0.01$, $p < 0.05$, and $0.05 < p$, respectively.	128
5-17	One subject's spirals in E1, P1, and E2.	130
5-18	One subject's spirals in P2, E3, and P3.	131
5-19	One subject's spirals in E4, P4, and E5.	131
5-20	One subject's periodic trajectories in E1, P1, and E2.	132
5-21	One subject's periodic trajectories in P2, E3, and P3.	132
5-22	One subject's periodic trajectories in E4, P4, and E5.	133
5-23	One subject's aperiodic trajectories in E1, P1, and E2.	133
5-24	One subject's aperiodic trajectories in P2, E3, and P3.	134
5-25	One subject's aperiodic trajectories in E4, P4, and E5.	134

List of Tables

3.1	Six control objectives for the six periodic/aperiodic motion controls.	51
3.2	Parameters for the periodic/aperiodic motion control experiments.	65
4.1	Parameters of the comparative experiments for the PDOB.	91
4.2	Parameters of the comparative experiments for the enhanced PDOB.	106
5.1	Parameters of the preliminary experiments.	115
5.2	Accuracy indexes when the separation frequency was $\rho = 0.01$ rad/s.	121
5.3	Counter-clockwise logarithmic spiral parameters.	124

Chapter 1

Introduction

1.1 Background

1.1.1 Periodicity and Aperiodicity in Filters and Controls

Periodicity repeats values in regular periods and results in a periodic signal composed of an infinite sum of sine and cosine waves called Fourier series. To process the periodic signal, comb filters that can eliminate the infinite sum of sine and cosine waves have been studied [1,2] and have been developed into optimal filters [3,4]. Classical band-pass and band-stop filters can extract and eliminate a limited number of sine and cosine waves but cannot handle the periodic signal. Unlike the band-pass and band-stop filters, the comb filter can eliminate the periodic signal including the infinite sum of sine and cosine waves by using delay elements. Consequently, comb filters have been practically used for pulsed radar systems [5], video signal processing [6,7], speech signal processing [8,9], ultrasonics [10], and electronics [11–13]. In addition to the periodic-signal elimination using a comb filter, decomposition based on both periodicity and aperiodicity have also been considered. In the speech synthesis field, periodic/aperiodic decomposition has been studied using the discrete Fourier transform [14–16], where a harmonic pulse noise model defines a periodic signal and aperiodic signal as a limited number of time-varying harmonics and the residual signal from an original signal, respectively [17–19]. Hence, the methods are nonlinear and unfeasible for real-time calculation of control owing to the discrete Fourier transform. Furthermore, they utilize only a limited number of harmonics, unlike the comb filters.

In the field of control, a periodic state has been controlled for high-precision control with repetitive control (RC) [20–22]. The RC was proposed to eliminate errors caused by an exogenous periodic com-

mand and disturbance [23, 24]. The repetitive controller realizes an internal model of a periodic signal including an infinite number of poles on the imaginary axis by using a delay element similar to the comb filters. As industrial automatic systems typically work periodically and require precise operations, RCs have been developed and applied to hard disk devices [25], ball-screw-driven stages [26], converters and inverters [27–29], aircraft ground power unit [30], microgrids [31], and wind turbines [32].

In addition to the controls for a periodic state, periodicity time-varying systems have been studied [33–35], and robust controls for the periodic systems were further proposed [36–38]. Similarly, a spatially periodic system was considered [39]. As a practical application, a periodic system has been developed for helicopter rotors [40]. According to the nonlinearity that the periodic system has periodically time-varying system matrices, a lifting technique has been used to transform the periodically time-varying system into a time-invariant system [41–43]. These studies showed the usefulness of the lifting technique for periodicity.

Frequency estimation of a periodic state has also been studied as adaptive filters and adaptive controls. Adaptive notch filters have been studied for frequency estimation [44–46], and adaptive repetitive control has been studied for frequency-varying periodic-disturbance compensation [47, 48].

Since periodicity of a signal, state, and system is a usual phenomenon in automatic systems, comb filters, RCs, and periodic systems have been studied. Moreover, the speech synthesis studies have focused on not only periodicity but also aperiodicity of a signal as periodic/aperiodic decomposition. The comb filters and RCs demonstrated that a delay element can express periodicity of a signal and state. Also, the control studies for periodic systems showed that a lifting technique is a useful calculation approach to handle periodicity, and the adaptive notch filters and adaptive repetitive controls showed that adaptivity is useful to handle frequency-varying periodicity. However, controls for periodicity and aperiodicity were not studied because the comb filters, RCs, and periodic systems only consider periodicity. Furthermore, the periodic/aperiodic decomposition, which causes the nonlinearity, long calculation time, and limited definition of a periodic signal, is not applicable to control.

1.1.2 Periodicity and Aperiodicity in Motion Controls

In the field of applied control, motion control systems such as mechatronics and robotics systems have been studied for industrial and human support systems [49, 50]. Previous studies focused on and controlled one of motion elements: velocity (position) [51–53], force [54–56], and impedance [57, 58] in order to improve control performance: speed, precision, and adaptivity against humans and environ-

ments. In the motion controls, there is a principle that only one of the motion elements can be controlled by one-degree-of-control-freedom. Hence, the velocity, force, and impedance controls cannot be simultaneously achieved. To acquire multiple functions accomplishing multiple motion control objectives, hybrid controls, that assign conflicting motion control objectives to independent control freedom such as different axes and actuators, have been studied [59, 60]. Similarly, bilateral control based on a master-slave structure has two-degree-of-control-freedom [61–63]. Optimal control adjusts and balances states between conflicting motion control objectives but cannot achieve both the objectives simultaneously [64, 65]. Only when motion control objectives do not conflict as a velocity objective calculated from a force objective, velocity and force responses can be simultaneously controlled [66]. Motion-copying systems also control consistent position and force with one-degree-of-control-freedom [67–69], where motion data that correspond to consistent position and force are stored through the bilateral control in a motion-saving phase, and the data are reproduced with one-degree-of-control-freedom in a motion-reproducing phase.

Consequently, one control objective for one-degree-of-control-freedom was a standard approach such as position, force, and impedance controls in the motion controls. Alternatively, increase in axes and actuators or use of consistent trajectories is required to achieve additional control objectives. Periodicity and aperiodicity of motion had not been addressed for simultaneous achievement of multiple motion control objectives.

1.1.3 Periodicity and Aperiodicity in Disturbances

The motion control systems are based on an acceleration control system (ACS) using a disturbance observer (DOB) [70–72]. Classically, an inner acceleration controller compensates for disturbances, and an outer motion controller adjusts the motion elements [73]. The DOB enables the separation of the disturbance-compensation and tracking issues as a two-degree-of-freedom controller and has a Q-filter that can design sensitivity and complementary sensitivity functions directly. The sensitivity function corresponds to disturbance suppression performance, and the complementary sensitivity function corresponds to robust stability and noise sensitivity. Accordingly, the sensitivity function is typically set to a high-pass filter, and the complementary sensitivity function is accordingly set to a low-pass filter on the basis of a tradeoff between the functions [74, 75].

Industrial automatic systems are usually required to operate precisely and repetitively, but the repetitive operations typically cause periodic disturbances including an infinite number of harmonics [76, 77].

Then, the periodic disturbances impair the precision of the industrial automatic systems [78,79]. In order to eliminate the periodic disturbance, the high-pass characteristic of the DOB is not sufficient because an infinite number of band-stop characteristics is necessary to eliminate an infinite number of sine and cosine waves. To overcome the problem of the DOB, high-order DOBs whose sensitivity function includes several band-stop characteristics were studied [80,81]. However, the high-order DOBs and their limited number of band-stop characteristics are still not sufficient to eliminate the periodic disturbance.

The RCs are effective methods that can compensate for all harmonics of a periodic disturbance using delay elements. However, the repetitive controllers are not two-degree-of-freedom controllers, amplify aperiodic disturbances, and are difficult to design their complementary sensitivity functions. Although RCs based on the DOB structure have been studied [82–84], they are not two-degree-of-freedom controllers and their delay elements affect nominal stability. Besides, consideration of both periodicity and aperiodicity of a disturbance is necessary for practical applications [85].

Since industrial automatic systems usually face periodic disturbances impairing their precision, periodic-disturbance compensation is a significant issue for the industry. Although the previous studies proposed the high-order DOBs as two-degree-of-freedom controllers and RCs for periodic-disturbance elimination, the high-order DOBs and RCs lack the periodic-disturbance suppression performance and two-degree-of-freedom characteristic, respectively.

1.1.4 Periodicity and Aperiodicity in Industrial Inspection and Human Behavior

Periodicity and aperiodicity exist at inspection for food product packing. In our society, many foods and drinks are provided after packing to secure their freshness [86]. However, package leaks, which accordingly occur, expose safety of the products to danger and require product inspection to guarantee the safety [87]. In particular, automatic production processes require automatic product inspection, where products are periodically inspected for detecting aperiodic anomaly [88–90]. In a previous study, a haptic leak detector was developed for inspection of all packages using anomalous force information due to a leak [86]. However, the previous detection method lacks robustness against environmental changes, which causes misdetection.

Besides, periodicity and aperiodicity also exist in human behavior. Recently, the number of stroke survivors has increased as the number of older people has increased in the world. In the United States, on average, someone has a stroke every 40 seconds [91]. Although stroke survivors usually need rehabilitation to reacquire lost motor skills caused by brain injury, the number of therapists is limited.

Consequently, automatic therapy and automatic clinical diagnosis using robots are required [92, 93]. Motor learning, which is a change of motor function based on brain plasticity, has been investigated with healthy people according to the rehabilitation mechanism based on the motor learning [94–96]. Typically, the motor learning requires periodic practice, but human behavior is always variable aperiodically. However, proficiency diagnosis based on the periodicity and aperiodicity had not been studied.

In industrial inspection for food product packing, inspection of all packages periodically measures food products, and anomaly appears aperiodically. Besides, in motor learning, practice is periodic, and human behavior is aperiodically variable. Therefore, there are possibilities that the concept of periodicity and aperiodicity for filters and controls could practically improve the industrial inspection and diagnosis of motor proficiency.

1.2 Motivation

1.2.1 Periodicity and Aperiodicity for Filters and Controls

I focused on control of a periodic/aperiodic state that includes both a periodic state and aperiodic state. Although the previous studies proposed filters and controls considering periodicity of a state or periodicity/aperiodicity of a speech signal, they were insufficient to control the periodic/aperiodic state.

The comb filters and repetitive controls proposed by the previous studies aim to eliminate a periodic signal from a signal and do not define an aperiodic signal. Although the periodic/aperiodic decomposition methods were proposed for periodic and aperiodic signals in a signal, they are difficult to be used for control owing to the discrete Fourier transform. Furthermore, their periodic signal is nonlinearly defined as a limited number of time-varying harmonics. Besides, the studies for the periodic systems were different from the studies for the periodic/aperiodic state because the periodicity of a periodic system belongs to a system.

My research began by definitions of the periodic state and aperiodic state, which compose the periodic/aperiodic state [97]. On the basis of the definitions, I constructed a periodic/aperiodic separation filter (PASF) to separate the periodic/aperiodic state into the periodic state and aperiodic state. The PASF is linear and feasible to control, unlike the conventional periodic/aperiodic decomposition methods. Then, the PASF enabled to construct periodic/aperiodic state feedback control, which separately controls the periodic and aperiodic states in a similar manner to classical state feedback control. I further revealed that the control, observation, and separation of the periodic/aperiodic state can be independently de-

signed through the separation principle. This facilitates the simple design of the periodic/apperiodic state feedback control, and an additional proposition demonstrates that stability of the control can be designed in a similar manner to classical state feedback control. In addition, I constructed a frequency estimator based on an adaptive notch filter to enable to acquire a varying frequency of the periodic/apperiodic state in [98].

1.2.2 Periodicity and Aperiodicity for Motion Controls

I expanded the concept of the periodic/apperiodic state feedback control into motion control as periodic/apperiodic motion control [99]. As the periodic state and aperiodic state can be separately controlled by the periodic/apperiodic state feedback control, the periodic motion and aperiodic motion can be separately designed under one-degree-of-control-freedom. This solved the problem that one-degree-of-control-freedom can achieve only one control objective such as position, force, and impedance controls. Two control objectives assigned to periodic motion and aperiodic motion can be simultaneously achieved by the periodic/apperiodic motion control.

To this end, I used the PASF to separate velocity and force into periodic velocity, aperiodic velocity, periodic force, and aperiodic force. Then, I designed six types of periodic/apperiodic motion controls that assign position, force, or impedance control to periodic motion and aperiodic motion. Experiments using a multi-axis manipulator validated the practicality of the six periodic/apperiodic motion controls.

1.2.3 Periodicity and Aperiodicity for Disturbances

I further focused on periodicity and aperiodicity of a disturbance, which is an exogenous signal, unlike the state. In particular, periodic disturbances are an inherent problem for industrial automatic systems because their repetitive works induce periodic disturbances that impair their precision.

The conventional methods: DOBs and RCs for periodic-disturbance compensation have problems that the DOBs and RCs lack the periodic-disturbance suppression performance and two-degree-of-freedom characteristic, respectively. To overcome the problems of the conventional methods, I constructed a periodic-disturbance observer (PDOB) that uses both advantages of a DOB and RC [98, 100]. The PDOB can compensate for all of an infinite harmonic of a periodic disturbance similar to RC, and its delay used for the compensation does not affect the nominal stability and command tracking performance on the basis of the two-degree-of-freedom structure. In addition, I developed the PDOB into an enhanced PDOB in order to enhance its aperiodic-disturbance compensation performance [101]. The enhanced PDOB

consists of the PDOB and DOB that compensate for periodic and aperiodic disturbances, respectively. The enhanced PDOB is more practical than the PDOB because both periodic and aperiodic disturbances usually occur in actual applications.

1.2.4 Periodicity and Aperiodicity for Industrial Inspection and Human Behavior

I further addressed more practical problems in industry and rehabilitation using the periodicity and aperiodicity. For package-leak detection, I found that repetitive inspection and package leak correspond to periodicity and aperiodicity, respectively. I applied the PASF for the haptic package-leak detection, which is one of the previous leak detection methods [86], to pick up aperiodic anomalous packages from the periodic inspection process. The PASF improved the robustness of the detection against a slow environmental change at measurement. The improved robustness was verified through 10,000 packages inspection simulation based on 388 experimental yank data.

For motor proficiency diagnosis, I found that repetitive practice and variable human behaviors are periodicity and aperiodicity, respectively. I further applied the PASF for motor proficiency diagnosis to detect a small change of motor proficiency by eliminating aperiodic variations of human behavior. To evaluate the effect of the PASF on the diagnosis, I designed a motor learning experiment based on a logarithmic spiral drawing task with twenty subjects. According to the minimum jerk model of motor control [102], an angular trajectory for the logarithmic spiral was designed to satisfy minimum jerk. Then, the PASF was used to separate the drawn logarithmic spirals into periodic and aperiodic trajectories and achieved to evaluate the drawing proficiency accurately.

1.3 Chapter Organization

According to the motivations and studies, I constructed the chapters of this dissertation as shown in Fig. 1-1. Chapter 2 describes the basis of my studies. Section 2.2 shows definitions for the periodic/aperiodic state and the PASF in [97]. Section 2.3 mentions a frequency estimator for fundamental frequency estimation of the periodic/aperiodic state according to [97]. Chapter 3 is for control of the periodic/aperiodic state. Section 3.2 constructs the periodic/aperiodic state feedback control using the PASF and proves the separation principle for the periodic/aperiodic state feedback control according to [97]. The periodic/aperiodic motion control is described in Section 3.3 according to [99]. Chapter 4 is for periodicity and aperiodicity in a disturbance. Section 4.2 constructs the PDOB for periodic-disturbance sup-

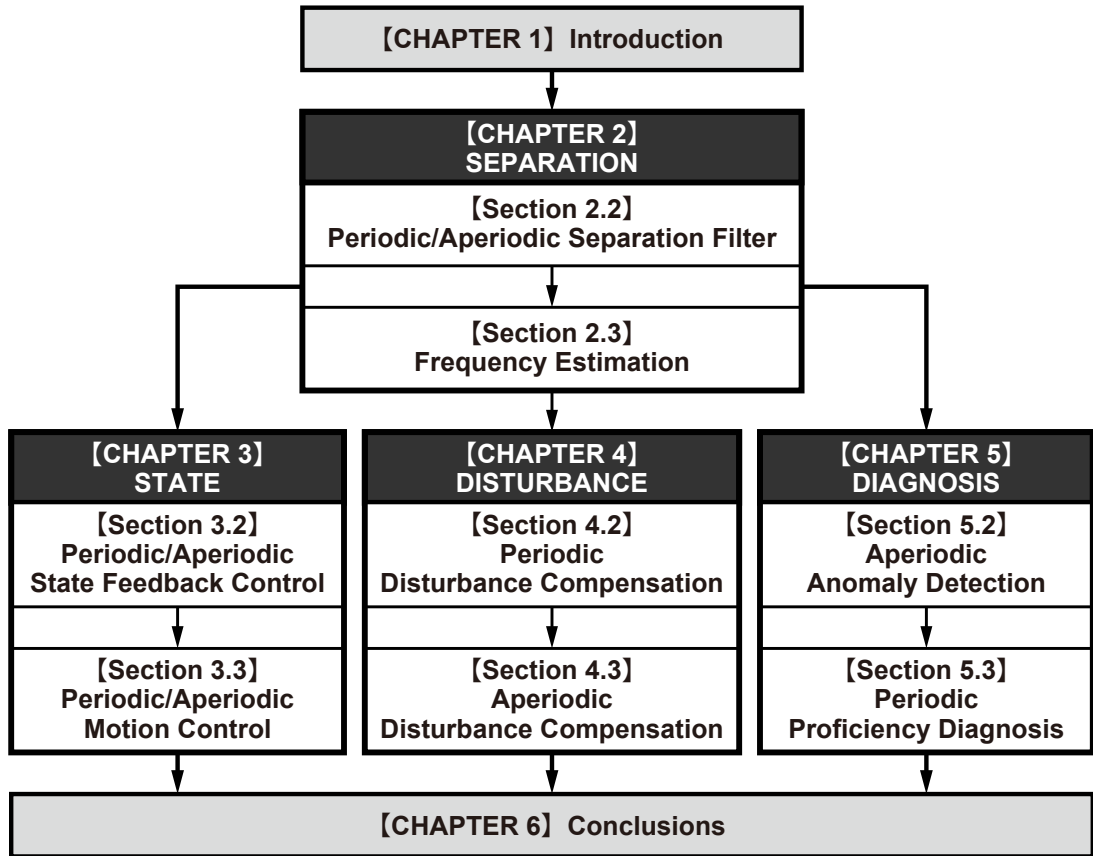


Fig. 1-1: Chapters of this dissertation.

pression, and Section 4.3 develops the PDOB into the enhanced PDOB to improve aperiodic-disturbance suppression performance. The PDOB and enhanced PDOB were proposed in [98,100] and [101], respectively. Chapter 5 is for practical diagnoses based on periodicity and aperiodicity. Section 5.2 describes the PASF-based haptic leak detection for practical package-leak inspection. Section 5.3 describes the PASF-based proficiency diagnosis for motor learning evaluation. Finally, Chapter 6 concludes this dissertation.

Chapter 2

Periodic/Aperiodic Separation

2.1 Outline

Chapter 2 focuses on periodicity and aperiodicity for separation.

This research begins by definitions of a periodic/aperiodic state and separation of the periodic/aperiodic state into periodic and aperiodic states in Section 2.2. Subsections 2.2.1 and 2.2.2 describe the definitions and the PASF for the separation, respectively. As the lowest-order infinite-impulse-response filter, a first-order PASF is designed in Subsection 2.2.3. The concept and PASF are the basis of the studies for the state control, disturbance compensation, and diagnosis based on periodicity and aperiodicity.

In order to adapt to frequency-varying periodicity, Section 2.3 describes frequency estimation for the periodic/aperiodic state. Subsection 2.3.1 constructs a frequency estimator based on an adaptive notch filter. Subsections 2.3.2 and 2.3.3 mention the adaptive algorithm and its convergence, respectively. Frequency-estimation examples for design parameter evaluation are shown in Subsection 2.3.4.

2.2 Periodic/Aperiodic Separation Filter

2.2.1 Definitions for Periodic/Aperiodic State

A discrete-time state $\boldsymbol{x}(t)$ is defined to be a periodic/aperiodic state composed of a periodic state $\boldsymbol{x}_p(t)$ and aperiodic state $\boldsymbol{x}_a(t)$ as

$$\boldsymbol{x}(t) = \boldsymbol{x}_p(t) + \boldsymbol{x}_a(t) \in \mathbb{R}^n. \quad (2.1)$$

In the periodic state, a perfect periodic state is defined by

$$\mathbf{x}_p(t + \Pi) = \mathbf{x}_p(t). \quad (2.2)$$

The perfect periodic state can be expressed by the Fourier series as

$$x_p(t) = \frac{a_0}{2} + \sum_{n=1}^{\infty} [a_n \cos(n\omega_0 T_s t) + b_n \sin(n\omega_0 T_s t)], \quad (2.3)$$

where

$$\omega_0 = \frac{2\pi}{\Pi T_s}. \quad (2.4)$$

a_0 , a_n , and b_n denote Fourier coefficients, and ω_0 , Π , and T_s denote the fundamental frequency, period that is an integer, and sampling time, respectively. The lifting technique:

$$\mathbf{x}_\tau(k) := \mathbf{x}(k\Pi + \tau) \quad (2.5)$$

is introduced to transform the perfect periodic state into a constant state, where

$$\mathbf{x}(t) = \mathbf{x}(k\Pi + \tau). \quad (2.6)$$

The perfect periodic state and lifting technique in (2.2) and (2.5) provide a lifted perfect periodic state

$$\mathbf{x}_{\tau p}(k + 1) = \mathbf{x}_{\tau p}(k), \quad (2.7)$$

which shows the constant characteristic. Because the lifted perfect periodic state is a constant state as $\mathbf{x}_{\tau p}(0) = \mathbf{x}_{\tau p}(1) = \mathbf{x}_{\tau p}(2) = \dots$, the lifted periodic state and lifted aperiodic state are defined as

$$\mathcal{F}[\mathbf{x}_\tau(k)] = \sum_{k=-\infty}^{\infty} \mathbf{x}_\tau(k) e^{-j\omega T_s \Pi k} = \begin{cases} \mathcal{F}[\mathbf{x}_{\tau p}], & \text{if } \omega \leq \rho \\ \mathcal{F}[\mathbf{x}_{\tau a}], & \text{if } \rho < \omega \end{cases}, \quad (2.8)$$

where $\mathcal{F}[\]$ denotes the the discrete-time Fourier transform. The lifted periodic state $\mathbf{x}_{\tau p}$ and lifted aperiodic state $\mathbf{x}_{\tau a}$ are low-frequency and high-frequency elements of the lifted periodic/aperiodic state \mathbf{x}_τ , respectively. ρ is the separation frequency that is a boundary frequency between the lifted periodic and aperiodic states. Fig. 2-1 illustrates the definitions of the periodic and aperiodic states.

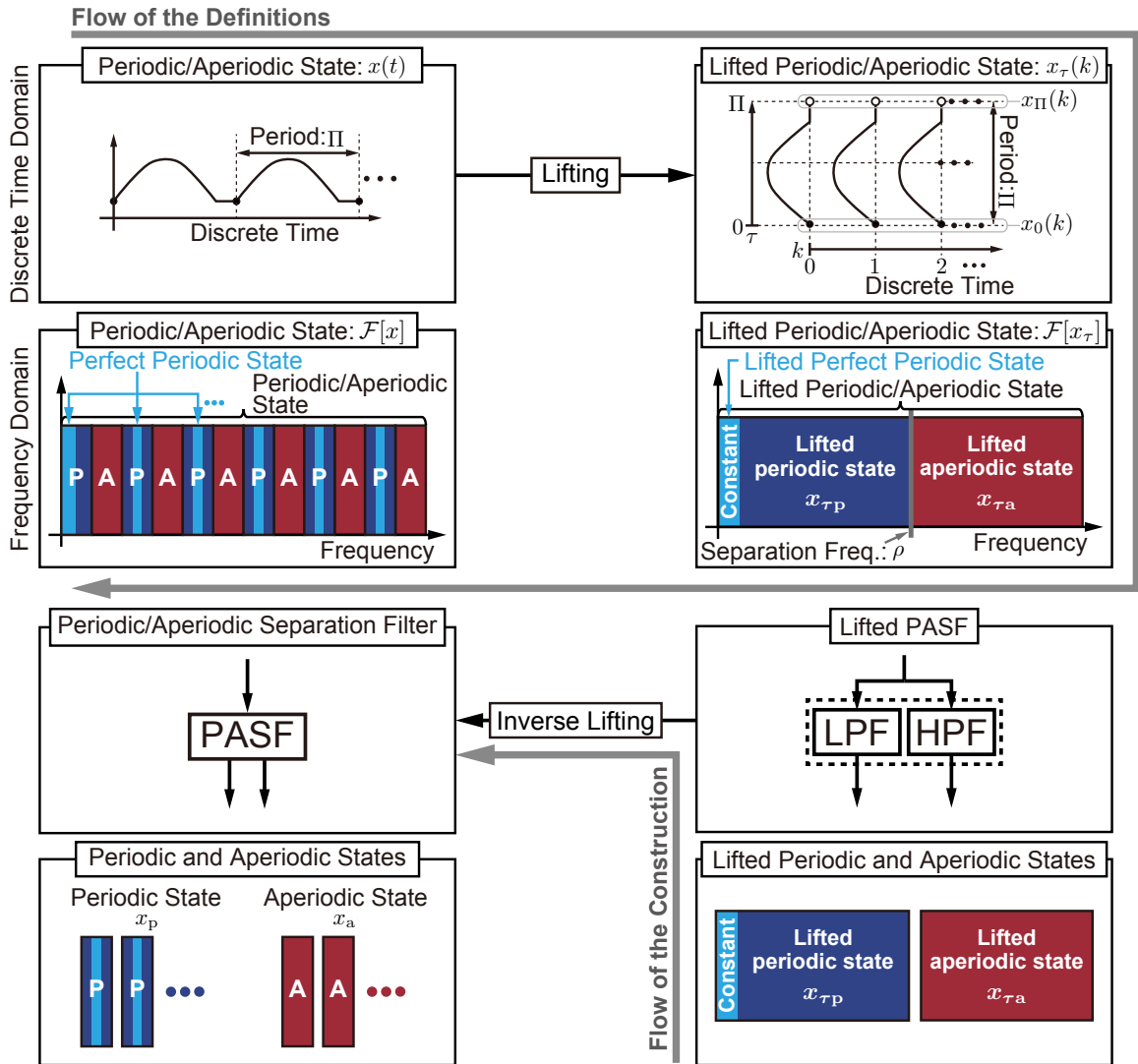


Fig. 2-1: Conceptual diagram of the periodic/aperiodic states, lifted periodic/aperiodic states, PASF, and lifted PASF.

2.2.2 Construction of Periodic/Aperiodic Separation Filter

General Periodic/Aperiodic Separation Filter

A PASF is constructed to separate the periodic/aperiodic state x into the periodic state x_p and aperiodic state x_a . Firstly, a lifted PASF, that separates the lifted periodic/aperiodic state x_τ into the lifted

periodic state $\mathbf{x}_{\tau p}$ and lifted aperiodic state $\mathbf{x}_{\tau a}$, is constructed as

$$\begin{cases} \hat{\mathbf{x}}_{\tau p}(k) = \sum_{i=0}^{l-1} [p_i \hat{\mathbf{x}}_{\tau p}(k-1-i) + q_i \mathbf{x}_{\tau}(k-i)] \\ \hat{\mathbf{x}}_{\tau a}(k) = \mathbf{x}_{\tau}(k) - \hat{\mathbf{x}}_{\tau p}(k) \end{cases}, \quad (2.9)$$

where the coefficients p_i and q_i perform a low-pass filter. l and the symbol $\hat{\cdot}$ denote the order of the PASF and an estimated variable. As shown in the right diagram of Fig. 2-1, the lifted periodic state and the lifted aperiodic state are low and high frequency elements of the lifted periodic/aperiodic state, respectively. Hence, a low-pass filter is employed to extract the lifted periodic state from the lifted periodic/aperiodic state, and the complementary high-pass filter extracts the lifted aperiodic state.

Next, the PASF is constructed from the lifted PASF. According to the lifting technique in (2.5), the lifted periodic/aperiodic states in (2.9) can be inversely transformed into the states

$$\hat{\mathbf{x}}_{\tau}(k) = \hat{\mathbf{x}}(k\Pi + \tau) \quad (2.10)$$

$$\hat{\mathbf{x}}_{\tau}(k-1-i) = \hat{\mathbf{x}}(k\Pi + \tau - \Pi - i\Pi) \quad (2.11)$$

$$\hat{\mathbf{x}}_{\tau}(k-i) = \hat{\mathbf{x}}(k\Pi + \tau - i\Pi). \quad (2.12)$$

By using these equations for (2.9), the lifted PASF becomes

$$\begin{cases} \hat{\mathbf{x}}_p(k\Pi + \tau) = \sum_{i=0}^{l-1} [p_i \hat{\mathbf{x}}_p(k\Pi + \tau - \Pi - i\Pi) + q_i \mathbf{x}(k\Pi + \tau - i\Pi)] \\ \hat{\mathbf{x}}_a(k\Pi + \tau) = \mathbf{x}(k\Pi + \tau) - \hat{\mathbf{x}}_p(k\Pi + \tau) \end{cases}, \quad (2.13)$$

and (2.6) further transforms (2.13) into the PASF:

$$\begin{cases} \hat{\mathbf{x}}_p(t) = \sum_{i=0}^{l-1} [p_i \hat{\mathbf{x}}_p(t - \Pi - i\Pi) + q_i \mathbf{x}(t - i\Pi)] \\ \hat{\mathbf{x}}_a(t) = \mathbf{x}(t) - \hat{\mathbf{x}}_p(t) \end{cases}. \quad (2.14)$$

Fig. 2-1 illustrates a difference between the periodic/aperiodic state and lifted periodic/aperiodic state and design flow from the lifted PASF to the PASF. A block diagram of the general PASF is shown in Fig. 2-2.

First-Order Periodic/Aperiodic Separation Filter

As a design example for the general PASF, this dissertation shows a first-order PASF based on an infinite-impulse-response low-pass filter. Consider the continuous-time low-pass filter

$$LPF(s) = \frac{\rho}{s + \rho}. \quad (2.15)$$

Using the bilinear transform

$$s = \frac{2}{\Pi T_s} \frac{1 - Z^{-1}}{1 + Z^{-1}}, \quad (2.16)$$

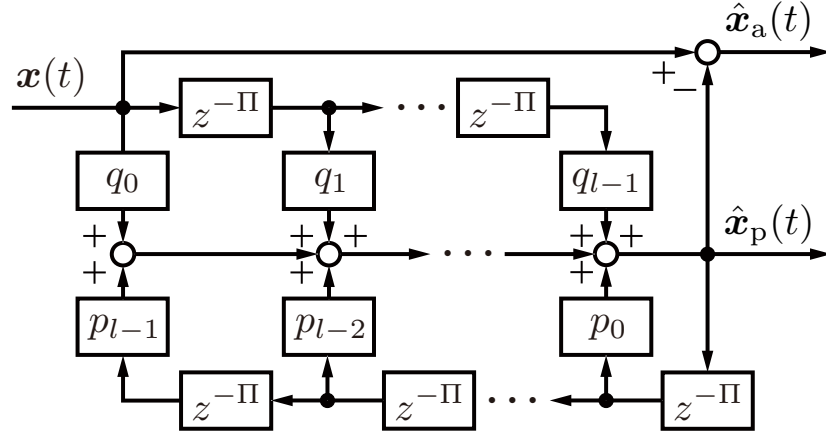


Fig. 2-2: Block diagram of the general periodic/apperiodic separation filter.

the continuous-time low-pass filter is transformed into the discrete-time low-pass filter

$$LPF(Z^{-1}) = \frac{\rho\Pi T_s + \rho\Pi T_s Z^{-1}}{(\rho\Pi T_s + 2) + (\rho\Pi T_s - 2)Z^{-1}}, \quad (2.17)$$

which is the first-order lifted PASF. Z^{-1} denotes the Z operator whose sampling time is ΠT_s . Using the first-order lifted PASF, relation between the estimated lifted periodic state $\hat{x}_{\tau p}(k)$ and the lifted periodic/apperiodic state $x_{\tau}(k)$ is

$$\hat{x}_{\tau p}(k) = \frac{2 - \rho\Pi T_s}{2 + \rho\Pi T_s} \hat{x}_{\tau p}(k - 1) + \frac{\rho\Pi T_s}{2 + \rho\Pi T_s} x_{\tau}(k) + \frac{\rho\Pi T_s}{2 + \rho\Pi T_s} x_{\tau}(k - 1). \quad (2.18)$$

According to the lifted PASF in (2.9), coefficients of the first-order lifted PASF are

$$p_0 = \frac{2 - \rho\Pi T_s}{2 + \rho\Pi T_s}, \quad q_0 = \frac{\rho\Pi T_s}{2 + \rho\Pi T_s}, \quad q_1 = \frac{\rho\Pi T_s}{2 + \rho\Pi T_s}. \quad (2.19)$$

By substituting the coefficients for the PASF in (2.14), the first-order PASF is derived as

$$\begin{cases} \hat{x}_p(t) = \frac{2 - \rho\Pi T_s}{2 + \rho\Pi T_s} \hat{x}_{\tau p}(t - \Pi) + \frac{\rho\Pi T_s}{2 + \rho\Pi T_s} x_{\tau}(t) + \frac{\rho\Pi T_s}{2 + \rho\Pi T_s} x_{\tau}(t - \Pi) \\ \hat{x}_a(t) = x(t) - \hat{x}_p(t) \end{cases}. \quad (2.20)$$

Transfer functions of the first-order PASF are

$$\begin{cases} \hat{x}_p(z^{-1}) = F(z^{-1})x(z^{-1}) \\ \hat{x}_a(z^{-1}) = [1 - F(z^{-1})]x(z^{-1}) \end{cases}, \quad (2.21)$$

where

$$F(z^{-1}) = \frac{\rho\Pi T_s + \rho\Pi T_s z^{-\Pi}}{(\rho\Pi T_s + 2) + (\rho\Pi T_s - 2)z^{-\Pi}}. \quad (2.22)$$

A block diagram of the first-order PASF is shown in Fig. 2-3.

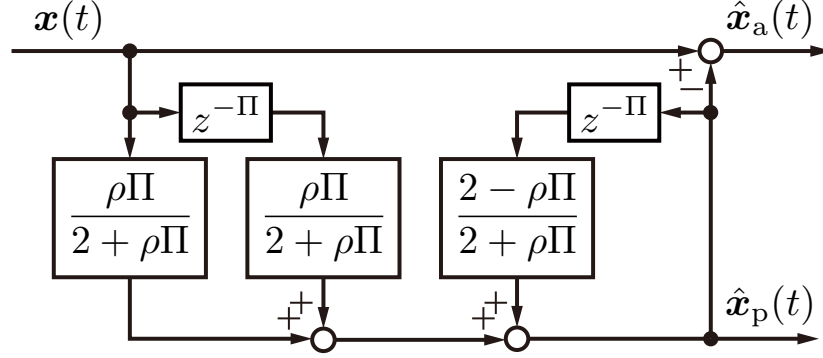


Fig. 2-3: Block diagram of the first-order periodic/aperiodic separation filter.

Design of Separation Frequency

The separation frequency ρ defines a boundary between periodic and aperiodic states as in (2.8). Bode diagrams of the transfer functions of the periodic-state extraction $F(z^{-1})$ and of the aperiodic-state extraction $1 - F(z^{-1})$ are shown in Fig. 2-4 with variations in the separation frequency ρ , respectively. The period of the target periodic state is

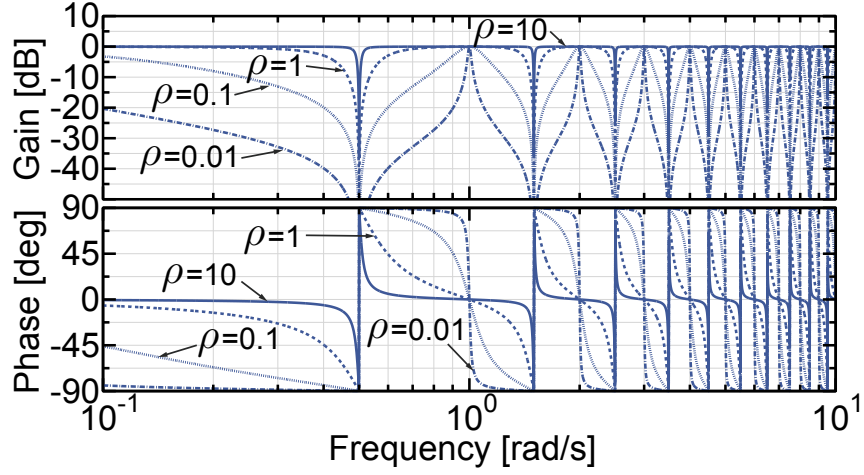
$$\Pi T_s = \frac{2\pi}{\omega_0} = 2\pi, \quad (2.23)$$

and the fundamental frequency and harmonics of the target perfect periodic state are $\omega_0 = 1$ and $n\omega_0$, respectively. The Bode diagrams indicate that a periodic state x_p is extracted only around frequencies of a perfect periodic state, and an aperiodic state x_a close to a state x is extracted, in a case of a small separation frequency such as $\rho = 0.01$ rad/s. In a case of a large separation frequency such as $\rho = 10$ rad/s, a periodic state x_p close to a state x is extracted, and an aperiodic state x far from frequencies of a perfect periodic state is extracted. Therefore, a periodic state that is consistent with our image of periodicity may be provided by a small separation frequency.

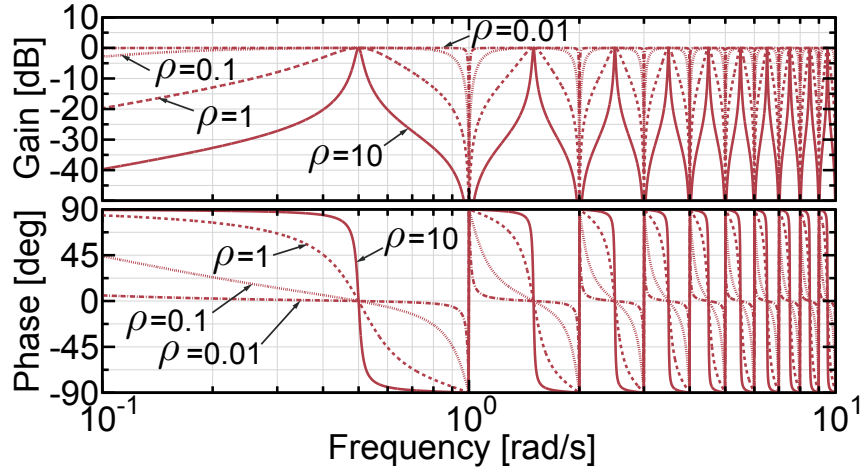
The separation frequency ρ also determines a time constant T_c of the first-order PASF as

$$T_c = \frac{1}{\rho} \quad (2.24)$$

because the separation frequency is used as a cutoff frequency of the low-pass filter in (2.15). Fig. 2-5 shows the four convergence examples of the first-order PASF with four separation frequencies (a) $\rho =$



(a) Periodic-state extraction $F(z^{-1})$.

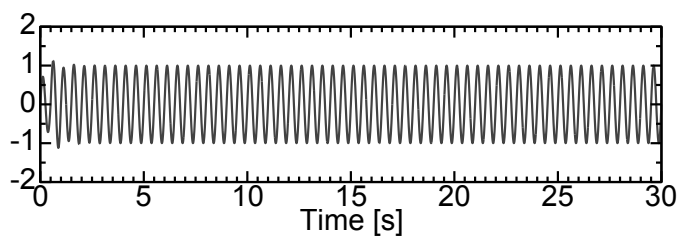


(b) Aperiodic-state extraction $1 - F(z^{-1})$.

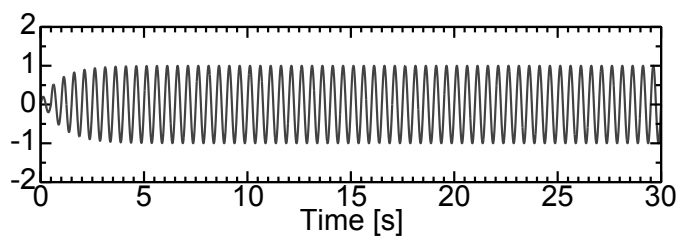
Fig. 2-4: Bode diagrams of the extraction characteristics of the first-order PASF with variations in the separation frequency ρ . The fundamental frequency is $\omega_0 = 2\pi/IT_s = 1$ rad/s.

10 rad/s, (b) $\rho = 1$ rad/s, (c) $\rho = 0.1$ rad/s, and (d) $\rho = 0.01$ rad/s. The time constants (a) $T_c = 0.1$ s, (b) $T_c = 1$ s, (c) $T_c = 10$ s, and (d) $T_c = 100$ s can be confirmed. s denotes the second, which is the base unit of time. (2.24) and the convergence examples indicate that rapid convergence requires a large separation frequency.

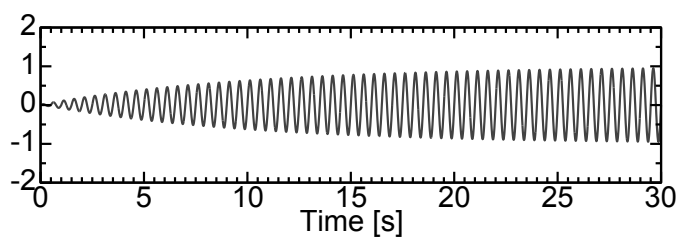
According to the above requirements, there is a tradeoff between the proper periodic-state extraction and rapid convergence. The tradeoff provides the following design strategy of the separation frequency



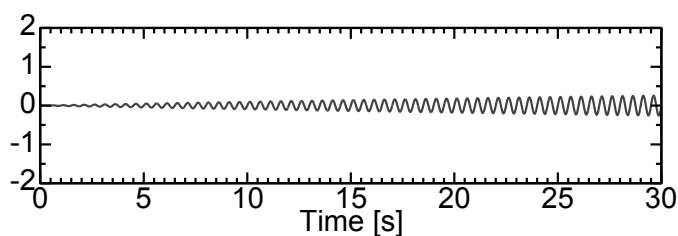
(a) $\rho = 10$ rad/s.



(b) $\rho = 1$ rad/s.



(c) $\rho = 0.1$ rad/s.



(d) $\rho = 0.01$ rad/s.

Fig. 2-5: Four convergence examples of the periodic state \hat{x}_p using the first-order PASF. The input signal is $\sin(4\pi t)$.

ρ . The desired time constant T_{\max} determines an upper limit of the time constant as

$$T_c \leq T_{\max}. \quad (2.25)$$

Using (2.24), the inequality is transformed into

$$\frac{1}{T_{\max}} \leq \rho. \quad (2.26)$$

Since the proper periodic-state extraction requires a minimum separation frequency, the separation frequency can be determined as

$$\rho = \frac{1}{T_{\max}}. \quad (2.27)$$

In order to realize both proper separation and rapid convergence, two separation frequencies for transient response and steady-state response can be used.

Interference Between Estimated Periodic and Aperiodic States

The lifted periodic state $\mathbf{x}_{\tau p}$ and lifted aperiodic state $\mathbf{x}_{\tau a}$ are defined as low-frequency elements and high-frequency elements of a lifted periodic/aperiodic state \mathbf{x}_{τ} , respectively. Although the lifted PASF is designed based on a low-pass filter, it is impossible to separate the lifted periodic/aperiodic state ideally because only an ideal low-pass filter can extract low-frequency elements ideally. Consequently, an actual PASF based on an actual low-pass filter causes interference between the estimated periodic state $\hat{\mathbf{x}}_p$ and estimated aperiodic state $\hat{\mathbf{x}}_a$. The interference can be approximately confirmed as an estimated aperiodic state of an estimated periodic state $\hat{\mathbf{x}}_{ap}$ and an estimated periodic state of an estimated aperiodic state $\hat{\mathbf{x}}_{pa}$. They can be calculated as

$$\begin{cases} \hat{\mathbf{x}}_{ap}(z^{-1}) = [1 - F(z^{-1})]F(z^{-1})\mathbf{x}(z^{-1}) \\ \hat{\mathbf{x}}_{pa}(z^{-1}) = F(z^{-1})[1 - F(z^{-1})]\mathbf{x}(z^{-1}) \end{cases}, \quad (2.28)$$

and

$$\hat{\mathbf{x}}_{ap}(z^{-1}) = \hat{\mathbf{x}}_{pa}(z^{-1}). \quad (2.29)$$

Fig. 2-6 shows Bode diagram of $[1 - F(z^{-1})]F(z^{-1})$, which is an interference transfer function from the state $\mathbf{x}(z^{-1})$ to the interferences $\hat{\mathbf{x}}_{ap}$ and $\hat{\mathbf{x}}_{pa}$. The gain of the transfer function is -5dB at the most; hence, the interference is usually smaller than estimated periodic and aperiodic states. In addition, the Bode diagrams indicate that the interferences of $\rho = 0.1 \text{ rad/s}$ and $\rho = 1 \text{ rad/s}$ are larger than those of $\rho = 0.01 \text{ rad/s}$ and $\rho = 10 \text{ rad/s}$. Fig. 2-7 shows a separation example using $\rho = 1 \text{ rad/s}$ if $tT_s < 20 \text{ s}$ and $\rho = 0.01 \text{ rad/s}$ if $20 \text{ s} \leq tT_s$. The inputted signal was

$$x(t) = \sin 4\pi T_s t + v(t) + w(t), \quad (2.30)$$

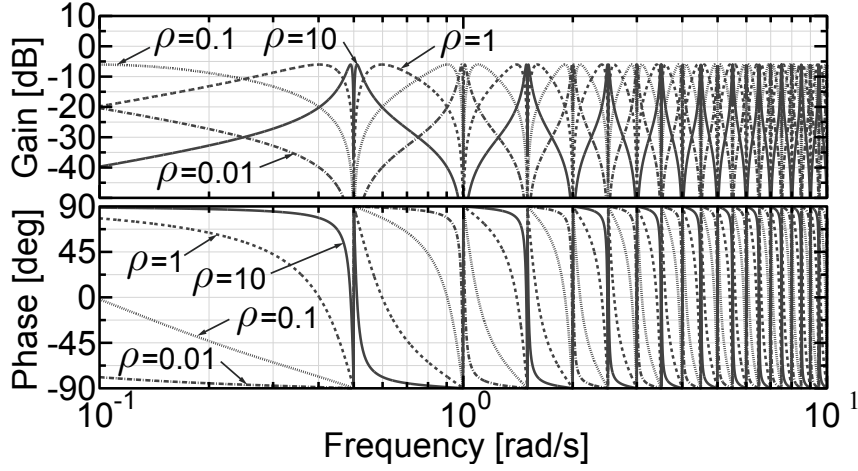


Fig. 2-6: Bode diagram of the interference transfer functions $[1 - F(z^{-1})]F(z^{-1})$. The fundamental frequency is $\omega_0 = 2\pi/\Pi T_s = 1$ rad/s.

where

$$v(t) = \begin{cases} 1 & \text{if } 5.00 \text{ s} \leq tT_s < 5.01 \text{ s or } 20.00 \text{ s} \leq tT_s < 20.01 \text{ s} \\ 0 & \text{otherwise} \end{cases} \quad (2.31)$$

$$w(t) \sim \begin{cases} N(0, 0.1) & \text{if } 10 \text{ s} < tT_s < 13 \text{ s or } 25 \text{ s} < tT_s < 28 \text{ s} \\ N(0, 0) & \text{otherwise} \end{cases} . \quad (2.32)$$

The PASF converged between 0 s and 5 s. The separation example shows that the interference was smaller than the estimated periodic and aperiodic states. Furthermore, the interference of $\rho = 0.01$ rad/s (5 s – 20 s) was smaller than that of $\rho = 1$ rad/s (20 s – 30 s) consistent with the suggestion from the Bode diagram in Fig. 2-6. Therefore, the small interference may be typically ignorable. However, it should be noted that the interference can not be eliminated without using an ideal low-pass filter.

2.2.3 Separation Examples

Separation of Single Sine Wave

Different separation characteristics using the different separation frequencies $\rho = 10$ rad/s, $\rho = 1$ rad/s, $\rho = 0.1$ rad/s, and $\rho = 0.01$ rad/s were verified through separation examples using a sine wave, as shown in Fig 2-8. The initial separation frequency was set to 1 for fast convergence of the PASF in $t \leq 5$ s. The original signal shown in Fig. 2-8(a) was

$$x(t) = \sin 4\pi T_s t + v(t) + w(t), \quad (2.33)$$

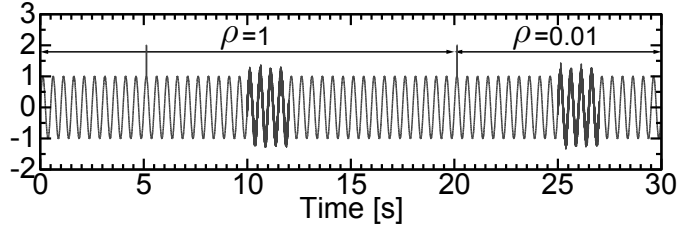
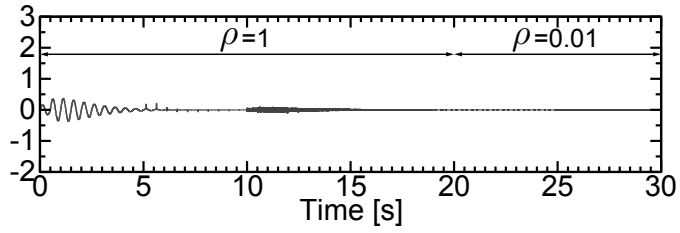
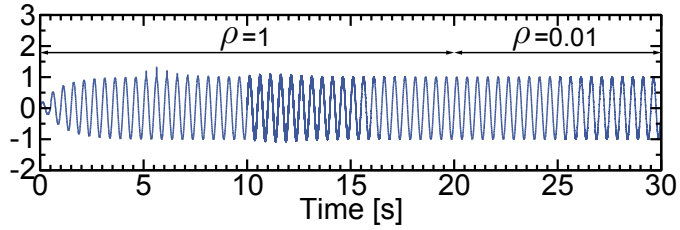
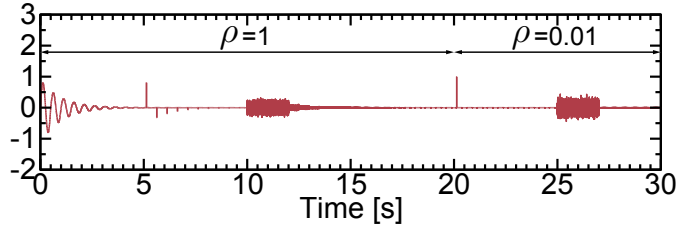

 (a) Original signal x .

 (b) Interference \hat{x}_{ap} and \hat{x}_{pa} .

 (c) Estimated periodic state \hat{x}_p .

 (d) Estimated aperiodic state \hat{x}_a .

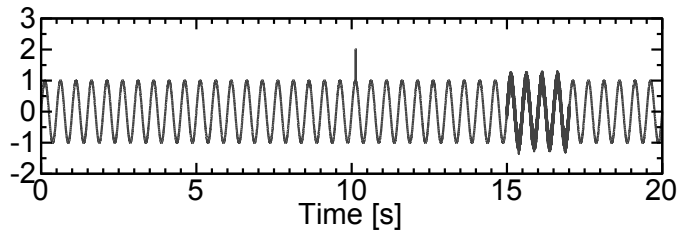
Fig. 2-7: Effects of the interference on the separation. The separation frequencies are $\rho = 1$ rad/s if $tT_s < 20$ s and $\rho = 0.01$ rad/s if $20 \text{ s} \leq tT_s$.

where

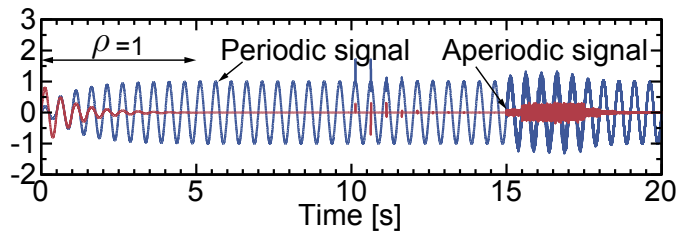
$$v(t) = \begin{cases} 1 & \text{if } 10.125 \text{ s} \leq tT_s < 10.135 \text{ s} \\ 0 & \text{otherwise} \end{cases} \quad (2.34)$$

$$w(t) \sim \begin{cases} N(0, 0.1) & \text{if } 15 \text{ s} < tT_s < 17 \text{ s} \\ N(0, 0) & \text{otherwise} \end{cases} . \quad (2.35)$$

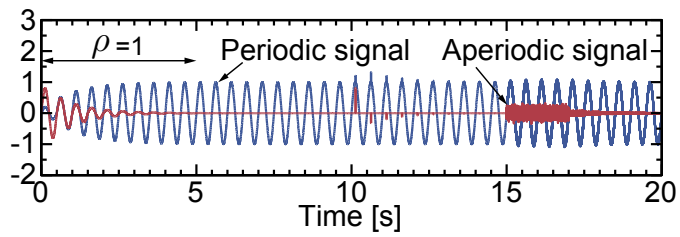
In the case of the largest separation frequency $\rho = 10$ rad/s, the periodic signal was much affected by the pseudo impulse signal $v(t)$ in $10.125 \text{ s} \leq tT_s < 10.135 \text{ s}$ and by the pseudo white noise $w(t)$ in $15 \text{ s} < tT_s < 17 \text{ s}$. In the case of the smallest separation frequency $\rho = 0.01$ rad/s, the sine wave $\sin 4\pi t$ was accurately extracted as the periodic state. Thus, the time range, in which the effects remain after the pseudo impulse signal and pseudo white noise, increases as the separation frequency increases.



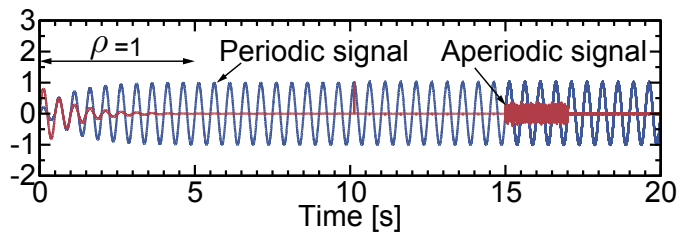
(a) Original signal.



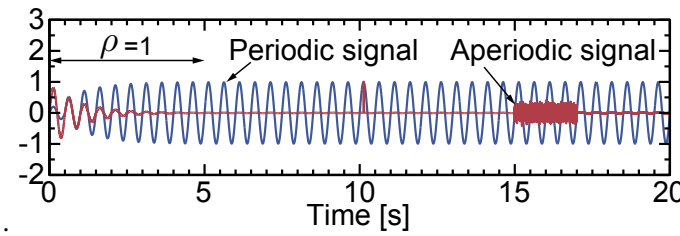
(b) $\rho = 10$ rad/s.



(c) $\rho = 1$ rad/s.



(d) $\rho = 0.1$ rad/s.



(e) $\rho = 0.01$ rad/s.

Fig. 2-8: Estimated periodic states \hat{x}_p of four separation examples using the first-order PASF with variations in the separation frequency ρ . The input signal is (2.33).

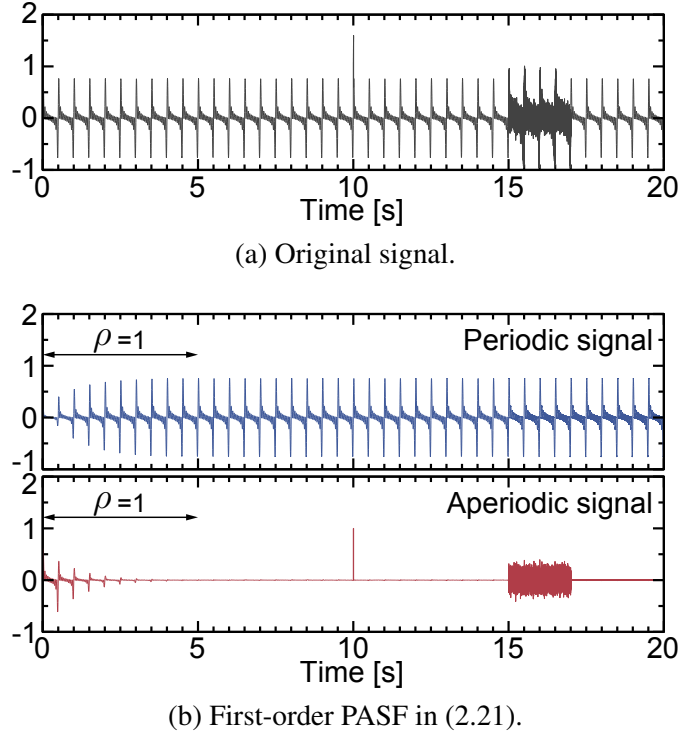


Fig. 2-9: Separation example of the multiple sine waves in (2.36) using the first-order PASF.

Separation of Multiple Sine Waves

The first-order PASF was compared with low-pass and high-pass filters, band-pass and band-stop filters, and comb filters through separation of multiple sine waves. The original signal shown in Fig. 2-9(a) was

$$x(t) = \sum_{i=1}^{10} 0.1 \sin(4\pi iT_s t) + v(t) + w(t), \quad (2.36)$$

where

$$v(t) = \begin{cases} 1 & \text{if } 10.00 \text{ s} \leq tT_s < 10.01 \text{ s} \\ 0 & \text{otherwise} \end{cases} \quad (2.37)$$

$$w(t) \sim \begin{cases} N(0, 0.1) & \text{if } 15 \text{ s} < tT_s < 17 \text{ s} \\ N(0, 0) & \text{otherwise} \end{cases}. \quad (2.38)$$

The low-pass and high-pass filters were

$$\text{LPF}(z^{-1}) = \frac{\mu T_s + \mu T_s z^{-1}}{(\mu T_s + 2) + (\mu T_s - 2)z^{-1}} \quad (2.39)$$

$$\text{HPF}(z^{-1}) = 1 - \text{LPF}(z^{-1}), \quad (2.40)$$

the band-pass and band-stop filters were

$$\text{BPF}(z^{-1}) = \frac{2\mu T_s(1 - z^{-1})}{(\omega_0^2 T_s^2 + 2\mu T_s + 4) + 2(\omega_0^2 T_s^2 - 4)z^{-1} + (\omega_0^2 T_s^2 - 2\mu T_s + 4)z^{-2}} \quad (2.41)$$

$$\text{BSF}(z^{-1}) = 1 - \text{BPF}(z^{-1}), \quad (2.42)$$

and the comb filter proposed by [13] extracted an aperiodic signal and its complementary filter extracted a periodic signal. μ of the low-pass filter and that of the band-pass filter are cutoff frequency and design frequency, respectively. The separation results using the first-order PASF are shown in Fig. 2-9(b), and the separation results using the classical filters are shown in Fig. 2-10. The low-pass and high-pass filters only separated the original signal into the low-frequency and high-frequency waves, respectively, and the band-pass and band-stop filters separated it into the sine wave and the others, respectively. Consequently, they were impossible to extract the periodic signal, which includes a fundamental wave and harmonics. The comb filter could extract the periodic signal, but the extracted periodic signal was much affected by the pseudo impulse signal $v(t)$ and pseudo white noise $w(t)$. Only the first-order PASF achieved to separate the original signal into the periodic signal $\sum_{i=1}^{10} 0.1 \sin(4\pi i \Pi t)$ and the aperiodic signals $v(t)$ and $w(t)$.

2.3 Frequency Estimation

2.3.1 Frequency Estimator

This study developed a frequency estimator to estimate a fundamental frequency ω_0 of a periodic state x_p in a periodic/aperiodic state. Firstly, the band-pass filter:

$$\text{BPF}(z^{-1}, \hat{\omega}_0) = \left[\frac{2g_b T_s(1 - z^{-1})}{(\hat{\omega}_0^2 T_s^2 + 2g_b T_s + 4) + 2(\hat{\omega}_0^2 T_s^2 - 4)z^{-1} + (\hat{\omega}_0^2 T_s^2 - 2g_b T_s + 4)z^{-2}} \right]^2, \quad (2.43)$$

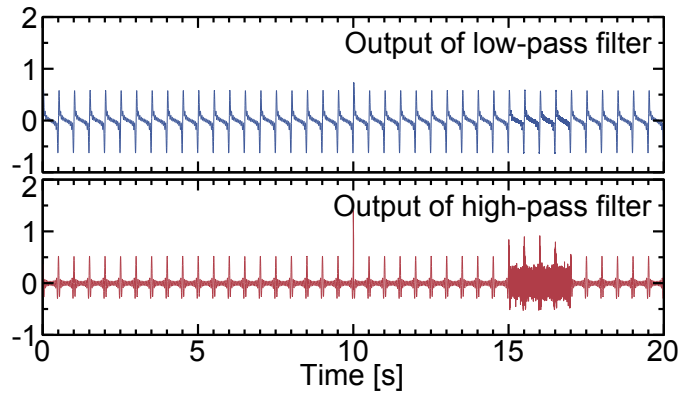
is used to extract a fundamental wave x_p^{fw} from the periodic state x_p including harmonics as

$$\hat{x}_p^{\text{fw}} = \text{BPF}x_p, \quad (2.44)$$

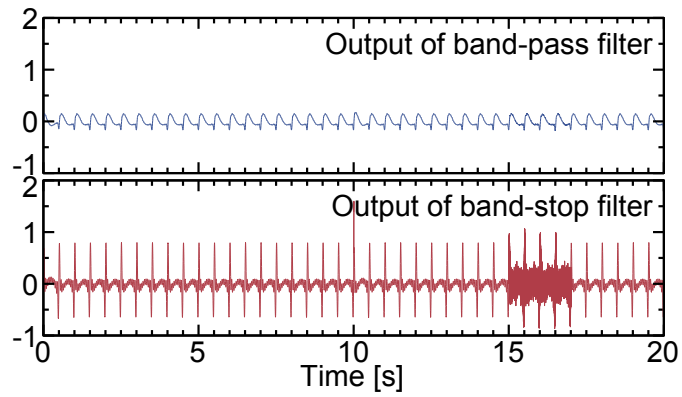
where

$$x_p^{\text{fw}} := a_1 \cos(\omega_0 T_s t) + b_1 \sin(\omega_0 T_s t) \quad (2.45)$$

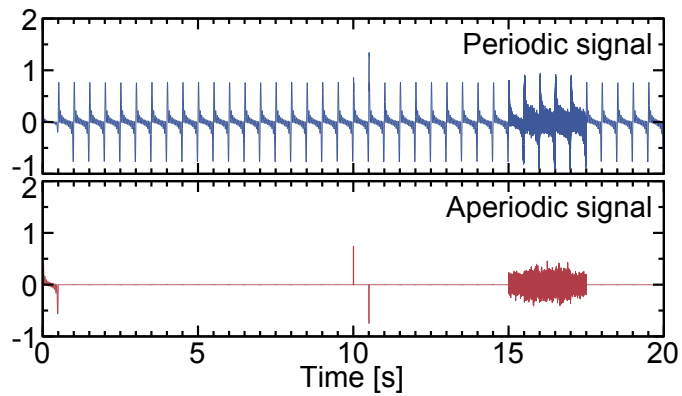
according to (2.3). \hat{x}_p^{fw} denotes the estimated fundamental wave of the periodic state x_p . The design frequency g_b governs the bandwidth, as shown in Fig. 2-11. Since the role of the band-pass filter is to



(a) Low-pass filter and high-pass filter in (2.39) and (2.40).



(b) Band-pass filter and band-stop filter in (2.41) and (2.42).



(c) Comb filter in [13].

Fig. 2-10: Separation examples of the multiple sine waves in (2.36) using the classical filters.

extract the fundamental wave, the parameter g_b needs to be small when amplitudes of harmonics of the periodic state are much larger than that of the fundamental wave. The estimated fundamental wave \hat{x}_p^{fw} is

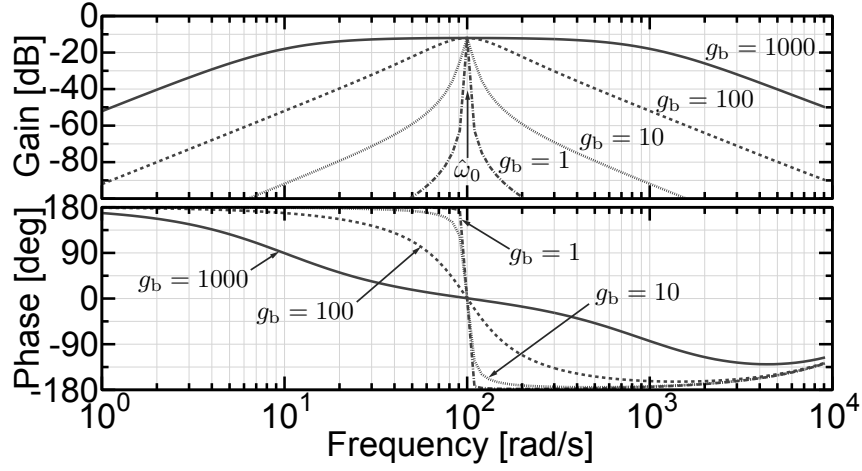


Fig. 2-11: Bode diagram of the band-pass filters with variations in g_b . The other parameters are $\hat{\omega}_0 = 100$ rad/s and $T_s = 0.1$ ms.

inputted into an adaptive notch filter:

$$\hat{\eta}(t) = \alpha(t)\hat{\xi}(t) + \beta(t) \quad (2.46)$$

$$\alpha(t) = -r\hat{\eta}(t-1) + \hat{x}_p^{fw}(t-1) \quad (2.47)$$

$$\beta(t) = -r^2\hat{\eta}(t-2) + \hat{x}_p^{fw}(t) + \hat{x}_p^{fw}(t-2) \quad (2.48)$$

$$\hat{\xi}(t) = -2 \cos[T_s \tilde{\omega}_0(t)], \quad (2.49)$$

where $\eta(t)$, $\hat{\xi}(t)$, r , and $\tilde{\omega}_0(t)$ denote the output, adaptive variable, notch parameter, and fundamental frequency estimated by the adaptive notch filter, respectively. The notch parameter r varies in $0 < r < 1$ and governs the bandwidth of the gain, as shown in Fig. 2-12. The adaptive variable $\hat{\xi}(t)$ is modified by the adaptive algorithm:

$$g(h) = \frac{P(h-1)\alpha(h)}{\lambda + P(h-1)\alpha^2(h)} \quad (2.50)$$

$$e(h) = 0 - \hat{\eta}(h) \quad (2.51)$$

$$\hat{\xi}(h) = \hat{\xi}(h-1) + g(h)e(h) \quad (2.52)$$

$$P(h) = \frac{1}{\lambda}[P(h-1) - g(h)\alpha(h)P(h-1)]. \quad (2.53)$$

h is the discrete-time using the sampling time T_h , which is a slower sampling time than T_s as

$$T_h = \kappa T_s \quad (2.54)$$

$$0 < \kappa. \quad (2.55)$$

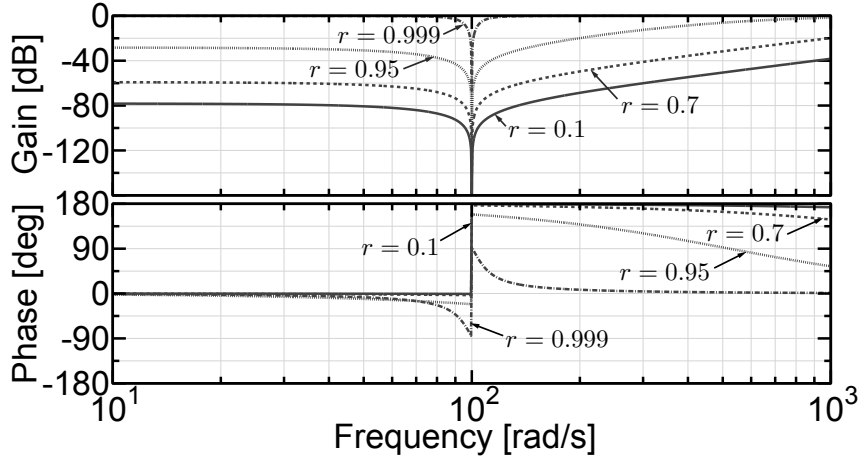


Fig. 2-12: Bode diagram of the notch filters with variations in r . The other parameters are $\xi = -2 \cos(100T_s)$ and $T_s = 0.1$ ms.

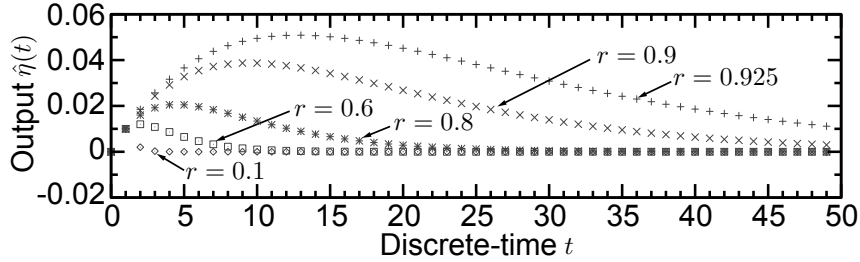


Fig. 2-13: Convergence of the notch filters with variations in the notch parameter r .

The aim of the adaptive notch filter is to estimate an unknown band-stop frequency of an unknown notch filter that eliminates the fundamental wave. To calculate the error in (2.51), the steady-state output of the unknown notch filter: $\eta(h) = 0$ is used. However, as shown in Fig. 2-13, a notch filter needs a transient response for the convergence. Thus, the adaptive algorithm is calculated under another sampling h , that is slower than t , to calculate $e = \eta - \hat{\eta} = 0 - \hat{\eta}$ using steady-state output of the adaptive notch filter. Derivation of the adaptive algorithm is shown in Section 2.3.2. The fundamental frequency $\tilde{\omega}_0(t)$ estimated by the adaptive notch filter is calculated from the estimated adaptive variable $\hat{\xi}(t)$ as

$$\tilde{\omega}_0(t) = \frac{1}{T_s} \cos^{-1}[-0.5\hat{\xi}(t)]. \quad (2.56)$$

Then, the frequency is inputted into a low-pass filter because $\tilde{\omega}_0(t)$ is usually oscillate

$$\hat{\omega}_0 = \text{LPF}\tilde{\omega}_0, \quad (2.57)$$

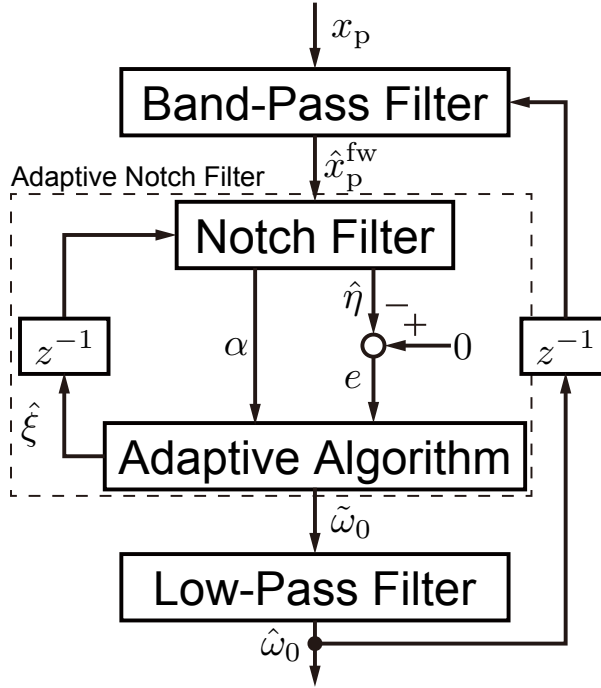


Fig. 2-14: Calculation flow of the frequency estimator.

where

$$\text{LPF}(z^{-1}) = \frac{gT_s + gT_s z^{-1}}{(gT_s + 2) + (gT_s - 2)z^{-1}}. \quad (2.58)$$

Finally, $\hat{\omega}_0(t)$ is the estimated fundamental frequency. An initial frequency for the estimated fundamental frequency needs to use a frequency closer to the fundamental frequency than those of harmonics to avoid convergence at a harmonic frequency. The estimated fundamental frequency is used by the band-pass filter $\text{BPF}(z^{-1}, \hat{\omega}_0)$ in (2.43). An estimated period is calculated by the estimated fundamental frequency as

$$\hat{\Pi} = \frac{2\pi}{\hat{\omega}_0 T_s}. \quad (2.59)$$

Overview of the frequency estimator is shown in Fig. 2-14.

2.3.2 Adaptive Algorithm

The ideal notch filter that eliminates the fundamental wave \hat{x}_p^{fw} is defined as

$$0 = \eta(n) = \alpha(n)\xi + \beta(n) - w(n), \quad (2.60)$$

where $w(n)$ is the effect of extraction errors at the band-pass filter in (2.43). The adaptive algorithm estimates the ideal adaptive variable $\xi(h)$. The error of the adaptive algorithm is calculated by (2.51) as a difference between the ideal output $\eta = 0$ and the output of the notch filter $\hat{\eta}$

$$\begin{aligned} e(h) &= \eta(h) - \hat{\eta}(h) \\ &= 0 - \hat{\eta}(h), \end{aligned} \quad (2.61)$$

where

$$\hat{\eta}(h) = \alpha(h)\hat{\xi}(h-1) + \beta(h). \quad (2.62)$$

The adaptive algorithm is based on the cost function for a recursive-least-square algorithm:

$$J(h) = \sum_{n=1}^h \lambda^{h-n} [e(n)]^2 + \delta \lambda^h [\hat{\xi}(h)]^2 \quad (2.63)$$

$$0 \ll \lambda < 1 \quad (2.64)$$

$$0 < \delta \quad (2.65)$$

according to [103]. λ and δ denote the forgetting factor and the regularization parameter, respectively.

The algorithm for the adaptive variable $\hat{\xi}(h)$ is obtained in accordance with the minimization of the cost function in (2.63) with respect to $\hat{\xi}(h)$. Using the transformed cost function:

$$\begin{aligned} J(h) &= \sum_{n=1}^h \lambda^{h-n} [e(n)]^2 + \delta \lambda^h [\hat{\xi}(h)]^2 \\ &= \sum_{n=1}^h \lambda^{h-n} [\eta(n) - \alpha(n)\hat{\xi}(n) - \beta(n)]^2 + \delta \lambda^h [\hat{\xi}(h)]^2, \end{aligned} \quad (2.66)$$

the condition, which satisfies the minimization of the cost function in (2.63), is calculated as

$$\begin{aligned} \frac{\partial J(h)}{\partial \hat{\xi}(h)} &= 0 \\ &= -2 \sum_{n=1}^h \lambda^{h-n} \alpha(n) [\eta(n) - \alpha(n)\hat{\xi}(h) - \beta(n)] + 2\delta \lambda^h \hat{\xi}(h). \end{aligned} \quad (2.67)$$

Using

$$P(h) = \frac{1}{\sum_{n=1}^h \lambda^{h-n} \alpha^2(n) + \delta \lambda^h}, \quad (2.68)$$

the $\hat{\xi}(h)$ satisfying $\frac{\partial J(h)}{\partial \hat{\xi}(h)} = 0$ is calculated from (2.67) as follows

$$0 = -2 \sum_{n=1}^h \lambda^{h-n} \alpha(n) [\eta(n) - \alpha(n) \hat{\xi}(h) - \beta(n)] + 2\delta \lambda^h \hat{\xi}(h) \quad (2.69)$$

$$2 \sum_{n=1}^h \lambda^{h-n} \alpha^2(n) \hat{\xi}(h) + 2\delta \lambda^h \hat{\xi}(h) = 2 \sum_{n=1}^h \lambda^{h-n} \alpha(n) [\eta(n) - \beta(n)] \quad (2.70)$$

$$\left[\sum_{n=1}^h \lambda^{h-n} \alpha^2(n) + \delta \lambda^h \right] \hat{\xi}(h) = \sum_{n=1}^h \lambda^{h-n} \alpha(n) [\eta(n) - \beta(n)] \quad (2.71)$$

$$\hat{\xi}(h) = P(h) \sum_{n=1}^h \lambda^{h-n} \alpha(n) [\eta(n) - \beta(n)]. \quad (2.72)$$

From (2.68), the recursive $P^{-1}(h)$ is

$$P^{-1}(h) = \lambda P^{-1}(h-1) + \alpha^2(h), \quad (2.73)$$

and $P^{-1}(h-1)$ is

$$P^{-1}(h-1) = \lambda^{-1} [P^{-1}(h) - \alpha^2(h)]. \quad (2.74)$$

(2.72) is further transformed into a recursive equation as follows

$$\begin{aligned} \hat{\xi}(h) &= P(h) \sum_{n=1}^h \lambda^{h-n} \alpha(n) [\eta(n) - \beta(n)] \\ &= P(h) \sum_{n=1}^{h-1} \lambda^{h-n} \alpha(n) [\eta(n) - \beta(n)] + P(h) \alpha(h) [\eta(h) - \beta(h)] \\ &= P(h) \lambda \sum_{n=1}^{h-1} \lambda^{h-1-n} \alpha(n) [\eta(n) - \beta(n)] + P(h) \alpha(h) [\eta(h) - \beta(h)] \\ &= P(h) \lambda P^{-1}(h-1) P(h-1) \sum_{n=1}^{h-1} \lambda^{h-1-n} \alpha(n) [\eta(n) - \beta(n)] + P(h) \alpha(h) [\eta(h) - \beta(h)] \\ &= P(h) \lambda P^{-1}(h-1) \hat{\xi}(h-1) + P(h) \alpha(h) [\eta(h) - \beta(h)] \\ &= P(h) \lambda \lambda^{-1} [P^{-1}(h) - \alpha^2(h)] \hat{\xi}(h-1) + P(h) \alpha(h) [\eta(h) - \beta(h)] \\ &= \hat{\xi}(h-1) - P(h) \alpha^2(h) \hat{\xi}(h-1) + P(h) \alpha(h) [\eta(h) - \beta(h)] \\ &= \hat{\xi}(h-1) + P(h) \alpha(h) [\eta(h) - \alpha(h) \hat{\xi}(h-1) - \beta(h)] \\ &= \hat{\xi}(h-1) + P(h) \alpha(h) e(h). \end{aligned} \quad (2.75)$$

The calculation of $\hat{\xi}(h)$ for the algorithm is obtained as

$$\hat{\xi}(h) = \hat{\xi}(h-1) + g(h)e(h), \quad (2.76)$$

with the gain $g(h)$:

$$g(h) = P(h)\alpha(h) \quad (2.77)$$

$$g(h) = \frac{P(h-1)\alpha(h)}{\lambda + P(h-1)\alpha^2(h)}. \quad (2.78)$$

From (2.73), $P(h)$ is further rewritten into

$$\begin{aligned} P(h) &= \frac{1}{\lambda P^{-1}(h-1) + \alpha^2(h)} \\ &= \frac{P(h-1)}{\lambda + P(h-1)\alpha^2(h)} \\ &= \frac{1}{\lambda} \frac{\lambda}{\lambda + P(h-1)\alpha^2(h)} P(h-1) \\ &= \frac{1}{\lambda} \left[1 - \frac{P(h-1)\alpha(h)}{\lambda + P(h-1)\alpha^2(h)} \alpha(h) \right] P(h-1) \\ &= \frac{1}{\lambda} [1 - g(h)\alpha(h)] P(h-1) \\ &= \frac{1}{\lambda} [P(h-1) - g(h)\alpha(h)P(h-1)]. \end{aligned} \quad (2.79)$$

The adaptive algorithm was thus obtained. A calculation flow of the adaptive notch filter is shown in Fig. 2-15.

2.3.3 Convergence of Adaptive Algorithm

This subsection evaluates convergence of the adaptive algorithm under a stationary environment that assumes a unity forgetting factor $\lambda = 1$. Existence of the estimated fundamental wave is assumed as

$$\hat{x}_p^{\text{fw}}(t) \neq 0. \quad (2.80)$$

In addition, this evaluation assumes

$$|r\hat{\eta}(t)| < |\hat{x}_p^{\text{fw}}(t)|, \quad (2.81)$$

because the steady-state output $\hat{\eta}(h)$ of the notch filter is smaller than the estimated fundamental wave $\hat{x}_p^{\text{fw}}(t)$ according to Fig. 2-12. Moreover, r is designed in $0 < r < 1$. The evaluation firstly considers

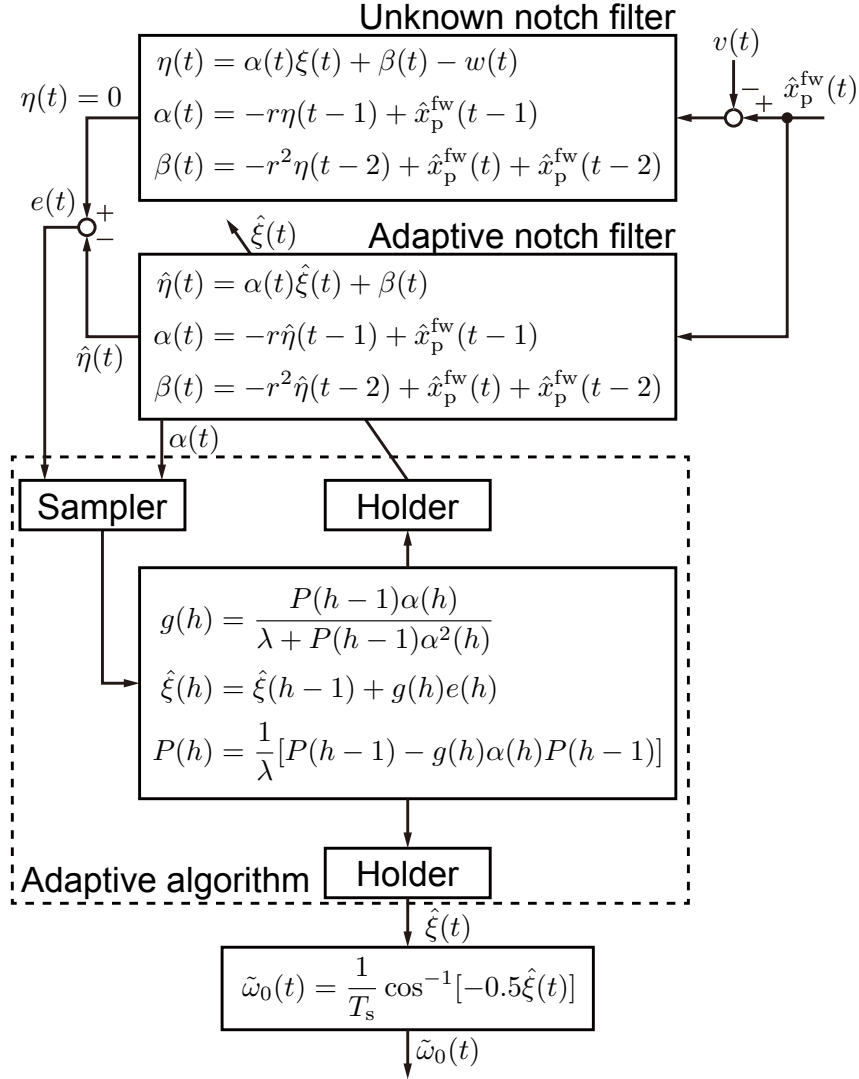


Fig. 2-15: Calculation flow of the adaptive notch filter.

convergence of $1/[\sum_{n=1}^h \alpha^2(n)]$ as

$$\lim_{h \rightarrow \infty} \frac{1}{\sum_{n=1}^h \alpha^2(n)} = \lim_{h \rightarrow \infty} \frac{1}{\sum_{n=1}^h [-r\hat{\eta}(n-1) + \hat{x}_p^{fw}(n-1)]^2}. \quad (2.82)$$

According to (2.81), $r\hat{\eta}(n-1)$ and $\hat{x}_p^{fw}(n-1)$ are not equal and provide

$$0 < [-r\hat{\eta}(n-1) + \hat{x}_p^{fw}(n-1)]^2. \quad (2.83)$$

This derives the convergence of (2.82) as

$$\lim_{h \rightarrow \infty} \frac{1}{\sum_{n=1}^h \alpha^2(n)} = \lim_{h \rightarrow \infty} \frac{1}{\sum_{n=1}^h [-r\hat{\eta}(n-1) + \hat{x}_p^{fw}(n-1)]^2} = 0. \quad (2.84)$$

According to (2.84) and (2.65), $P(h)$ converges at zero

$$\lim_{h \rightarrow \infty} P(h) = \lim_{h \rightarrow \infty} \frac{1}{\sum_{n=1}^h \alpha^2(n) + \delta} = 0. \quad (2.85)$$

Also, the gain $g(h)$ in (2.77) becomes zero

$$\lim_{h \rightarrow \infty} g(h) = \lim_{h \rightarrow \infty} P(h)\alpha(h) = 0, \quad (2.86)$$

and the estimated adaptive variable calculated by (2.76) becomes

$$\hat{\xi}(h) = \hat{\xi}(h-1). \quad (2.87)$$

In conclusion, $P(h)$, $g(h)$, and $\hat{\xi}(h)$ are convergent.

Next, the estimation accuracy is discussed. Although the band-pass filter in (2.43) extracts a fundamental wave of a periodic state x_p , the extraction errors $v(h)$ deteriorates accuracy of the adaptive variable estimation. Usually, the extraction errors $v(h)$ include harmonics and aperiodic disturbances, and the error affects the output of the unknown notch filter in (2.60) as

$$w(k) = [-rw(k-1) + v(k-1)]\xi - r^2w(k-2) + v(k) + v(k-2). \quad (2.88)$$

By substituting 1 for the forgetting factor λ , (2.71) is transformed into

$$\hat{\xi}(h) = \frac{\sum_{n=1}^h \alpha(n)[\eta(n) - \beta(n)]}{\sum_{n=1}^h \alpha^2(n) + \delta}. \quad (2.89)$$

This is further transformed as follows

$$\begin{aligned} \hat{\xi}(h) &= \frac{\sum_{n=1}^h \alpha(n)[\alpha(n)\xi + \beta(n) - w(n) - \beta(n)]}{\sum_{n=1}^h \alpha^2(n) + \delta} \\ &= \frac{\sum_{n=1}^h \alpha(n)[\alpha(n)\xi - w(n)]}{\sum_{n=1}^h \alpha^2(n) + \delta} \\ &= \frac{\sum_{n=1}^h \alpha^2(n)}{\sum_{n=1}^h \alpha^2(n) + \delta} \xi - \frac{\sum_{n=1}^h \alpha(n)}{\sum_{n=1}^h \alpha^2(n) + \delta} w(n). \end{aligned} \quad (2.90)$$

In order to let $\hat{\xi}(h)$ converge to the true value $\xi(h)$, $\frac{\sum_{n=1}^h \alpha^2(n)}{\sum_{n=1}^h \alpha^2(n) + \delta}$ and $\frac{\sum_{n=1}^h \alpha(n)w(n)}{\sum_{n=1}^h \alpha^2(n) + \delta}$ need to be 1 and 0, respectively. The regularization parameter δ adjusts them in the tradeoff: a small δ sets the first term to 1 and a large δ reduces the influence of $w(n)$. Alternatively, modification of the band-pass filter in (2.43) can directly reduce amplitude of $w(n)$.

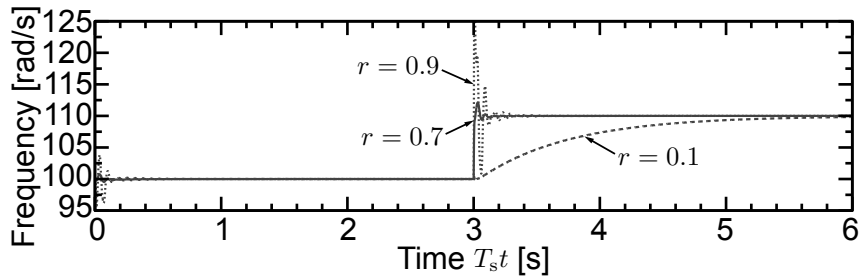


Fig. 2-16: Step frequency estimations for the frequency-varying sine wave in (2.91) with variations in r . The standard parameters are $\hat{\omega}_0(0) = 100$ rad/s, $\kappa = 10$, $\lambda = 0.999$, $\delta = 1000$, $g = 1000$ rad/s, $g_b = 1000$ rad/s, and $T_s = 0.1$ ms.

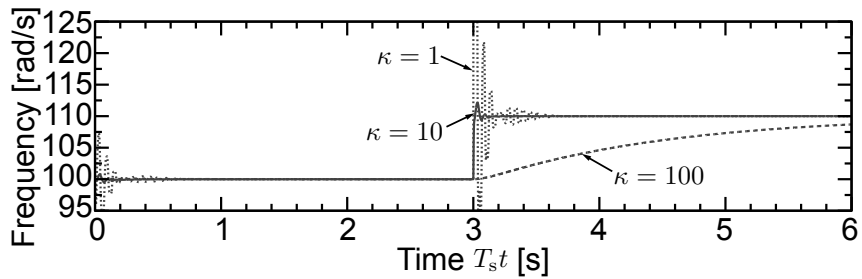


Fig. 2-17: Step frequency estimations for the frequency-varying sine wave in (2.91) with variations in κ . The standard parameters are $\hat{\omega}_0(0) = 100$ rad/s, $r = 0.7$, $\lambda = 0.999$, $\delta = 1000$, $g = 1000$ rad/s, $g_b = 1000$ rad/s, and $T_s = 0.1$ ms.

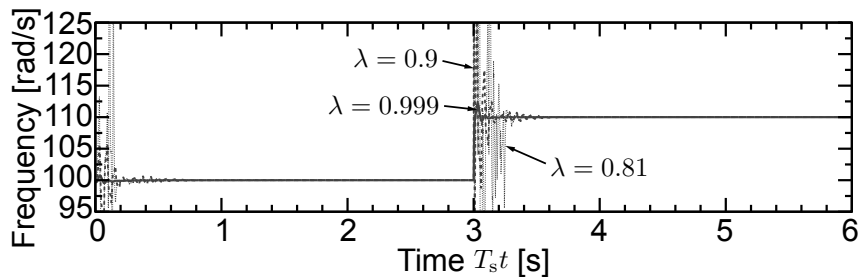


Fig. 2-18: Step frequency estimations for the frequency-varying sine wave in (2.91) with variations in λ . The standard parameters are $\hat{\omega}_0(0) = 100$ rad/s, $r = 0.7$, $\kappa = 10$, $\delta = 1000$, $g = 1000$ rad/s, $g_b = 1000$ rad/s, and $T_s = 0.1$ ms.

2.3.4 Frequency-Estimation Examples

The frequency estimator has the six design parameters: r , κ , λ , δ , g , and g_b . The effects of the variations in the parameters on the frequency estimation are shown with examples.

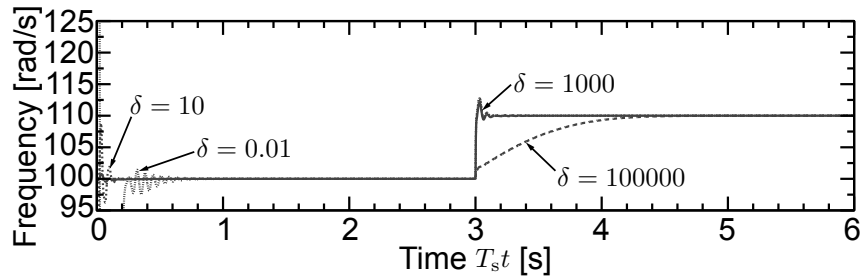


Fig. 2-19: Step frequency estimations for the frequency-varying sine wave in (2.91) with variations in δ . The standard parameters are $\hat{\omega}_0(0) = 100$ rad/s, $r = 0.7$, $\kappa = 10$, $\lambda = 0.999$, $g = 1000$ rad/s, $g_b = 1000$ rad/s, and $T_s = 0.1$ ms.

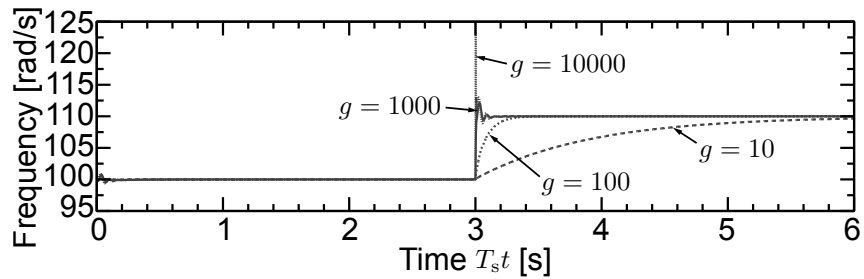


Fig. 2-20: Step frequency estimations for the frequency-varying sine wave in (2.91) with variations in g . The standard parameters are $\hat{\omega}_0(0) = 100$ rad/s, $r = 0.7$, $\kappa = 10$, $\lambda = 0.999$, $\delta = 1000$, $g_b = 1000$ rad/s, and $T_s = 0.1$ ms.

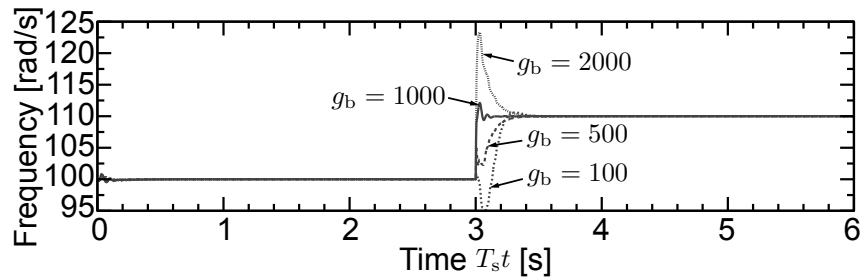


Fig. 2-21: Step frequency estimations for the frequency-varying sine wave in (2.91) with variations in g_b . The standard parameters are $\hat{\omega}_0(0) = 100$ rad/s, $r = 0.7$, $\kappa = 10$, $\lambda = 0.999$, $\delta = 1000$, $g = 1000$ rad/s, and $T_s = 0.1$ ms.

First, the frequency estimator is used to estimate a fundamental frequency of the frequency-varying

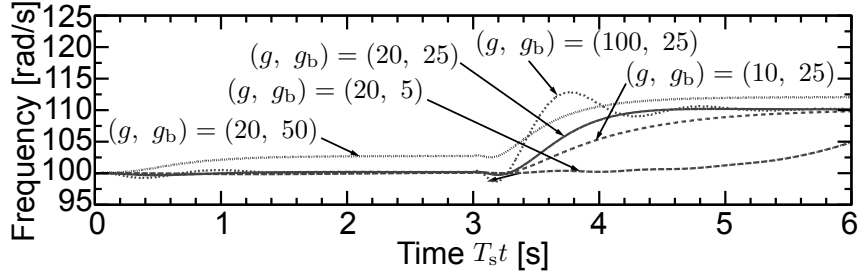


Fig. 2-22: Step frequency estimations for a periodic state including harmonics in (2.92). The other parameters are $\hat{\omega}_0(0) = 100$ rad/s, $r = 0.7$, $\kappa = 10$, $\lambda = 0.999$, $\delta = 1000$, and $T_s = 0.1$ ms.

sine wave:

$$x(t) = \begin{cases} \sin(100T_s t) & T_s t < 3 \text{ s} \\ \sin(110T_s t) & 3 \text{ s} \leq T_s t \end{cases} \quad (2.91)$$

Fig. 2-16 shows the oscillate response and slow convergence when the notch parameter r is large and small, respectively. Using r and Fig. 2-13, the multi-rate ratio κ can be determined to wait for the convergence of the notch filter. According to Fig. 2-17, a very small κ induces an oscillating response. The forgetting factor λ is typically selected as a positive value close to, but less than, unity. A small λ deteriorates the transient response, as shown in Fig. 2-18. A small δ realizes high-speed response and a large δ smooths the estimated frequency, as shown in Fig. 2-19. In Figs. 2-20 and 2-21, the cutoff frequency g of the low-pass filter suppresses oscillations of the estimated fundamental frequency, and the design frequency g_b of the band-pass filter changes the transient response. However, the two parameters should be designed in accordance with the example of the fundamental-frequency estimation from a periodic disturbance including harmonics.

Next, the frequency estimator is used to estimate a fundamental frequency of the frequency-varying multiple sine waves:

$$x(t) = \begin{cases} \sum_{n=1}^{10} \sin(n100T_s t) & T_s t < 3 \text{ s} \\ \sum_{n=1}^{10} \sin(n110T_s t) & 3 \text{ s} \leq T_s t \end{cases} \quad (2.92)$$

including ten harmonics. Fig. 2-22 shows the estimation results using five combinations of g and g_b . The cutoff frequency g and design frequency g_b modify the oscillations and steady-state offset caused by the harmonics, respectively. The cutoff frequencies g and g_b are determined with consideration of the characteristics and the convergence time.

2.4 Summary

In Section 2.2, the periodic/apperiodic state was transformed using the lifting technique into the lifted periodic/apperiodic state, in which a constant element was defined as the lifted perfect periodic state. The low-frequency elements were defined as the lifted periodic state, and the high-frequency elements were defined as the lifted aperiodic state. A boundary frequency between the lifted periodic and aperiodic states is called the separation frequency. Based on the definitions, the lifted PASF that separates the lifted periodic/apperiodic state into the lifted periodic and aperiodic states was constructed, and the inverse lifting derived the PASF that separates the periodic/apperiodic state into the periodic and aperiodic states. As a design example of the PASF, this section showed the first-order PASF. Then, the design of the separation frequency and interference of the first-order PASF were discussed. Finally, the separation examples using a sine wave validated the effect of the separation frequency, and the separation examples using multiple sine waves compared the first-order PASF with classical filters.

In Section 2.3, the frequency estimator was constructed based on an adaptive notch filter. The band-pass filter was used to extract a fundamental wave from a periodic/apperiodic state. Then, the adaptive notch filter estimates a fundamental frequency of the fundamental wave, and the low-pass filter attenuates oscillation of the estimated fundamental wave. The adaptive algorithm for the adaptive notch filter was derived in accordance with the minimization of square estimation error, and its convergence was analyzed. Finally, the frequency-estimation examples were shown with variations in six design parameters. Although the frequency estimator can be used for acquiring an unknown frequency for the PASF, this dissertation discusses the PASF without the frequency estimator. This is because the PASF is linear despite the nonlinear frequency estimator. In order to analyze the PASF under the linearity, the period used by the PASF is assumed to be constant or be given by a steady-state frequency estimator.

Chapter 3

Periodic/Aperiodic State Control

3.1 Outline

Chapter 3 focuses on periodicity and aperiodicity of state control.

Section 3.2 constructs periodic/aperiodic state feedback control for the periodic/aperiodic state by using the PASF. Subsection 3.2.1 describes the structure of the periodic/aperiodic state feedback control based on the PASF. Then, a separation principle and design proposition for the periodic/aperiodic state feedback control are proved as Theorem 1 and Proposition 1, respectively in Subsection 3.2.2. The separation principle and proposition guarantee the simplified design of the periodic/aperiodic state feedback control.

Section 3.3 constructs periodic/aperiodic motion control by developing the periodic/aperiodic state feedback control into motion control framework. Subsection 3.3.1 designs an ACS using a DOB for disturbance compensation, and Subsection 3.3.2 constructs six periodic/aperiodic motion controls by assigning velocity, force, and impedance controls to periodic and aperiodic motions upon the ACS. Subsection 3.3.3 shows experiments that validated practical performance of the six periodic/aperiodic motion controls.

3.2 Separated Periodic/Aperiodic State Feedback Control

3.2.1 Control System

Consider the discrete-time linear time-invariant system

$$\begin{cases} \mathbf{x}(t+1) = \mathbf{A}\mathbf{x}(t) + \mathbf{B}\mathbf{u}(t) \\ \mathbf{y}(t) = \mathbf{C}\mathbf{x}(t) + \mathbf{D}\mathbf{u}(t) \end{cases}, \quad (3.1)$$

where

$$\mathbf{x}(t) \in \mathbb{R}^n, \mathbf{y}(t) \in \mathbb{R}^m, \mathbf{u}(t) \in \mathbb{R}^p, \mathbf{A} \in \mathbb{R}^{n \times n}, \mathbf{B} \in \mathbb{R}^{n \times p}, \mathbf{C} \in \mathbb{R}^{m \times n}, \mathbf{D} \in \mathbb{R}^{m \times p}. \quad (3.2)$$

$\mathbf{x}(t)$ is the state variable, $\mathbf{y}(t)$ is the output, and $\mathbf{u}(t)$ is the input. \mathbf{A} , \mathbf{B} , \mathbf{C} , and \mathbf{D} are the system matrices. The system is assumed to be controllable and observable. A state observer

$$\begin{cases} \hat{\mathbf{x}}(t+1) = \mathbf{A}\hat{\mathbf{x}}(t) + \mathbf{B}\mathbf{u}(t) + \mathbf{L}\{\mathbf{y}(t) - \hat{\mathbf{y}}(t)\} \\ \hat{\mathbf{y}}(t) = \mathbf{C}\hat{\mathbf{x}}(t) + \mathbf{D}\mathbf{u}(t) \\ \mathbf{e}(t) := \mathbf{x}(t) - \hat{\mathbf{x}}(t) \in \mathbb{R}^n \end{cases} \quad (3.3)$$

is used to estimate the state of the system, where $\mathbf{e}(t)$ and $\mathbf{L} \in \mathbb{R}^{n \times m}$ are the estimation error and observation gain, respectively. The PASF is used to extract estimated periodic state $\tilde{\mathbf{x}}_p(t)$ and estimated aperiodic states $\tilde{\mathbf{x}}_a(t)$ from the estimated state $\hat{\mathbf{x}}(t)$ as

$$\begin{cases} \tilde{\mathbf{x}}_p(t) = \sum_{i=0}^{l-1} [p_i \tilde{\mathbf{x}}_p(t - \Pi - i\Pi) + q_i \hat{\mathbf{x}}(t - i\Pi)] \\ \tilde{\mathbf{x}}_a(t) = \hat{\mathbf{x}}(t) - \tilde{\mathbf{x}}_p(t) \\ \boldsymbol{\epsilon}(k) := \hat{\mathbf{x}}_p(k) - \tilde{\mathbf{x}}_p(k) \in \mathbb{R}^n \end{cases}, \quad (3.4)$$

where $\boldsymbol{\epsilon}(k)$ is the separation error. The control input is calculated by using the estimated periodic and aperiodic states as

$$\mathbf{u}(t) = \mathbf{u}_p(t) + \mathbf{u}_a(t), \quad (3.5)$$

where

$$\mathbf{u}_p(t) = -\mathbf{F}_p \tilde{\mathbf{x}}_p(t) \quad (3.6)$$

$$\mathbf{u}_a(t) = -\mathbf{F}_a \tilde{\mathbf{x}}_a(t). \quad (3.7)$$

$\mathbf{u}_p(t)$, $\mathbf{u}_a(t)$, $\mathbf{F}_p \in \mathbb{R}^{p \times n}$, and $\mathbf{F}_a \in \mathbb{R}^{p \times n}$ are the periodic input, aperiodic input, periodic feedback gain, and aperiodic feedback gain, respectively. A block diagram of the periodic/aperiodic state feedback control is shown in Fig. 3-1.

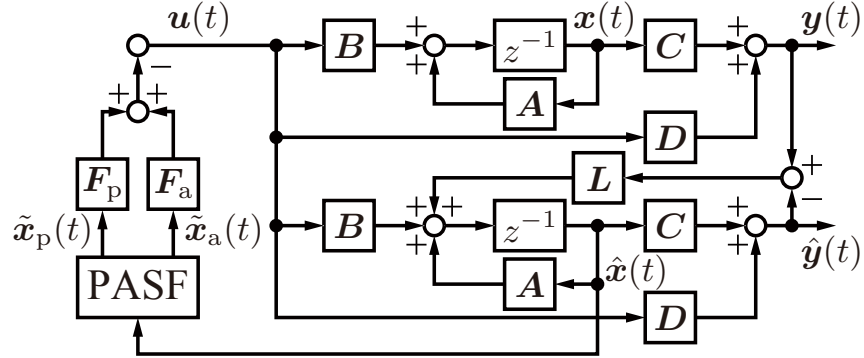


Fig. 3-1: Block diagram of the periodic/aperiodic state feedback control.

3.2.2 Separated Stabilities

Preliminaries

A lifted periodic/aperiodic state feedback control system is calculated as preliminaries using (2.5). The lifted linear discrete-time system is

$$\begin{cases} \mathbf{x}_\tau(k+1) = \tilde{\mathbf{A}}\mathbf{x}_\tau(k) + \tilde{\mathbf{B}}\mathbf{u}_\tau(k) \\ \mathbf{y}_\tau(k) = \tilde{\mathbf{C}}\mathbf{x}_\tau(k) + \tilde{\mathbf{D}}\mathbf{u}_\tau(k) \end{cases}, \quad (3.8)$$

where

$$\mathbf{y}_\tau(k) := \mathbf{y}(k\Pi + \tau) \in \mathbb{R}^m \quad (3.9)$$

$$\mathbf{u}_\tau(k) := \begin{bmatrix} \mathbf{u}(k\Pi + \tau) \\ \mathbf{u}(k\Pi + \tau + 1) \\ \vdots \\ \mathbf{u}(k\Pi + \tau + \Pi - 1) \end{bmatrix} \in \mathbb{R}^{p\Pi} \quad (3.10)$$

$$\tilde{\mathbf{A}} = \mathbf{A}^\Pi \in \mathbb{R}^{n \times n} \quad (3.11)$$

$$\tilde{\mathbf{B}} = [\mathbf{A}^{\Pi-1}\mathbf{B} \quad \mathbf{A}^{\Pi-2}\mathbf{B} \quad \dots \quad \mathbf{B}] \in \mathbb{R}^{n \times p\Pi} \quad (3.12)$$

$$\tilde{\mathbf{C}} = \mathbf{C} \in \mathbb{R}^{m \times n} \quad (3.13)$$

$$\tilde{\mathbf{D}} = [\mathbf{D} \quad \mathbf{0} \quad \dots \quad \mathbf{0}] \in \mathbb{R}^{m \times p\Pi}. \quad (3.14)$$

The lifted state observer is

$$\begin{cases} \hat{\mathbf{x}}_\tau(k+1) = \tilde{\mathbf{A}}\hat{\mathbf{x}}_\tau(k) + \tilde{\mathbf{B}}\mathbf{u}_\tau(k) + \tilde{\mathbf{L}}\{\eta_\tau(k) - \hat{\eta}_\tau(k)\} \\ \hat{\mathbf{y}}_\tau(k) = \tilde{\mathbf{C}}\hat{\mathbf{x}}_\tau(k) + \tilde{\mathbf{D}}\mathbf{u}_\tau(k) \\ \mathbf{e}_\tau(k) := \mathbf{x}_\tau(k) - \hat{\mathbf{x}}_\tau(k) \in \mathbb{R}^n \end{cases}, \quad (3.15)$$

where

$$\boldsymbol{\eta}_\tau(k) := \begin{bmatrix} \mathbf{y}_\tau(k) \\ \mathbf{y}_{\tau+1}(k) \\ \vdots \\ \mathbf{y}_{\tau+\Pi-1}(k) \end{bmatrix} \in \mathbb{R}^{m\Pi} \quad (3.16)$$

$$\tilde{\mathbf{L}} = [\mathbf{A}^{\Pi-1} \mathbf{L} \quad \mathbf{A}^{\Pi-2} \mathbf{L} \quad \dots \quad \mathbf{L}] \in \mathbb{R}^{n \times m\Pi}. \quad (3.17)$$

The lifted PASF is

$$\begin{cases} \tilde{\mathbf{x}}_{\tau p}(k) = \sum_{i=0}^{l-1} [p_i \tilde{\mathbf{x}}_{\tau p}(k-1-i) + q_i \hat{\mathbf{x}}_\tau(k-i)] \\ \tilde{\mathbf{x}}_{\tau a}(k) = \hat{\mathbf{x}}_\tau(k) - \tilde{\mathbf{x}}_{\tau p}(k) \\ \boldsymbol{\epsilon}_\tau(k) := \hat{\mathbf{x}}_{\tau p}(k) - \tilde{\mathbf{x}}_{\tau p}(k) \in \mathbb{R}^n \end{cases}, \quad (3.18)$$

and the lifted separation error $\boldsymbol{\epsilon}_\tau(k)$ is expressed as

$$\boldsymbol{\xi}_\tau(k) := \begin{bmatrix} \boldsymbol{\epsilon}_\tau(k-l+1) \\ \vdots \\ \boldsymbol{\epsilon}_\tau(k-1) \\ \boldsymbol{\epsilon}_\tau(k) \end{bmatrix} \in \mathbb{R}^{nl} \quad (3.19)$$

$$\boldsymbol{\Xi}_\tau(k) := \begin{bmatrix} \boldsymbol{\xi}_\tau(k) \\ \boldsymbol{\xi}_{\tau+1}(k) \\ \vdots \\ \boldsymbol{\xi}_{\tau+\Pi-1}(k) \end{bmatrix} \in \mathbb{R}^{n\Pi} \quad (3.20)$$

Assumption 1 is set to prove Theorem 1.

Assumption 1. The PASF ideally separates the estimated state $\hat{\mathbf{x}}(t)$ into the separated periodic state $\hat{\mathbf{x}}_p(t)$ and separated aperiodic state $\hat{\mathbf{x}}_a(t)$ as

$$\begin{cases} \hat{\mathbf{x}}_p(t) = \sum_{i=0}^{l-1} [p_i \hat{\mathbf{x}}_p(t-\Pi-i\Pi) + q_i \hat{\mathbf{x}}(t-i\Pi)] \\ \hat{\mathbf{x}}_a(t) = \hat{\mathbf{x}}(t) - \hat{\mathbf{x}}_p(t) \end{cases}, \quad (3.21)$$

if the initial lifted separation error $\boldsymbol{\epsilon}(0)$ is zero.

Separation Principle

The separation principle for the periodic/aperiodic state feedback control is established.

Theorem 1. The pole placement of the lifted periodic/aperiodic state feedback control system is equal to the independent pole placements of the closed-loop dynamics: $(\mathbf{A} - \mathbf{B}\mathbf{F}_p)^\Pi$ for the lifted periodic state $\mathbf{x}_{\tau p}(k)$, $(\mathbf{A} - \mathbf{B}\mathbf{F}_a)^\Pi$ for the lifted aperiodic state $\mathbf{x}_{\tau a}(k)$, $(\mathbf{A} - \mathbf{L}\mathbf{C})^\Pi$ for the lifted periodic estimation

error $e_{\tau p}(k)$ and lifted aperiodic estimation error $e_{\tau a}(k)$, and \mathcal{P} for the lifted periodic separation error $\Xi_{\tau p}(k)$ and lifted aperiodic separation error $\Xi_{\tau a}(k)$.

Proof. First, closed-loop dynamics of the PASF are considered with the lifted separation error $\epsilon_{\tau}(k)$ in (3.18). According to the separation of the lifted PASF in (3.18) and the ideal separation in (3.21) without the lifted separation error, the dynamics of the lifted separation error are calculated as follows

$$\begin{aligned} \epsilon_{\tau}(k) &= \hat{\mathbf{x}}_{\tau p}(k) - \tilde{\mathbf{x}}_{\tau p}(k) \\ &= \sum_{i=0}^{l-1} [p_i \hat{\mathbf{x}}_{\tau p}(k-1-i) + q_i \hat{\mathbf{x}}_{\tau}(k-i)] - \sum_{i=0}^{l-1} [p_i \tilde{\mathbf{x}}_{\tau p}(k-1-i) + q_i \hat{\mathbf{x}}_{\tau}(k-i)] \\ &= \sum_{i=0}^{l-1} p_i \epsilon_{\tau}(k-1-i). \end{aligned} \quad (3.22)$$

(3.22) is rewritten as

$$\xi_{\tau}(k+1) = \tilde{\mathbf{P}} \xi_{\tau}(k), \quad (3.23)$$

where

$$\tilde{\mathbf{P}} = \begin{bmatrix} \mathbf{0} & \mathbf{I} & \mathbf{0} & \cdots & \mathbf{0} \\ \vdots & \ddots & \ddots & \ddots & \vdots \\ \mathbf{0} & \cdots & \mathbf{0} & \mathbf{I} & \mathbf{0} \\ \mathbf{0} & \cdots & \mathbf{0} & \mathbf{0} & \mathbf{I} \\ p_{l-1} \mathbf{I} & p_{l-2} \mathbf{I} & \cdots & p_1 \mathbf{I} & p_0 \mathbf{I} \end{bmatrix} \in \mathbb{R}^{nl \times nl}. \quad (3.24)$$

Moreover, (3.23) is transformed into

$$\Xi_{\tau}(k+1) = \mathcal{P} \Xi_{\tau}(k), \quad (3.25)$$

where

$$\mathcal{P} = \begin{bmatrix} \tilde{\mathbf{P}} & \mathbf{0} & \cdots & \mathbf{0} \\ \mathbf{0} & \ddots & \ddots & \vdots \\ \vdots & \ddots & \tilde{\mathbf{P}} & \mathbf{0} \\ \mathbf{0} & \cdots & \mathbf{0} & \tilde{\mathbf{P}} \end{bmatrix} \in \mathbb{R}^{nl\Pi \times nl\Pi}. \quad (3.26)$$

(3.25) is transformed by the discrete-time Fourier transform and definition in (2.8) into

$$\mathcal{F}[\Xi_{\tau}(k+1)] = \begin{cases} \mathcal{F}[\Xi_{\tau p}(k+1)], & \text{if } \omega \leq \rho \\ \mathcal{F}[\Xi_{\tau a}(k+1)], & \text{if } \rho < \omega \end{cases} = \begin{cases} \mathcal{F}[\mathcal{P} \Xi_{\tau p}(k)], & \text{if } \omega \leq \rho \\ \mathcal{F}[\mathcal{P} \Xi_{\tau a}(k)], & \text{if } \rho < \omega \end{cases}. \quad (3.27)$$

The inverse discrete-time Fourier transform of (3.27) derives

$$\begin{cases} \Xi_{\tau p}(k+1) = \mathcal{P}\Xi_{\tau p}(k) \\ \Xi_{\tau a}(k+1) = \mathcal{P}\Xi_{\tau a}(k) \end{cases} \quad (3.28)$$

Next, closed-loop dynamics of the lifted estimation error $e_{\tau}(k)$ of the lifted state observer in (3.15) are considered. Dynamics of the estimation error $e(t)$ are calculated using (3.1) and (3.3) as follows

$$\begin{aligned} e(t+1) &= \mathbf{x}(t+1) - \hat{\mathbf{x}}(t+1) \\ &= \mathbf{A}\mathbf{x}(t) + \mathbf{B}\mathbf{u}(t) - \mathbf{A}\hat{\mathbf{x}}(t) - \mathbf{B}\mathbf{u}(t) - \mathbf{L}\{\mathbf{y}(t) - \hat{\mathbf{y}}(t)\} \\ &= \mathbf{A}e(t) - \mathbf{L}\{\mathbf{y}(t) - \hat{\mathbf{y}}(t)\} \\ &= (\mathbf{A} - \mathbf{L}\mathbf{C})e(t). \end{aligned} \quad (3.29)$$

Then, dynamics of the lifted estimation error $e_{\tau}(k)$ are

$$\mathbf{e}_{\tau+1}(k) = (\mathbf{A} - \mathbf{L}\mathbf{C})\mathbf{e}_{\tau}(k), \quad (3.30)$$

and

$$\mathbf{e}_{\tau+i}(k) = (\mathbf{A} - \mathbf{L}\mathbf{C})^i \mathbf{e}_{\tau}(k). \quad (3.31)$$

i satisfies

$$0 \leq i \leq \Pi. \quad (3.32)$$

$\mathbf{e}_{\tau+i}(k)$ is transformed by the discrete-time Fourier transform and definition in (2.8) into

$$\mathcal{F}[\mathbf{e}_{\tau+i}(k)] = \begin{cases} \mathcal{F}[\mathbf{e}_{(\tau+i)p}(k)], & \text{if } \omega \leq \rho \\ \mathcal{F}[\mathbf{e}_{(\tau+i)a}(k)], & \text{if } \rho < \omega \end{cases} = \begin{cases} \mathcal{F}[(\mathbf{A} - \mathbf{L}\mathbf{C})^i \mathbf{e}_{\tau p}(k)], & \text{if } \omega \leq \rho \\ \mathcal{F}[(\mathbf{A} - \mathbf{L}\mathbf{C})^i \mathbf{e}_{\tau a}(k)], & \text{if } \rho < \omega \end{cases} \quad (3.33)$$

The inverse discrete-time Fourier transform of (3.33) derives the dynamics of the lifted periodic estimation error $\mathbf{e}_{(\tau+i)p}(k)$ and lifted aperiodic estimation error $\mathbf{e}_{(\tau+i)a}(k)$ as

$$\begin{cases} \mathbf{e}_{(\tau+i)p}(k) = (\mathbf{A} - \mathbf{L}\mathbf{C})^i \mathbf{e}_{\tau p}(k) \\ \mathbf{e}_{(\tau+i)a}(k) = (\mathbf{A} - \mathbf{L}\mathbf{C})^i \mathbf{e}_{\tau a}(k) \end{cases} \quad (3.34)$$

In addition, the lifted estimation error $e_\tau(k+1)$ can be calculated using (3.8) and (3.15) as follows

$$\begin{aligned}
 e_\tau(k+1) &= \mathbf{x}_\tau(k+1) - \hat{\mathbf{x}}_\tau(k+1) \\
 &= \tilde{\mathbf{A}}\mathbf{x}_\tau(k) + \tilde{\mathbf{B}}\mathbf{u}_\tau(k) - \tilde{\mathbf{A}}\hat{\mathbf{x}}_\tau(k) - \tilde{\mathbf{B}}\mathbf{u}_\tau(k) - \tilde{\mathbf{L}}\{\boldsymbol{\eta}_\tau(k) - \hat{\boldsymbol{\eta}}_\tau(k)\} \\
 &= \tilde{\mathbf{A}}e_\tau(k) - \tilde{\mathbf{L}}\{\boldsymbol{\eta}_\tau(k) - \hat{\boldsymbol{\eta}}_\tau(k)\} \\
 &= \mathbf{A}^\Pi e_\tau(k) - \sum_{i=0}^{\Pi-1} \mathbf{A}^{\Pi-1-i} \mathbf{L}\mathbf{C}e_{\tau+i}(k) \\
 &= \mathbf{A}^\Pi e_\tau(k) - \sum_{i=0}^{\Pi-1} \mathbf{A}^{\Pi-1-i} \mathbf{L}\mathbf{C}(\mathbf{A} - \mathbf{L}\mathbf{C})^i e_\tau(k) \\
 &= (\mathbf{A} - \mathbf{L}\mathbf{C})^\Pi e_\tau(k).
 \end{aligned} \tag{3.35}$$

The discrete-time Fourier transform and definitions in (2.8) and the inverse discrete-time Fourier transform lead to

$$\mathcal{F}[e_\tau(k+1)] = \begin{cases} \mathcal{F}[e_{\tau p}(k+1)], & \text{if } \omega \leq \rho \\ \mathcal{F}[e_{\tau a}(k+1)], & \text{if } \rho < \omega \end{cases} = \begin{cases} (\mathbf{A} - \mathbf{L}\mathbf{C})^\Pi \mathcal{F}[e_{\tau p}(k)], & \text{if } \omega \leq \rho \\ (\mathbf{A} - \mathbf{L}\mathbf{C})^\Pi \mathcal{F}[e_{\tau a}(k)], & \text{if } \rho < \omega \end{cases}, \tag{3.36}$$

and

$$\begin{cases} e_{\tau p}(k+1) = (\mathbf{A} - \mathbf{L}\mathbf{C})^\Pi e_{\tau p}(k) \\ e_{\tau a}(k+1) = (\mathbf{A} - \mathbf{L}\mathbf{C})^\Pi e_{\tau a}(k) \end{cases}. \tag{3.37}$$

Finally, the closed-loop dynamics of the periodic and aperiodic states are considered. From the definitions of the errors:

$$\boldsymbol{\epsilon}(t) = \hat{\mathbf{x}}_p(t) - \tilde{\mathbf{x}}_p(t) \tag{3.38}$$

$$\mathbf{e}(t) = \mathbf{x}(t) - \hat{\mathbf{x}}(t), \tag{3.39}$$

the separated periodic and aperiodic states are

$$\tilde{\mathbf{x}}_p(t) = \mathbf{x}_p(t) - \mathbf{e}_p(t) - \boldsymbol{\epsilon}(t) \tag{3.40}$$

$$\tilde{\mathbf{x}}_a(t) = \mathbf{x}_a(t) - \mathbf{e}_a(t) + \boldsymbol{\epsilon}(t). \tag{3.41}$$

The control input in (3.5) with (3.6), (3.7), (3.40), and (3.41) expresses the state $\mathbf{x}(t+1)$ of the system in (3.1) as

$$\begin{aligned}
 \mathbf{x}(t+1) &= (\mathbf{A} - \mathbf{B}\mathbf{F}_p)\mathbf{x}_p(t) + (\mathbf{A} - \mathbf{B}\mathbf{F}_a)\mathbf{x}_a(t) \\
 &\quad + \mathbf{B}\mathbf{F}_p\{\mathbf{e}_p(t) + \boldsymbol{\epsilon}(t)\} + \mathbf{B}\mathbf{F}_a\{\mathbf{e}_a(t) - \boldsymbol{\epsilon}(t)\},
 \end{aligned} \tag{3.42}$$

and the lifted state $\mathbf{x}_{\tau+1}(k)$ becomes

$$\begin{aligned} \mathbf{x}_{\tau+1}(k) &= (\mathbf{A} - \mathbf{B}\mathbf{F}_p)\mathbf{x}_{\tau p}(k) + (\mathbf{A} - \mathbf{B}\mathbf{F}_a)\mathbf{x}_{\tau a}(k) \\ &\quad + \mathbf{B}\mathbf{F}_p\{\mathbf{e}_{\tau p}(t) + \boldsymbol{\epsilon}_\tau(t)\} + \mathbf{B}\mathbf{F}_a\{\mathbf{e}_{\tau a}(t) - \boldsymbol{\epsilon}_\tau(t)\}. \end{aligned} \quad (3.43)$$

(3.43) is transformed by the discrete-time Fourier transform and definitions in (2.8) as

$$\begin{aligned} \mathcal{F}[\mathbf{x}_{(\tau+1)}(k+1)] &= \begin{cases} \mathcal{F}[\mathbf{x}_{(\tau+1)p}(k+1)], & \text{if } \omega \leq \rho \\ \mathcal{F}[\mathbf{x}_{(\tau+1)a}(k+1)], & \text{if } \rho < \omega \end{cases} \\ &= \begin{cases} (\mathbf{A} - \mathbf{B}\mathbf{F}_p)\mathcal{F}[\mathbf{x}_{\tau p}(k)] + \mathbf{B}\mathbf{F}_p\mathcal{F}[\mathbf{e}_{\tau p}(t)] + \mathbf{B}(\mathbf{F}_p - \mathbf{F}_a)\mathcal{F}[\boldsymbol{\epsilon}_{\tau p}(t)], & \text{if } \omega \leq \rho \\ (\mathbf{A} - \mathbf{B}\mathbf{F}_a)\mathcal{F}[\mathbf{x}_{\tau a}(k)] + \mathbf{B}\mathbf{F}_a\mathcal{F}[\mathbf{e}_{\tau a}(t)] + \mathbf{B}(\mathbf{F}_p - \mathbf{F}_a)\mathcal{F}[\boldsymbol{\epsilon}_{\tau a}(t)], & \text{if } \rho < \omega \end{cases}, \end{aligned} \quad (3.44)$$

and inverse discrete-time Fourier transform provides

$$\begin{cases} \mathbf{x}_{(\tau+1)p}(k+1) = (\mathbf{A} - \mathbf{B}\mathbf{F}_p)\mathbf{x}_{\tau p}(k) + \mathbf{B}\mathbf{F}_p\mathbf{e}_{\tau p}(t) + \mathbf{B}(\mathbf{F}_p - \mathbf{F}_a)\boldsymbol{\epsilon}_{\tau p}(t) \\ \mathbf{x}_{(\tau+1)a}(k+1) = (\mathbf{A} - \mathbf{B}\mathbf{F}_a)\mathbf{x}_{\tau a}(k) + \mathbf{B}\mathbf{F}_a\mathbf{e}_{\tau a}(t) + \mathbf{B}(\mathbf{F}_p - \mathbf{F}_a)\boldsymbol{\epsilon}_{\tau a}(t) \end{cases}. \quad (3.45)$$

$\mathbf{x}_{(\tau+i)p}(k+1)$ and $\mathbf{x}_{(\tau+i)a}(k+1)$ can be calculated using $\mathbf{x}_{(\tau+1)p}(k+1)$ and $\mathbf{x}_{(\tau+1)a}(k+1)$ as

$$\begin{aligned} \mathbf{x}_{(\tau+i)p}(k) &= (\mathbf{A} - \mathbf{B}\mathbf{F}_p)^i \mathbf{x}_{\tau p}(k) + \sum_{j=0}^{i-1} (\mathbf{A} - \mathbf{B}\mathbf{F}_p)^{i-1-j} \mathbf{B}\mathbf{F}_p (\mathbf{A} - \mathbf{L}\mathbf{C})^j \mathbf{e}_{\tau p}(k) \\ &\quad + \sum_{j=0}^{i-1} (\mathbf{A} - \mathbf{B}\mathbf{F}_p)^{i-1-j} \mathbf{B}(\mathbf{F}_p - \mathbf{F}_a) \boldsymbol{\epsilon}_{(\tau+j)p}(k) \end{aligned} \quad (3.46)$$

$$\begin{aligned} \mathbf{x}_{(\tau+i)a}(k) &= (\mathbf{A} - \mathbf{B}\mathbf{F}_a)^i \mathbf{x}_{\tau a}(k) + \sum_{j=0}^{i-1} (\mathbf{A} - \mathbf{B}\mathbf{F}_a)^{i-1-j} \mathbf{B}\mathbf{F}_a (\mathbf{A} - \mathbf{L}\mathbf{C})^j \mathbf{e}_{\tau a}(k) \\ &\quad + \sum_{j=0}^{i-1} (\mathbf{A} - \mathbf{B}\mathbf{F}_a)^{i-1-j} \mathbf{B}(\mathbf{F}_p - \mathbf{F}_a) \boldsymbol{\epsilon}_{(\tau+j)a}(k). \end{aligned} \quad (3.47)$$

They can be simplified as

$$\begin{cases} \mathbf{x}_{(\tau+i)p}(k) = (\mathbf{A} - \mathbf{B}\mathbf{F}_p)^i \mathbf{x}_{\tau p}(k) + \mathcal{M}_{ip} \mathcal{B}_i \mathcal{F}_{ip} \mathcal{N}_i \mathbf{e}_{\tau p}(k) + \mathcal{M}_{ip} \mathcal{B}_i (\mathcal{F}_{ip} - \mathcal{F}_{ia}) \mathcal{R}_i \boldsymbol{\Xi}_{\tau p}(k) \\ \mathbf{x}_{(\tau+i)a}(k) = (\mathbf{A} - \mathbf{B}\mathbf{F}_a)^i \mathbf{x}_{\tau a}(k) + \mathcal{M}_{ia} \mathcal{B}_i \mathcal{F}_{ia} \mathcal{N}_i \mathbf{e}_{\tau a}(k) + \mathcal{M}_{ia} \mathcal{B}_i (\mathcal{F}_{ip} - \mathcal{F}_{ia}) \mathcal{R}_i \boldsymbol{\Xi}_{\tau a}(k) \end{cases}, \quad (3.48)$$

where

$$\mathcal{B}_i = \begin{bmatrix} \mathbf{B} & \mathbf{0} & \cdots & \mathbf{0} \\ \mathbf{0} & \ddots & \ddots & \vdots \\ \vdots & \ddots & \mathbf{B} & \mathbf{0} \\ \mathbf{0} & \cdots & \mathbf{0} & \mathbf{B} \end{bmatrix} \in \mathbb{R}^{ni \times pi} \quad (3.49)$$

$$\mathcal{F}_{ip} = \begin{bmatrix} F_p & \mathbf{0} & \cdots & \mathbf{0} \\ \mathbf{0} & \ddots & \ddots & \vdots \\ \vdots & \ddots & F_p & \mathbf{0} \\ \mathbf{0} & \cdots & \mathbf{0} & F_p \end{bmatrix} \in \mathbb{R}^{pi \times ni} \quad (3.50)$$

$$\mathcal{F}_{ia} = \begin{bmatrix} F_a & \mathbf{0} & \cdots & \mathbf{0} \\ \mathbf{0} & \ddots & \ddots & \vdots \\ \vdots & \ddots & F_a & \mathbf{0} \\ \mathbf{0} & \cdots & \mathbf{0} & F_a \end{bmatrix} \in \mathbb{R}^{pi \times ni} \quad (3.51)$$

$$\mathcal{N}_i = \begin{bmatrix} I \\ (A - LC) \\ \vdots \\ (A - LC)^{i-1} \end{bmatrix} \in \mathbb{R}^{ni \times n} \quad (3.52)$$

$$\mathcal{M}_{ip} = [(A - BF_p)^{i-1} \quad \cdots \quad (A - BF_p) \quad I] \in \mathbb{R}^{n \times ni} \quad (3.53)$$

$$\mathcal{M}_{ia} = [(A - BF_a)^{i-1} \quad \cdots \quad (A - BF_a) \quad I] \in \mathbb{R}^{n \times ni} \quad (3.54)$$

$$\mathbf{R} = [\mathbf{0} \quad \cdots \quad \mathbf{0} \quad I] \in \mathbb{R}^{n \times nl} \quad (3.55)$$

$$\mathcal{R}_i = \begin{bmatrix} \mathbf{R} & \mathbf{0} & \cdots & \mathbf{0} & \mathbf{0} & \cdots & \mathbf{0} \\ \mathbf{0} & \mathbf{R} & \ddots & \vdots & \mathbf{0} & \ddots & \vdots \\ \vdots & \ddots & \ddots & \mathbf{0} & \vdots & \ddots & \mathbf{0} \\ \mathbf{0} & \cdots & \mathbf{0} & \mathbf{R} & \mathbf{0} & \cdots & \mathbf{0} \end{bmatrix} \in \mathbb{R}^{ni \times n\Pi}, \quad (3.56)$$

$$\mathcal{B}_0 = \mathcal{F}_{0p} = \mathcal{F}_{0a} = \mathcal{N}_0 = \mathcal{M}_{0p} = \mathcal{M}_{0a} = \mathcal{R}_0 = \mathbf{0} \quad (3.57)$$

$$\mathbf{R}\xi_\tau(k) = \epsilon_\tau(k) \quad (3.58)$$

$$\mathcal{R}_i \Xi_\tau(k) = \begin{bmatrix} \epsilon_\tau(k) \\ \epsilon_{\tau+1}(k) \\ \vdots \\ \epsilon_{\tau+i-1}(k) \end{bmatrix}. \quad (3.59)$$

From the lifted system in (3.8) and the control input in (3.5) with (3.6), (3.7), (3.10), (3.40), and (3.41), $\mathbf{x}_\tau(k+1)$ can be calculated as follows

$$\begin{aligned} \mathbf{x}_\tau(k+1) &= \tilde{\mathbf{A}}\mathbf{x}_\tau(k) + \tilde{\mathbf{B}}[\mathbf{u}_{\tau p}(k) + \mathbf{u}_{\tau a}(k)] \\ &= \tilde{\mathbf{A}}\mathbf{x}_\tau(k) - \tilde{\mathbf{B}}\mathcal{F}_{\Pi p} \begin{bmatrix} \tilde{\mathbf{x}}_{\tau p}(k) \\ \tilde{\mathbf{x}}_{(\tau+1)p}(k) \\ \vdots \\ \tilde{\mathbf{x}}_{(\tau+\Pi-1)p}(k) \end{bmatrix} - \tilde{\mathbf{B}}\mathcal{F}_{\Pi a} \begin{bmatrix} \tilde{\mathbf{x}}_{\tau a}(k) \\ \tilde{\mathbf{x}}_{(\tau+1)a}(k) \\ \vdots \\ \tilde{\mathbf{x}}_{(\tau+\Pi-1)a}(k) \end{bmatrix} \end{aligned}$$

$$\begin{aligned}
 &= \tilde{\mathbf{A}}\mathbf{x}_{\tau p}(k) + \tilde{\mathbf{A}}\mathbf{x}_{\tau a}(k) - \sum_{i=0}^{\Pi-1} \mathbf{A}^{\Pi-1-i} \mathbf{B} [\mathbf{F}_p \tilde{\mathbf{x}}_{(\tau+i)p}(k) + \mathbf{F}_a \tilde{\mathbf{x}}_{(\tau+i)a}(k)] \\
 &= \mathbf{A}^{\Pi} \mathbf{x}_{\tau p}(k) - \sum_{i=0}^{\Pi-1} \mathbf{A}^{\Pi-1-i} \mathbf{B} \mathbf{F}_p \mathbf{x}_{(\tau+i)p}(k) \\
 &\quad + \mathbf{A}^{\Pi} \mathbf{x}_{\tau a}(k) - \sum_{i=0}^{\Pi-1} \mathbf{A}^{\Pi-1-i} \mathbf{B} \mathbf{F}_a \mathbf{x}_{(\tau+i)a}(k) \\
 &\quad + \sum_{i=0}^{\Pi-1} \mathbf{A}^{\Pi-1-i} \mathbf{B} [\mathbf{F}_p \mathbf{e}_{(\tau+i)p}(k) + \mathbf{F}_a \mathbf{e}_{(\tau+i)a}(k)] \\
 &\quad + \sum_{i=0}^{\Pi-1} \mathbf{A}^{\Pi-1-i} \mathbf{B} (\mathbf{F}_p - \mathbf{F}_a) \boldsymbol{\epsilon}_{(\tau+i)}(k). \tag{3.60}
 \end{aligned}$$

Using (3.20), (3.34), and (3.48), (3.60) is expressed as

$$\begin{aligned}
 \mathbf{x}_{\tau}(k+1) &= \mathbf{A}^{\Pi} \mathbf{x}_{\tau p}(k) - \sum_{i=0}^{\Pi-1} \mathbf{A}^{\Pi-1-i} \mathbf{B} \mathbf{F}_p (\mathbf{A} - \mathbf{B} \mathbf{F}_p)^i \mathbf{x}_{\tau p}(k) \\
 &\quad + \mathbf{A}^{\Pi} \mathbf{x}_{\tau a}(k) - \sum_{i=0}^{\Pi-1} \mathbf{A}^{\Pi-1-i} \mathbf{B} \mathbf{F}_a (\mathbf{A} - \mathbf{B} \mathbf{F}_a)^i \mathbf{x}_{\tau a}(k) \\
 &\quad + \left[\tilde{\mathbf{B}} \mathcal{F}_{\Pi p} \mathcal{N}_{\Pi} - \sum_{i=1}^{\Pi-1} \mathbf{A}^{\Pi-1-i} \mathbf{B} \mathbf{F}_p \mathcal{M}_{ip} \mathcal{B}_i \mathcal{F}_{ip} \mathcal{N}_i \right] \mathbf{e}_{\tau p}(k) \\
 &\quad + \left[\tilde{\mathbf{B}} \mathcal{F}_{\Pi a} \mathcal{N}_{\Pi} - \sum_{i=1}^{\Pi-1} \mathbf{A}^{\Pi-1-i} \mathbf{B} \mathbf{F}_a \mathcal{M}_{ia} \mathcal{B}_i \mathcal{F}_{ia} \mathcal{N}_i \right] \mathbf{e}_{\tau a}(k) \\
 &\quad + \tilde{\mathbf{B}} (\mathcal{F}_{\Pi p} - \mathcal{F}_{\Pi a}) \mathcal{R}_{\Pi} \boldsymbol{\Xi}_{\tau}(k) \\
 &\quad - \sum_{i=1}^{\Pi-1} \mathbf{A}^{\Pi-1-i} \mathbf{B} \mathbf{F}_p \mathcal{M}_{ip} \mathcal{B}_i (\mathcal{F}_{ip} - \mathcal{F}_{ia}) \mathcal{R}_i \boldsymbol{\Xi}_{\tau p}(k) \\
 &\quad - \sum_{i=1}^{\Pi-1} \mathbf{A}^{\Pi-1-i} \mathbf{B} \mathbf{F}_a \mathcal{M}_{ia} \mathcal{B}_i (\mathcal{F}_{ip} - \mathcal{F}_{ia}) \mathcal{R}_i \boldsymbol{\Xi}_{\tau a}(k). \tag{3.61}
 \end{aligned}$$

Moreover, the equation is simplified into

$$\begin{aligned}
 \mathbf{x}_{\tau}(k+1) &= (\mathbf{A} - \mathbf{B} \mathbf{F}_p)^{\Pi} \mathbf{x}_{\tau p}(k) + (\mathbf{A} - \mathbf{B} \mathbf{F}_a)^{\Pi} \mathbf{x}_{\tau a}(k) \\
 &\quad + \Phi_p \mathbf{e}_{\tau p}(k) + \Phi_a \mathbf{e}_{\tau a}(k) + \Psi_p \boldsymbol{\Xi}_{\tau p}(k) + \Psi_a \boldsymbol{\Xi}_{\tau a}(k), \tag{3.62}
 \end{aligned}$$

where

$$\Phi_p = \tilde{B}\mathcal{F}_{\Pi p}(\mathcal{N}_{\Pi} - \mathcal{S}_p) \quad (3.63)$$

$$\Phi_a = \tilde{B}\mathcal{F}_{\Pi a}(\mathcal{N}_{\Pi} - \mathcal{S}_a) \quad (3.64)$$

$$\Psi_p = \tilde{B}(\mathcal{F}_{\Pi p} - \mathcal{F}_{\Pi a})\mathcal{R}_{\Pi} - \tilde{B}\mathcal{F}_{\Pi p}\mathcal{T}_p \quad (3.65)$$

$$\Psi_a = \tilde{B}(\mathcal{F}_{\Pi p} - \mathcal{F}_{\Pi a})\mathcal{R}_{\Pi} - \tilde{B}\mathcal{F}_{\Pi a}\mathcal{T}_a \quad (3.66)$$

$$\mathcal{S}_p = \begin{bmatrix} \mathbf{0} \\ \mathcal{M}_{1p}\mathcal{B}_1\mathcal{F}_{1p}\mathcal{N}_1 \\ \vdots \\ \mathcal{M}_{(\Pi-1)p}\mathcal{B}_{(\Pi-1)p}\mathcal{F}_{(\Pi-1)p}\mathcal{N}_{(\Pi-1)} \end{bmatrix} \in \mathbb{R}^{n\Pi \times n} \quad (3.67)$$

$$\mathcal{S}_a = \begin{bmatrix} \mathbf{0} \\ \mathcal{M}_{1a}\mathcal{B}_1\mathcal{F}_{1a}\mathcal{N}_1 \\ \vdots \\ \mathcal{M}_{(\Pi-1)a}\mathcal{B}_{(\Pi-1)a}\mathcal{F}_{(\Pi-1)a}\mathcal{N}_{(\Pi-1)} \end{bmatrix} \in \mathbb{R}^{n\Pi \times n} \quad (3.68)$$

$$\mathcal{T}_p = \begin{bmatrix} \mathbf{0} \\ \mathcal{M}_{1p}\mathcal{B}_1\{\mathcal{F}_{1p} - \mathcal{F}_{1a}\}\mathcal{R}_1 \\ \vdots \\ \mathcal{M}_{(\Pi-1)p}\mathcal{B}_{(\Pi-1)p}\{\mathcal{F}_{(\Pi-1)p} - \mathcal{F}_{(\Pi-1)a}\}\mathcal{R}_{(\Pi-1)} \end{bmatrix} \in \mathbb{R}^{n\Pi \times n\Pi} \quad (3.69)$$

$$\mathcal{T}_a = \begin{bmatrix} \mathbf{0} \\ \mathcal{M}_{1a}\mathcal{B}_1\{\mathcal{F}_{1p} - \mathcal{F}_{1a}\}\mathcal{R}_1 \\ \vdots \\ \mathcal{M}_{(\Pi-1)a}\mathcal{B}_{(\Pi-1)a}\{\mathcal{F}_{(\Pi-1)p} - \mathcal{F}_{(\Pi-1)a}\}\mathcal{R}_{(\Pi-1)} \end{bmatrix} \in \mathbb{R}^{n\Pi \times n\Pi}. \quad (3.70)$$

Finally, (3.62) is transformed using the discrete-time Fourier transform and definition in (2.8) into

$$\begin{aligned} \mathcal{F}[\mathbf{x}_{\tau}(k+1)] &= \begin{cases} \mathcal{F}[\mathbf{x}_{\tau p}(k+1)], & \text{if } \omega \leq \rho \\ \mathcal{F}[\mathbf{x}_{\tau a}(k+1)], & \text{if } \rho < \omega \end{cases} \\ &= \begin{cases} (\mathbf{A} - \mathbf{B}\mathbf{F}_p)^{\Pi}\mathbf{x}_{\tau p}(k) + \Phi_p\mathbf{e}_{\tau p}(k) + \Psi_p\Xi_{\tau p}(k), & \text{if } \omega \leq \rho \\ (\mathbf{A} - \mathbf{B}\mathbf{F}_a)^{\Pi}\mathbf{x}_{\tau a}(k) + \Phi_a\mathbf{e}_{\tau a}(k) + \Psi_a\Xi_{\tau a}(k), & \text{if } \rho < \omega \end{cases}, \end{aligned} \quad (3.71)$$

and

$$\begin{cases} \mathbf{x}_{\tau p}(k+1) = (\mathbf{A} - \mathbf{B}\mathbf{F}_p)^{\Pi}\mathbf{x}_{\tau p}(k) + \Phi_p\mathbf{e}_{\tau p}(k) + \Psi_p\Xi_{\tau p}(k) \\ \mathbf{x}_{\tau a}(k+1) = (\mathbf{A} - \mathbf{B}\mathbf{F}_a)^{\Pi}\mathbf{x}_{\tau a}(k) + \Phi_a\mathbf{e}_{\tau a}(k) + \Psi_a\Xi_{\tau a}(k) \end{cases}. \quad (3.72)$$

From (3.28), (3.37), and (3.72), the whole closed-loop dynamics of the lifted periodic/aperiodic state

feedback control system are

$$\begin{bmatrix} \mathbf{x}_{\tau_p}(k+1) \\ \mathbf{x}_{\tau_a}(k+1) \\ \mathbf{e}_{\tau_p}(k+1) \\ \mathbf{e}_{\tau_a}(k+1) \\ \Xi_{\tau_p}(k+1) \\ \Xi_{\tau_a}(k+1) \end{bmatrix} = \begin{bmatrix} (\mathbf{A} - \mathbf{BF}_p)^\Pi & \mathbf{0} & \Phi_p & \mathbf{0} & \Psi_p & \mathbf{0} \\ \mathbf{0} & (\mathbf{A} - \mathbf{BF}_a)^\Pi & \mathbf{0} & \Phi_a & \mathbf{0} & \Psi_a \\ \mathbf{0} & \mathbf{0} & (\mathbf{A} - \mathbf{LC})^\Pi & \mathbf{0} & \mathbf{0} & \mathbf{0} \\ \mathbf{0} & \mathbf{0} & \mathbf{0} & (\mathbf{A} - \mathbf{LC})^\Pi & \mathbf{0} & \mathbf{0} \\ \mathbf{0} & \mathbf{0} & \mathbf{0} & \mathbf{0} & \mathcal{P} & \mathbf{0} \\ \mathbf{0} & \mathbf{0} & \mathbf{0} & \mathbf{0} & \mathbf{0} & \mathcal{P} \end{bmatrix} \begin{bmatrix} \mathbf{x}_{\tau_p}(k) \\ \mathbf{x}_{\tau_a}(k) \\ \mathbf{e}_{\tau_p}(k) \\ \mathbf{e}_{\tau_a}(k) \\ \Xi_{\tau_p}(k) \\ \Xi_{\tau_a}(k) \end{bmatrix}. \quad (3.73)$$

The eigenvalues of (3.73) are those of $(\mathbf{A} - \mathbf{BF}_p)^\Pi$, $(\mathbf{A} - \mathbf{BF}_a)^\Pi$, $(\mathbf{A} - \mathbf{LC})^\Pi$, and \mathcal{P} because it is an upper triangular matrix. Therefore, poles of the lifted periodic/aperiodic state feedback control system can be designed by placing the poles of $(\mathbf{A} - \mathbf{BF}_p)^\Pi$, $(\mathbf{A} - \mathbf{BF}_a)^\Pi$, $(\mathbf{A} - \mathbf{LC})^\Pi$, and \mathcal{P} . Furthermore, the pole placements of $(\mathbf{A} - \mathbf{BF}_p)^\Pi$ for the lifted periodic state $\mathbf{x}_{\tau_p}(k)$, $(\mathbf{A} - \mathbf{BF}_a)^\Pi$ for the lifted aperiodic state $\mathbf{x}_{\tau_a}(k)$, $(\mathbf{A} - \mathbf{LC})^\Pi$ for the lifted periodic estimation error $\mathbf{e}_{\tau_p}(k)$ and lifted aperiodic estimation error $\mathbf{e}_{\tau_a}(k)$, and \mathcal{P} for the lifted periodic separation error $\Xi_{\tau_p}(k)$ and lifted aperiodic separation error $\Xi_{\tau_a}(k)$ are independent. \square

Proposition 1. The closed-loop dynamics in (3.73) are stable when the dynamics $\mathbf{A} - \mathbf{BF}_p$, $\mathbf{A} - \mathbf{BF}_a$, $\mathbf{A} - \mathbf{LC}$, and \mathcal{P} are stable.

Proof. The eigenvalues of (3.73) are

$$\{\lambda_{p1}^\Pi, \dots, \lambda_{pn}^\Pi\}, \{\lambda_{a1}^\Pi, \dots, \lambda_{an}^\Pi\}, \{\lambda_{o1}^\Pi, \dots, \lambda_{on}^\Pi\}, \{\lambda_{f1}, \dots, \lambda_{fnl\Pi}\}, \quad (3.74)$$

when eigenvalues of $\mathbf{A} - \mathbf{BF}_p$, $\mathbf{A} - \mathbf{BF}_a$, $\mathbf{A} - \mathbf{LC}$, and \mathcal{P} are

$$\{\lambda_{p1}, \dots, \lambda_{pn}\}, \{\lambda_{a1}, \dots, \lambda_{an}\}, \{\lambda_{o1}, \dots, \lambda_{on}\}, \{\lambda_{f1}, \dots, \lambda_{fnl\Pi}\}. \quad (3.75)$$

Hence, λ_{pi}^Π , λ_{ai}^Π , λ_{oi}^Π , and λ_{fi} satisfy

$$|\lambda_{pi}^\Pi| \leq 1, |\lambda_{ai}^\Pi| \leq 1, |\lambda_{oi}^\Pi| \leq 1, |\lambda_{fi}| \leq 1, \quad (3.76)$$

if and only if

$$|\lambda_{pi}| \leq 1, |\lambda_{ai}| \leq 1, |\lambda_{oi}| \leq 1, |\lambda_{fi}| \leq 1. \quad (3.77)$$

Therefore, the eigenvalues of (3.73) are stable if and only if the eigenvalues of the dynamics: $\mathbf{A} - \mathbf{BF}_p$, $\mathbf{A} - \mathbf{BF}_a$, $\mathbf{A} - \mathbf{LC}$, and \mathcal{P} are stable, because the stability condition for a linear discrete-time system is $|\lambda| \leq 1$ for every poles. □

According to Theorem 1 and Proposition 1, stability of the periodic/aperiodic state feedback control can be independently designed by $\mathbf{A} - \mathbf{BF}_p$, $\mathbf{A} - \mathbf{BF}_a$, $\mathbf{A} - \mathbf{LC}$, and \mathcal{P} , in which the closed-loop dynamics: $\mathbf{A} - \mathbf{BF}_p$, $\mathbf{A} - \mathbf{BF}_a$, and $\mathbf{A} - \mathbf{LC}$ have the same structure as the closed-loop dynamics: $\mathbf{A} - \mathbf{BF}$ and $\mathbf{A} - \mathbf{LC}$ of the classical state feedback control system. \mathcal{P} determines stability of the PASF.

3.3 Periodic/Aperiodic Motion Control

3.3.1 Acceleration Control System

An ACS based on a DOB is employed to address a tracking issue and disturbance compensation issue separately. The periodic/aperiodic motion control and the acceleration control handle the tracking issue and disturbance compensation issue, respectively.

For ACS design, consider the motor system:

$$v(z^{-1}) = \frac{1}{\mathcal{D}(z^{-1})} \left[\frac{K_t}{M} I(z^{-1}) - f(z^{-1}) \right] \quad (3.78)$$

$$f(z^{-1}) = \frac{Z_e(z^{-1})}{\mathcal{D}(z^{-1})} a^{\text{ref}}(z^{-1}) + f^{\text{exo}}(z^{-1}) \quad (3.79)$$

$$v^{\text{out}}(z^{-1}) = v(z^{-1}) - n_v(z^{-1}) \quad (3.80)$$

$$f^{\text{out}}(z^{-1}) = f(z^{-1}) - n_f(z^{-1}), \quad (3.81)$$

where

$$\mathcal{D}(z^{-1}) = \frac{2}{T_s} \frac{1 - z^{-1}}{1 + z^{-1}} \quad (3.82)$$

$$Z_e(z^{-1}) = D + \frac{K}{\mathcal{D}(z^{-1})}. \quad (3.83)$$

$v(z^{-1})$, $v^{\text{out}}(z^{-1})$, $f(z^{-1})$, $f^{\text{out}}(z^{-1})$, $f^{\text{exo}}(z^{-1})$, K_t , M , $I(z^{-1})$, $a^{\text{ref}}(z^{-1})$, $n_v(z^{-1})$, $n_f(z^{-1})$, $\mathcal{D}(z^{-1})$, $Z_e(z^{-1})$, D , and K denote the velocity, output velocity, force, output force, exogenous force, thrust

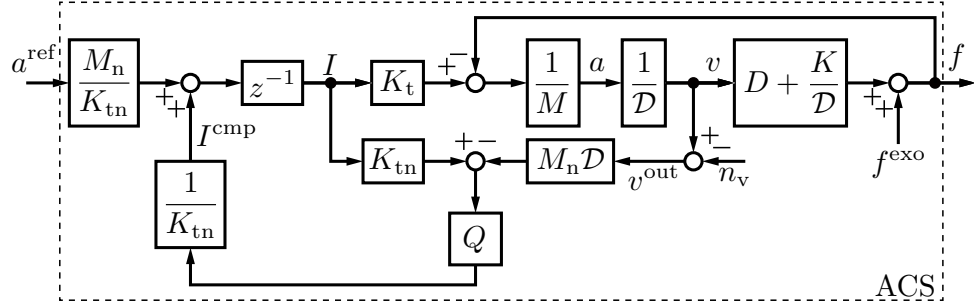


Fig. 3-2: Block diagram of the ACS.

constant, mass, current, acceleration reference, velocity noise, force noise, discrete differentiator, environmental function, viscosity, and stiffness, respectively. A DOB:

$$I^{\text{cmp}} = Q(z^{-1})[K_{tn}I(z^{-1}) - M_n \mathcal{D}(z^{-1})v^{\text{out}}(z^{-1})] \quad (3.84)$$

$$Q(z^{-1}) = \frac{g_{\text{dob}}T_s + g_{\text{dob}}T_s z^{-1}}{(g_{\text{dob}}T_s + 2) + (g_{\text{dob}}T_s - 2)z^{-1}}. \quad (3.85)$$

is used to eliminate $f(z^{-1})$ from $v(z^{-1})$ in (3.78). $Q(z^{-1})$, I^{cmp} , n , and g_{dob} denote the Q-filter, compensation current, nominal variable, and cutoff frequency, respectively. The ACS uses the compensation current as

$$I = z^{-1} \left[\frac{M_n}{K_{tn}} a^{\text{ref}} + I^{\text{cmp}} \right]. \quad (3.86)$$

A block diagram of the ACS is shown in Fig. 3-2. The ACS, which compensates for disturbances such as external force and modeling errors, can be approximately expressed by assuming complete disturbance elimination as

$$v(z^{-1}) = \frac{1}{\mathcal{D}(z^{-1})} a^{\text{ref}}(z^{-1}) \quad (3.87)$$

$$f(z^{-1}) = \frac{Z_e(z^{-1})}{\mathcal{D}(z^{-1})} a^{\text{ref}}(z^{-1}) + f^{\text{exo}}(z^{-1}), \quad (3.88)$$

which is the approximate ACS used to construct and design the periodic/aperiodic motion control.

Table 3.1: Six control objectives for the six periodic/aperiodic motion controls.

Control	Periodic motion	Aperiodic motion
PVAF	$v_p^{\text{cmd}} - \hat{v}_p = 0$	$f_a^{\text{cmd}} - \hat{f}_a = 0$
PFAV	$f_p^{\text{cmd}} - \hat{f}_p = 0$	$v_a^{\text{cmd}} - \hat{v}_a = 0$
PVAI	$v_p^{\text{cmd}} - \hat{v}_p = 0$	$M_v \dot{v}_a^{\text{cmd}} + D_v v_a^{\text{cmd}} + K_v \int_{t_0}^{t_f} v_a^{\text{cmd}} dt = \hat{f}_a$
PIAV	$M_v \dot{v}_p^{\text{cmd}} + D_v v_p^{\text{cmd}} + K_v \int_{t_0}^{t_f} v_p^{\text{cmd}} dt = \hat{f}_p$	$v_a^{\text{cmd}} - \hat{v}_a = 0$
PFAI	$f_p^{\text{cmd}} - \hat{f}_p = 0$	$M_v \dot{v}_a^{\text{cmd}} + D_v v_a^{\text{cmd}} + K_v \int_{t_0}^{t_f} v_a^{\text{cmd}} dt = \hat{f}_a$
PIAF	$M_v \dot{v}_p^{\text{cmd}} + D_v v_p^{\text{cmd}} + K_v \int_{t_0}^{t_f} v_p^{\text{cmd}} dt = \hat{f}_p$	$f_a^{\text{cmd}} - \hat{f}_a = 0$

3.3.2 Six Periodic/Aperiodic Motion Controls

Six Control Objectives and Construction

This study defines periodic/aperiodic velocity and periodic/aperiodic force as

$$v = v_p + v_a \quad (3.89)$$

$$f = f_p + f_a, \quad (3.90)$$

where v_p , v_a , f_p , and f_a denote the periodic velocity, aperiodic velocity, periodic force, and aperiodic force, respectively. Six types of periodic/aperiodic motion control are constructed by designing position, force, or impedance control for the periodic velocity, aperiodic velocity, periodic force, or aperiodic force as follows.

- Periodic velocity and aperiodic force (PVAF) control
- Periodic force and aperiodic velocity (PFAV) control
- Periodic velocity and aperiodic impedance (PVAI) control
- Periodic impedance and aperiodic velocity (PIAV) control
- Periodic force and aperiodic impedance (PFAI) control
- Periodic impedance and aperiodic force (PIAF) control

Six motion control objectives for the six periodic/aperiodic motion controls are summarized in Table 3.1, where $^{\text{cmd}}$, M_v , D_v , and K_v denote a command variable, virtual mass, virtual viscosity, and virtual stiffness, respectively. Accordingly, this study designs the six periodic/aperiodic motion systems, as

D_v , and virtual stiffness K_v . Moreover, the first-order PASF in (2.21) and (2.22) separates the output velocity and force into the estimated periodic velocity \hat{v}_p^{out} , estimated aperiodic velocity \hat{v}_a^{out} , estimated periodic force \hat{f}_p^{out} , and estimated aperiodic force \hat{f}_a^{out} as

$$\begin{cases} \hat{v}_p^{\text{out}}(z^{-1}) = F(z^{-1})v^{\text{out}}(z^{-1}) \\ \hat{v}_a^{\text{out}}(z^{-1}) = [1 - F(z^{-1})]v^{\text{out}}(z^{-1}) \end{cases} \quad (3.92)$$

$$\begin{cases} \hat{f}_p^{\text{out}}(z^{-1}) = F(z^{-1})f^{\text{out}}(z^{-1}) \\ \hat{f}_a^{\text{out}}(z^{-1}) = [1 - F(z^{-1})]f^{\text{out}}(z^{-1}) \end{cases} \quad (3.93)$$

The input-output periodic/aperiodic transfer functions of the six periodic/aperiodic motion control systems are calculated as follows

PVAF control:

$$\hat{v}_p = \frac{1}{\varphi_{\text{pvaf}}} F [C_v(v_p^{\text{cmd}} + \hat{n}_{\text{vp}}) + K_f(f_a^{\text{cmd}} - \hat{f}_a^{\text{exo}} + \hat{n}_{\text{fa}})] \quad (3.94)$$

$$\hat{f}_a = \frac{1}{\varphi_{\text{pvaf}}} (1 - F) Z_e [C_v(v_p^{\text{cmd}} + \hat{n}_{\text{vp}}) + K_f(f_a^{\text{cmd}} - \hat{f}_a^{\text{exo}} + \hat{n}_{\text{fa}})] \quad (3.95)$$

PFAV control:

$$\hat{f}_p = \frac{1}{\varphi_{\text{pfav}}} F Z_e [K_f(f_p^{\text{cmd}} - \hat{f}_p^{\text{exo}} + \hat{n}_{\text{fp}}) + C_v(v_a^{\text{cmd}} + \hat{n}_{\text{va}})] \quad (3.96)$$

$$\hat{v}_a = \frac{1}{\varphi_{\text{pfav}}} (1 - F) [K_f(f_p^{\text{cmd}} - \hat{f}_p^{\text{exo}} + \hat{n}_{\text{fp}}) + C_v(v_a^{\text{cmd}} + \hat{n}_{\text{va}})] \quad (3.97)$$

PVAI control:

$$\hat{v}_p = \frac{1}{\varphi_{\text{pvai}}} F C_v [H_v(v_p^{\text{cmd}} + v_a^{\text{cmd}} + n_v) - \hat{f}_a^{\text{exo}} + \hat{n}_{\text{fa}}] \quad (3.98)$$

$$\hat{v}_a = \frac{1}{\varphi_{\text{pvai}}} (1 - F) C_v [H_v(v_p^{\text{cmd}} + v_a^{\text{cmd}} + n_v) - \hat{f}_a^{\text{exo}} + \hat{n}_{\text{fa}}] \quad (3.99)$$

PIAV control:

$$\hat{v}_p = \frac{1}{\varphi_{\text{piav}}} F C_v [H_v(v_p^{\text{cmd}} + v_a^{\text{cmd}} + n_v) - \hat{f}_p^{\text{exo}} + \hat{n}_{\text{fp}}] \quad (3.100)$$

$$\hat{v}_a = \frac{1}{\varphi_{\text{piav}}} (1 - F) C_v [H_v(v_p^{\text{cmd}} + v_a^{\text{cmd}} + n_v) - \hat{f}_p^{\text{exo}} + \hat{n}_{\text{fp}}] \quad (3.101)$$

PFAI control:

$$\hat{f}_p = \frac{1}{\varphi_{\text{pfai}}} F Z_e [f_p^{\text{cmd}} - f^{\text{exo}} + n_f + Z_v(v_a^{\text{cmd}} + \hat{n}_{\text{va}})] \quad (3.102)$$

$$\hat{v}_a = \frac{1}{\varphi_{\text{pfai}}} (1 - F) [f_p^{\text{cmd}} - f^{\text{exo}} + n_f + Z_v(v_a^{\text{cmd}} + \hat{n}_{\text{va}})] \quad (3.103)$$

PIAF control:

$$\hat{v}_p = \frac{1}{\varphi_{piaf}} F [Z_v (v_p^{cmd} + \hat{n}_{vp}) + f_a^{cmd} - f^{exo} + n_f] \quad (3.104)$$

$$\hat{f}_a = \frac{1}{\varphi_{piaf}} (1 - F) Z_e [Z_v (v_p^{cmd} + \hat{n}_{vp}) + f_a^{cmd} - f^{exo} + n_f], \quad (3.105)$$

where

$$H_v = M_v \mathcal{D} + Z_v \quad (3.106)$$

$$Z_v = D_v + \frac{K_v}{\mathcal{D}}. \quad (3.107)$$

The characteristic equations are as follows

PVAF control:

$$\varphi_{pvaf}(z) = \mathcal{D}z + K_f Z_e + (C_v - K_f Z_e) F \quad (3.108)$$

PFAV control:

$$\varphi_{pfav}(z) = \mathcal{D}z + C_v + (K_f Z_e - C_v) F \quad (3.109)$$

PVAI control:

$$\varphi_{pvai}(z) = (\mathcal{D}z + C_v) H_v + C_v Z_e (1 - F) \quad (3.110)$$

PIAV control:

$$\varphi_{piaf}(z) = (\mathcal{D}z + C_v) H_v + C_v Z_e F \quad (3.111)$$

PFAI control:

$$\varphi_{pfai}(z) = M_v \mathcal{D}z + Z_e + Z_v (1 - F) \quad (3.112)$$

PIAF control:

$$\varphi_{piaf}(z) = M_v \mathcal{D}z + Z_e + Z_v F. \quad (3.113)$$

By using Assumption 1 for the periodic velocity v_p , aperiodic velocity v_a , periodic force f_p , and aperiodic force f_a , the input-output transfer functions in (3.94) – (3.105) become as follows

PVAF control:

$$\hat{v}_p = \frac{C_v}{\mathcal{D}z + C_v} (v_p^{cmd} + \hat{n}_{vp}) \quad (3.114)$$

$$\hat{f}_a = \frac{K_f Z_e}{\mathcal{D}z + K_f Z_e} (f_a^{cmd} - \hat{f}_a^{exo} + \hat{n}_{fa}) \quad (3.115)$$

PFAV control:

$$\hat{f}_p = \frac{K_f Z_e}{\mathcal{D}z + K_f Z_e} (f_p^{\text{cmd}} - \hat{f}_p^{\text{exo}} + \hat{n}_{fp}) \quad (3.116)$$

$$\hat{v}_a = \frac{C_v}{\mathcal{D}z + C_v} (v_a^{\text{cmd}} + \hat{n}_{va}) \quad (3.117)$$

PVAI control:

$$\hat{v}_p = \frac{C_v}{\mathcal{D}z + C_v} (v_p^{\text{cmd}} + \hat{n}_{vp}) \quad (3.118)$$

$$\frac{C_v}{\mathcal{D}z + RC_v} (v_a^{\text{cmd}} + \hat{n}_{va}) - \hat{v}_a = \frac{C_v}{\mathcal{D}z + RC_v} \frac{1}{H_v} (\hat{f}_a^{\text{exo}} - \hat{n}_{fa}) \quad (3.119)$$

PIAV control:

$$\frac{C_v}{\mathcal{D}z + RC_v} (v_p^{\text{cmd}} + \hat{n}_{vp}) - \hat{v}_p = \frac{C_v}{\mathcal{D}z + RC_v} \frac{1}{H_v} (\hat{f}_p^{\text{exo}} - \hat{n}_{fp}) \quad (3.120)$$

$$\hat{v}_a = \frac{C_v}{\mathcal{D}z + C_v} (v_a^{\text{cmd}} + \hat{n}_{va}) \quad (3.121)$$

PFAI control:

$$\hat{f}_p = \frac{Z_e}{M_v \mathcal{D}z + Z_e} (f_p^{\text{cmd}} - \hat{f}_p^{\text{exo}} + \hat{n}_{fp}) \quad (3.122)$$

$$Z_v (v_a^{\text{cmd}} + \hat{n}_{va}) - RH_v \hat{v}_a = (\hat{f}_a^{\text{exo}} - \hat{n}_{fa}) \quad (3.123)$$

PIAF control:

$$Z_v (v_p^{\text{cmd}} + \hat{n}_{vp}) - RH_v \hat{v}_p = (\hat{f}_p^{\text{exo}} - \hat{n}_{fp}) \quad (3.124)$$

$$\hat{f}_a = \frac{Z_e}{M_v \mathcal{D}z + Z_e} (f_a^{\text{cmd}} - \hat{f}_a^{\text{exo}} + \hat{n}_{fa}), \quad (3.125)$$

where

$$R = 1 + \frac{Z_e}{H_v}. \quad (3.126)$$

The approximate input-output transfer functions based on Assumption 1 in (3.114) – (3.125) are the same as transfer functions of the classical velocity, force, and impedance controls. Hence, the gain and impedance parameters: K_I , K_P , K_F , M_v , D_v , and K_v of the six periodic/aperiodic motion controls can be designed in a similar manner to the classical velocity, force, and impedance controls.

Robust Stability

Robust stability of the six periodic/aperiodic motion control systems, which guarantees stability under various uncertainties, is evaluated through their complementary sensitivity functions. A modeling error Δ of the motor system in (3.78) and (3.79) is defined by

$$v(z^{-1}) = (1 + \Delta) \frac{K_{tn}}{M_n \mathcal{D}(z^{-1}) + Z_e} I. \quad (3.127)$$

The modeling error Δ consists of the weighting function $W(s)$ and variation $\delta(s)$ as

$$\Delta(z^{-1}) = W(z^{-1})\delta(z^{-1}), \quad (3.128)$$

where the variation satisfies

$$\|\delta(z^{-1})\|_\infty \leq 1. \quad (3.129)$$

If the periodic/aperiodic motion control system and the modeling error are nominally stable, a robust stability condition is

$$\|W(s)T(s)\|_\infty < 1 \quad (3.130)$$

according to the small-gain theorem. Nominal stability of the six periodic/aperiodic motion control systems can be designed and evaluated by using the characteristic equations in (3.108) – (3.113). Complementary sensitivity functions $T(s)$ of the periodic/aperiodic motion control systems, which are indexes to evaluate the robust stability, are as follows

PVAF control:

$$T_{pvaf}(z) = -\frac{Q\mathcal{D}z + K_f Z_e + (C_v - K_f Z_e)F}{\mathcal{D}z + M_n^{-1}(1 - Q)Z_e + K_f Z_e + (C_v - K_f Z_e)F} \quad (3.131)$$

PFAV control:

$$T_{pfav}(z) = -\frac{Q\mathcal{D}z + C_v + (K_f Z_e - C_v)F}{\mathcal{D}z + M_n^{-1}(1 - Q)Z_e + C_v + (K_f Z_e - C_v)F} \quad (3.132)$$

PVAI control:

$$T_{pvai}(z) = -\frac{QH_v \mathcal{D}z + C_v H_v + C_v Z_e(1 - F)}{[\mathcal{D}z + M_n^{-1}(1 - Q)Z_e + C_v]H_v + C_v Z_e(1 - F)} \quad (3.133)$$

PIAV control:

$$T_{\text{piav}}(z) = -\frac{QH_v\mathcal{D}z + C_vH_v + C_vZ_eF}{[\mathcal{D}z + M_n^{-1}(1-Q)Z_e + C_v]H_v + C_vZ_eF} \quad (3.134)$$

PFAI control:

$$T_{\text{pfai}}(z) = -\frac{QM_v\mathcal{D}z + Z_e + Z_v(1-F)}{M_v[\mathcal{D}z + M_n^{-1}(1-Q)Z_e] + Z_e + Z_v(1-F)} \quad (3.135)$$

PIAF control:

$$T_{\text{piaf}}(z) = -\frac{QM_v\mathcal{D}z + Z_e + Z_vF}{M_v[\mathcal{D}z + M_n^{-1}(1-Q)Z_e] + Z_e + Z_vF}. \quad (3.136)$$

To satisfy the robust stability condition in (3.130), the cutoff frequency g_{dob} of the DOB and control parameters for the periodic/aperiodic motion controls: K_I , K_P , K_F , M_v , D_v , and K_v can adjust the complementary sensitivity functions. Figs. 3-4 – 3-9 show Bode diagrams of the complementary sensitivity functions with variations in the environmental parameters: the viscosity D and stiffness K . The Bode diagrams illustrated that the periodic/aperiodic motion control systems are robustly stable against usual modeling errors, which occur for high frequencies.

3.3.3 Experiments

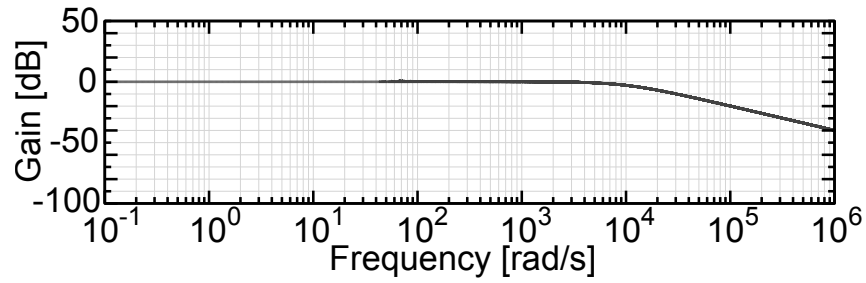
Setup

Six experiments were conducted for the proposed six periodic/aperiodic motion controls. A six axes manipulator: MOTOMAN YR-UPJ3-B00 was used, as shown in Fig. 3-10. Manipulator angle responses were measured by position encoders and torque responses were estimated by reaction torque observers (RTOBs). The controlled joints, initial posture, and parameters are summarized in Table 3.2. The separation frequency ρ of the first-order PASF was set to 1.0 if $t < 10$ s for fast convergence, and 0.01 otherwise for proper separation. The controllers were implemented using the real-time application interface for Linux, where the source code for the controllers was written in C++. Each control was implemented with the ACS in the joint space. The experimental control commands were set as follows

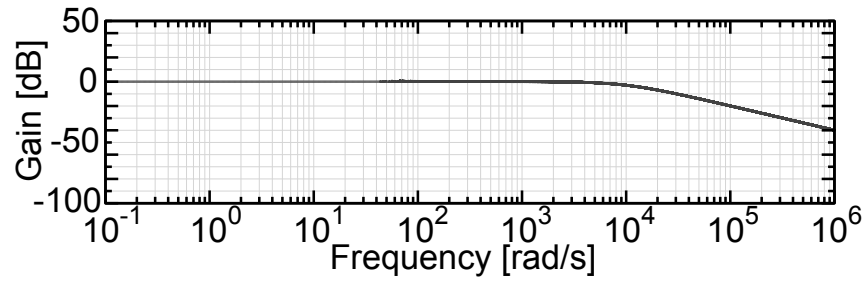
PVAF control:

$$v_p^{\text{cmd}}/s = 50[1 - \cos(\pi t)] \text{ mm} \quad (3.137)$$

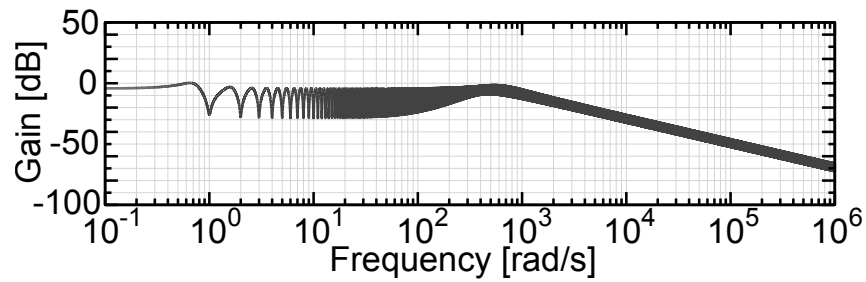
$$f_a^{\text{cmd}} = \begin{cases} -100 \text{ N} & \text{if } 36 \text{ s} < t \leq 38 \text{ s} \\ 0 \text{ N} & \text{otherwise} \end{cases} \quad (3.138)$$



(a) $g_{dob} = 10000$ rad/s
 $D = 1$ Ns/m
 $K = 500$ N/m.

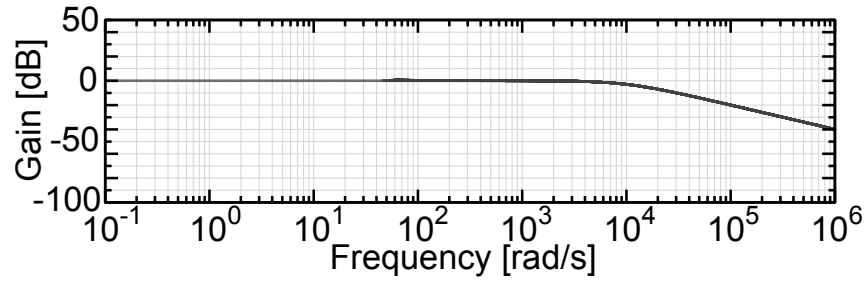


(b) $g_{dob} = 1000$ rad/s
 $D = 100$ Ns/m
 $K = 500$ N/m.

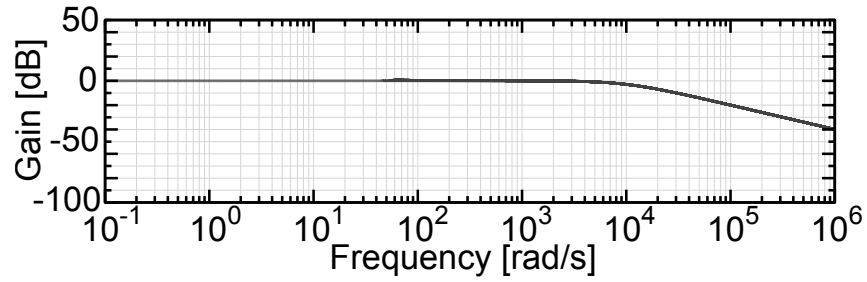


(c) $g_{dob} = 1$ rad/s
 $D = 100$ Ns/m
 $K = 50000$ N/m.

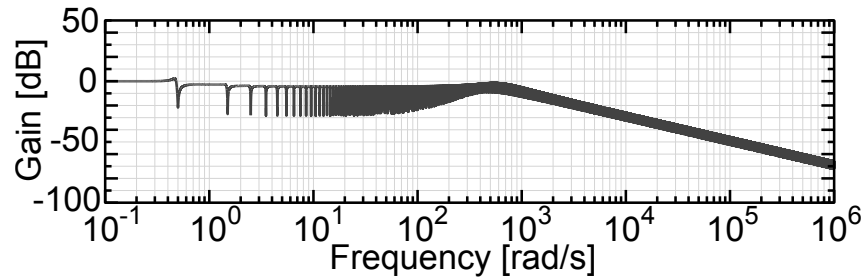
Fig. 3-4: Bode diagrams of the complementary sensitivity functions of the PVAF control system in (3.131). The other parameters are $M_n = 0.3$, $K_{tn} = 0.24$, $K_I = 6400$, $K_P = 240$, $K_F = 5$, $M_v = 0.1$, $D_v = 50$, $K_v = 800$, $\rho = 1$ rad/s, and $\Pi = 2\pi$ s.



(a) $g_{dob} = 10000$ rad/s
 $D = 1$ Ns/m
 $K = 500$ N/m.

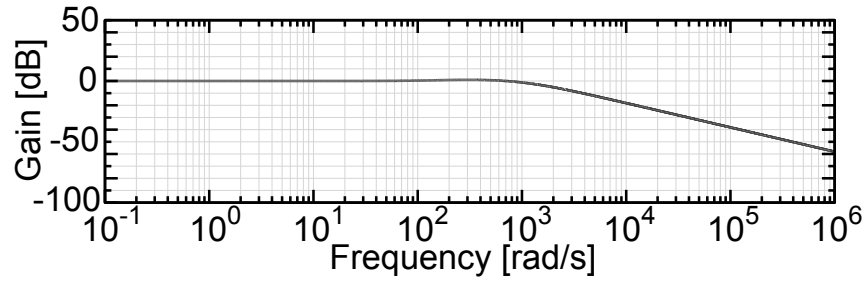


(b) $g_{dob} = 1000$ rad/s
 $D = 100$ Ns/m
 $K = 500$ N/m.

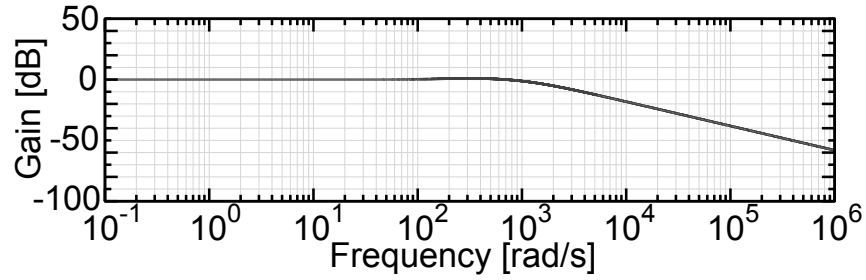


(c) $g_{dob} = 1$ rad/s
 $D = 100$ Ns/m
 $K = 50000$ N/m.

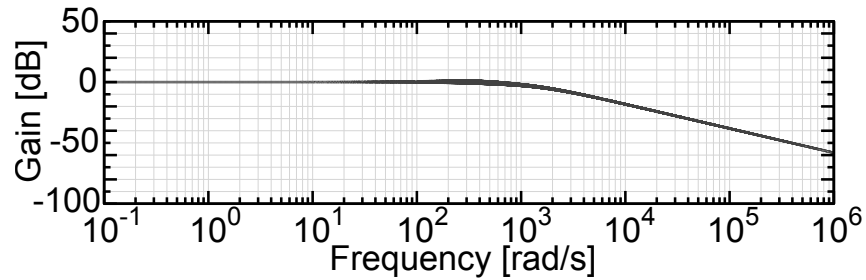
Fig. 3-5: Bode diagrams of the complementary sensitivity functions of the PFAV control system in (3.132). The other parameters are $M_n = 0.3$, $K_{tn} = 0.24$, $K_I = 6400$, $K_P = 240$, $K_F = 5$, $M_v = 0.1$, $D_v = 50$, $K_v = 800$, $\rho = 1$ rad/s, and $\Pi = 2\pi$ s.



(a) $g_{\text{dob}} = 1000$ rad/s
 $D = 0$ Ns/m
 $K = 0$ N/m.

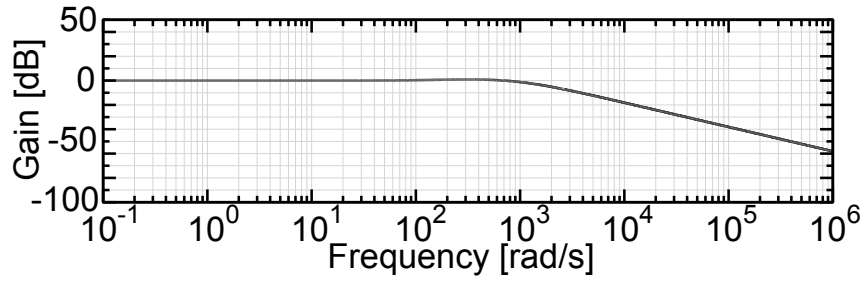


(b) $g_{\text{dob}} = 1000$ rad/s
 $D = 1$ Ns/m
 $K = 500$ N/m.

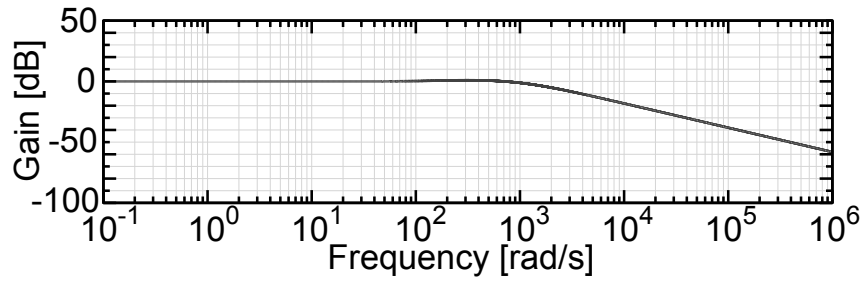


(c) $g_{\text{dob}} = 1000$ rad/s
 $D = 100$ Ns/m
 $K = 500$ N/m.

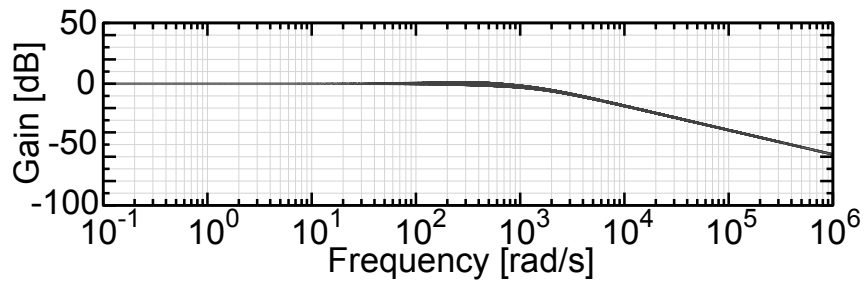
Fig. 3-6: Bode diagrams of the complementary sensitivity functions of the PVAI control system in (3.133). The other parameters are $M_n = 0.3$, $K_{tn} = 0.24$, $K_I = 6400$, $K_P = 240$, $K_F = 5$, $M_v = 0.1$, $D_v = 50$, $K_v = 800$, $\rho = 1$ rad/s, and $\Pi = 2\pi$ s.



(a) $g_{dob} = 1000$ rad/s
 $D = 0$ Ns/m
 $K = 0$ N/m.

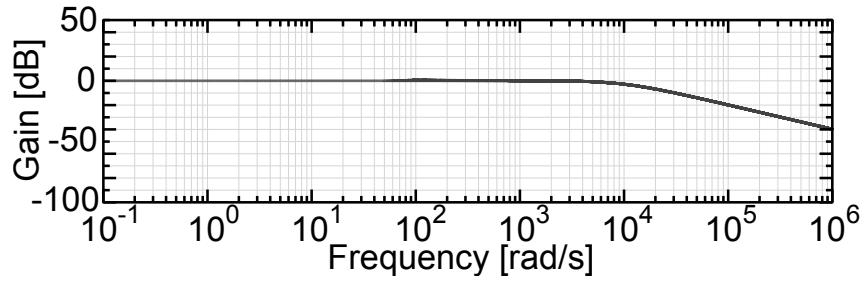


(b) $g_{dob} = 1000$ rad/s
 $D = 1$ Ns/m
 $K = 500$ N/m.

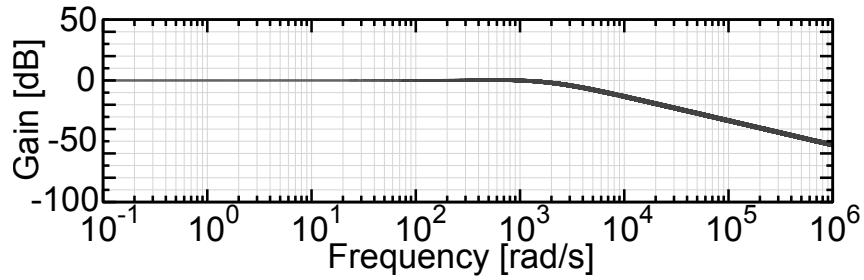


(c) $g_{dob} = 1000$ rad/s
 $D = 100$ Ns/m
 $K = 500$ N/m.

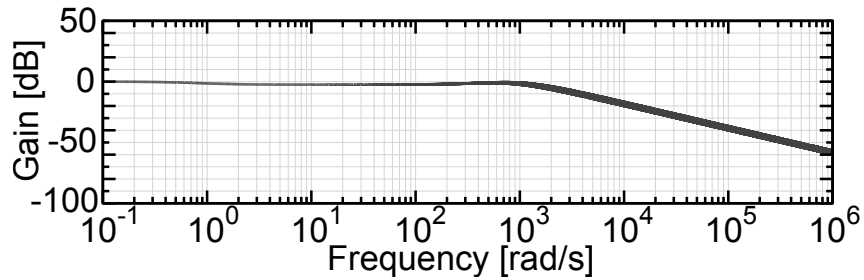
Fig. 3-7: Bode diagrams of the complementary sensitivity functions of the PIAV control system in (3.134). The other parameters are $M_n = 0.3$, $K_{tn} = 0.24$, $K_I = 6400$, $K_P = 240$, $K_F = 5$, $M_v = 0.1$, $D_v = 50$, $K_v = 800$, $\rho = 1$ rad/s, and $\Pi = 2\pi$ s.



(a) $g_{dob} = 10000$ rad/s
 $D = 1$ Ns/m
 $K = 500$ N/m.

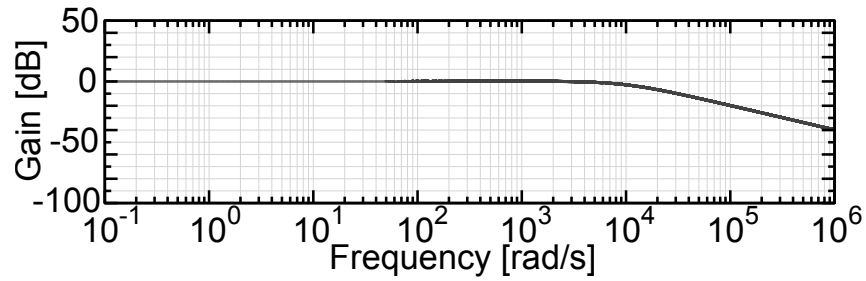


(b) $g_{dob} = 1000$ rad/s
 $D = 100$ Ns/m
 $K = 500$ N/m.

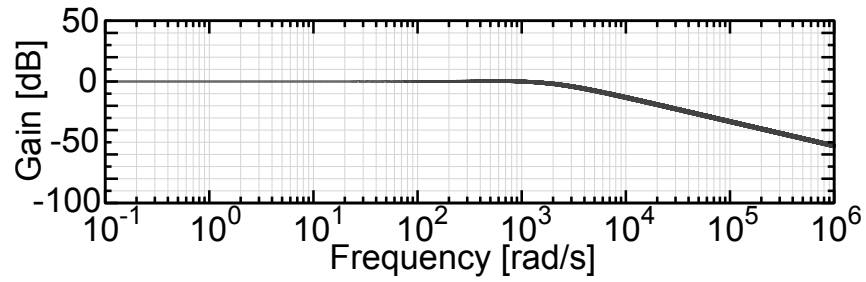


(c) $g_{dob} = 1$ rad/s
 $D = 100$ Ns/m
 $K = 50000$ N/m.

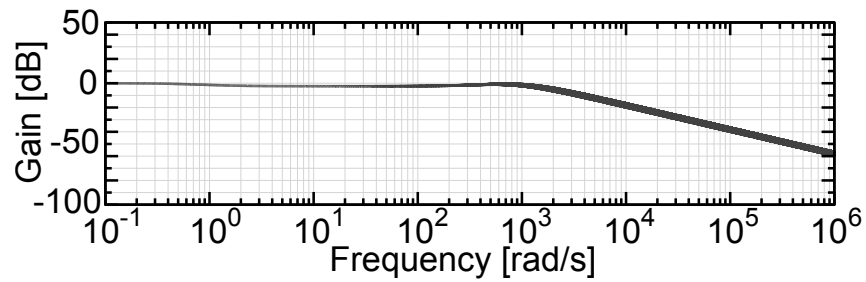
Fig. 3-8: Bode diagrams of the complementary sensitivity functions of the PFAI control system in (3.135). The other parameters are $M_n = 0.3$, $K_{tn} = 0.24$, $K_I = 6400$, $K_P = 240$, $K_F = 5$, $M_v = 0.1$, $D_v = 50$, $K_v = 800$, $\rho = 1$ rad/s, and $\Pi = 2\pi$ s.



(a) $g_{dob} = 10000$ rad/s
 $D = 1$ Ns/m
 $K = 500$ N/m.



(b) $g_{dob} = 1000$ rad/s
 $D = 100$ Ns/m
 $K = 500$ N/m.



(c) $g_{dob} = 1$ rad/s
 $D = 100$ Ns/m
 $K = 50000$ N/m.

Fig. 3-9: Bode diagrams of the complementary sensitivity functions of the PIAF control system in (3.136). The other parameters are $M_n = 0.3$, $K_{tn} = 0.24$, $K_I = 6400$, $K_P = 240$, $K_F = 5$, $M_v = 0.1$, $D_v = 50$, $K_v = 800$, $\rho = 1$ rad/s, and $\Pi = 2\pi$ s.

PFAV control:

$$f_p^{\text{cmd}} = 50[1 - \cos(\pi t)] \text{ N} \quad (3.139)$$

$$v_a^{\text{cmd}}/s = \begin{cases} 50 \sin\{0.5\pi(t - 36)\} & \text{mm} \quad \text{if } 36 \text{ s} < t \leq 38 \text{ s} \\ 0 & \text{mm} \quad \text{otherwise} \end{cases} \quad (3.140)$$

PVAI control:

$$v_{px}^{\text{cmd}}/s = 50[\cos(\pi t) - 1] \text{ mm} \quad (3.141)$$

$$v_{py}^{\text{cmd}}/s = 50 \sin(\pi t) \text{ mm} \quad (3.142)$$

PIAV control:

$$v_a^{\text{cmd}}/s = 0 \text{ mm} \quad (3.143)$$

PFAI control:

$$f_p^{\text{cmd}} = 50[1 - \cos(\pi t)] \text{ N} \quad (3.144)$$

PIAF control:

$$f_a^{\text{cmd}} = 0 \text{ N}. \quad (3.145)$$

In the PVAI and PFAI control experiments, an operator contacted the manipulator at approximately 36 s to verify their impedance characteristics. The operator moved the manipulator at all times during the experiments for the PIAV and PIAF controls. During the experiments on the six periodic/aperiodic motion controls, the position, force, or impedance control was used if $t < 10$ s for the convergence of the PASF. The PVAF and PVAI controls used the position control, PFAV and PFAI controls used the force control, and PIAV and PIAF controls used the impedance control. The periodic/aperiodic motion controls were applied otherwise.

Results

In the graphs of the experimental results, the position or force command signals for the impedance controls were calculated from the force (torque) or position (angle) responses and virtual impedance parameters in Table 3.2.

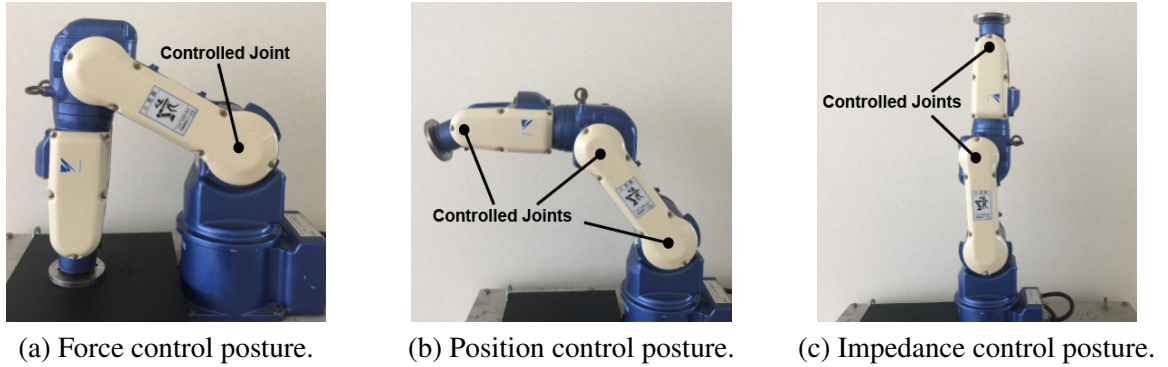


Fig. 3-10: Initial postures of the experimental manipulator.

Table 3.2: Parameters for the periodic/aperiodic motion control experiments.

Description	Symbol	PVAF	PFAV	PVAI	PIAV	PFAI	PIAF
Controlled joint		1st	1st	1st, 2nd, 3rd	2nd, 3rd	1st	1st
Initial posture from Fig. 3-10		(a)	(a)	(b)	(c)	(a)	(a)
Sampling time	T_s [ms]	0.1					
Length	L [m]	0.26, 0.27, 0.09					
Gear ratio	G_r	192, 120, 80					
Torque const.	K_{tn} [Nm/A]	0.59, 0.59, 0.238					
Inertia	J_n [Kgm ²]	1.28	1.28	7.3, 0.86, 0.008	0.86, 0.008	1.28	1.28
Period	Π [s]	2					
Separation freq.	ρ [rad/s]	1.0 if $t < 10$ s, 0.01 otherwise					
Cutoff frequencies [rad/s]							
Pseudo derivative for velocity		1000					
RTOB for torque estimation		500	500	100, 100, 100	300, 300	500	500
DOB		500	500	100, 100, 100	300, 300	500	500
Control parameters							
Integral gain	K_I	6400	6400	400, 400, 400	400, 400	-	-
Differential gain	K_D	160	240	40, 40, 40	40, 40	-	-
Proportional gain	K_F	5	2	-	-	3	3
Virtual inertia	J_v [Kgm ²]	-	-	3, 2, 0.1	2, 0.1	0.5	0.5
Virtual viscosity	D_v [Nms/rad]	-	-	100, 50, 0.5	50, 5	10	10
Virtual stiffness	K_v [Nm/rad]	-	-	600, 400, 1	300, 100	1000	1000

- PVAF and PFAV controls

According to Figs. 3-11(b) and 3-12(c), the periodic position tracking and aperiodic force tracking were realized by the PVAF control, while the aperiodic position and periodic force were not handled by the PVAF control according to Figs. 3-11(c) and 3-12(b). Conversely, the periodic force and aperiodic position were controlled by the PFAV control according to Figs. 3-13 and 3-14.

- PVAI and PIAV controls

Figs. 3-15 – 3-18 show the representative experimental results for the second joint of the manipulator. The simultaneous realization of the periodic position and aperiodic impedance controls was validated as Figs. 3-15(b) and (c), and that of the periodic impedance and aperiodic position controls was validated as Fig. 3-17(b) and (c).

- PFAI and PIAF controls

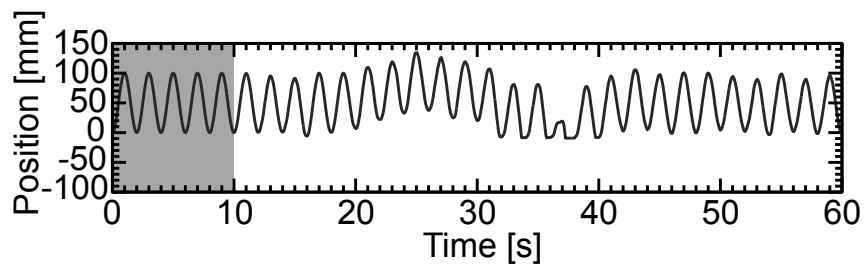
According to Fig. 3-20(b) and (c), the PFAI control achieved force and impedance controls for periodic and aperiodic motions. Conversely, the PIAF control achieved periodic impedance control and aperiodic force control according to Fig. 3-22(b) and (c).

The experiments showed the simultaneous realization of two periodic/aperiodic motion control objectives, and there is a limitation that only one of periodic motion controls and only one of aperiodic motion controls can be realized.

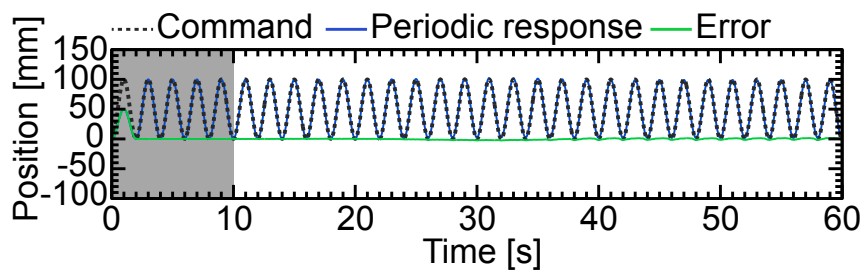
3.4 Summary

Section 3.2 constructed the periodic/aperiodic state feedback control using the PASF. Then, the separation principle for control, observation, and separation of the periodic/aperiodic state was proved in Theorem 1. Furthermore, this section proved Proposition 1, which indicates that stability of the periodic/aperiodic state feedback control can be designed in a similar way to the classical state feedback control design.

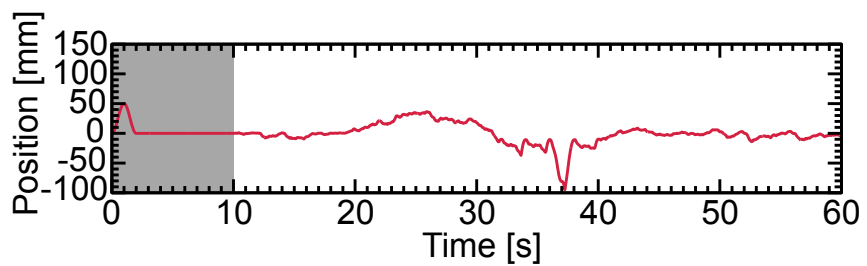
Section 3.3 expanded the periodic/aperiodic state feedback control into the motion control framework. The ACS using a DOB was constructed to suppress disturbances that impair the periodic/aperiodic motion control. Then, the six periodic/aperiodic motion controls that assign position, force, and impedance controls to periodic motion and aperiodic motion were constructed and analyzed in terms of the input-output transfer functions and robust stability. The experiments validated the practicality of the six periodic/aperiodic motion controls.



(a) Position.

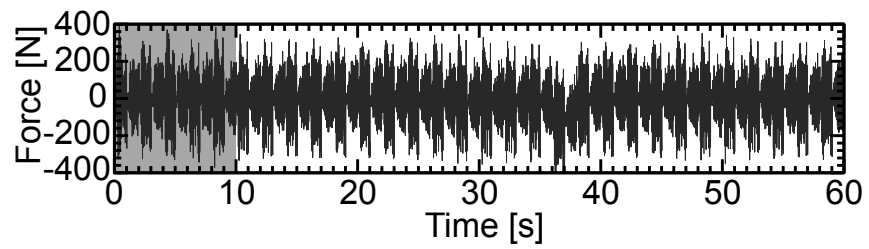


(b) Periodic position.

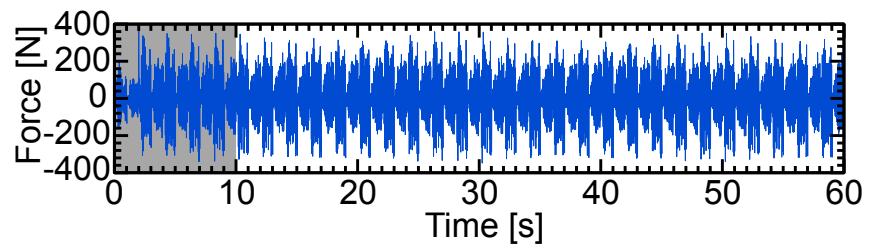


(c) Aperiodic position.

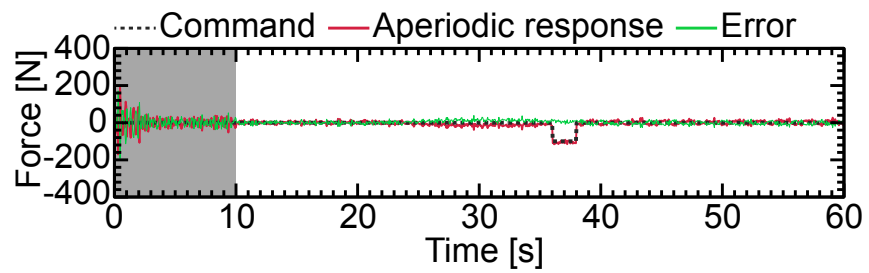
Fig. 3-11: Experimental position results of the PVAf control.



(a) Force.



(b) Periodic force.



(c) Aperiodic force.

Fig. 3-12: Experimental force results of the PVAF control.

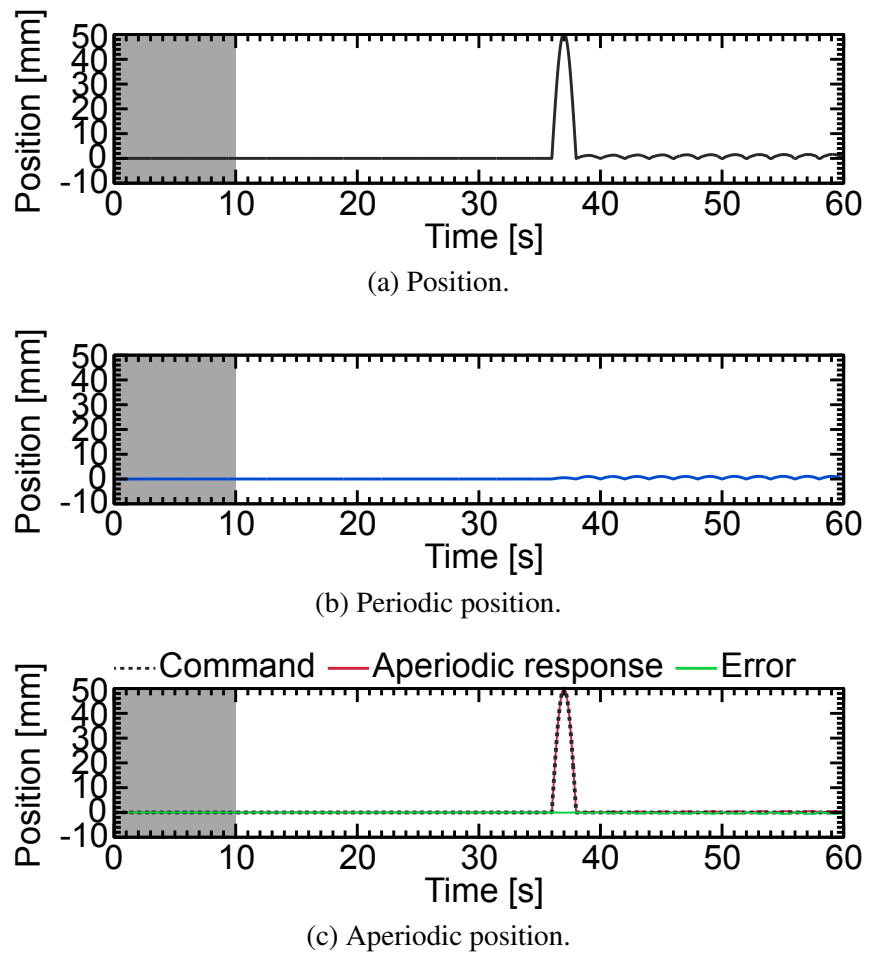
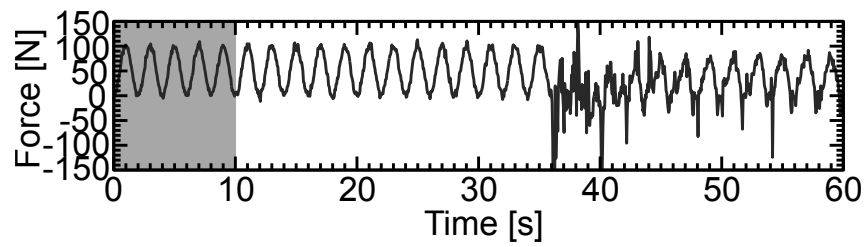
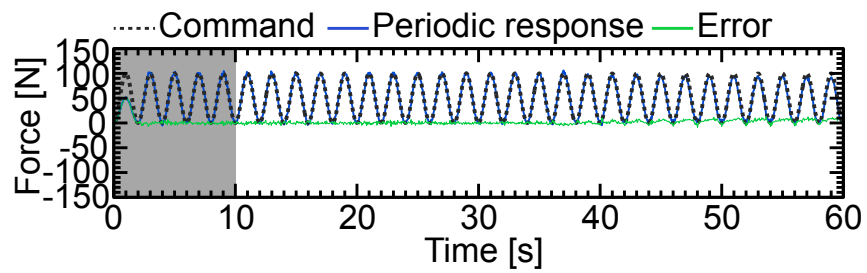


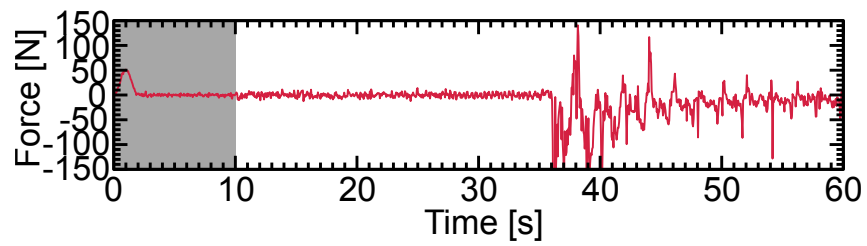
Fig. 3-13: Experimental position results of the PFAV control.



(a) Force.

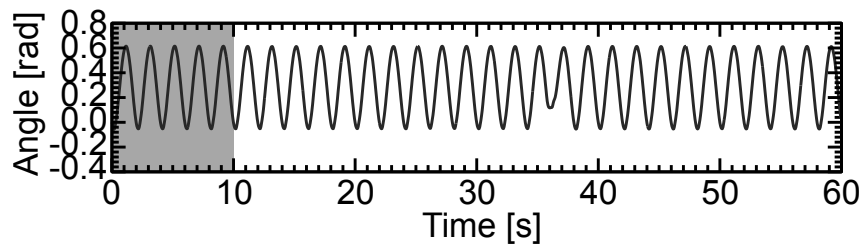


(b) Periodic force.

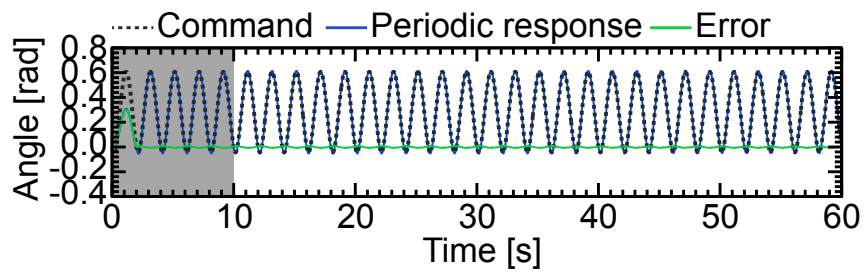


(c) Aperiodic force.

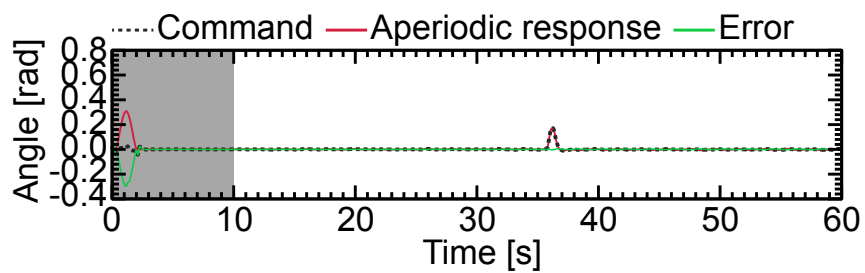
Fig. 3-14: Experimental force results of the PFAV control.



(a) Angle.

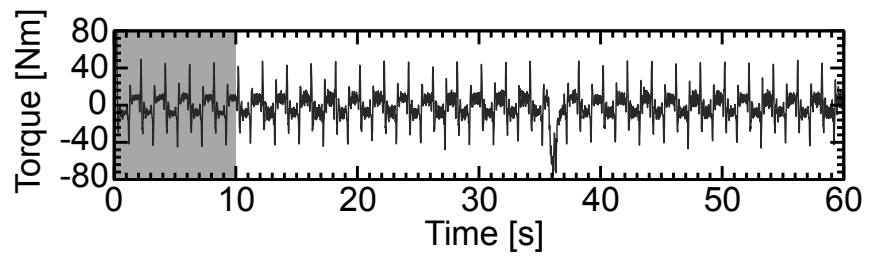


(b) Periodic angle.

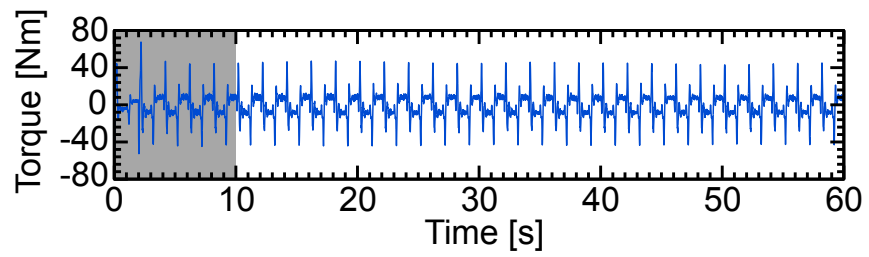


(c) Aperiodic angle.

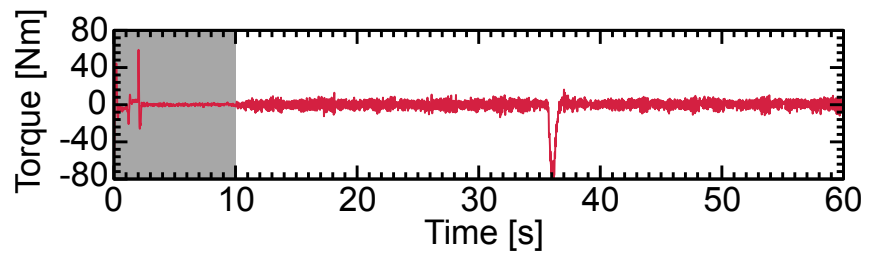
Fig. 3-15: Experimental angle results of the PVAI control.



(a) Torque.

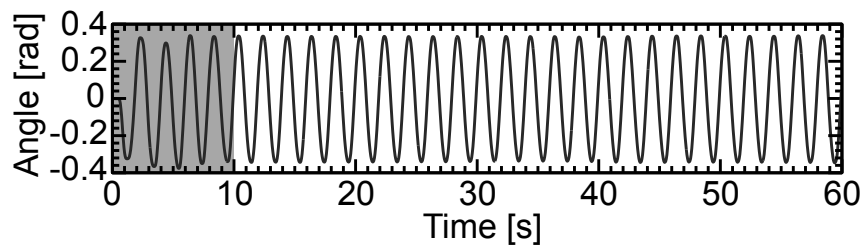


(b) Periodic torque.

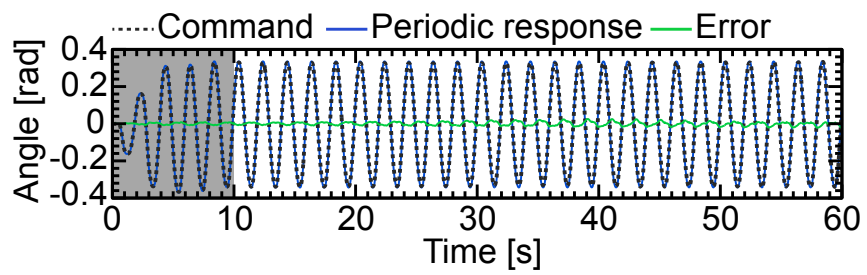


(c) Aperiodic torque.

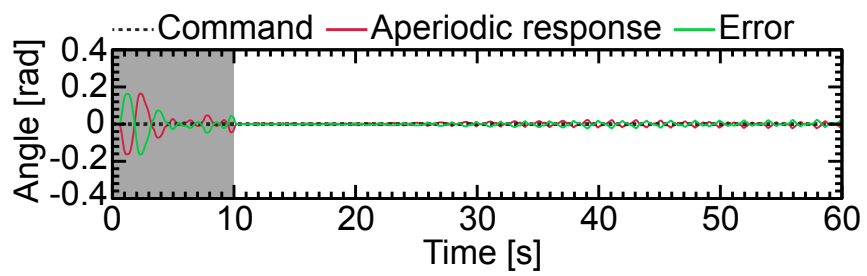
Fig. 3-16: Experimental torque results of the PVAI control.



(a) Position.

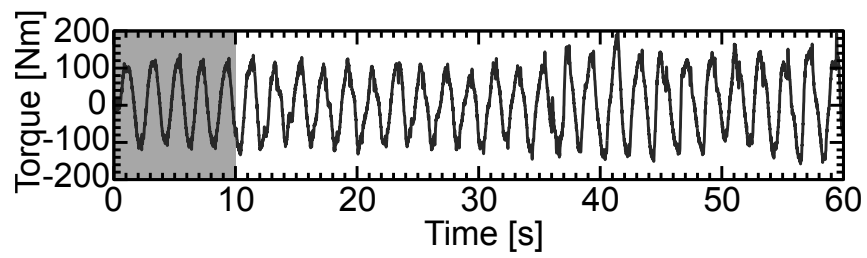


(b) Periodic position.

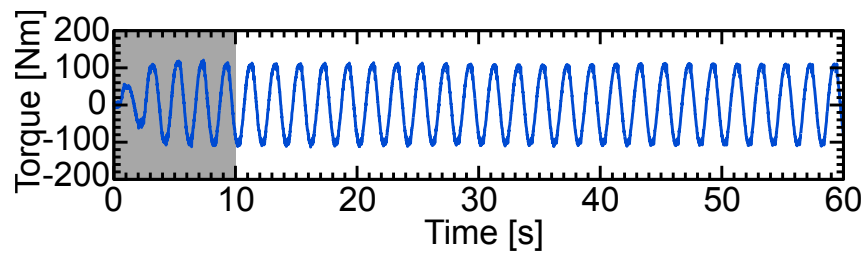


(c) Aperiodic position.

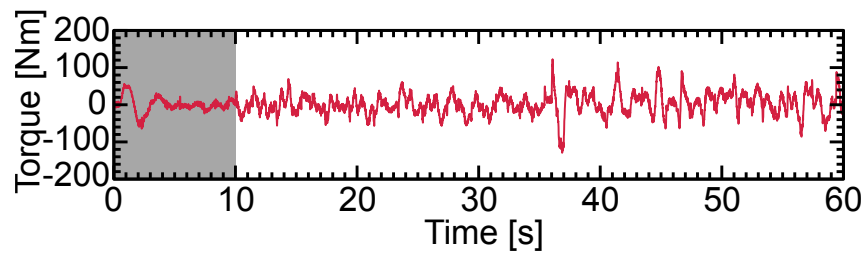
Fig. 3-17: Experimental position results of the PIAV control.



(a) Force.

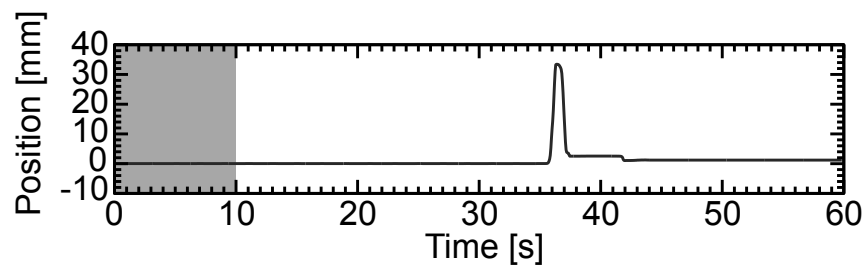


(b) Periodic force.

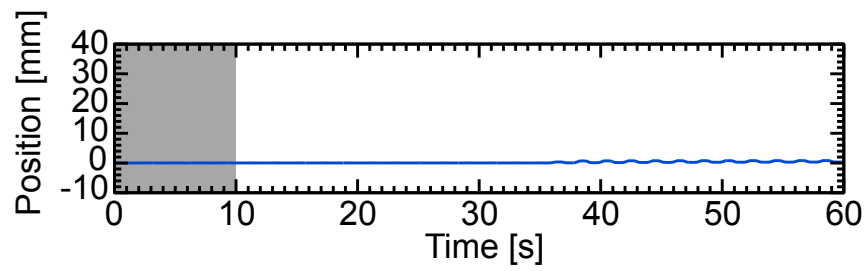


(c) Aperiodic force.

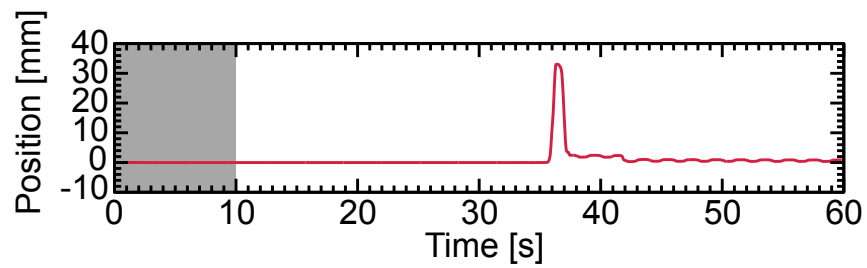
Fig. 3-18: Experimental force results of the PIAV control.



(a) Position.

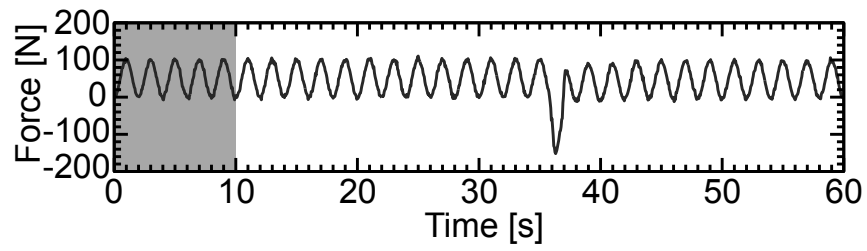


(b) Periodic position.

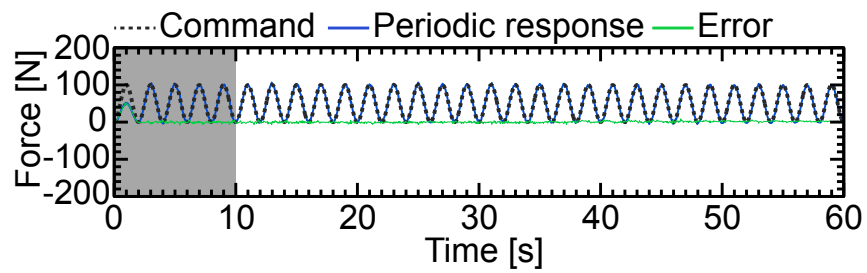


(c) Aperiodic position.

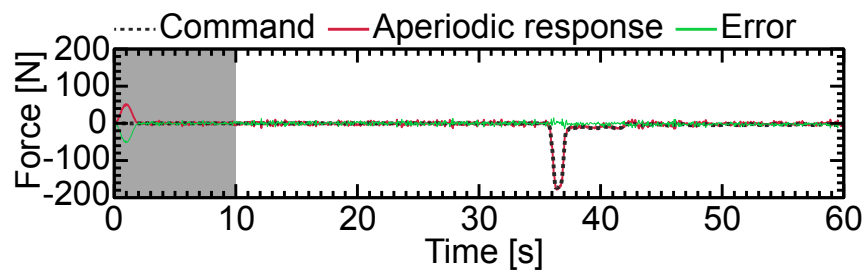
Fig. 3-19: Experimental position results of the PFAI control.



(a) Force.



(b) Periodic force.



(c) Aperiodic force.

Fig. 3-20: Experimental force results of the PFAI control.

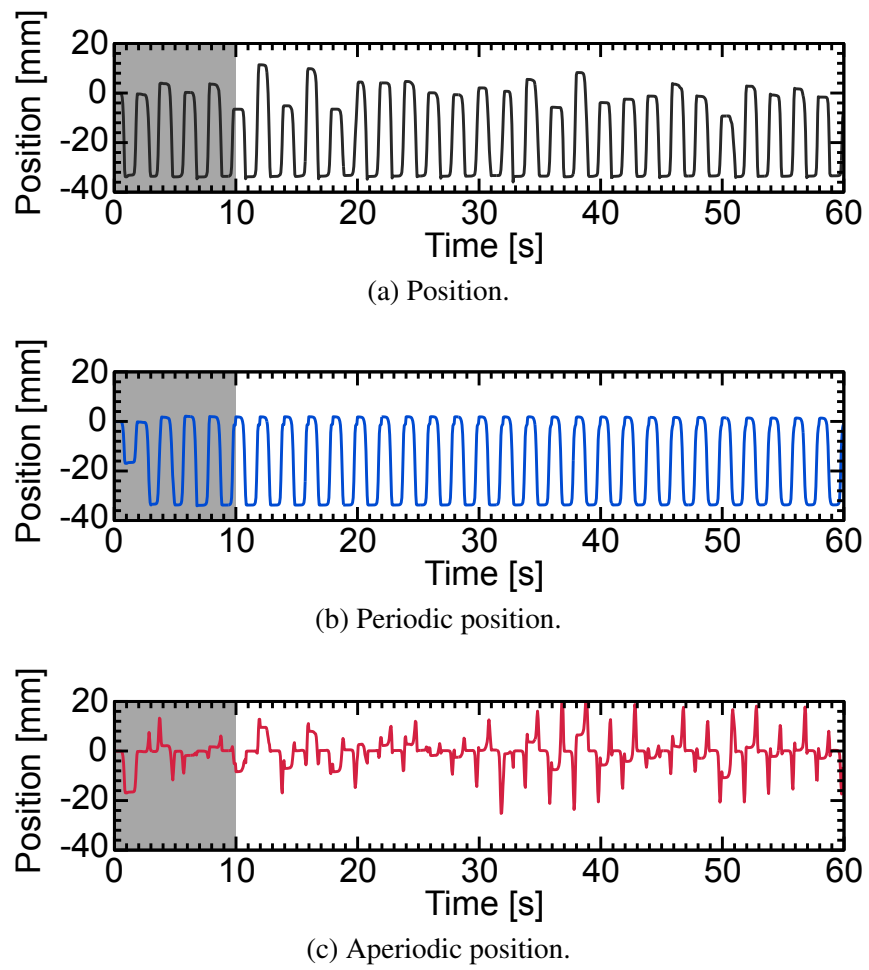
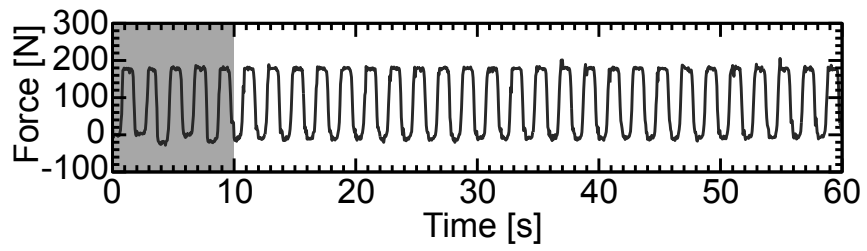
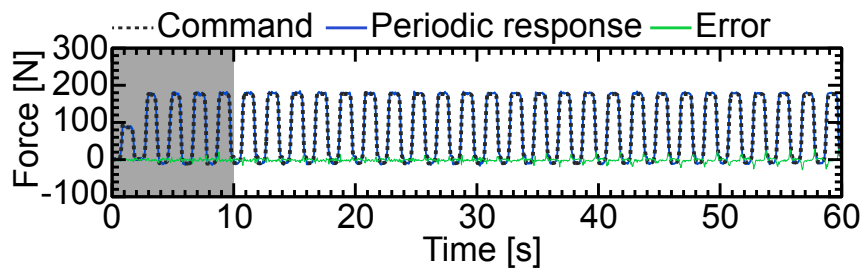


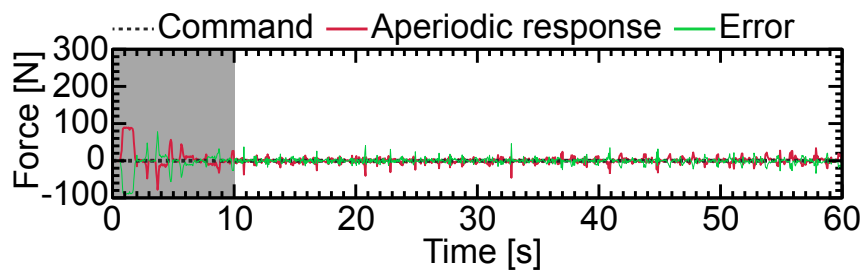
Fig. 3-21: Experimental position results of the PIAF control.



(a) Force.



(b) Periodic force.



(c) Aperiodic force.

Fig. 3-22: Experimental force results of the PIAF control.

Chapter 4

Periodic/Aperiodic Disturbance Compensation

4.1 Outline

Chapter 4 focuses on periodicity and aperiodicity of a disturbance.

Section 4.2 describes periodic-disturbance compensation. The PDOB, which estimates and compensates for a periodic disturbance, is constructed for improvement in precision of periodically working automatic systems in Subsection 4.2.1. Subsection 4.2.2 shows comparative experiments that compared the PDOB with a DOB and RC using a multi-axis manipulator.

Section 4.3 develops the PDOB to estimate and compensate not only for a periodic disturbance but also for an aperiodic disturbance because the periodic and aperiodic disturbances typically occur simultaneously in practical applications. Subsection 4.3.1 mentions the issue of the PDOB concerning an aperiodic disturbance. To improve the aperiodic-disturbance suppression performance of the PDOB, the enhanced PDOB is constructed on the basis of the combination design of the PDOB and DOB in Subsection 4.3.2. Experiments that compared the enhanced PDOB with the PDOB and DOB are shown in Subsection 4.3.3.

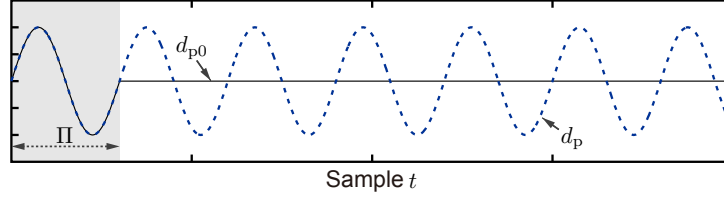


Fig. 4-1: Conceptual diagram of the periodic disturbance model.

4.2 Periodic-Disturbance Compensation

4.2.1 Periodic-Disturbance Observer

Periodic-Disturbance Model

A periodic disturbance $d_p(t)$ is modeled by

$$d_p(t + \Pi) = d_p(t) + d_{p0}(t) \quad (4.1)$$

$$d_{p0}(t) = \begin{cases} d_0(t) & t < \Pi \\ 0 & \Pi \leq t \end{cases}, \quad (4.2)$$

based on the perfect periodic state in (2.2). The periodic-disturbance model is illustrated by Fig. 4-1 and is Z transformed into

$$d_p(z^{-1}) = \frac{1}{1 - z^{-\Pi}} d_{p0}(z^{-1}). \quad (4.3)$$

A PDOB is constructed to compensate for the Z transformed periodic disturbance.

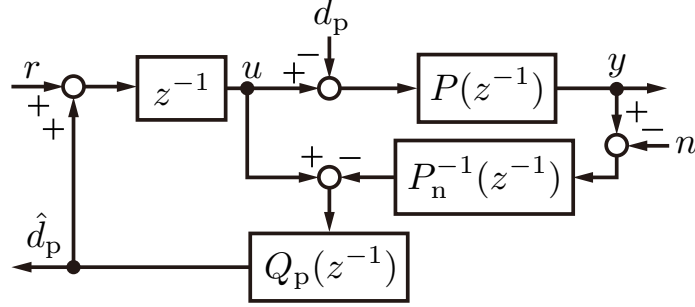
Q-filter

Consider the general DOB shown in Fig. 4-2(a), and the equivalent nominal structure shown in Fig. 4-2(b) is used to construct the PDOB. r , y , n , $P(z^{-1})$, $P_n^{-1}(z^{-1})$, and $Q_p(z^{-1})$ denote the reference, output, noise, plant, inverse nominal plant, and Q-filter of the PDOB, respectively. The DOB structure compensates for the periodic disturbance as $[1 - Q_p(z^{-1})z^{-1}]d_p$ according to Fig. 4-2(b), and the compensated periodic disturbance is expressed by

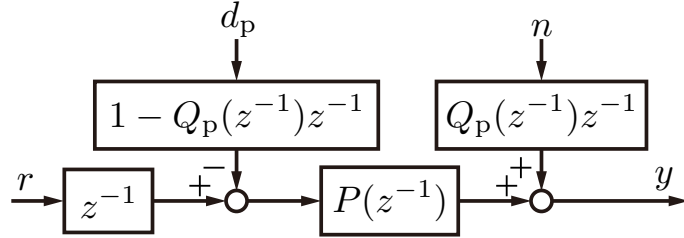
$$[1 - Q_p(z^{-1})z^{-1}]d_p = \frac{1 - Q_p(z^{-1})z^{-1}}{1 - z^{-\Pi}} d_{p0}(z^{-1}). \quad (4.4)$$

In order to set the compensated periodic disturbance in (4.4) to zero when $\Pi \leq t$, a control objective for the Q-filter design is designed as

$$\frac{1 - Q_p(z^{-1})}{1 - z^{-\Pi}} d_{p0}(z^{-1}) = \gamma d_{p0}(z^{-1}). \quad (4.5)$$



(a) Basic structure.



(b) Nominal equivalent structure.

Fig. 4-2: Block diagrams of a DOB.

This is based on

$$\gamma d_{p0}(t) = 0, \text{ if } \Pi \leq t, \quad (4.6)$$

which is caused by

$$d_{p0}(t) = 0, \text{ if } \Pi \leq t \quad (4.7)$$

because of (4.2). γ is a design parameter that is an integer. In the control objective, z^{-1} of $[1 - Q_p(z^{-1})z^{-1}]d_p$ is ignored to make the Q-filter causal. The Q-filter of the PDOB is derived from the

control objective in (4.5) as follows

$$[1 - Q_p(z^{-1})]d_{p0}(z^{-1}) = (1 - z^{-\Pi})\gamma d_{p0}(z^{-1}) \quad (4.8)$$

$$-Q_p(z^{-1})d_{p0}(z^{-1}) = (1 - z^{-\Pi})\gamma d_{p0}(z^{-1}) - d_{p0}(z^{-1}) \quad (4.9)$$

$$-Q_p(z^{-1}) = (1 - z^{-\Pi})\gamma - 1 \quad (4.10)$$

$$Q_p(z^{-1}) = 1 - \gamma(1 - z^{-\Pi}). \quad (4.11)$$

As shown in Fig. 4-2(b), $1 - Q_p(z^{-1})z^{-1}$ is a sensitivity function, which is a disturbance suppression characteristic, and $Q_p(z^{-1})z^{-1}$ is a complementary sensitivity function, which is sensitivity for noise and robust stability. Bode diagrams of the sensitivity and complementary sensitivity functions using the Q-filter in (4.11) are shown in Fig. 4-3. The sensitivity function $1 - Q_p(z^{-1})z^{-1}$ realizes a high-pass characteristic and an infinite number of band-stop characteristics, which eliminate a constant element, fundamental wave, and harmonics of a periodic disturbance. However, the complementary sensitivity function lacks a low-pass characteristic. Consequently, the stability of the Q-filter is not robust against modeling errors and is sensitive to noise at high frequencies. To improve the complementary sensitivity function in the high-frequency range, a low-pass filter $q_p(z^{-1})$ is added into the Q-filter in (4.11) as

$$Q_p(z^{-1}) = q_p(z^{-1})[1 - \gamma(1 - z^{-\Pi})]. \quad (4.12)$$

This study employs the first-order low-pass filter

$$q_p(z^{-1}) = \frac{g_p T_s + g_p T_s z^{-1}}{(g_p T_s + 2) + (g_p T_s - 2)z^{-1}}, \quad (4.13)$$

where g_p is the cutoff frequency of the low-pass filter for the PDOB. Bode diagrams of sensitivity and complementary sensitivity functions using the modified Q-filter in (4.12) are shown in Fig. 4-4. Although the periodic-disturbance compensation performance deteriorates in the high-frequency range, the gain of the complementary sensitivity function is attenuated in the high-frequency range. Finally, a block diagram of the PDOB is shown in Fig. 4-5.

Modified Calculation of Delay

The use of a low-pass filter has a problem that frequencies of the band-stop characteristics are moved as shown in Fig. 4-6 when the delay Π is calculated by

$$\Pi = \frac{2\pi}{T_s \omega_0}. \quad (4.14)$$

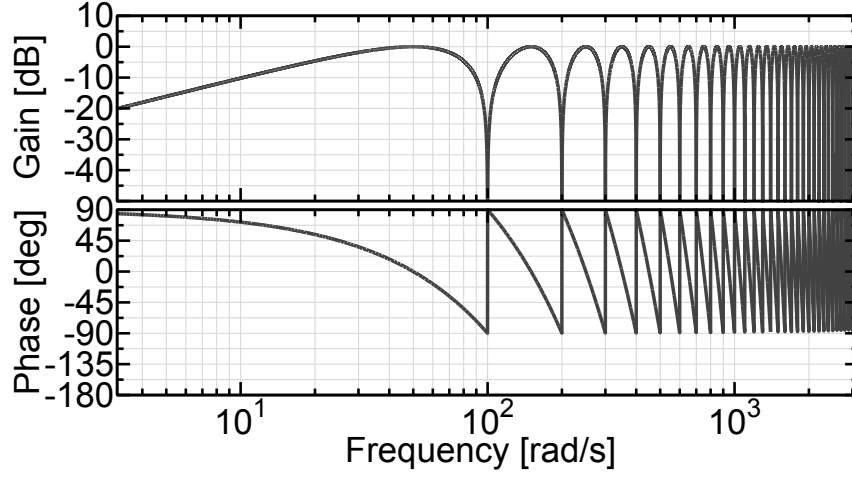
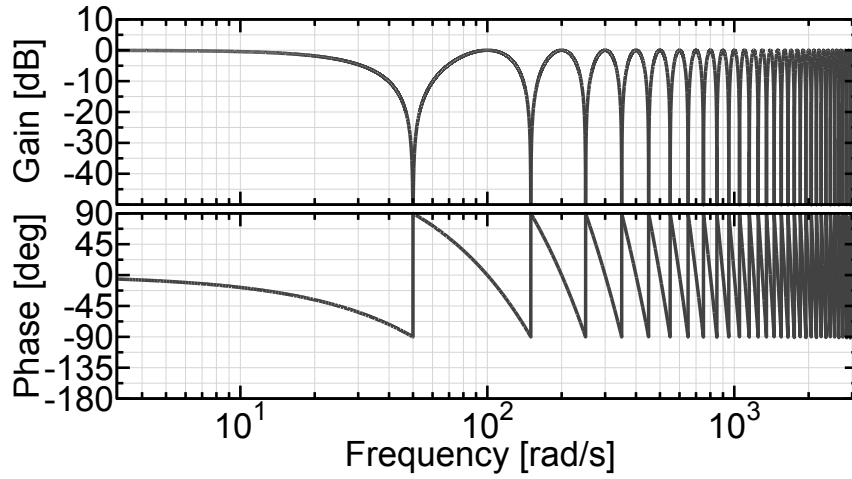

 (a) Sensitivity function $1 - Q_p(z^{-1})z^{-1}$.

 (b) Complementary sensitivity function $Q_p(z^{-1})z^{-1}$.

Fig. 4-3: Bode diagrams of the sensitivity and complementary sensitivity functions of the PDOB without the low-pass filter $q_p(z^{-1})$ in (4.13). The parameters are $\omega_0 = 100$ rad/s, $\gamma = 0.5$, $g_p = 1000$ rad/s, and $T_s = 0.01$ ms.

To correct the frequencies, Π is calculated as

$$\Pi = \frac{2\pi g_p \gamma - \omega_0}{T_s g_p \omega_0 \gamma}. \quad (4.15)$$

(4.15) can be derived as follows. First, a correct delay Π is defined as

$$\Pi = \frac{2\pi}{T_s \omega_0} (1 + \sigma), \quad (4.16)$$

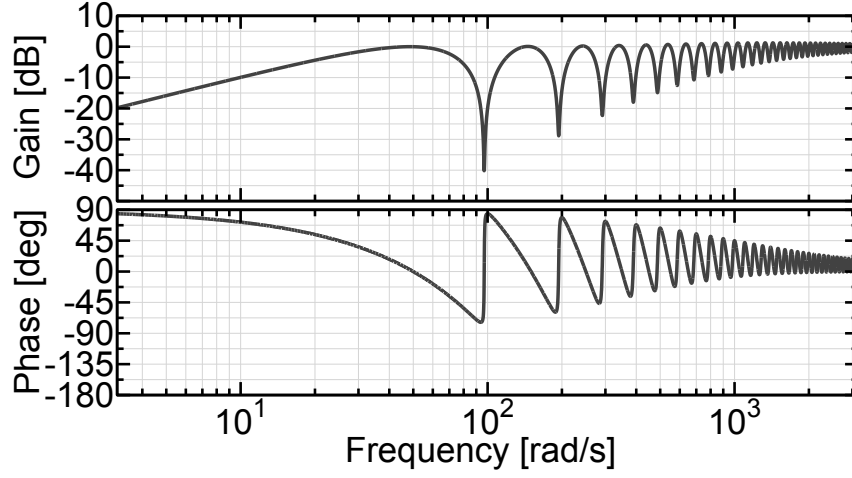
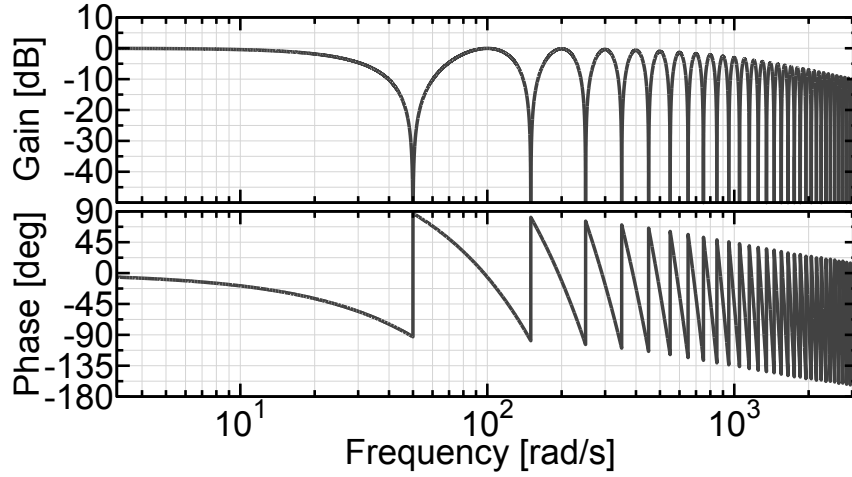

 (a) Sensitivity function $1 - Q_p(z^{-1})z^{-1}$.

 (b) Complementary sensitivity function $Q_p(z^{-1})z^{-1}$.

Fig. 4-4: Bode diagrams of the sensitivity and complementary sensitivity functions of the PDOB with the low-pass filter $q_p(z^{-1})$ in (4.13). The parameters are $\omega_0 = 100$ rad/s, $\gamma = 0.5$, $g_p = 1000$ rad/s, and $T_s = 0.01$ ms.

where σ is a small variation satisfying $|2\pi\sigma| < 1$ caused by the low-pass filter $q_p(z^{-1})$ in (4.13). The variation σ decreases as the cutoff frequency g_p increases. For the frequency adjustment, an objective for the sensitivity characteristic at the fundamental frequency ω_0 is set as

$$1 - Q_p(e^{-j\omega_0 T_s}) = 0, \quad (4.17)$$

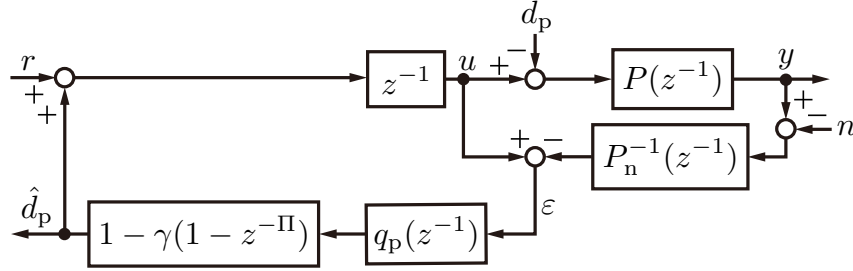


Fig. 4-5: Block diagram of the PDOB.

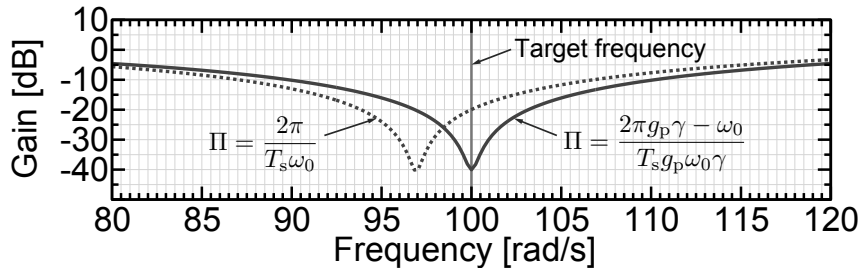


Fig. 4-6: Effect of the delay calculation in (4.15) on the frequency change of the sensitivity function $1 - Q_p(z^{-1})z^{-1}$ around the fundamental frequency, which is caused by the low-pass filter $q_p(z^{-1})$ in (4.13). The parameters are $\omega_0 = 100$ rad/s, $\gamma = 0.5$, $g_p = 1000$ rad/s, and $T_s = 0.01$ ms.

where z^{-1} is ignored. By substituting the Q-filter in (4.12) for (4.17) and $\frac{g_p}{g_p + j\omega_0}$ for q_p , an approximate objective is given as

$$\frac{g_p \gamma (1 - e^{-j\omega_0 T_s \Pi}) + j\omega_0}{g_p + j\omega_0} = 0. \quad (4.18)$$

Using the approximation of the time delay element

$$e^{-j\omega_0 T_s \Pi} = e^{-j2\pi} e^{-j2\pi\sigma} = e^{-j2\pi\sigma} \approx 1 - j2\pi\sigma \quad (4.19)$$

based on (4.16) and $|2\pi\sigma| < 1$, the objective in (4.18) is further approximated as

$$\frac{j2\pi g_p \gamma \sigma + j\omega_0}{g_p + j\omega_0} = 0, \quad (4.20)$$

and this provides

$$2\pi g_p \gamma \sigma + \omega_0 = 0. \quad (4.21)$$

The modified delay calculation in (4.15) is derived by solving (4.16) and (4.21) in terms of the delay Π .

Transfer Functions

Six transfer functions of the PDOB from r , d_p , and n to y , u , and \hat{d}_p are

$$\begin{bmatrix} y \\ u \\ \hat{d}_p \end{bmatrix} = \frac{1}{\phi} \begin{bmatrix} P_N^2 Q_D (1 + \Delta) z^{-1} & -P_N^2 (Q_D - Q_N z^{-1}) (1 + \Delta) & P_N Q_N P_D (1 + \Delta) z^{-1} \\ P_N P_D Q_D z^{-1} & P_N Q_N P_D (1 + \Delta) z^{-1} & Q_N P_D^2 z^{-1} \\ -P_N Q_N \Delta P_D z^{-1} & P_N Q_N P_D (1 + \Delta) & Q_N P_D^2 \end{bmatrix} \begin{bmatrix} r \\ d_p \\ n \end{bmatrix}, \quad (4.22)$$

where the characteristic polynomial is

$$\phi(z^{-1}) = P_N P_D (Q_D + Q_N \Delta z^{-1}), \quad (4.23)$$

and the modeling error and system polynomials are defined by

$$P(z^{-1}) = (1 + \Delta) P_n(z^{-1}) \quad (4.24)$$

$$P_n(z^{-1}) = \frac{P_N(z^{-1})}{P_D(z^{-1})} \quad (4.25)$$

$$Q_p(z^{-1}) = \frac{Q_N(z^{-1})}{Q_D(z^{-1})} = \frac{(g_p T_s + g_p T_s z^{-1}) \{1 - \gamma(1 - z^{-\Pi})\}}{(g_p T_s + 2) + (g_p T_s - 2)z^{-1}}. \quad (4.26)$$

P_n denotes the nominal plant. Nominally, the transfer functions become

$$\begin{bmatrix} y \\ u \\ \hat{d}_p \end{bmatrix} = \frac{1}{\phi_n} \begin{bmatrix} P_N^2 Q_D z^{-1} & -P_N^2 (Q_D - Q_N z^{-1}) & P_N Q_N P_D z^{-1} \\ P_N P_D Q_D z^{-1} & P_N Q_N P_D z^{-1} & Q_N P_D^2 z^{-1} \\ 0 & P_N Q_N P_D & Q_N P_D^2 \end{bmatrix} \begin{bmatrix} r \\ d_p \\ n \end{bmatrix}, \quad (4.27)$$

where the nominal characteristic polynomial is

$$\phi_n(z^{-1}) = P_N P_D Q_D. \quad (4.28)$$

Nominal Stability

According to the nominal characteristic polynomial in (4.28), nominal stability depends on a numerator polynomial of a nominal plant P_N , denominator polynomial of a nominal plant P_D , and denominator polynomial of the Q-filter:

$$Q_D(z^{-1}) = (g_p T_s + 2) + (g_p T_s - 2)z^{-1}. \quad (4.29)$$

A pole of $Q_D = 0$ can be calculated as follows

$$Q_D(z^{-1}) = (g_p T_s + 2) + (g_p T_s - 2)z^{-1} = 0 \quad (4.30)$$

$$(g_p T_s + 2)z = -(g_p T_s - 2) \quad (4.31)$$

$$z = \frac{2 - g_p T_s}{2 + g_p T_s}. \quad (4.32)$$

The numerator of the pole in (4.32) is smaller than the denominator of the pole as

$$|2 - g_p T_s| < |2 + g_p T_s| \quad (4.33)$$

because

$$0 < g_p T_s. \quad (4.34)$$

Hence, the pole $z = \frac{2 - g_p T_s}{2 + g_p T_s}$ is stable because

$$|z| = \left| \frac{2 - g_p T_s}{2 + g_p T_s} \right| < 1, \because |2 - g_p T_s| < |2 + g_p T_s|. \quad (4.35)$$

Therefore, the PDOB is nominally stable if and only if a plant does not have unstable zeros and poles.

Optimal Design Parameter

The low-pass filter is set to $q_p(z^{-1}) = 1$ and the Z -operators z^{-1} in $1 - Q_p(z^{-1})z^{-1}$ and $Q_p(z^{-1})z^{-1}$ are ignored to simplify design of γ . The design parameter γ especially affects $1 - Q_p(z^{-1})$ and $Q_p(z^{-1})$ at the frequencies ω_{b1} and ω_{b2} :

$$\omega_{b1} = (2n) \frac{\omega_0}{2}, \quad \omega_{b2} = (2n + 1) \frac{\omega_0}{2}, \quad n = 0, 1, 2, \dots, \quad (4.36)$$

as shown in Fig. 4-7. At the frequencies ω_{b1} and ω_{b2} , the gains of the functions

$$|1 - Q_p(e^{-j\omega T_s})| = \left| 2\gamma \sin \left(-\frac{\Pi T_s}{2} \omega \right) \right| \quad (4.37)$$

$$|Q_p(e^{-j\omega T_s})| = \left| \sqrt{1 + 4\gamma(\gamma - 1) \sin^2 \left(-\frac{\Pi T_s}{2} \omega \right)} \right| \quad (4.38)$$

become as follows

$$|1 - Q_p(e^{-j\omega_{b1} T_s})| = 0 \quad (4.39)$$

$$|1 - Q_p(e^{-j\omega_{b2} T_s})| = |2\gamma| \quad (4.40)$$

$$|Q_p(e^{-j\omega_{b1} T_s})| = 1 \quad (4.41)$$

$$|Q_p(e^{-j\omega_{b2} T_s})| = |1 - 2\gamma|. \quad (4.42)$$

The minimum complementary sensitivity characteristic at ω_{b2} : $|Q_p(e^{-j\omega_{b2} T_s})| = 0$ provides the optimal design parameter:

$$\gamma = 0.5. \quad (4.43)$$

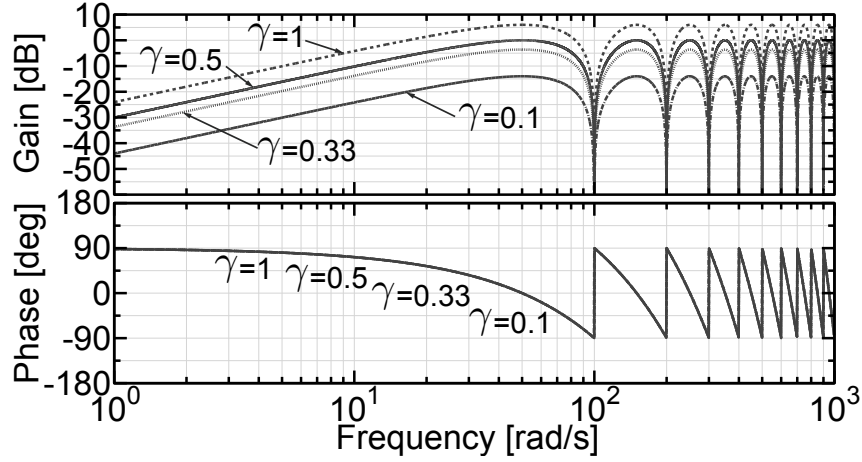
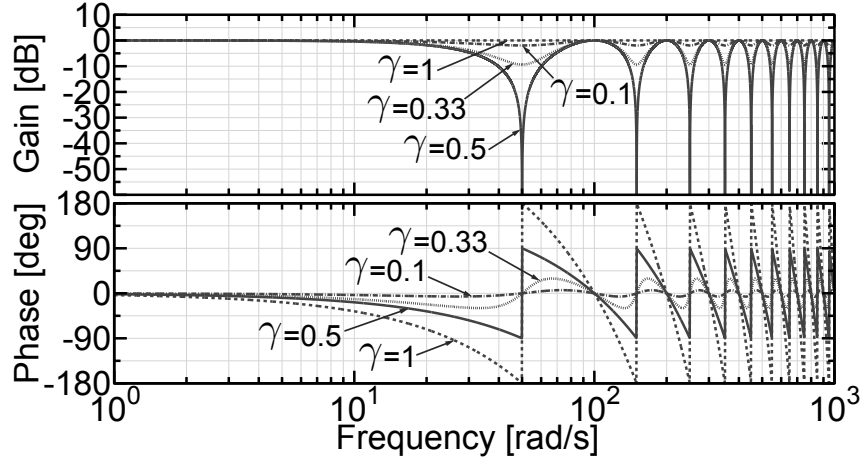

 (a) Sensitivity function $1 - Q_p(z^{-1})z^{-1}$.

 (b) Complementary sensitivity function $Q_p(z^{-1})z^{-1}$.

Fig. 4-7: Bode diagrams of the sensitivity and complementary sensitivity functions of the PDOB with variations in the design parameter γ . The parameters are $\omega_0 = 100$ rad/s, $g_p = 1000$ rad/s, and $T_s = 0.01$ ms.

Design of Cutoff Frequency

The design parameter γ is set to 0.5 and the Z -operators z^{-1} in $1 - Q_p(z^{-1})z^{-1}$ and $Q_p(z^{-1})z^{-1}$ are ignored to simplify design of g_p . The cutoff frequency g_p of (4.13) is designed in accordance with two objectives: fundamental-wave attenuation and robust stability.

First, a lower limit for g_p is given by the fundamental-wave attenuation performance. At the funda-

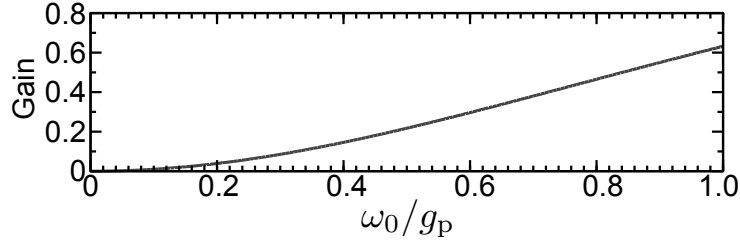


Fig. 4-8: Fundamental-wave attenuation performance of the PDOB with variations in ω_0/g_p .

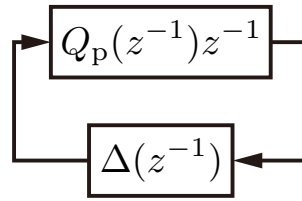


Fig. 4-9: Equivalent block diagram of the DOB structure in Fig. 4-2(a).

mental frequency, the gain of $1 - Q_p(e^{-j\omega_0 T_s})$ using (4.15) is

$$|1 - Q_p(e^{-j\omega_0 T_s})| = \frac{\left\{ 1 - \cos\left(2\frac{\omega_0}{g_p}\right) \right\} + 2\frac{\omega_0}{g_p} \left\{ \frac{\omega_0}{g_p} - \sin\left(2\frac{\omega_0}{g_p}\right) \right\}}{2 \left\{ 1 + \left(\frac{\omega_0}{g_p}\right)^2 \right\}}, \quad (4.44)$$

which depends only on ω_0/g_p . Fig. 4-8 shows the gain variation in (4.44) with respect to ω_0/g_p . A lower limit for ω_0/g_p can be determined with the required precision from Fig. 4-8.

Next, an upper limit for g_p is determined in accordance with the robust stability based on the equivalent block diagram of the PDOB for the small-gain theorem in Fig. 4-9. The modeling error consists of the weighting function $W(z^{-1})$ and the variation $\delta(z^{-1})$

$$\Delta(z^{-1}) = W(z^{-1})\delta(z^{-1}), \quad (4.45)$$

where the variation satisfies

$$\|\delta(z^{-1})\|_\infty \leq 1. \quad (4.46)$$

By assuming a nominally stable PDOB and modeling error, the robust-stability condition based on the small-gain theorem and Fig. 4-9 is

$$\|W(z^{-1})Q_p(z^{-1})z^{-1}\|_\infty = \|W(z^{-1})Q_p(z^{-1})\|_\infty < 1. \quad (4.47)$$

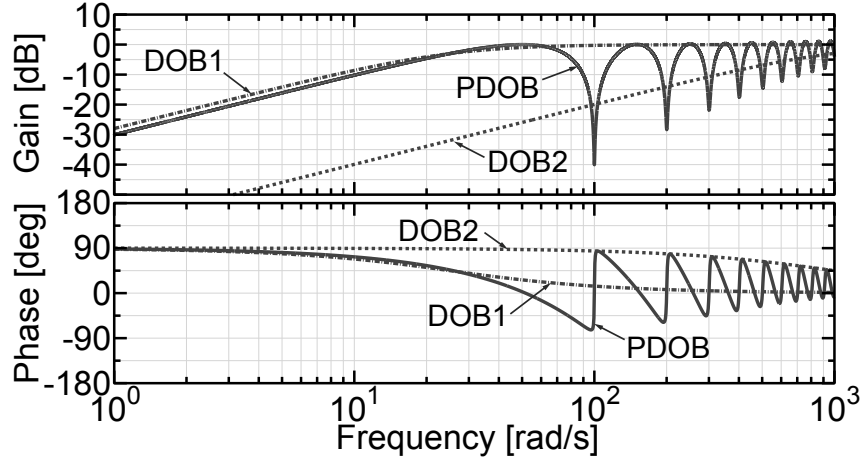
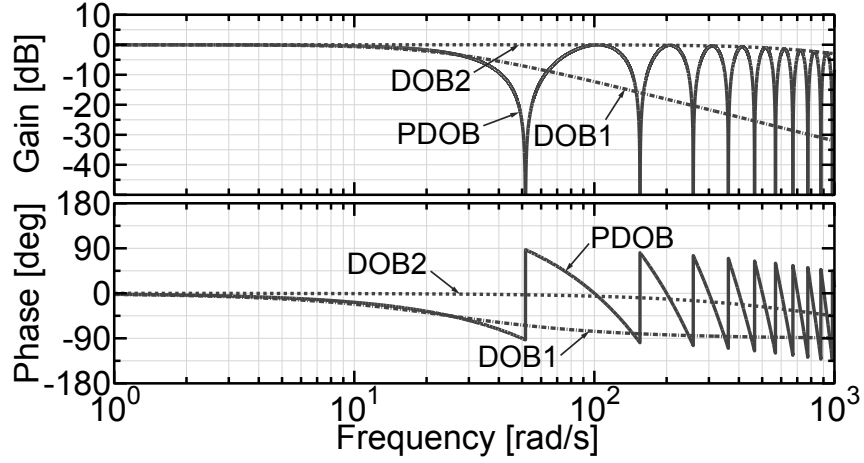

 (a) Sensitivity function $1 - Q_p(z^{-1})z^{-1}$.

 (b) Complementary sensitivity function $Q_p(z^{-1})z^{-1}$.

Fig. 4-10: Comparative Bode diagrams of the PDOB and DOBs. The parameters for the PDOB are $\omega_0 = 100$ rad/s, $\gamma = 0.5$, $g_p = 1000$ rad/s, and $T_s = 0.01$ ms. The cutoff frequencies for DOB1 and DOB2 are 25 rad/s and 100 rad/s, respectively.

It can be rewritten as

$$\left| \frac{g_p}{g_p + j\omega} 0.5(1 + e^{-j\omega T_s}) e^{-j\omega T_s} \right| \leq \left| \frac{g_p}{g_p + j\omega} \right| < \left| \frac{1}{W(e^{-j\omega T_s})} \right|, \quad \forall \omega. \quad (4.48)$$

Hence, its sufficient condition is

$$\left| \frac{g_p}{g_p + j\omega} \right| < \left| \frac{1}{W(e^{-j\omega T_s})} \right|, \quad (4.49)$$

which determines the upper limit for g_p .

Table 4.1: Parameters of the comparative experiments for the PDOB.

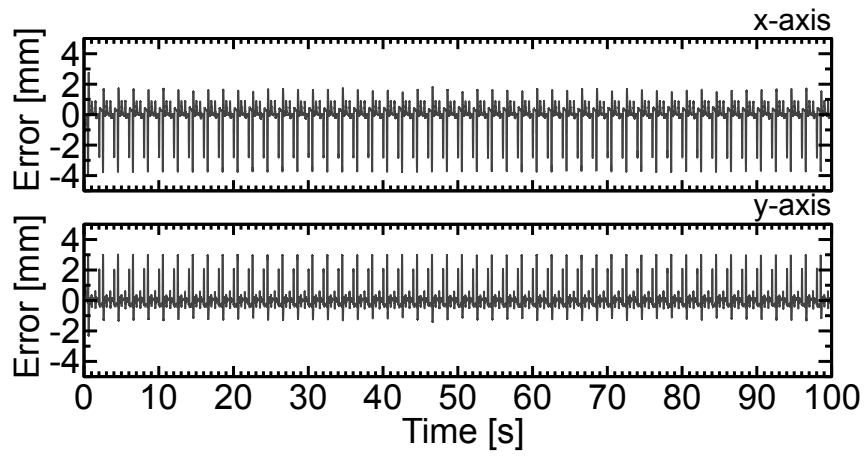
Parameter	Symbol	Value (1st, 2nd, 3rd) Joint
Sampling time	T_s [ms]	0.1
Proportional gain	K_P	400, 400, 400
Differential gain	K_D	40, 40, 40
Nominal inertia	J_n [kgm ²]	7.0, 3.0, 0.3
Nominal torque constant	K_{tn} [Nm/A]	0.59, 0.59, 0.238
Gear ratio	G_r	192, 120, 80
Length	L [m]	0.26, 0.27, 0.09
Identified fundamental freq.	ω_0 [rad/s]	3, 3, 3
Design parameter	γ	0.5, 0.5, 0.5
Cutoff freq. for the PDOB	g_p [rad/s]	200, 200, 200
Cutoff freq. for the DOB	—	200, 200, 200
Cutoff freq. for the RC	—	30, 30, 30

Comparisons with Disturbance Observers

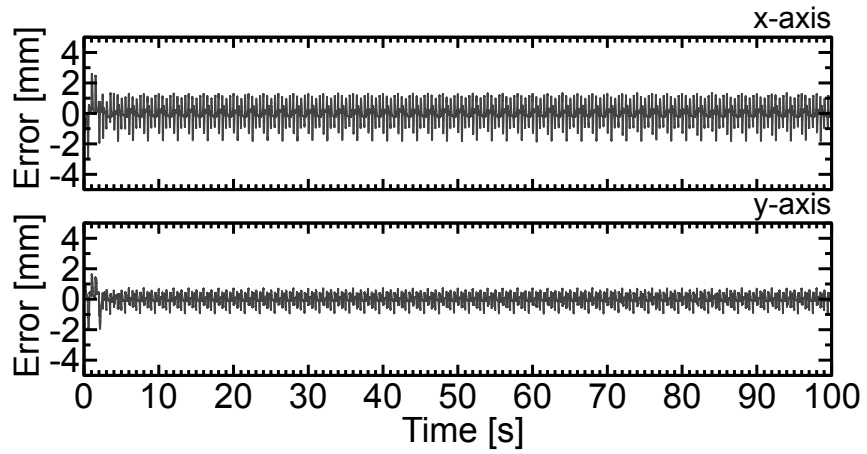
The sensitivity and complementary sensitivity functions of the PDOB are compared with those of DOBs: DOB1 and DOB2, as shown in Fig. 4-10. In the sensitivity functions shown in Fig. 4-10(a), the PDOB achieves the lowest gain against the periodic disturbance, which consists of a fundamental wave at 100 rad/s and harmonics at 200, 300, \dots rad/s. Compared with DOB1, the sensitivity function of the PDOB includes not only a high-pass characteristic but also an infinite number of band-stop characteristics. Thus, the PDOB improves the sensitivity function only at the frequencies of the periodic disturbance in the tradeoff between sensitivity and complementary sensitivity functions. Moreover, the periodic-disturbance suppression characteristic of the PDOB is better than that of DOB2, and the gain of the complementary sensitivity function of the PDOB has an infinite number of band-stop characteristics in addition to the low-pass characteristic same as DOB2. Thus, both the periodic-disturbance suppression characteristic and robust stability of the PDOB are better than those of DOB2 in the tradeoff.

4.2.2 Experiments

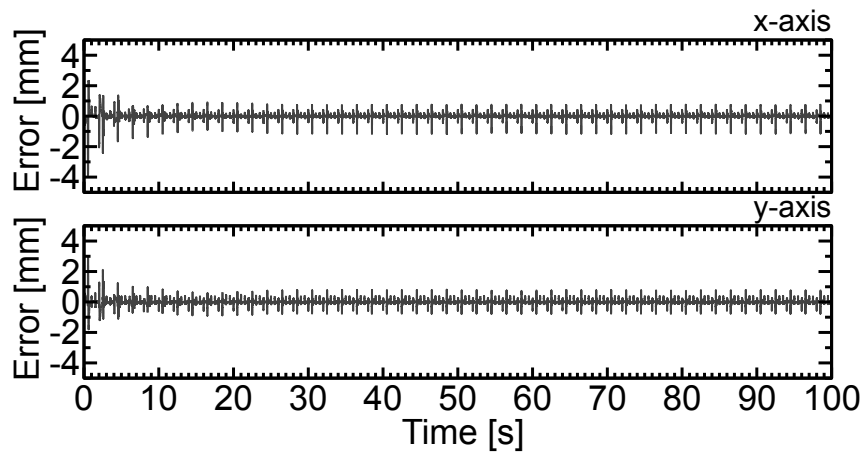
The PDOB was comparatively validated by the experiments using the multi-axis manipulator shown in Fig. 3-10. The experimental parameters are summarized in Table 4.1. The experiments compared the PDOB with a DOB and RC under proportional and derivative position control. The PDOB and RC were implemented with a DOB because they do not compensate for aperiodic disturbances. The position commands for x and y axes in the workspaces were set as



(a) DOB.



(b) RC+DOB.



(c) PDOB+DOB.

Fig. 4-11: Results of the comparative experiments for the PDOB.

$$x^{\text{cmd}}(t) = \begin{cases} x_0 \text{ mm} & \text{if } \tilde{t} < 0.5 \\ x_0 + 100(\tilde{t} - 0.5) \text{ mm} & \text{if } 0.5 \leq \tilde{t} < 1.0 \\ x_0 + 50 \text{ mm} & \text{if } 1.0 \leq \tilde{t} < 1.5 \\ x_0 + 100(2.0 - \tilde{t}) \text{ mm} & \text{if } 1.5 \leq \tilde{t} < 2.0 \end{cases} \quad (4.50)$$

$$y^{\text{cmd}}(t) = \begin{cases} y_0 \text{ mm} & \text{if } \tilde{t} < 0.5 \\ y_0 + 100(\tilde{t} - 0.5) \text{ mm} & \text{if } 0.5 \leq \tilde{t} < 1.0 \\ y_0 + 50 \text{ mm} & \text{if } 1.0 \leq \tilde{t} < 1.5 \\ y_0 + 100(2.0 - \tilde{t}) \text{ mm} & \text{if } 1.5 \leq \tilde{t} < 2.0 \end{cases} \quad (4.51)$$

$$\tilde{t} = T_s t \bmod 2. \quad (4.52)$$

Error results of the comparative experiments for the PDOB are shown in Fig. 4-11, where the PDOB+DOB performed the best precision in the three methods. In the frequency domain calculated by the discrete Fourier transform shown in Fig. 4-12, the fundamental wave and harmonics attenuation can be confirmed at $3n \text{ rad/s}$, $n = 1, 2, 3 \dots$

4.3 Aperiodic-Disturbance Compensation

4.3.1 Problem of Periodic-Disturbance Observer

The PDOB, which was designed to estimate and compensate for a periodic disturbance, has a problem regarding aperiodic disturbances. According to the Q-filter in (4.12), sensitivity function $S(z^{-1})$ and complementary sensitivity function $T(z^{-1})$ of the PDOB are

$$S(z^{-1}) = 1 - Q_p(z^{-1})z^{-1} = 1 - q_p(z^{-1})\{1 - \gamma(1 - z^{-\Pi})\}z^{-1} \quad (4.53)$$

$$T(z^{-1}) = Q_p(z^{-1})z^{-1} = q_p(z^{-1})\{1 - \gamma(1 - z^{-\Pi})\}z^{-1}. \quad (4.54)$$

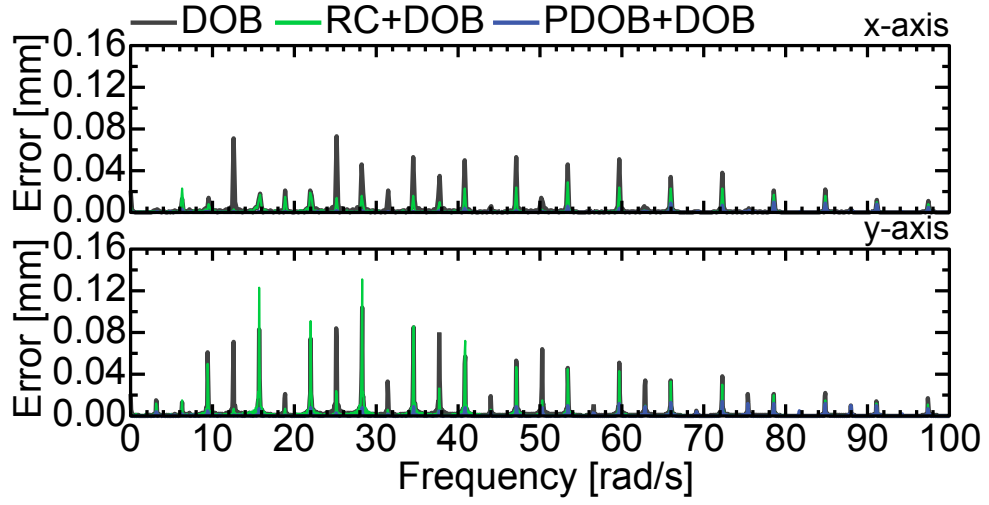
Substituting the first-order low-pass filter:

$$q_p(z^{-1}) = \frac{g_p T_s + g_p T_s z^{-1}}{(g_p T_s + 2) + (g_p T_s - 2)z^{-1}}, \quad (4.55)$$

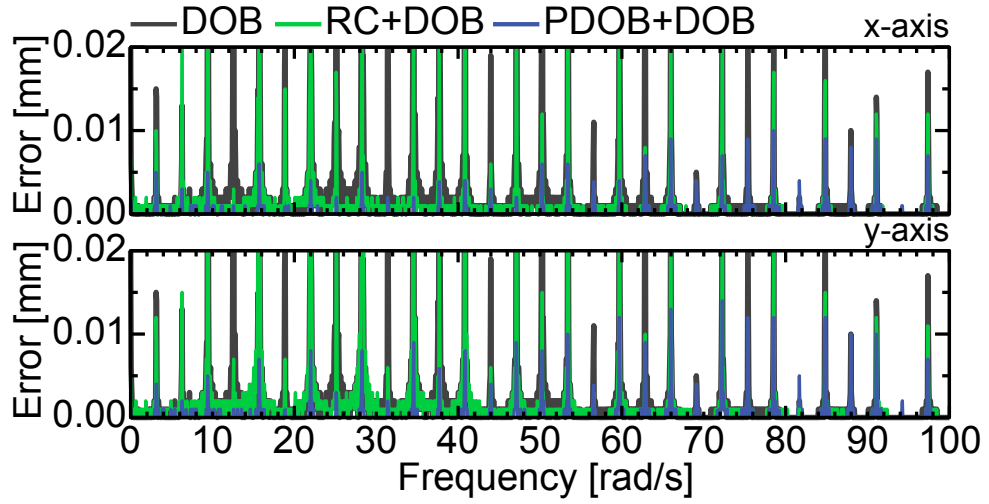
for $q_p(z^{-1})$, the sensitivity and complementary sensitivity functions become

$$S(z^{-1}) = 1 - \frac{g_p T_s + g_p T_s z^{-1}}{(g_p T_s + 2) + (g_p T_s - 2)z^{-1}} \{1 - \gamma(1 - z^{-\Pi})\}z^{-1} \quad (4.56)$$

$$T(z^{-1}) = \frac{g_p T_s + g_p T_s z^{-1}}{(g_p T_s + 2) + (g_p T_s - 2)z^{-1}} \{1 - \gamma(1 - z^{-\Pi})\}z^{-1}, \quad (4.57)$$



(a) Overall view.



(b) Enlarged view.

Fig. 4-12: Discrete Fourier transform results of Fig. 4-11 between 20 s and 100 s.

and frequency characteristics are

$$S(e^{-j\omega T_s}) = 1 - \frac{g_p T_s + g_p T_s e^{-j\omega T_s}}{(g_p T_s + 2) + (g_p T_s - 2)e^{-j\omega T_s}} \{1 - \gamma(1 - e^{-j\omega T_s \Pi})\} e^{-j\omega T_s} \quad (4.58)$$

$$T(e^{-j\omega T_s}) = \frac{g_p T_s + g_p T_s e^{-j\omega T_s}}{(g_p T_s + 2) + (g_p T_s - 2)e^{-j\omega T_s}} \{1 - \gamma(1 - e^{-j\omega T_s \Pi})\} e^{-j\omega T_s}. \quad (4.59)$$

Based on the bilinear transform:

$$z^{-1} \approx \frac{2 - T_s s}{2 + T_s s}, \quad (4.60)$$

$e^{-j\omega T_s}$ can be approximately transformed into

$$e^{-j\omega T_s} \approx \frac{2 - T_s j\omega}{2 + T_s j\omega}. \quad (4.61)$$

Using (4.61), the low-pass filter $q_p(z^{-1})$ in (4.55) is approximated into

$$q(e^{-j\omega T_s}) \approx \frac{1}{1 + j\Omega} \quad (4.62)$$

$$\Omega_p = \frac{\omega}{g_p}, \quad (4.63)$$

and (4.62) changes (4.58) and (4.59) to

$$S(e^{-j\omega T_s}) \approx \bar{S}(e^{-j\omega T_s}) = 1 - \frac{1}{1 + j\Omega_p} \{1 - \gamma(1 - e^{-j\omega T_s \Pi})\} e^{-j\omega T_s} \quad (4.64)$$

$$T(e^{-j\omega T_s}) \approx \bar{T}(e^{-j\omega T_s}) = \frac{1}{1 + j\Omega_p} \{1 - \gamma(1 - e^{-j\omega T_s \Pi})\} e^{-j\omega T_s}. \quad (4.65)$$

To emphasize the other major frequency characteristic rather than the one sampling delay z^{-1} , frequency characteristics of the approximate sensitivity and complementary sensitivity functions are derived by ignoring $e^{-j\omega T_s}$ as

$$\bar{S}(e^{-j\omega T_s}) \approx \bar{S}(j\omega) = \frac{j\Omega_p}{1 + j\Omega_p} + \frac{1}{1 + j\Omega_p} \gamma(1 - e^{-j\omega T_s \Pi}) \quad (4.66)$$

$$\bar{T}(e^{-j\omega T_s}) \approx \bar{T}(j\omega) = \frac{1}{1 + j\Omega_p} \{1 - \gamma(1 - e^{-j\omega T_s \Pi})\}. \quad (4.67)$$

The sensitivity function $\bar{S}(j\omega)$ has different frequency characteristics in the different frequency ranges as follows

$\Omega_p \ll 1$:

$$\lim_{\Omega_p \rightarrow 0} \bar{S}(j\omega) = \gamma(1 - e^{-j\omega T_s \Pi}) \quad (4.68)$$

$\Omega_p = 1$:

$$\bar{S}(jg_p) = \frac{\gamma(1 - e^{-jg_p T_s \Pi}) + j}{1 + j} \quad (4.69)$$

$1 \ll \Omega_p$:

$$\lim_{\Omega_p \rightarrow \infty} \bar{S}(j\omega) = 1. \quad (4.70)$$

In the low frequency range satisfying $\Omega_p \ll 1$, the sensitivity characteristic satisfies

$$|\bar{S}(j\omega_{b1})| = 0 \quad (4.71)$$

$$|\bar{S}(j\omega_{b2})| = |2\gamma|, \quad (4.72)$$

where

$$\omega_{b1} = (2n) \frac{\omega_0}{2} \quad (n = 0, 1, 2, \dots) \quad (4.73)$$

$$\omega_{b2} = (2n + 1) \frac{\omega_0}{2} \quad (n = 0, 1, 2, \dots). \quad (4.74)$$

This is because

$$e^{-j\omega_{b1}T_s\Pi} = e^{-j(2n)\frac{\omega_0}{2}T_s\Pi} = e^{-j(2n)\frac{\omega_0}{2}T_s\frac{2\pi}{T_s\omega_0}} = e^{-j2n\pi} = 1 \quad (4.75)$$

$$e^{-j\omega_{b2}T_s\Pi} = e^{-j(2n+1)\frac{\omega_0}{2}T_s\Pi} = e^{-j(2n+1)\frac{\omega_0}{2}T_s\frac{2\pi}{T_s\omega_0}} = e^{-j(2n+1)\pi} = e^{-j2n\pi}e^{-j\pi} = -1. \quad (4.76)$$

(4.71) and (4.72) indicate that the PDOB can eliminate disturbances at the frequencies of ω_{b1} , which are fundamental and harmonic frequencies of a periodic disturbance. In contrast, the PDOB does not attenuate disturbances at the frequencies ω_{b2} , which are frequencies of aperiodic disturbances. Although the PDOB cannot compensate for disturbances at ω_{b2} , the PDOB has a high-pass characteristic. The sensitivity function in (4.68) can be expressed by Taylor series as

$$\begin{aligned} \lim_{\Omega_p \rightarrow 0} \bar{S}(j\omega) &= \gamma(1 - e^{-j\omega T_s\Pi}) \\ &= \gamma(j\omega T_s\Pi - \frac{(-j\omega T_s\Pi)^2}{2} - \frac{(-j\omega T_s\Pi)^3}{3} - \dots), \text{ if } \Omega_p \ll 1. \end{aligned} \quad (4.77)$$

Using

$$\omega T_s\Pi = 2\pi \frac{\omega}{\omega_0}, \quad (4.78)$$

the sensitivity characteristic in (4.77) approximately satisfies

$$\lim_{\Omega_p \rightarrow 0} \bar{S}(j\omega) \approx j \frac{2\pi\gamma}{\omega_0} \omega, \text{ if } \Omega_p \ll 1 \text{ and } 2\pi \frac{\omega}{\omega_0} \ll 1, \quad (4.79)$$

and gain of (4.79) is

$$20 \log \left| j \frac{2\pi\gamma}{\omega_0} \omega \right| = 20 \log \left| \frac{2\pi\gamma}{\omega_0} \right| + 20 \log |\omega| \text{ [dB]}, \text{ if } \Omega_p \ll 1 \text{ and } \omega \ll \frac{\omega_0}{2\pi}. \quad (4.80)$$

This frequency characteristic performs a differentiator including 20 dB/decade gradient when frequency of a disturbance ω is much smaller than $\omega_0/2\pi$ in the frequency range $\Omega_p \ll 1$. The cutoff frequency is the minimum positive solution of

$$\omega_{\text{cut}} = \frac{\omega_0}{\pi} \sin^{-1} \left(\frac{1}{2\sqrt{2}\gamma} \right), \quad (4.81)$$

which can be calculated from the following transformation:

$$\begin{aligned} |\gamma(1 - e^{-j\omega_{\text{cut}}T_s\Pi})| &= |\gamma[1 - \cos(\omega_{\text{cut}}T_s\Pi) + j \sin(\omega_{\text{cut}}T_s\Pi)]| \\ &= |\gamma\sqrt{[1 - \cos(\omega_{\text{cut}}T_s\Pi)]^2 + \sin^2(\omega_{\text{cut}}T_s\Pi)}| \\ &= |\gamma\sqrt{1 - 2\cos(\omega_{\text{cut}}T_s\Pi) + \cos^2(\omega_{\text{cut}}T_s\Pi) + \sin^2(\omega_{\text{cut}}T_s\Pi)}| \\ &= |\gamma\sqrt{2[1 - \cos(\omega_{\text{cut}}T_s\Pi)]}| \\ &= |\gamma\sqrt{4[\sin^2(0.5\omega_{\text{cut}}T_s\Pi)]}| \\ &= |2\gamma \sin(0.5\omega_{\text{cut}}T_s\Pi)| \\ &= |2\gamma \sin(\pi \frac{\omega_{\text{cut}}}{\omega_0})| \end{aligned} \quad (4.82)$$

$$|2\gamma \sin(\pi \frac{\omega_{\text{cut}}}{\omega_0})| := \frac{1}{\sqrt{2}} \quad (4.83)$$

$$2\gamma \sin(\pi \frac{\omega_{\text{cut}}}{\omega_0}) = \frac{1}{\sqrt{2}} \quad (4.84)$$

$$\pi \frac{\omega_{\text{cut}}}{\omega_0} = \sin^{-1} \left(\frac{1}{2\sqrt{2}\gamma} \right) \quad (4.85)$$

$$\omega_{\text{cut}} = \frac{\omega_0}{\pi} \sin^{-1} \left(\frac{1}{2\sqrt{2}\gamma} \right). \quad (4.86)$$

If the design parameter γ is 0.5 according to (4.43), the cutoff frequency is

$$\omega_{\text{cut}} = \frac{\omega_0}{4}. \quad (4.87)$$

Therefore, the PDOB can attenuate low-frequency aperiodic disturbances in the frequency range satisfying $\omega \ll g_p$ and $\omega \ll \frac{\omega_0}{4} < \frac{\omega_0}{2\pi}$. However, if a fundamental frequency ω_0 of a periodic disturbance is in the low-frequency range, the PDOB cannot attenuate the low-frequency aperiodic disturbances because aperiodic-disturbance suppression performance of the PDOB is (4.72) even if the cutoff frequency g_p is in the high-frequency range. This indicates that the aperiodic-disturbance suppression performance of the PDOB depends on a fundamental frequency of a periodic disturbance. In order to compensate for the low-frequency aperiodic disturbances regardless of the fundamental frequency of a periodic disturbance, this study constructed an enhanced PDOB.

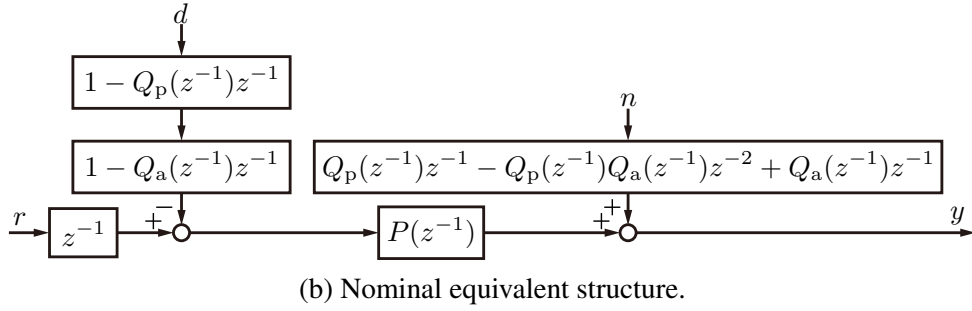
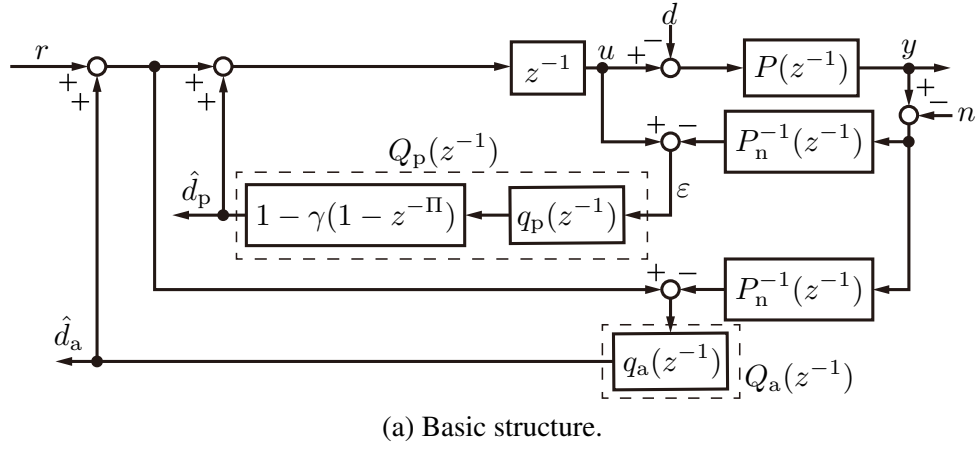


Fig. 4-13: Block diagrams of the enhanced PDOB.

4.3.2 Enhanced Periodic-Disturbance Observer

Combination Design for Enhanced Periodic-Disturbance Observer

A periodic/apperiodic disturbance d is defined to be composed of a periodic disturbance d_p and an aperiodic disturbance d_a on the basis of (2.1) as

$$d(t) = d_p(t) + d_a(t). \quad (4.88)$$

According to the control objective of the PDOB in (4.5) and Fig. 4-2(b), the PDOB can compensate for the disturbance as

$$[1 - Q_p(z^{-1})z^{-1}]d(z^{-1}) = \gamma d_{p0}(z^{-1}) + [1 - Q_p(z^{-1})z^{-1}]d_a(z^{-1}). \quad (4.89)$$

(4.6) modifies (4.89) as

$$[1 - Q_p(z^{-1})z^{-1}]d(z^{-1}) = [1 - Q_p(z^{-1})z^{-1}]d_a(z^{-1}), \text{ if } \Pi \leq t. \quad (4.90)$$

In order to estimate and compensate for the remaining aperiodic disturbance:

$$\tilde{d}_a = [1 - Q_p(z^{-1})z^{-1}]d_a(z^{-1}), \quad (4.91)$$

a classical DOB is additionally used and combined with the PDOB, as shown in Fig. 4-13(a). Q-filter of the DOB uses a first-order low-pass filter

$$Q_a(z^{-1}) = q_a(z^{-1}) = \frac{g_a T_s + g_a T_s z^{-1}}{(g_a T_s + 2) + (g_a T_s - 2)z^{-1}}, \quad (4.92)$$

and the DOB compensates for the remaining aperiodic disturbance \tilde{d}_a through the high-pass filter (sensitivity function) $1 - Q_a(z^{-1})z^{-1}$. The enhanced PDOB, which is the combination of the PDOB and DOB, is thus constructed.

Frequency Characteristics of Enhanced Periodic-Disturbance Observer

Sensitivity and complementary sensitivity functions of the enhanced PDOB are

$$S(z^{-1}) = [1 - Q_p(z^{-1})z^{-1}][1 - Q_a(z^{-1})z^{-1}] \quad (4.93)$$

$$T(z^{-1}) = Q_p(z^{-1})z^{-1} - Q_p(z^{-1})Q_a(z^{-1})z^{-1} + Q_a(z^{-1}), \quad (4.94)$$

as shown in Fig. 4-13(b), which is the nominal equivalent block diagram of the enhanced PDOB. The complementary sensitivity function reflects the effects of the entire enhanced PDOB, including both the PDOB and DOB. The sensitivity function is approximated and expressed using the Q-filters of the PDOB in (4.12) and (4.13) and the DOB in (4.92) as

$$\begin{aligned} S(z^{-1}) &\approx \bar{S}(z^{-1}) = \{1 - Q_p(z^{-1})\}\{1 - Q_a(z^{-1})\} \\ &= \frac{2(1 - z^{-1})}{(g_a T_s + 2) + (g_a T_s - 2)z^{-1}} + \frac{g_p T_s + g_p T_s z^{-1}}{(g_p T_s + 2) + (g_p T_s - 2)z^{-1}} \gamma(1 - z^{-\Pi}). \end{aligned} \quad (4.95)$$

By using the approximation in (4.61) based on the bilinear transform, the frequency characteristic of the sensitivity function becomes

$$\bar{S}(e^{-j\omega T_s}) \approx \bar{S}(j\omega) = \frac{j\Omega_a}{1 + j\Omega_a} + \frac{1}{1 + j\Omega_p} \gamma(1 - z^{-\Pi}), \quad (4.96)$$

where

$$\Omega_p = \frac{\omega}{g_p} \quad (4.97)$$

$$\Omega_a = \frac{\omega}{g_a}. \quad (4.98)$$

Consequently, the frequency characteristics in the frequency ranges are as follows

$\Omega_p \ll 1$:

$$\lim_{\Omega_p \rightarrow 0} \bar{S}(j\omega) = \frac{j\Omega_a}{1 + j\Omega_a} \gamma (1 - e^{-j\omega T_s \Pi}) \quad (4.99)$$

$\Omega_p = 1$:

$$\bar{S}(jg_p) = \frac{j\Omega_a}{1 + j\Omega_a} \frac{\gamma(1 - e^{-jg_p T_s \Pi}) + j}{1 + j} \quad (4.100)$$

$1 \ll \Omega_p$:

$$\lim_{\Omega_p \rightarrow \infty} \bar{S}(j\omega) = \frac{j\Omega_a}{1 + j\Omega_a}. \quad (4.101)$$

At ω_{b1} and ω_{b2} in (4.73) and (4.74) satisfying $\Omega \ll 1$, the gain of (4.99) becomes

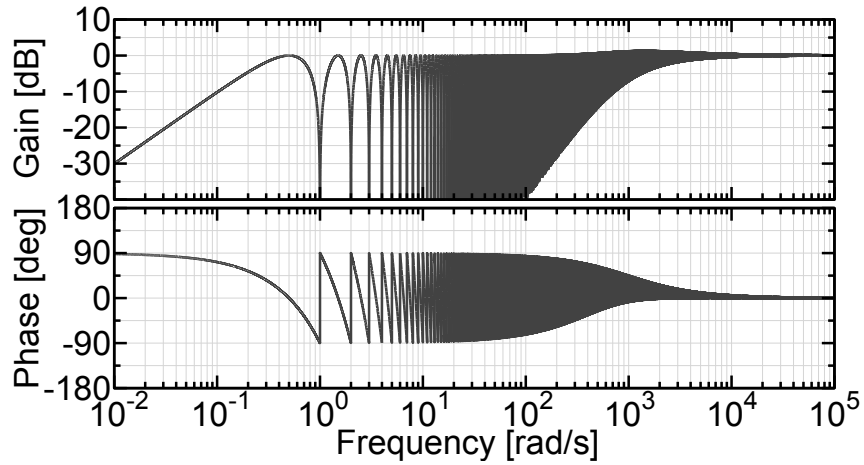
$$|\bar{S}(j\omega_{b1})| = 0 \quad (4.102)$$

$$|\bar{S}(j\omega_{b2})| = 2\gamma \frac{\Omega_a}{\sqrt{1 + \Omega_a^2}}. \quad (4.103)$$

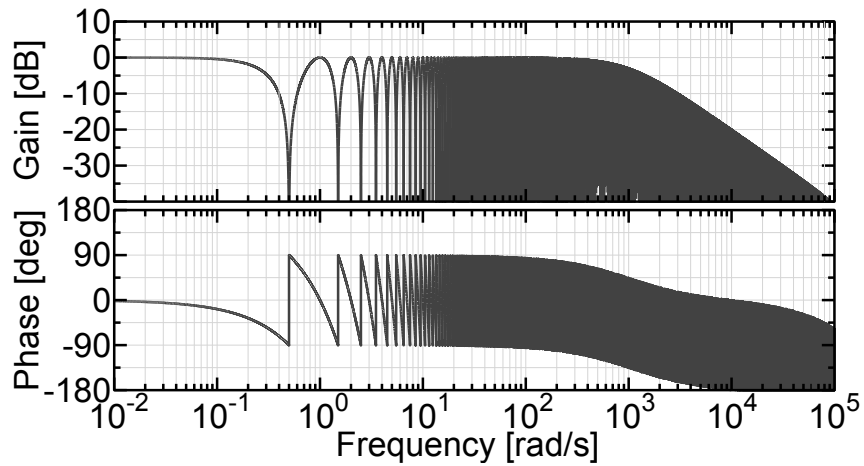
In comparison of (4.103) with (4.72), the enhanced PDOB additionally realizes the high-pass characteristic $\frac{\Omega_a}{\sqrt{1 + \Omega_a^2}}$, which is able to attenuate the remaining aperiodic disturbance \tilde{d}_a . Figs. 4-14, 4-15, and 4-16 show Bode diagrams of sensitivity and complementary sensitivity functions of the PDOB, DOB, and enhanced PDOB, respectively. A number of band-stop characteristics of the PDOB at ω_{b1} and band-pass characteristics at ω_{b2} can be confirmed in Fig. 4-14. By combining the PDOB shown in Fig. 4-14 and the DOB shown in Fig. 4-15 as the enhanced PDOB, the gain of the sensitivity function of the enhanced PDOB acquires both the band-stop characteristics and high-pass characteristic, as shown in Fig. 4-16. This enables the suppression of both periodic and aperiodic disturbances. An enlarged view of the Bode diagrams is shown in Fig. 4-17, which shows that the enhanced PDOB realizes the multiple performance of the PDOB and DOB.

Design of Cutoff Frequencies

This dissertation suggests designing the cutoff frequencies g_p and g_a as the same value $g_p = g_a$ because the same value of the frequencies enables to simplify effects of the frequencies on the sensitivity and tradeoff between sensitivity and complementary sensitivity functions.

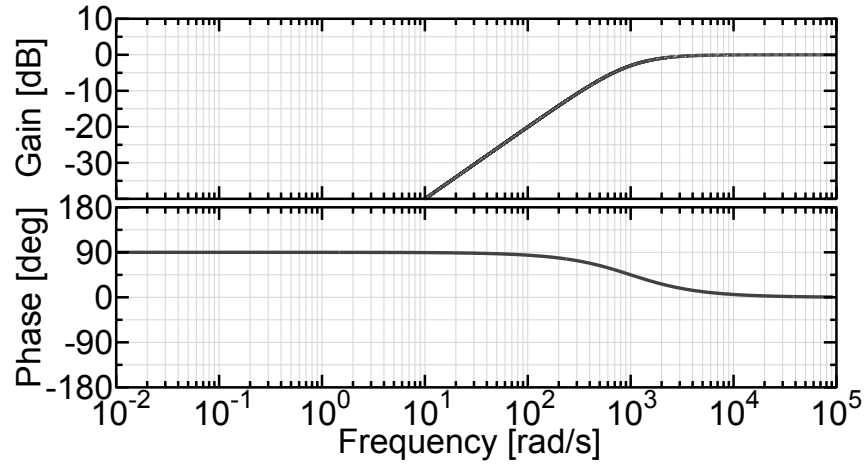


(a) Sensitivity function $1 - Q_p(z^{-1})z^{-1}$.

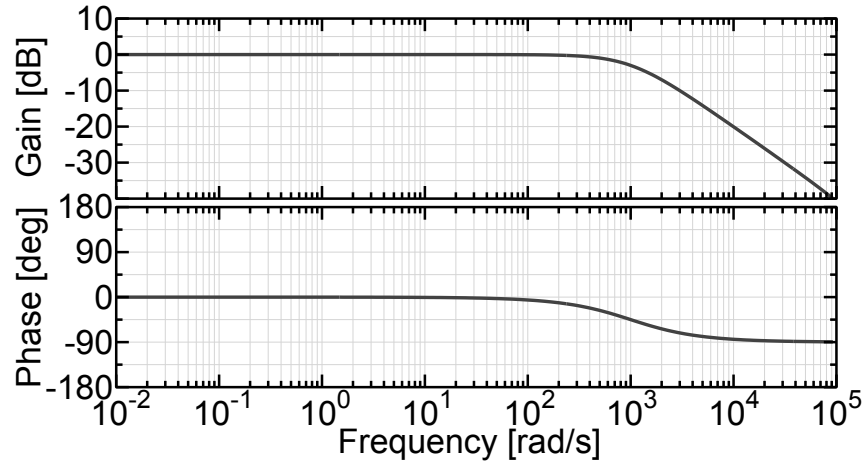


(b) Complementary sensitivity function $Q_p(z^{-1})z^{-1}$.

Fig. 4-14: Bode diagrams of the PDOB. The parameters are $\omega_0 = 100$ rad/s, $\gamma = 0.5$, $g_p = 1000$ rad/s, and $T_s = 0.01$ ms.

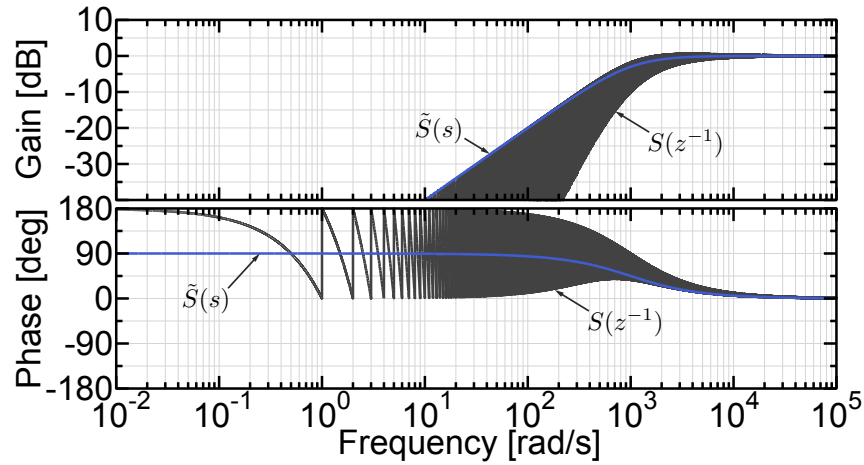


(a) Sensitivity function $1 - Q_a(z^{-1})z^{-1}$.

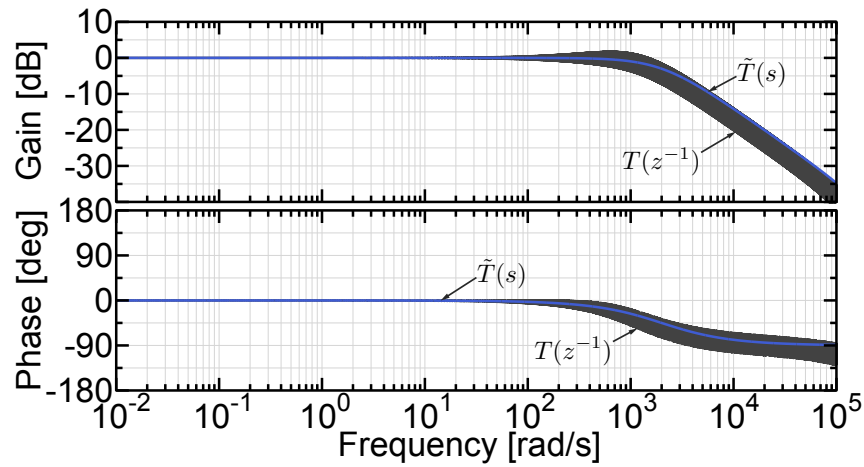


(b) Complementary sensitivity function $Q_a(z^{-1})z^{-1}$.

Fig. 4-15: Bode diagrams of the DOB. The parameters are $g_a = 1000$ rad/s and $T_s = 0.01$ ms.



(a) Sensitivity function $S(z^{-1}) = [1 - Q_p(z^{-1})z^{-1}][1 - Q_a(z^{-1})z^{-1}]$ and $\tilde{S}(s)$ calculated from (4.116).



(b) Complementary sensitivity function $T(z^{-1}) = Q_p(z^{-1})z^{-1} - Q_p(z^{-1})Q_a(z^{-1})z^{-2} + Q_a(z^{-1})z^{-1}$ and $\tilde{T}(s)$ calculated from (4.117).

Fig. 4-16: Bode diagrams of the enhanced PDOB. The parameters are $\omega_0 = 100$ rad/s, $\gamma = 0.5$, $g_p = 1000$ rad/s, $g_a = 1000$ rad/s, and $T_s = 0.01$ ms.

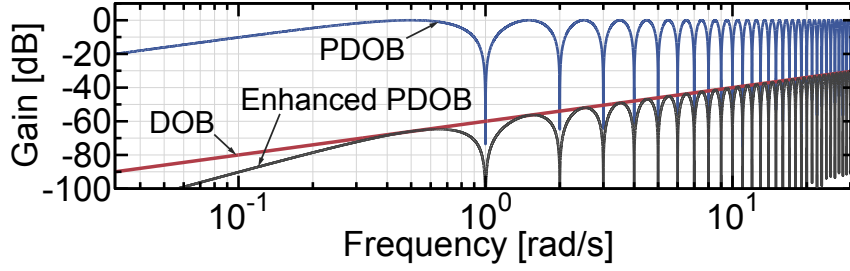


Fig. 4-17: Enlarged view of the sensitivity functions of the PDOB, DOB, and enhanced PDOB in Figs. 4-14(a), 4-15(a), and 4-16(a).

First, the sensitivity and complementary sensitivity functions of the enhanced PDOB in (4.93) and (4.94) can be transformed into

$$\bar{\bar{S}}(j\omega) = \frac{-\Omega^2 + j\Omega\gamma(1 - e^{-j\omega T_s\Pi})}{(1 + j\Omega)^2} \quad (4.104)$$

$$\bar{\bar{T}}(j\omega) = \frac{1 + j\Omega[2 - \gamma(1 - e^{-j\omega T_s\Pi})]}{(1 + j\Omega)^2} \quad (4.105)$$

$$\Omega := \Omega_p = \Omega_a, \quad (4.106)$$

and they are expressed as follows in the frequency ranges

$\Omega \ll 1$:

$$\lim_{\Omega^2 \rightarrow 0} \bar{\bar{S}}(j\omega) = \frac{j\Omega}{1 + j2\Omega} \gamma(1 - e^{-j\omega T_s\Pi}) \quad (4.107)$$

$$\lim_{\Omega^2 \rightarrow 0} \bar{\bar{T}}(j\omega) = \frac{1}{1 + j2\Omega} + \frac{j\Omega}{1 + j2\Omega} [2 - \gamma(1 - e^{-j\omega T_s\Pi})] \quad (4.108)$$

$\Omega = 1$:

$$\bar{\bar{S}}(jg_p) = \frac{\gamma(1 - e^{-jg_p L}) + j}{2} \quad (4.109)$$

$$\bar{\bar{T}}(jg_p) = \frac{[2 - \gamma(1 - e^{-jg_p L})] - j}{2} \quad (4.110)$$

$1 \ll \Omega$:

$$\lim_{\Omega^{-2} \rightarrow 0} \bar{\bar{S}}(j\omega) = \frac{j0.5\Omega}{1 + j0.5\Omega} + \frac{1}{1 + j0.5\Omega} \frac{\gamma}{2} (1 - e^{-j\omega T_s\Pi}) \quad (4.111)$$

$$\lim_{\Omega^{-2} \rightarrow 0} \bar{\bar{T}}(j\omega) = \frac{1}{1 + j0.5\Omega} [1 - \frac{\gamma}{2} (1 - e^{-j\omega T_s\Pi})]. \quad (4.112)$$

Using the design parameter: $\gamma = 0.5$ according to (4.43) and

$$\left| \frac{1 - e^{-j\omega T_s\Pi}}{2} \right|, \left| \frac{3 + e^{-j\omega T_s\Pi}}{4} \right| \leq 1, \quad (4.113)$$

an inequality for the sensitivity function in the low-frequency range and that for the complementary sensitivity function in the high-frequency range can be obtained as

$\Omega \ll 1$:

$$\lim_{\Omega^2 \rightarrow 0} |\bar{S}(j\omega)| = \left| \frac{j\Omega}{1 + j2\Omega} \frac{1 - e^{-j\omega T_s \Pi}}{2} \right| \leq |\tilde{S}(j\omega)| \quad (4.114)$$

$1 \ll \Omega$:

$$\lim_{\Omega^{-2} \rightarrow 0} |\bar{T}(j\omega)| = \left| \frac{1}{1 + j0.5\Omega} \frac{3 + e^{-j\omega T_s \Pi}}{4} \right| \leq |\tilde{T}(j\omega)|, \quad (4.115)$$

where

$$\tilde{S}(j\omega) = \frac{j\Omega}{1 + j\Omega} = \frac{j\omega}{g + j\omega} \quad (4.116)$$

$$\tilde{T}(j\omega) = \frac{j\Omega}{1 + j0.5\Omega} = \frac{2g}{2g + j\omega}. \quad (4.117)$$

Fig. 4-16 compares Bode diagrams of the functions: $S(z^{-1})$, $\tilde{S}(s)$, $T(z^{-1})$, and $\tilde{T}(s)$. These indicate that the gain of the sensitivity function S is approximately smaller than that of \tilde{S} in the low-frequency range. Also, the gain of the complementary sensitivity function T is approximately smaller than that of \tilde{T} in the high-frequency range. Therefore, the cutoff frequency g of the enhanced PDOB can be designed with \tilde{S} and \tilde{T} in a similar manner to a classical DOB. A lower limit for g can be determined by a required cutoff frequency of the high-pass characteristic \tilde{S} for disturbance compensation, and an upper limit for $2g$ can be determined by a required cutoff frequency of the low-pass characteristic \tilde{T} for robust stability. It should be noted that the approximate sensitivity function $\tilde{S}(s)$ and the approximate complementary sensitivity function $\tilde{T}(s)$ do not satisfy the upper limits of the original sensitivity function $S(z^{-1})$ and original complementary sensitivity function $T(z^{-1})$ around the cutoff frequency g , as shown in Fig. 4-16. Accordingly, the approximate sensitivity and complementary sensitivity functions satisfy the tradeoff $S + T = 1$ only in the low and high frequency ranges except around the cutoff frequency g as follows

$\omega \ll g$:

$$\lim_{\omega \rightarrow 0} [\tilde{S}(j\omega) + \tilde{T}(j\omega)] = 1 \quad (4.118)$$

$\omega = g$:

$$\tilde{S}(jg) + \tilde{T}(jg) = \frac{1 + j2}{1 + j3} < 1 \quad (4.119)$$

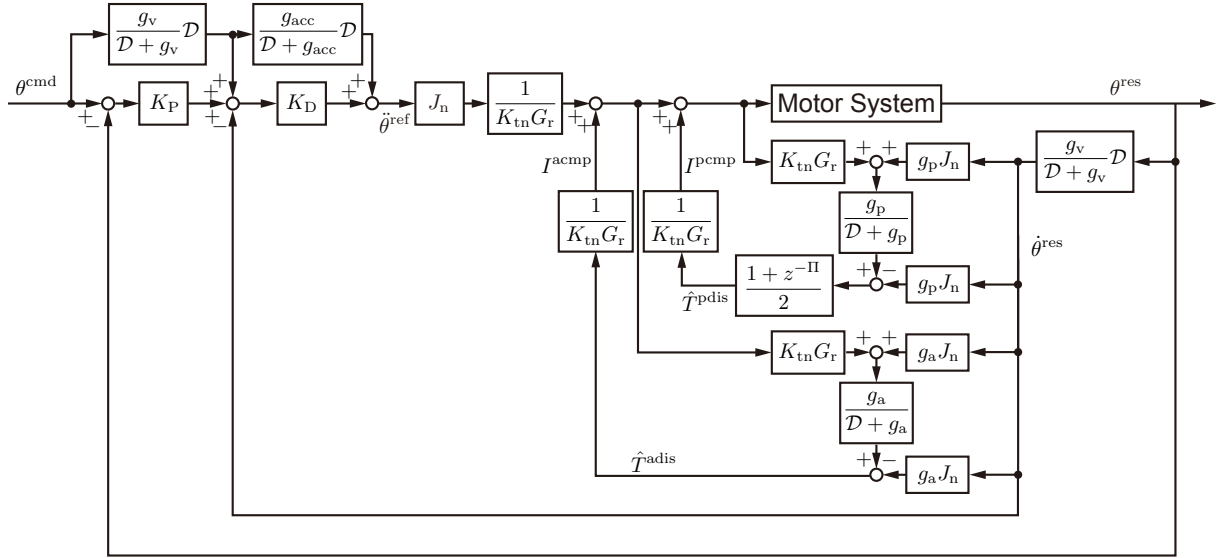


Fig. 4-18: Block diagram of the position control system using the enhanced PDOB.

Table 4.2: Parameters of the comparative experiments for the enhanced PDOB.

Parameter	Symbol	Value (1st, 2nd, 3rd) Joint
Sampling time	T_s	0.1 ms
Proportional gain	K_P	100, 100, 100
Differential gain	K_D	40, 40, 40
Nominal inertia	J_n	7.0, 3.0, 0.3 kgm ²
Nominal torque constant	K_{tn}	0.59, 0.59, 0.238 Nm/A
Gear ratio	G_r	192, 120, 80
Length	L	0.26, 0.27, 0.09 m
Fundamental frequency	ω_0	3, 3, 3 rad/s
Design parameter	γ	0.5, 0.5, 0.5
Cutoff frequencies	g_p	200, 200, 200 rad/s
	g_a	200, 200, 200 rad/s
	g_v	1000, 1000, 1000 rad/s
	g_{acc}	500, 500, 500 rad/s

$g \ll \omega :$

$$\lim_{\omega \rightarrow \infty} [\tilde{S}(j\omega) + \tilde{T}(j\omega)] = 1. \quad (4.120)$$

4.3.3 Experiments

Experiments were conducted to compare the enhanced PDOB with the DOB and PDOB using the multi-axis manipulator shown in Fig. 3-10. The workspace position commands:

$$x^{\text{cmd}}(t) = \begin{cases} x_0 \text{ mm} & \text{if } \tilde{t} < 0.5 \\ x_0 + 100(\tilde{t} - 0.5) \text{ mm} & \text{if } 0.5 \leq \tilde{t} < 1.0 \\ x_0 + 50 \text{ mm} & \text{if } 1.0 \leq \tilde{t} < 1.5 \\ x_0 + 100(2.0 - \tilde{t}) \text{ mm} & \text{if } 1.5 \leq \tilde{t} < 2.0 \end{cases} \quad (4.121)$$

$$y^{\text{cmd}}(t) = \begin{cases} y_0 \text{ mm} & \text{if } \tilde{t} < 0.5 \\ y_0 - 100(\tilde{t} - 0.5) \text{ mm} & \text{if } 0.5 \leq \tilde{t} < 1.0 \\ y_0 - 50 \text{ mm} & \text{if } 1.0 \leq \tilde{t} < 1.5 \\ y_0 - 100(2.0 - \tilde{t}) \text{ mm} & \text{if } 1.5 \leq \tilde{t} < 2.0 \end{cases} \quad (4.122)$$

$$\tilde{t} = T_s t \bmod 2 \quad (4.123)$$

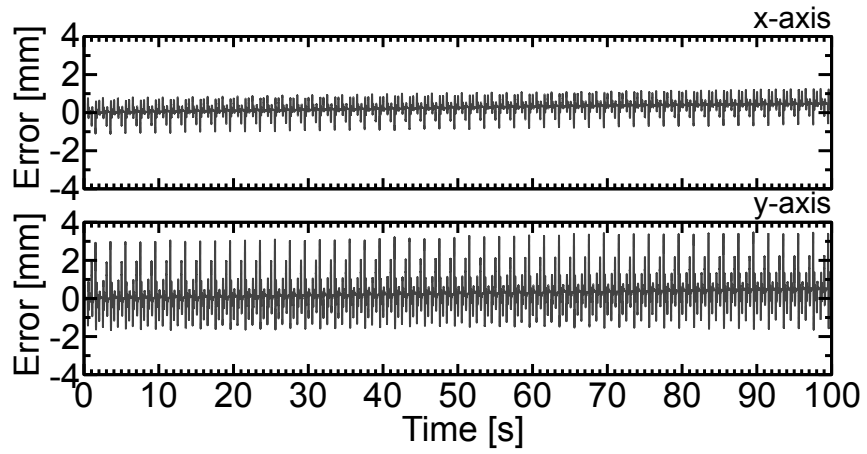
were used by transforming into the joint space to control angles of the motors. A block diagram of the position control system based on the enhanced PDOB is shown in Fig. 4-18, and the experimental parameters are shown in Table 4.2. g_v , g_{acc} , J_n , K_{tn} , G_r , θ^{cmd} , θ^{res} , $\dot{\theta}^{\text{res}}$, $\ddot{\theta}^{\text{ref}}$, \hat{T}^{pdis} , \hat{T}^{adis} , I^{pcmp} , and I^{acmp} denote the cutoff frequency for the velocity calculation, cutoff frequency for the acceleration calculation, nominal inertia, nominal torque constant, gear ratio, angle command, angle response, angular velocity response, angular acceleration response, periodic-disturbance torque, aperiodic-disturbance torque, periodic compensation current, and aperiodic compensation current, respectively.

Errors of the experimental results are shown in Fig. 4-19. Fig. 4-19(a) shows the largest errors of the DOB in the three methods owing to the periodic disturbance. The PDOB solved the periodic disturbance problem and improved the steady-state performance, but the transient errors deteriorated and low-frequency disturbances still remained, as shown in Fig. 4-19(b). The enhanced PDOB improved the transient performance and low-frequency errors and achieved the best performance, as shown in Fig. 4-19(c). The discrete Fourier transform results shown in Fig. 4-20 clarify the steady-state difference of the DOB, PDOB, and enhanced PDOB. The DOB could not sufficiently eliminate the periodic disturbance, whose fundamental frequency was 3 rad/s, and the PDOB successfully suppressed the periodic disturbance, but low-frequency errors exist under 3 rad/s. The enhanced PDOB realized the suppression of both the periodic disturbance and low-frequency errors.

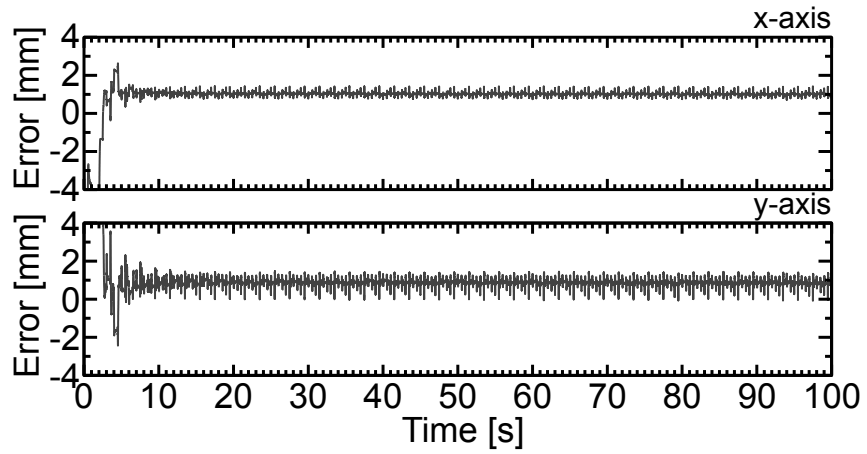
4.4 Summary

Section 4.2 constructed the PDOB for periodic-disturbance compensation. The model of a periodic disturbance was firstly constructed. The Q-filter of the PDOB was designed to be able to eliminate the periodic disturbance on the basis of the model. Since the PDOB needs to determine the delay Π , design parameter γ , and cutoff frequency g_p , the design of the parameters was discussed with the sensitivity and complementary sensitivity functions. The nominal stability analysis based on the characteristic equation clarified that the delay does not affect the nominal stability of the PDOB. According to the comparison with the classical DOBs using sensitivity and complementary sensitivity functions, the improved periodic-disturbance suppression performance and robust stability in the tradeoff were confirmed. The experiments validated the practicality of the PDOB.

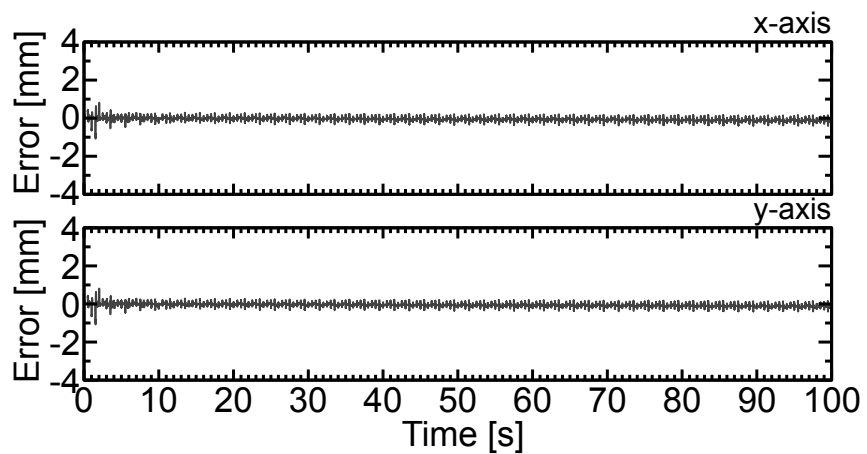
Section 4.3 developed the PDOB into the enhanced PDOB. Firstly, the problem of the aperiodic-disturbance suppression performance of the PDOB was shown. Then, the enhanced PDOB was constructed by the combination design of the PDOB and DOB to overcome the problem. The enhanced performance was evaluated through the sensitivity and complementary sensitivity functions, and the design strategy for the functions was demonstrated. The experiments validated the improved practicality of the enhanced PDOB compared with the DOB and PDOB.



(a) DOB.

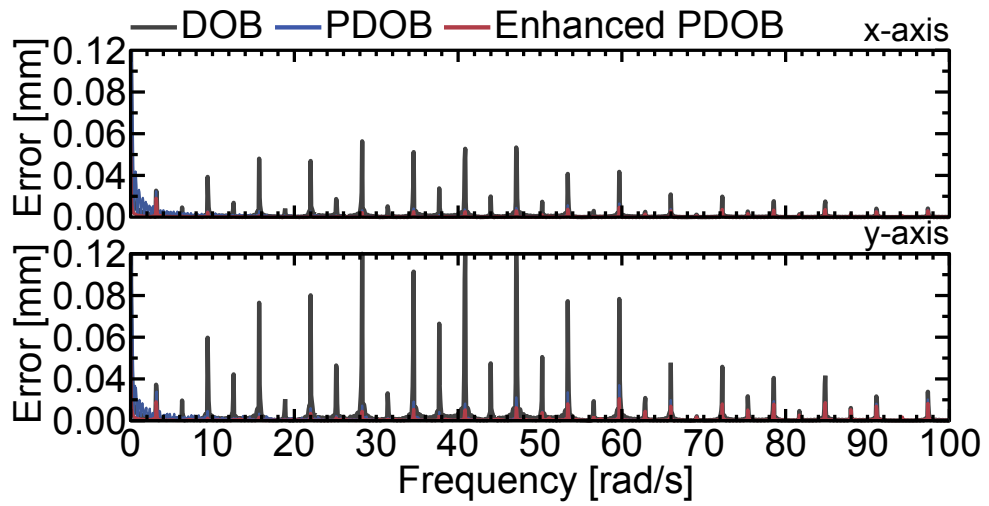


(b) PDOB.

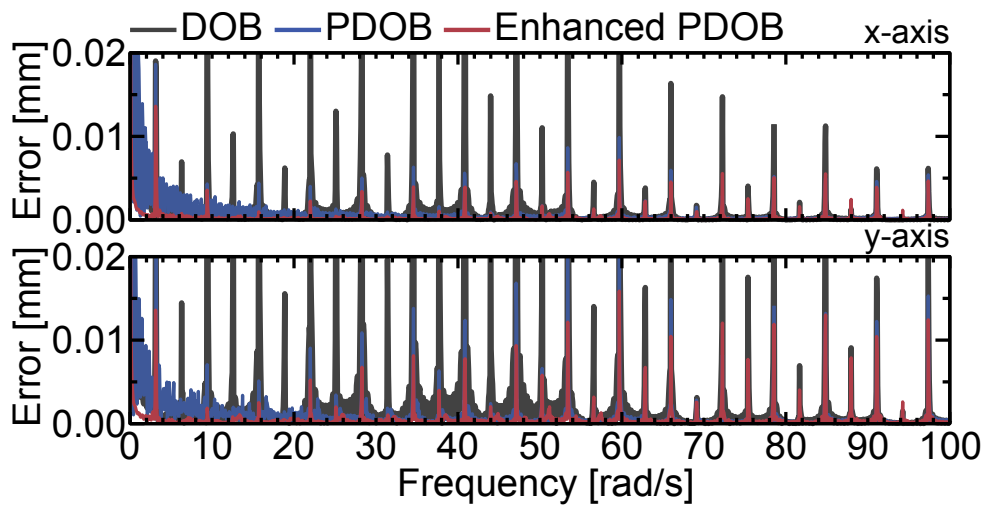


(c) Enhanced PDOB.

Fig. 4-19: Results of the comparative experiments for the enhanced PDOB.



(a) Overall view.



(b) Enlarged view.

Fig. 4-20: Discrete Fourier transform results of Fig. 4-19 between 10 s and 100 s.

Chapter 5

Periodic/Aperiodic Diagnosis

5.1 Outline

Chapter 5 focuses on periodicity and aperiodicity of industrial inspection and human behavior.

Section 5.2 focuses on periodicity and aperiodicity of the industrial inspection for the food product packing, and this study applied the PASF to the haptic leak detection. In particular, this study focuses on yank (differential force) information from packages, which represents leak effects due to holes or sealing errors on packages. The PASF is applied to separate measured yank into periodic yank and aperiodic yank because the periodic yank typically corresponds to a normal product and slow environmental change, and the aperiodic yank accordingly corresponds to an anomalous product. Subsection 5.2.1 describes a detection flow of the PASF-based haptic leak detection, and Subsection 5.2.2 shows 10,000 packages inspection simulation based on experimental package data.

Section 5.3 focuses on periodicity and aperiodicity of human behavior for the motor learning, and this study applied the PASF to motor proficiency diagnosis. The PASF-based proficiency diagnosis enables to evaluate the motor learning accurately by eliminating aperiodic behavior. Subsection 5.3.1 describes the setup for the motor learning experiment based on a drawing task of a minimum-angular-jerk logarithmic spiral, and Subsection 5.3.2 shows evaluation results that the PASF-based proficiency diagnosis facilitated the accurate proficiency diagnosis.

5.2 Aperiodic Leak Detection

5.2.1 PASF-Based Haptic Leak Detection

Package-Leak Model

Periodic normal package condition is modeled by the ideal gas law:

$$PV = nRT, \quad (5.1)$$

and aperiodic anomalous condition of a leaked package is

$$PV = \begin{cases} (n - \mathcal{L}T_s t)RT & \text{if } 0 \leq n - \mathcal{L}T_s t \\ 0 & \text{otherwise} \end{cases}. \quad (5.2)$$

$P, V, n, R, T,$ and \mathcal{L} denote the pressure, volume, number of moles, universal gas constant, temperature, and leak coefficient, respectively. This study focuses on the time range satisfying $0 \leq n - \mathcal{L}T_s t$. $\mathcal{L}T_s t$ corresponds to the leak effect, which reduces amount of the contained air. A haptic detector using a linear motor measures reaction force $F(t)$ with a detection area S from a package as

$$\begin{aligned} F(t) &= -SP(t) + F^{\text{ext}}(t) \\ &= -(n - \mathcal{L}T_s t) \frac{SRT}{V} + F^{\text{ext}}(t), \end{aligned} \quad (5.3)$$

where

$$\begin{aligned} \frac{SRT}{V} &= \frac{SRT_n[1 + \Delta T(t)]}{V_n[1 + \Delta V(t)]} \\ &= \frac{SRT_n}{V_n} + \delta(t) \end{aligned} \quad (5.4)$$

$$\delta(t) = \frac{SRT_n[\Delta V(t) - \Delta T(t)]}{V_n[1 + \Delta V(t)]} \quad (5.5)$$

$$n, R, S, \mathcal{L}, T_s, T_n, V_n = \text{constant}. \quad (5.6)$$

Consequently, the reaction force $F(t)$ and one-sample-period-ahead reaction force $F(t + 1)$ are

$$F(t) = -(n - \mathcal{L}T_s t) \frac{SRT_n}{V_n} - (n - \mathcal{L}T_s t)\delta(t) + F^{\text{ext}}(t) \quad (5.7)$$

$$F(t + 1) = -(n - \mathcal{L}T_s t) \frac{SRT_n}{V_n} + \mathcal{L}T_s \frac{SRT_n}{V_n} - (n - \mathcal{L}T_s t)\delta(t + 1) + \mathcal{L}T_s \delta(t + 1) + F^{\text{ext}}(t + 1). \quad (5.8)$$

$F^{\text{ext}}(t), T_n, \Delta T(t), V_n,$ and $\Delta V(t)$ denote the external force, nominal temperature, temperature change, nominal volume, and volume change, respectively. The amount of contained air $n,$ gas constant $R,$ and

the detection area S are constant, whereas the temperature T changes on the basis of the four seasons and measurement environment. The external force F^{ext} represents mechanical wear of the haptic detector. Finally, yank \mathcal{Y} measured by the haptic detector is

$$\mathcal{Y}(t) = \frac{F(t+1) - F(t)}{T_s} = \mathcal{L} \frac{SRT_n}{V_n} + \Delta(t) \quad (5.9)$$

$$\Delta(t) = \mathcal{L}\delta(t+1) - (n - \mathcal{L}T_s t) \frac{\delta(t+1) - \delta(t)}{T_s} + \frac{F^{\text{ext}}(t+1) - F^{\text{ext}}(t)}{T_s}, \quad (5.10)$$

using (5.7) and (5.8). Hence, the aim of the haptic leak detection is to pick up the leak term $\mathcal{L} \frac{SRT}{V}$ from the yank $\mathcal{Y}(t)$ under the disturbance term $\Delta(t)$. The temperature change ΔT , volume change ΔV , and external factor such as mechanical wear F^{ext} are empirically slow changes in the case of the leak detection. Thus, the disturbance term $\Delta(t)$ and the leak term $\mathcal{L} \frac{SRT}{V}$ correspond to the periodic element and aperiodic element, respectively. Therefore, this study used the PASF to pick up the aperiodic leak term as aperiodic yank from the yank $\mathcal{Y}(t)$ under the periodic disturbance term $\Delta(t)$.

Detection Flow

Overview. This study developed the PASF-based haptic leak detection shown in Fig. 5-1. The detection flow is composed of five steps: pushing package, yank measurement, aperiodic yank extraction, mean yank calculation, and detection.

Pushing Package. In the pushing package step, the haptic leak detector using a linear motor shown in Fig. 5-2 pushes packages. The linear motor is controlled by velocity control in accordance with the following processes.

1. (Approaching) The velocity command is 100 mm/s until the reaction force F from a package becomes stronger than -60 N.
2. (Contact) The velocity command is 0 mm/s for 0.4 s.
3. (Disengaging) The velocity command is -100 mm/s until the linear motor reaches the initial position before approaching.

Yank Measurement and Aperiodic Yank Extraction. During the contact, the reaction force of a package is measured using a reaction force observer (RFOB), and yank is calculated as follows.

- 2-1. The RFOB estimates 800 reaction force samples under the sampling time: 0.25 ms in the steady state from 0.2 s to 0.4 s from a package.

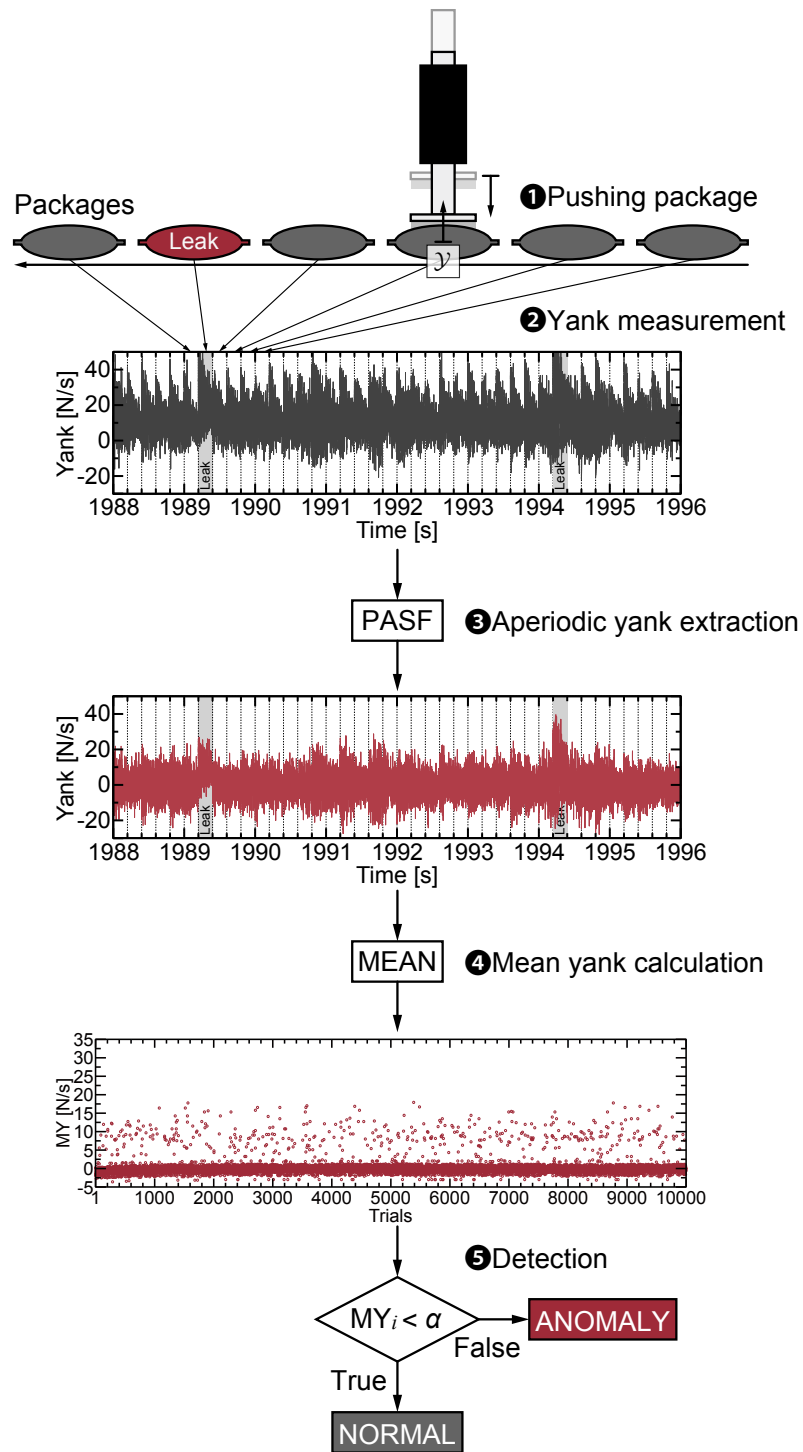


Fig. 5-1: Overview of the PASF-based haptic leak detection.

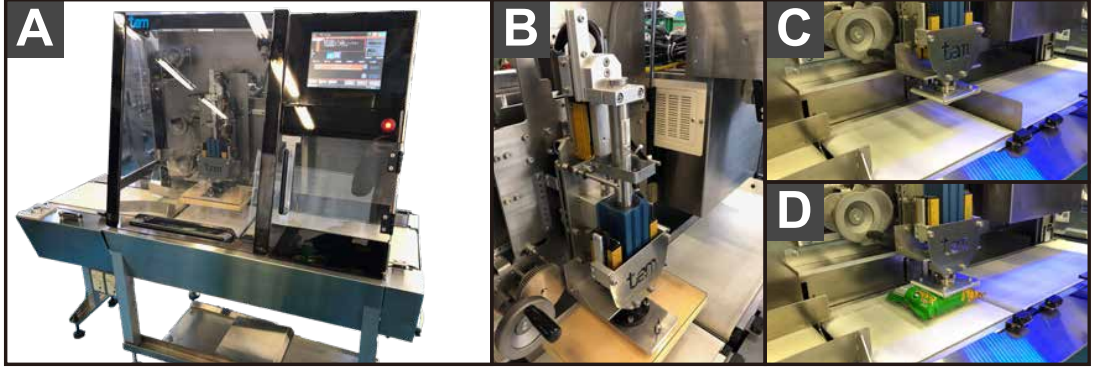


Fig. 5-2: Haptic leak detector using a linear motor.

Table 5.1: Parameters of the preliminary experiments.

Parameter	Symbol	Value	Parameter	Symbol	Value
Sampling time	T_s	0.25 ms	Proportional gain	K_P	200
Integral gain	K_I	10000	Nominal mass	M_n	2 kg
Nominal thrust constant	K_{tn}	53.1 Nm/A	Cutoff freq. for DOB	g_{dob}	250 rad/s
Cutoff freq. for RDOB	g_{rfob}	3000 rad/s	Cutoff freq. for velocity	g_v	2000 rad/s

2-2. A pseudo differentiator whose cutoff frequency is 30 rad/s calculates the yank $Y(800i), \dots, Y(800i + 799)$ from the reaction force of the $i + 1$ th package.

2-3. The first-order PASF extracts the aperiodic yank $Y_a(800i), \dots, Y_a(800i + 799)$ from the yank.

Mean yank calculation. Mean yank for the $i + 1$ th package is calculated using the aperiodic yank as

$$MY_i = \frac{1}{800} \sum_{j=0}^{799} \mathcal{Y}_a(800i + j). \quad (5.11)$$

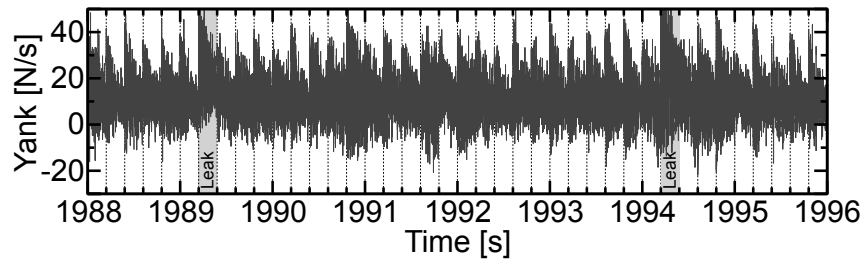
Detection. The conditional expression judges whether the package is normal or anomalous

$$MY_i < \alpha, \quad (5.12)$$

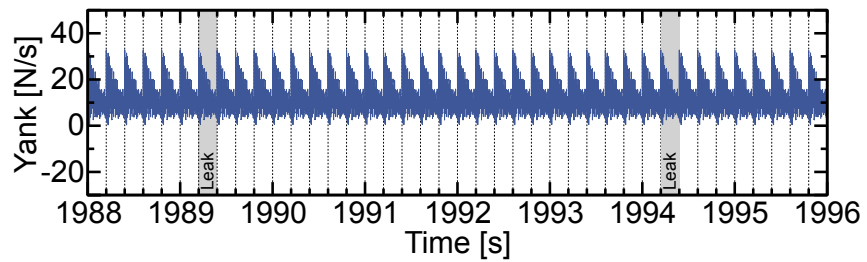
where α denotes a threshold.

5.2.2 Package Inspection Simulation

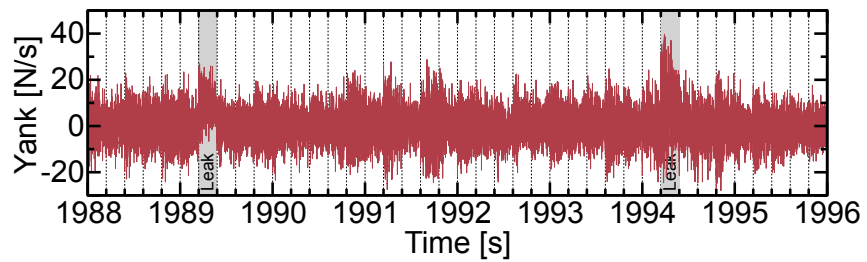
As preliminaries, this study measured 188 package data from normal packages and 200 package data from anomalous packages caused by artificial 5 mm holes. The experimental parameters are summarized



(a) Yank.



(b) Periodic yank.



(c) Aperiodic yank.

Fig. 5-3: Yank waveforms between 1988 s and 1996 s in Simulation 1.

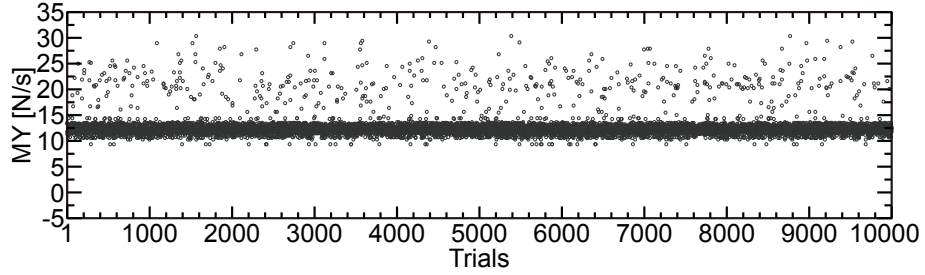
in Table 5.1. Random reaction force data composed of 10,000 packages for 2,000 s were generated using the Mersenne Twister, which is a pseudo random number generator for uniform distribution. The ratio between normal packages and anomalous packages was set to 95:5. Using the generated reaction force data, this study designed the three simulations in terms of the disturbance term Δ_i as follows:

Simulation 1

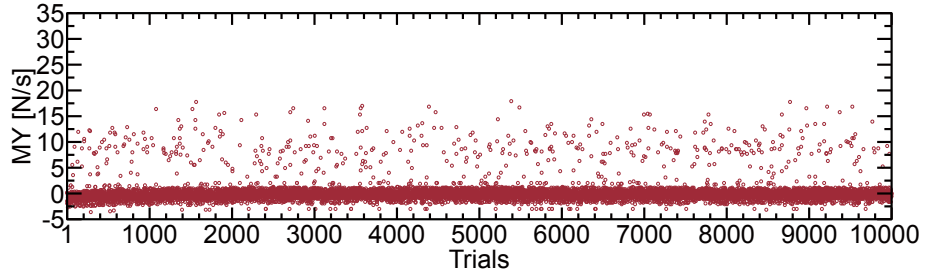
$$\Delta_i = 0 \tag{5.13}$$

Simulation 2

$$\Delta_i = 0.0005i \tag{5.14}$$



(a) Mean yank calculated from the yank.



(b) Mean yank calculated from the aperiodic yank.

Fig. 5-4: Mean yank values in Simulation 1.

Simulation 3

$$\Delta_i = 2.5 \sin(0.0002\pi i). \quad (5.15)$$

The disturbance term Δ_i for the $i + 1$ th package was inserted into the calculated yank as (5.4) in the simulation phase. Each simulation was conducted 61 times to investigate different 61 thresholds.

Fig. 5-3(a) shows the yank waveforms between 1988 s and 1996 s in Simulation 1. The PASF extracted the aperiodic yank in Fig. 5-3(c) by eliminating the periodic yank in Fig. 5-3(b). Fig. 5-4(a) and (b) show the mean yank values calculated from the yank and aperiodic yank, respectively. The yank waveforms of Simulations 2 and 3 are shown in Figs. 5-5 and 5-6, respectively, and their mean yank values are shown in Figs. 5-7 and 5-8, respectively. Simulations 2 and 3 verified robustness of the PASF-based haptic leak-detection against the disturbances: (5.14) and (5.15). The mean aperiodic yank in Simulations 2 and 3 could provide similar results to Simulation 1 because the aperiodic yank attenuated the disturbance effects, as shown in Figs. 5-7 and Figs. 5-8. To compare the haptic leak-detection without the PASF and the proposed PASF-based haptic leak-detection, this study used the true positive rate and false positive

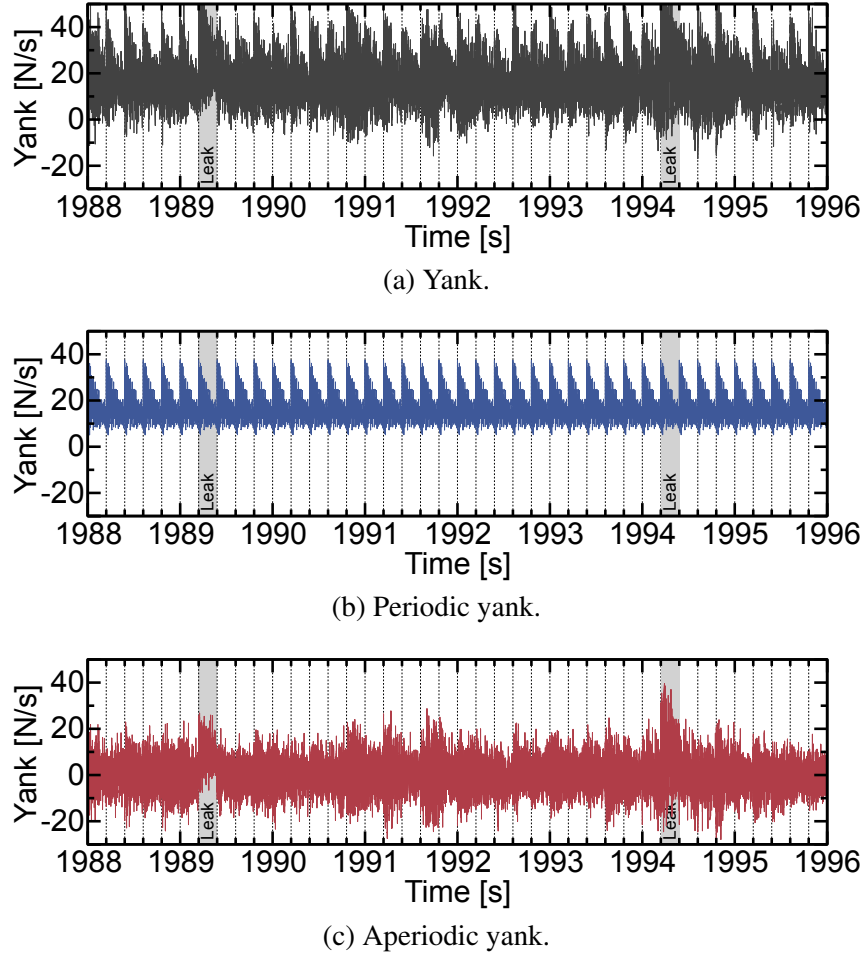


Fig. 5-5: Yank waveforms between 1988 s and 1996 s in Simulation 2.

rate

$$\text{True positive rate} = \frac{\text{The number of detected normal packages}}{\text{The number of normal packages}} \quad (5.16)$$

$$\text{False positive rate} = \frac{\text{The number of undetected anomalous packages}}{\text{The number of anomalous packages}}. \quad (5.17)$$

The evaluation indexes describe a receiver operating characteristic (ROC) curve, as shown in Fig. 5-9. The true positive rate and false positive rate vary between 0 and 1, and true positive rate = 1 and false positive rate = 0 indicate perfect detection. According to Fig. 5-9, both the detections with and without the PASF showed the high detection accuracy in Simulation 1, whereas the detection without the PASF was not robust against the disturbances Δ_i and deteriorated the accuracy in Simulations 2 and 3. In contrast, the proposed PASF-based haptic leak-detection maintained the detection accuracy even in

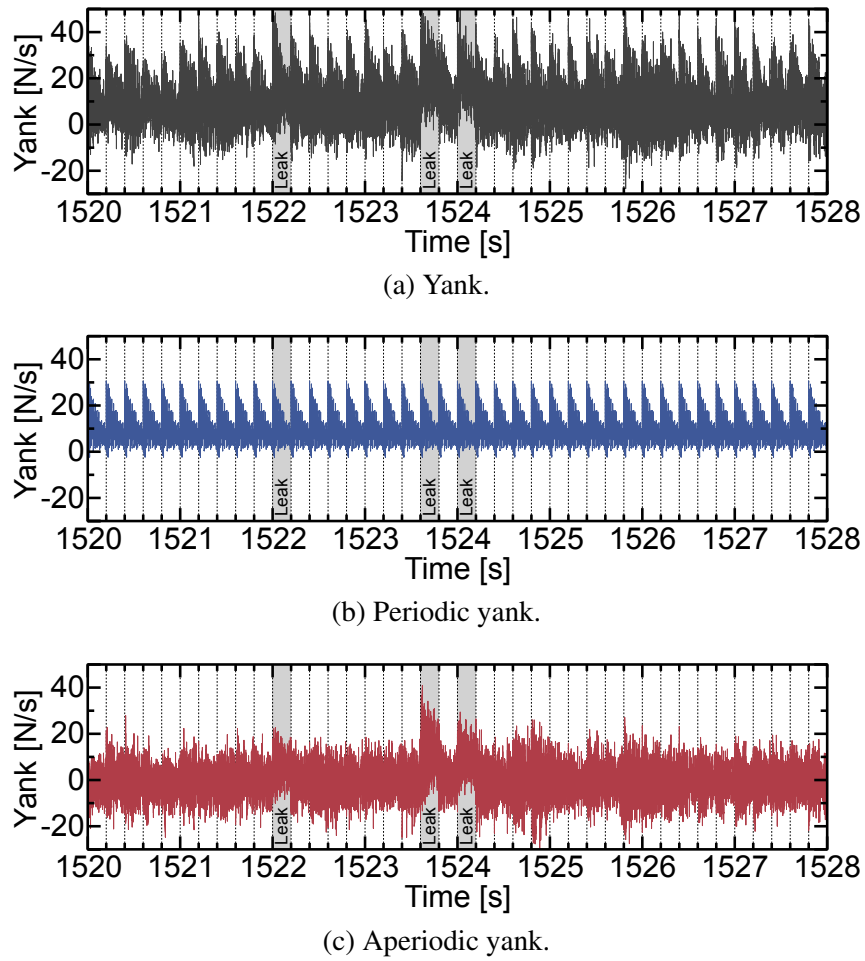
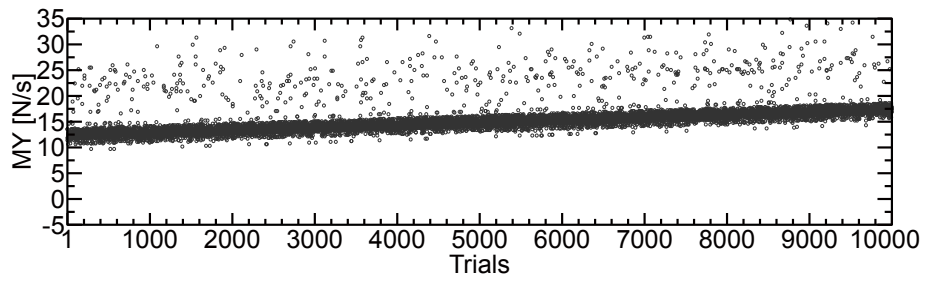
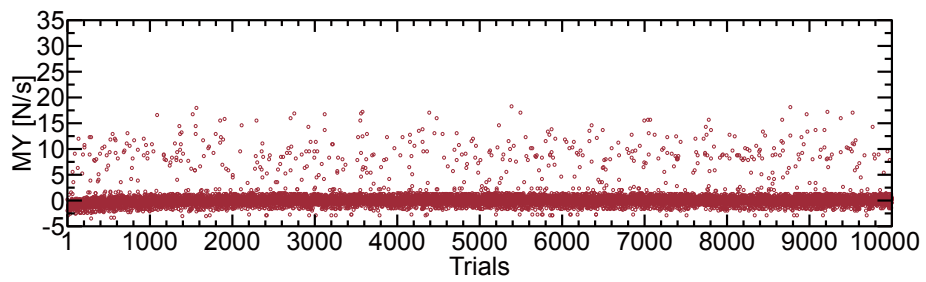


Fig. 5-6: Yank waveforms between 1520 s and 1528 s in Simulation 3.

Simulations 2 and 3. Therefore, the robustness of the proposed method was thus verified. In addition, the PASF-based haptic leak detection was compared with anomaly detection using a variational autoencoder (VAE) composed of 9 layers [104–106]. Dimensions of the layers from the input layer to the output layer were set to 800, 800, 600, 400, 20, 400, 600, 800, and 800, respectively. The VAE was trained by the 188 measured normal package data with 300 epochs, and a mean of the reproduction errors of the VAE was used to detect anomaly. Since the VAE was trained by the normal packages, the errors become large when the VAE reproduces an anomalous package. The ROC curve also shows the results of the VAE, and the VAE performed the worst results at all simulations. The difficulty of the VAE in reproducing time-series data might cause the worst results at Simulation 1. Moreover, the VAE, whose performance depends on the training data, did not have the robustness against the disturbances.

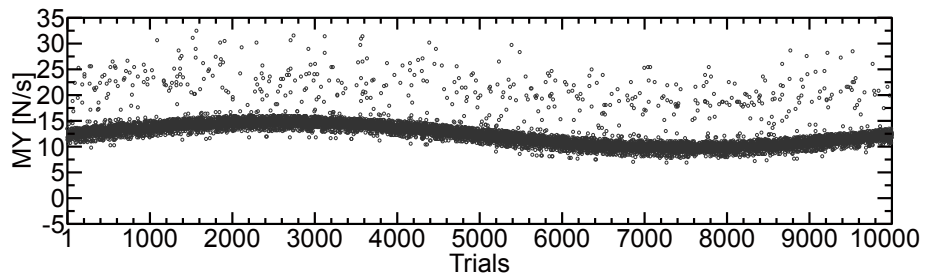


(a) Yank

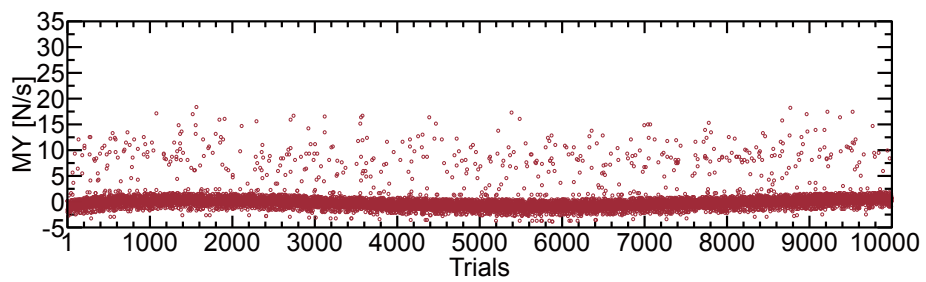


(b) Aperiodic yank.

Fig. 5-7: Mean yank values in Simulation 2.



(a) Yank



(b) Aperiodic yank.

Fig. 5-8: Mean yank values in Simulation 3.

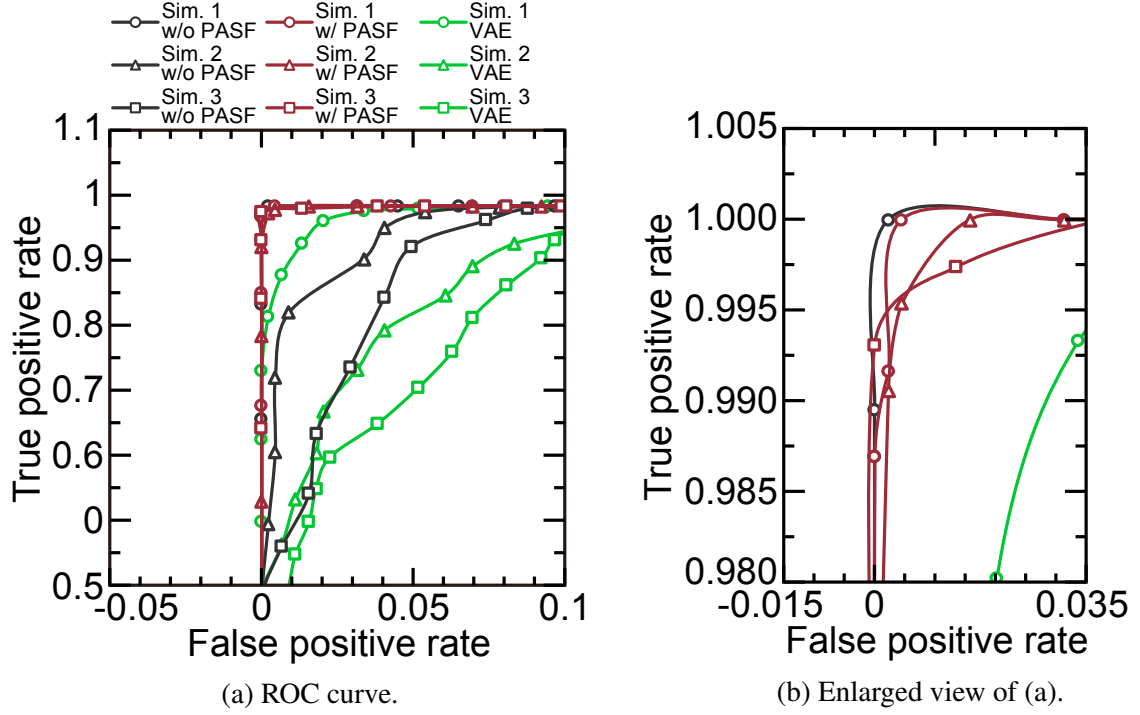


Fig. 5-9: Comparison of the detection performance with and without the PASF using the ROC curve.

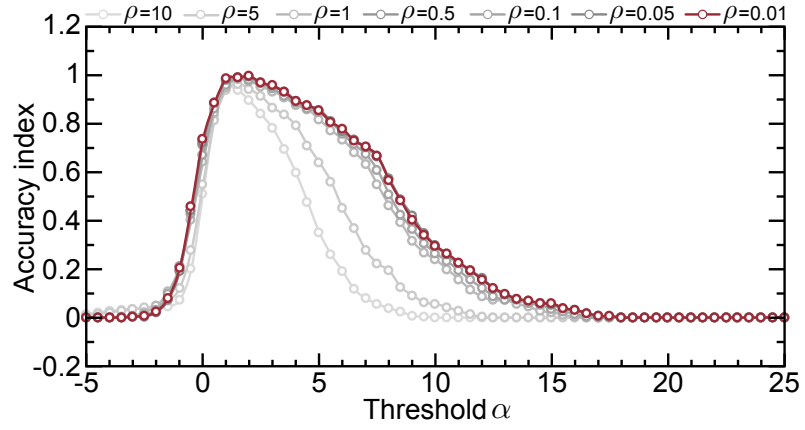
Table 5.2: Accuracy indexes when the separation frequency was $\rho = 0.01$ rad/s.

Threshold	$\alpha = 1.0$	$\alpha = 1.5$	$\alpha = 2.0$	$\alpha = 2.5$	$\alpha = 3.0$
Simulation 1	0.986919	0.989395	0.9954955	0.9684685	0.9572072
Simulation 2	0.946944	0.988351	0.9909122	0.9842342	0.9684685
Simulation 3	0.954584	0.993093	0.9839059	0.9617117	0.9459459
Average	0.962816	0.990280	0.9901045	0.9714715	0.9572072

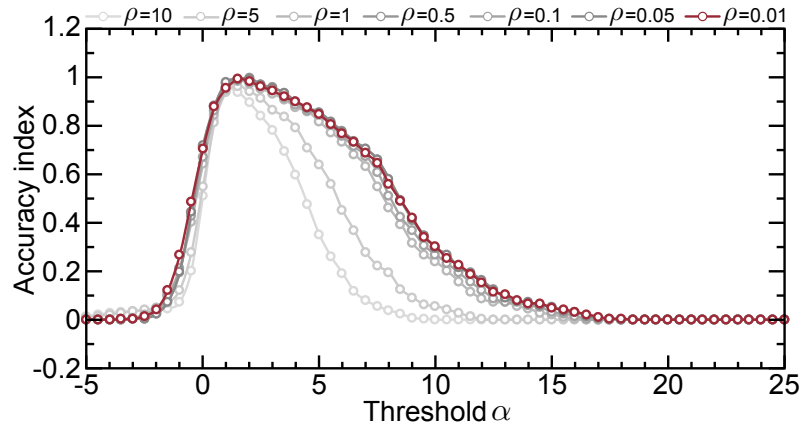
Accuracy of the PASF-based haptic leak-detection depends on the separation frequency of the PASF ρ and threshold α . They can be determined on the basis of the accuracy index:

$$\text{Accuracy index} = \text{True positive rate} \times (1 - \text{False positive rate}). \quad (5.18)$$

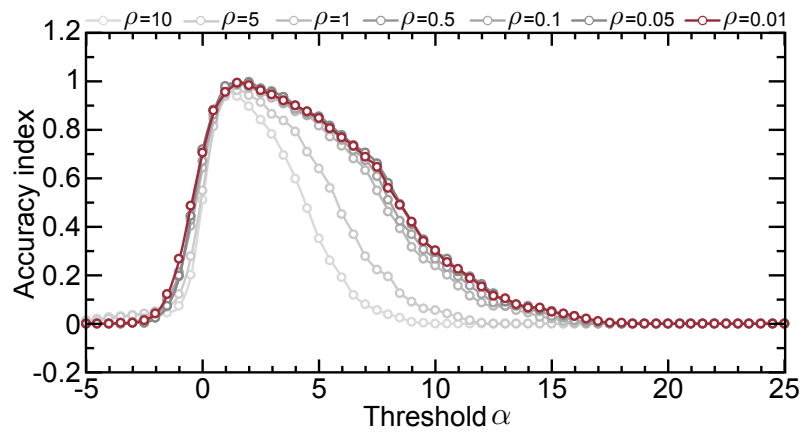
The accuracy index varies between 0 and 1, and accuracy index = 1 means perfect detection. According to Fig. 5-10, the small separation frequency $\rho = 0.01$ rad/s realized the widest accuracy in terms of the threshold at all Simulations 1, 2, and 3. Furthermore, Table 5.2 summarized the high accuracy indexes from Fig. 5-10 and showed that $\alpha = 1.5$ performed the best accuracy on average. According to the above accuracy evaluation, the optimal separation frequency $\rho = 0.01$ rad/s and optimal threshold $\alpha = 1.5$ are determined.



(a) Simulation 1.



(b) Simulation 2.



(c) Simulation 3.

Fig. 5-10: Accuracy index for threshold design.

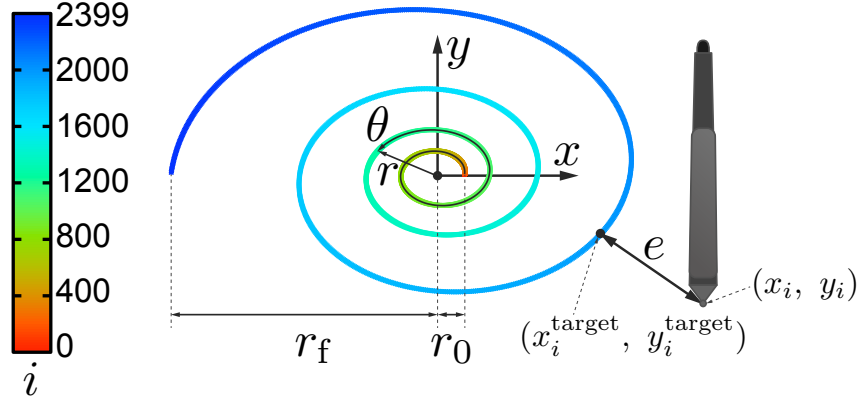


Fig. 5-11: Counter-clockwise logarithmic spiral trajectory for the motor learning experiment.

5.3 Periodic Proficiency Diagnosis

5.3.1 Proficiency Diagnosis for Motor Learning

Minimum-Angular-Jerk Logarithmic Spiral

A motor learning experiment was designed using a drawing task of a minimum-angular-jerk counter-clockwise logarithmic spiral, as shown in Fig. 5-11. The spiral was defined in the polar coordinate system as

$$r = r_0 e^{a\theta}, \quad (5.19)$$

where

$$a = \frac{\ln(r_f/r_0)}{\theta_f} \quad (5.20)$$

$$0 < r_0, r_f, \theta_f \quad (5.21)$$

$$r_0 < r_f. \quad (5.22)$$

r_0 , r_f , θ , and θ_f denote the initial radius, final radius, spiral angle, and final angle, respectively. A minimum-angular-jerk trajectory for the angle θ was derived by solving the variational problem:

$$\begin{aligned} \min \int_0^{\tau_f} \ddot{\theta}^2 d\tau \\ \text{s.t. } \theta(0) = 0, \theta(\tau_f) = \theta_f, \dot{\theta}(0) = \dot{\theta}_0, \dot{\theta}(\tau_f) = \dot{\theta}_f, \ddot{\theta}(0) = 0, \ddot{\theta}(\tau_f) = 0, \end{aligned} \quad (5.23)$$

where this study used the spiral parameters shown in Table 5.3. τ denotes the continuous time. Using

Table 5.3: Counter-clockwise logarithmic spiral parameters.

Parameter	Symbol	Value	Parameter	Symbol	Value
Initial radius	r_0	0.01 m	Final radius	r_f	0.1 m
Final angle	θ_f	7π rad	Initial angular velocity	$\dot{\theta}_0$	3 rad/s
Final angular velocity	$\dot{\theta}_f$	3 rad/s	Trial time	τ_f	6 s

an Euler equation:

$$\frac{d^3}{d\tau^3} \frac{\partial \ddot{\theta}^2}{\partial \ddot{\theta}} = 0, \quad (5.24)$$

the minimum-angular-jerk trajectory was calculated as

$$\theta(\tau) = \frac{1}{120}C_1\tau^5 + \frac{1}{24}C_2\tau^4 + \frac{1}{6}C_3\tau^3 + C_5\tau, \quad (5.25)$$

where

$$C_1 = 720 \frac{\theta_f}{\tau_f^5} - 360 \frac{\dot{\theta}_0}{\tau_f^4} - 360 \frac{\dot{\theta}_f}{\tau_f^4} \quad (5.26)$$

$$C_2 = -360 \frac{\theta_f}{\tau_f^4} + 192 \frac{\dot{\theta}_0}{\tau_f^3} + 168 \frac{\dot{\theta}_f}{\tau_f^3} \quad (5.27)$$

$$C_3 = 60 \frac{\theta_f}{\tau_f^3} - 36 \frac{\dot{\theta}_0}{\tau_f^2} - 24 \frac{\dot{\theta}_f}{\tau_f^2} \quad (5.28)$$

$$C_5 = \dot{\theta}_0. \quad (5.29)$$

Consequently, the position, velocity, and acceleration of the spiral were as follows:

Position:

$$\begin{cases} r(\tau) = r_0 e^{a\theta(\tau)} \\ \theta(\tau) = \frac{1}{120}C_1\tau^5 + \frac{1}{24}C_2\tau^4 + \frac{1}{6}C_3\tau^3 + C_5\tau \end{cases} \quad (5.30)$$

Velocity:

$$\begin{cases} \dot{r}(\tau) = r_0 a \dot{\theta} e^{a\theta(\tau)} \\ \dot{\theta}(\tau) = \frac{1}{24}C_1\tau^4 + \frac{1}{6}C_2\tau^3 + \frac{1}{2}C_3\tau^2 + C_5 \end{cases} \quad (5.31)$$

Acceleration:

$$\begin{cases} \ddot{r}(\tau) = r_0 a \ddot{\theta} e^{a\theta(\tau)} + r_0 a^2 \dot{\theta}^2 e^{a\theta(\tau)} \\ \ddot{\theta}(\tau) = \frac{1}{6}C_1\tau^3 + \frac{1}{2}C_2\tau^2 + C_3\tau \end{cases} \quad (5.32)$$

Fig. 5-12 illustrates the trajectories. The spiral trajectory was used by transforming into the orthogonal coordinate system as the target spiral: x_i^{target} and y_i^{target} .

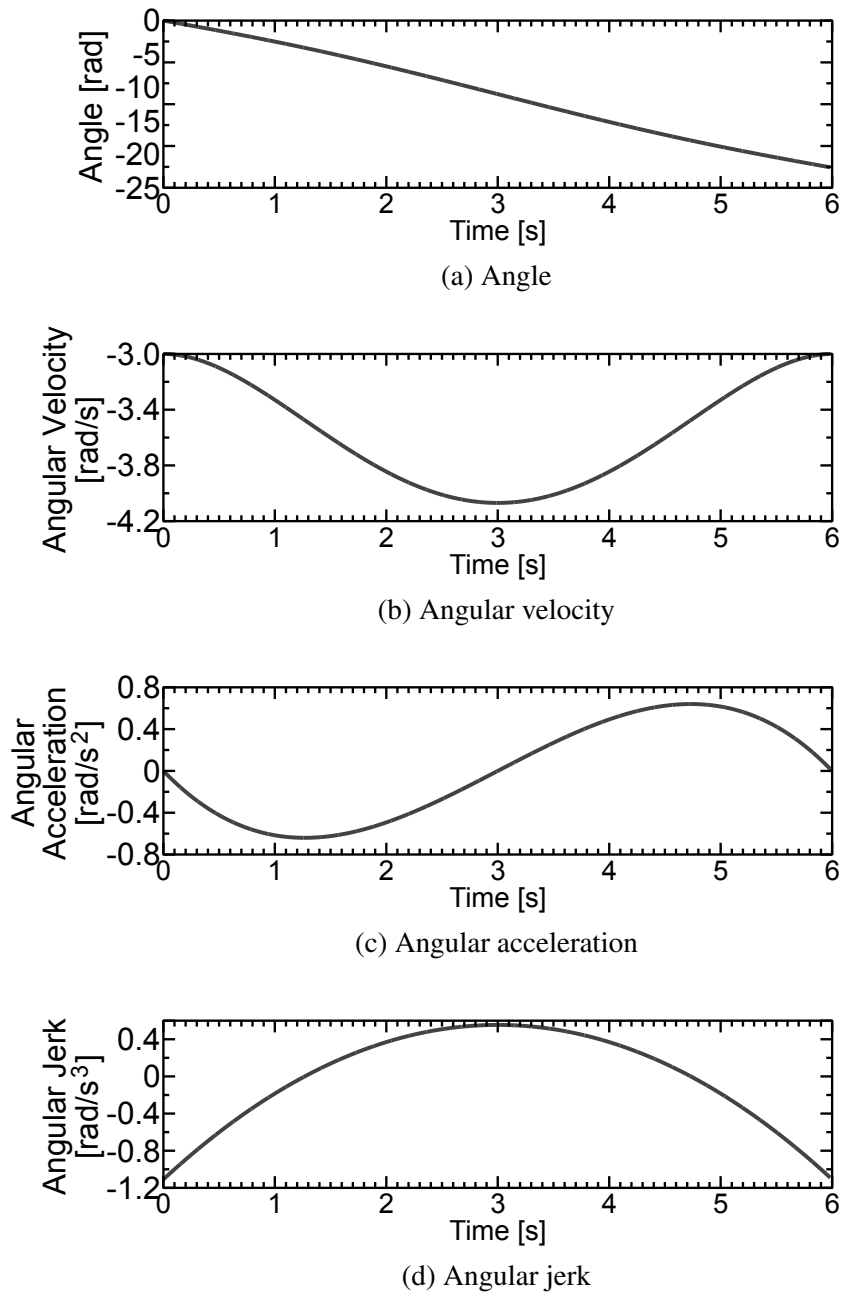


Fig. 5-12: Angle, angular velocity, angular acceleration, and angular jerk waveforms of θ satisfying the minimum-angular-jerk in (5.23).

Experimental Setup

In the experiment, participants held a stylus attached to the end effector of the robot in a power grip, as shown in Fig. 5-13. They are instructed to draw the spiral as accurately as possible in terms of the

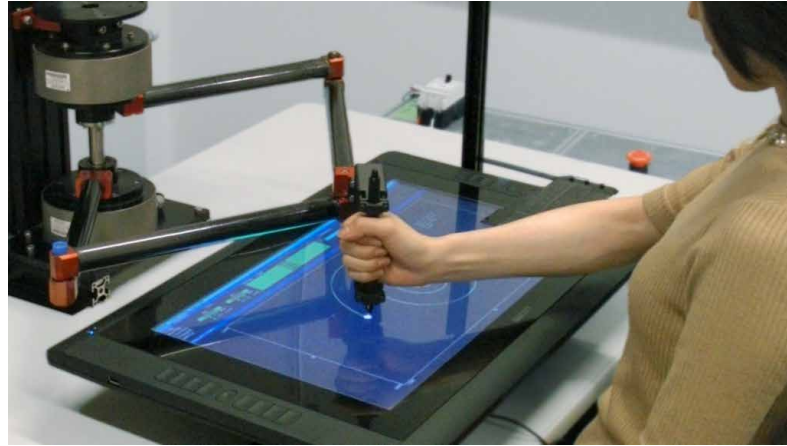


Fig. 5-13: Experimental system.

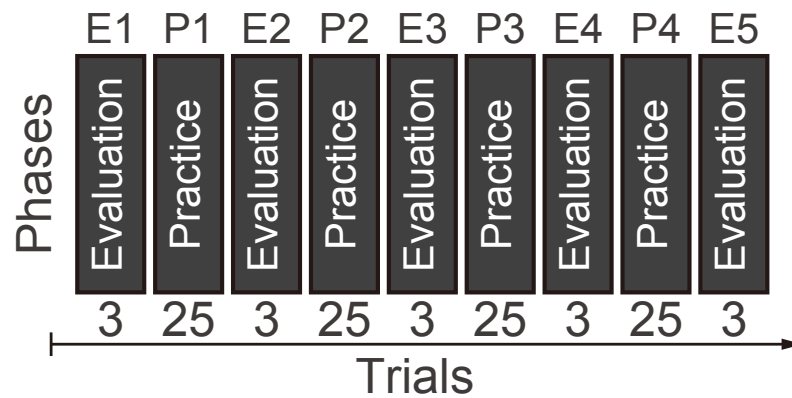
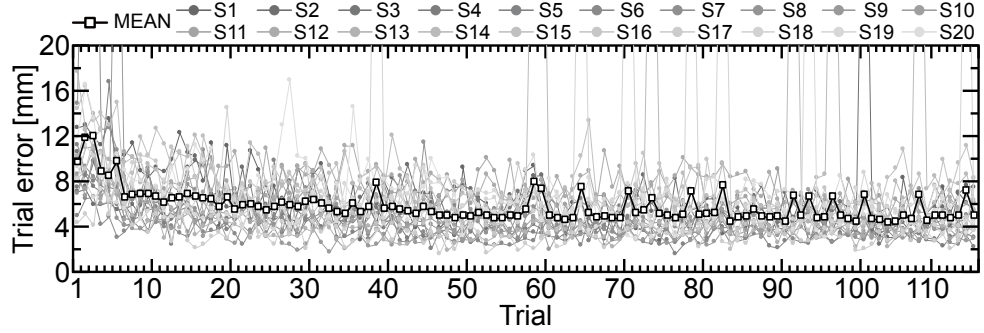


Fig. 5-14: Schedule of the drawing practice.

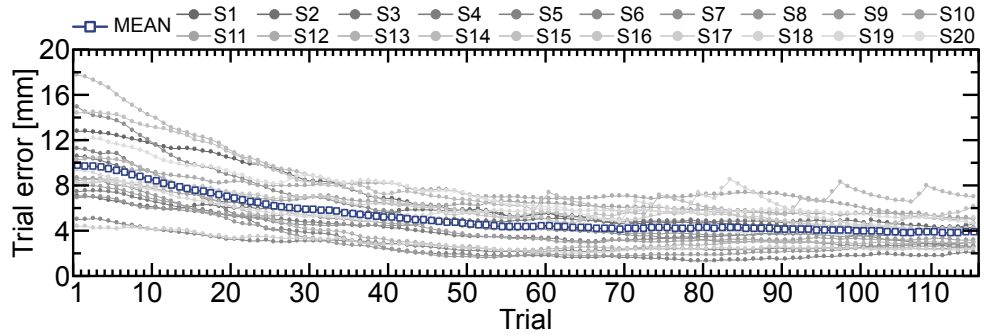
path and time course. The robot was used to measure the stylus position. Twenty students participated in the experiment and practiced according to the practice schedule, which is composed of evaluation and practice phases including 3 and 25 trials, respectively. The two phases were alternately conducted, as shown in Fig. 5-14. In the practice phases, participants performed the drawing task and received visual feedback of a written spiral after each trial. In the evaluation phases, participants performed the task without the visual feedback.

5.3.2 PASF-Based Proficiency Diagnosis

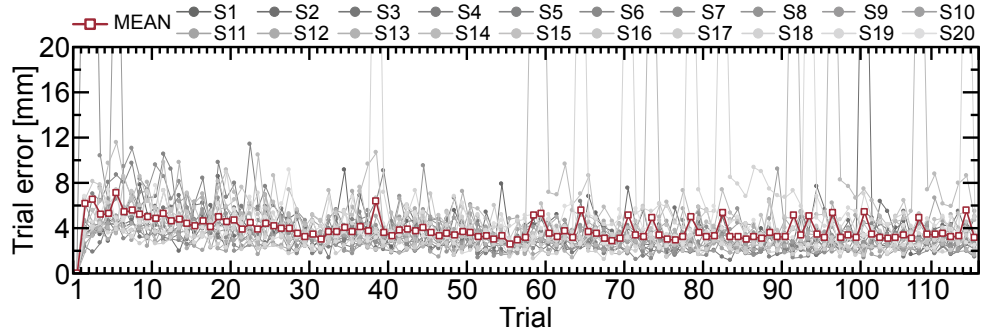
A drawn spiral was calculated by measured stylus position x_i and y_i at all trials. The spiral was spatially numbered from 0 to 2399, as Fig. 5-11. Along the number, the spirals were separated by the



(a) Trial errors of the spirals.



(b) Periodic trajectories of the trial errors.

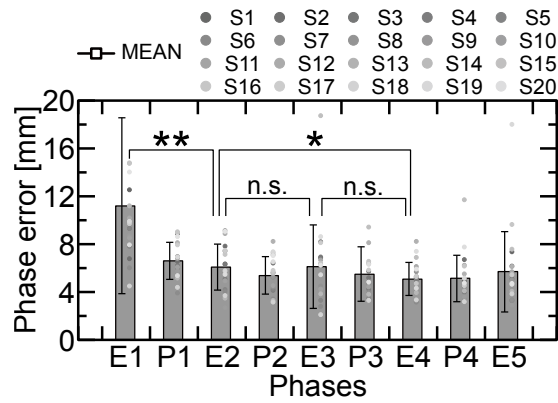


(c) Aperiodic trajectories of the trial errors.

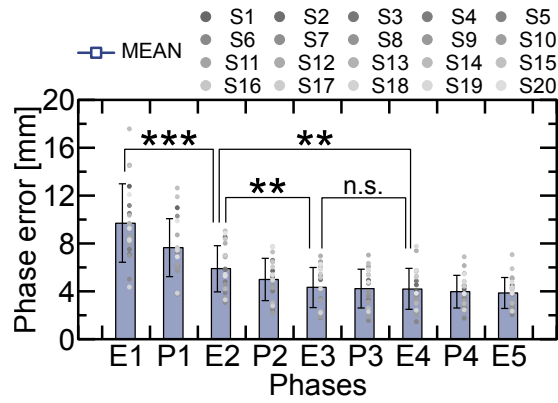
Fig. 5-15: Twenty subjects' trial errors.

first-order PASF into periodic and aperiodic trajectories. A trial error, which is a difference between the target spiral x_i^{target} and y_i^{target} and the spiral x_i and y_i in Fig. 5-11, was calculated as

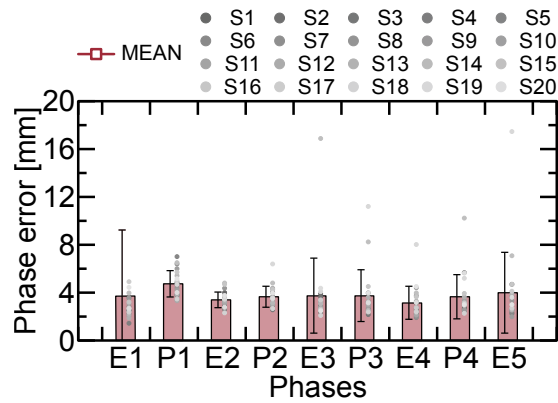
$$\text{Trial error} = \frac{1}{2400} \sum_{i=0}^{2399} \sqrt{(x_i^{\text{target}} - x_i)^2 + (y_i^{\text{target}} - y_i)^2}. \quad (5.33)$$



(a) Phase errors of the spirals.



(b) Phase errors of the periodic trajectories.



(c) Phase errors of the aperiodic trajectories.

Fig. 5-16: Twenty subjects' phase errors at the evaluation and practice phases. The error bars stand for SDs, and the symbols ***, **, *, and n.s. stand for the statistic results: $p < 0.001$, $p < 0.01$, $p < 0.05$, and $0.05 < p$, respectively.

Trial errors for the periodic trajectory x_{pi} and y_{pi} and aperiodic trajectory x_{ai} and y_{ai} were calculated as

$$\text{Trial error} = \frac{1}{2400} \sum_{i=0}^{2399} \sqrt{(x_i^{\text{target}} - x_{pi})^2 + (y_i^{\text{target}} - y_{pi})^2}, \quad (5.34)$$

and

$$\text{Trial error} = \frac{1}{2400} \sum_{i=0}^{2399} \sqrt{x_{ai}^2 + y_{ai}^2}, \quad (5.35)$$

respectively. Fig. 5-15 shows transition of the trial errors and Fig. 5-15(b) illustrates that the trial errors of the periodic trajectories continuously decrease by eliminating the variable aperiodic trajectories shown in Fig. 5-15(c). From the trial errors, a phase error that is a mean of the trial errors at each phase was calculated, as shown in Fig. 5-16. Each subject's phase errors at the evaluation phases were calculated by

$$\text{Phase error} = \frac{1}{3} \sum_{j=1}^3 \text{Trial error}_j, \quad (5.36)$$

and those at the practice phases were calculated by

$$\text{Phase error} = \frac{1}{25} \sum_{j=1}^{25} \text{Trial error}_j. \quad (5.37)$$

In Fig. 5-16(a) for the spirals, the phase errors at E2 and E4 were significantly smaller than those at E1 and E2, respectively. In Fig. 5-16(b) for the periodic trajectories, the phase error at E3 was additionally significantly smaller than that at E2. Therefore, the PASF-based proficiency diagnosis enabled to detect the small change from E2 to E3. In details, Figs. 5-17–5-25 shows one subject's spirals, periodic trajectories, and aperiodic trajectories at each trial. Compared to proficiency transition of the spiral in Figs. 5-17, 5-18, and 5-19, continuous improvement in the periodic trajectories in Figs. 5-20, 5-21, and 5-22 can be confirmed as a result of eliminating the aperiodic behavior shown in Figs. 5-23, 5-24, and 5-25.

5.4 Summary

Section 5.2 showed the PASF-based haptic leak-detection for the inspection of food product packing. Firstly, the package-leak model and detection flow were explained. Then, the 10,000 packages inspection simulation, that was generated by randomly connecting the 388 experimental reaction force data, was

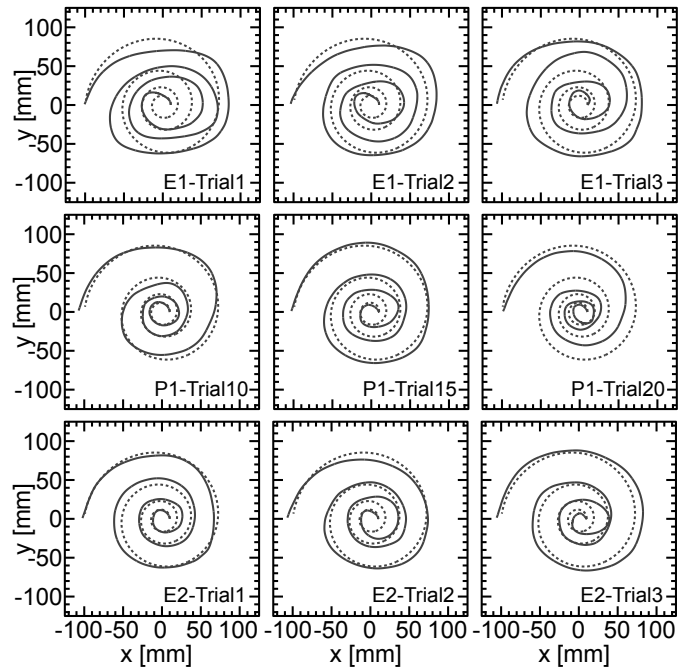


Fig. 5-17: One subject's spirals in E1, P1, and E2.

conducted. The simulation validated that the PASF-based haptic leak-detection has the robustness against the disturbance effects owing to the PASF.

Section 5.3 showed the PASF-based proficiency diagnosis. The minimum-angular-jerk trajectory and practice schedule for the motor learning experiment were mentioned. Then, the trial errors, phase errors, and drawn spirals were shown. According to the trial errors and drawn spirals, the periodic trajectories enabled to evaluate continuous improvements in motor proficiency. According to the phase errors, the periodic trajectories enabled to detect the small change from E2 to E3. Therefore, the PASF-based proficiency diagnosis may be able to detect small proficiency improvement accurately.

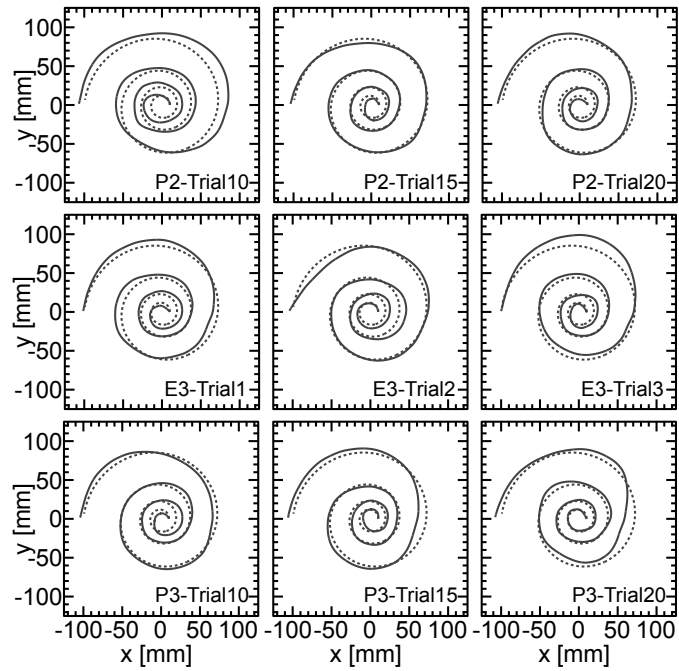


Fig. 5-18: One subject's spirals in P2, E3, and P3.

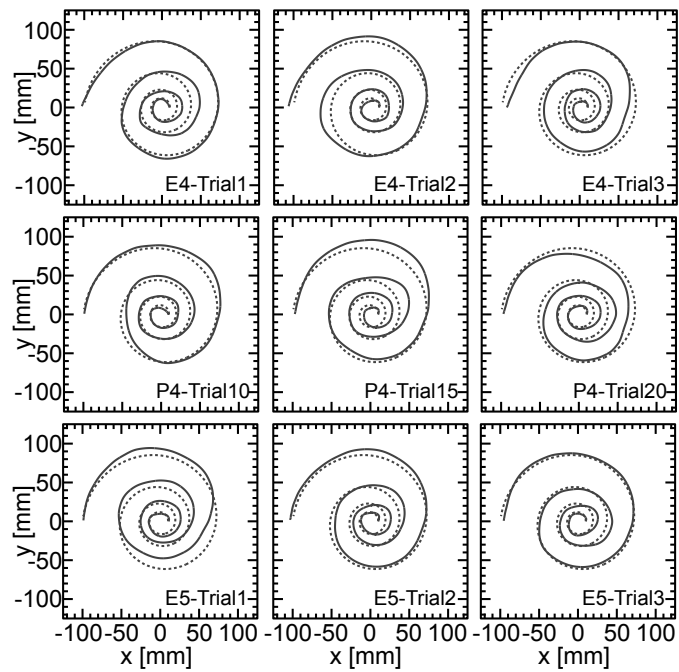


Fig. 5-19: One subject's spirals in E4, P4, and E5.

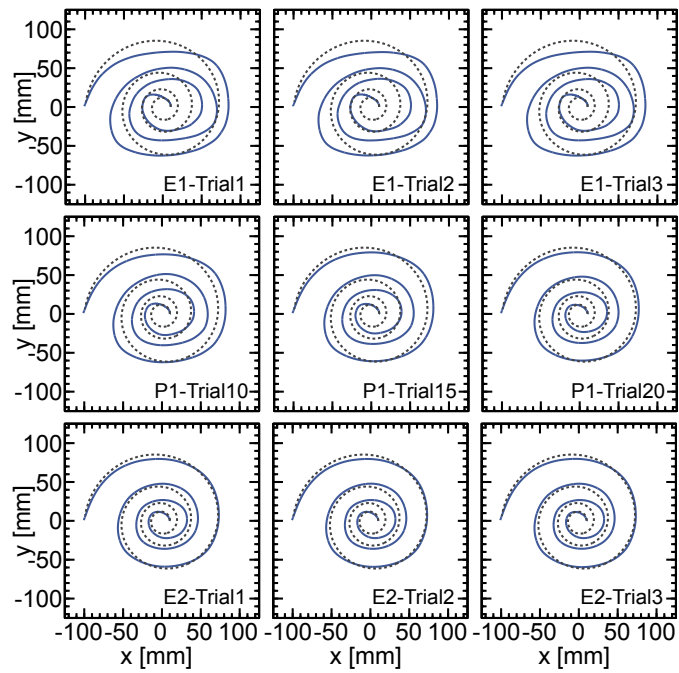


Fig. 5-20: One subject's periodic trajectories in E1, P1, and E2.

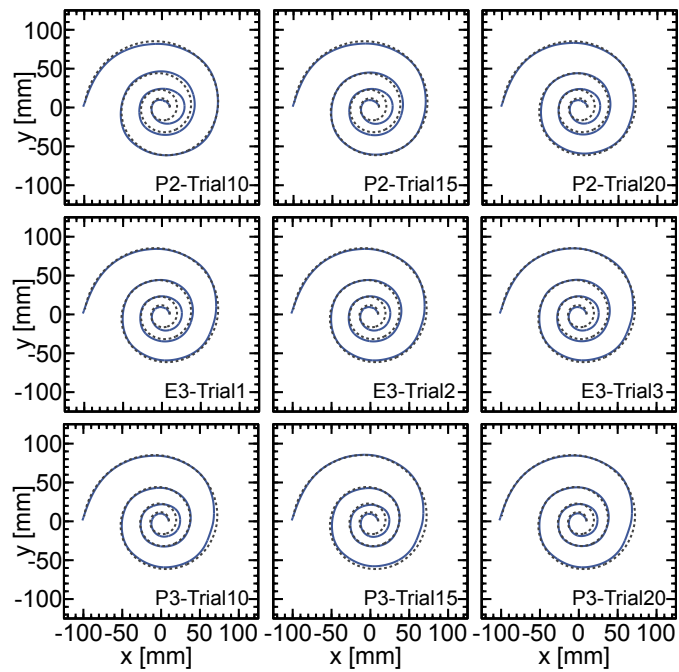


Fig. 5-21: One subject's periodic trajectories in P2, E3, and P3.

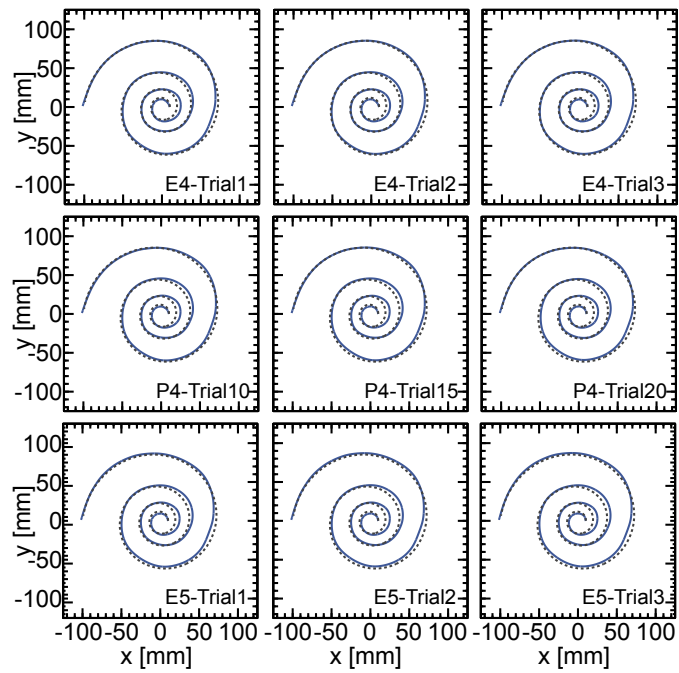


Fig. 5-22: One subject's periodic trajectories in E4, P4, and E5.

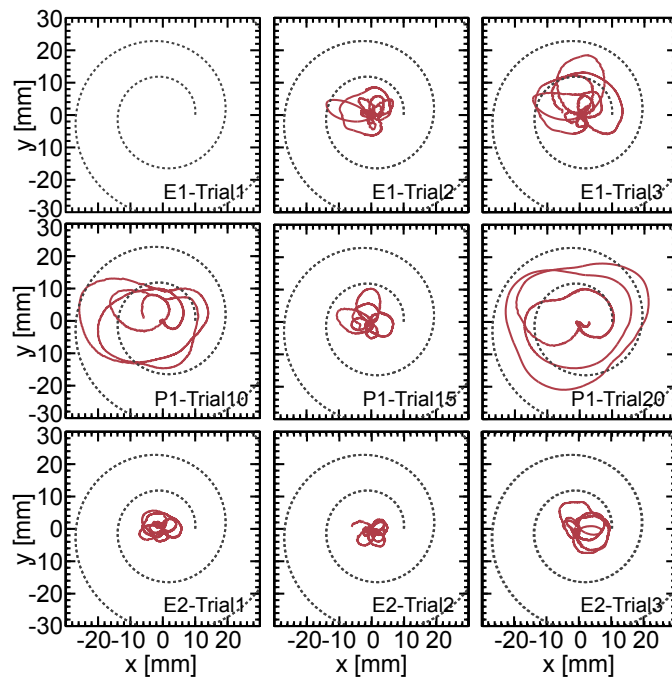


Fig. 5-23: One subject's aperiodic trajectories in E1, P1, and E2.

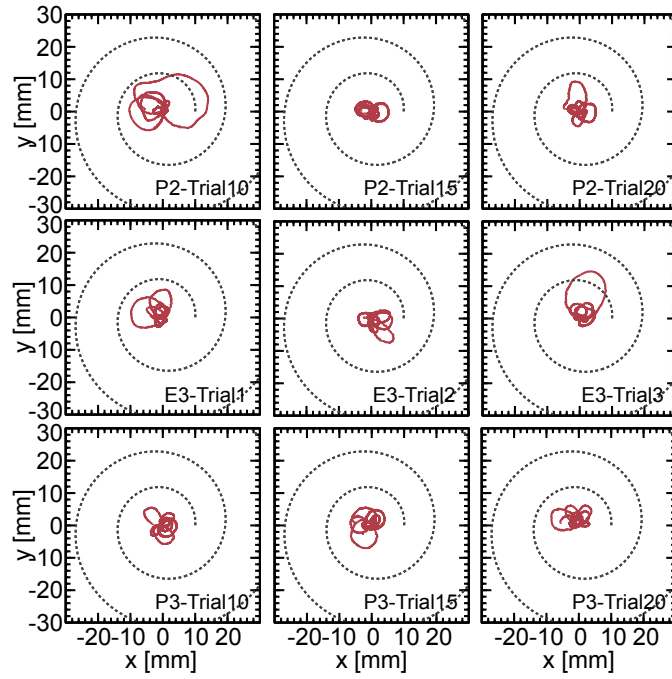


Fig. 5-24: One subject's aperiodic trajectories in P2, E3, and P3.

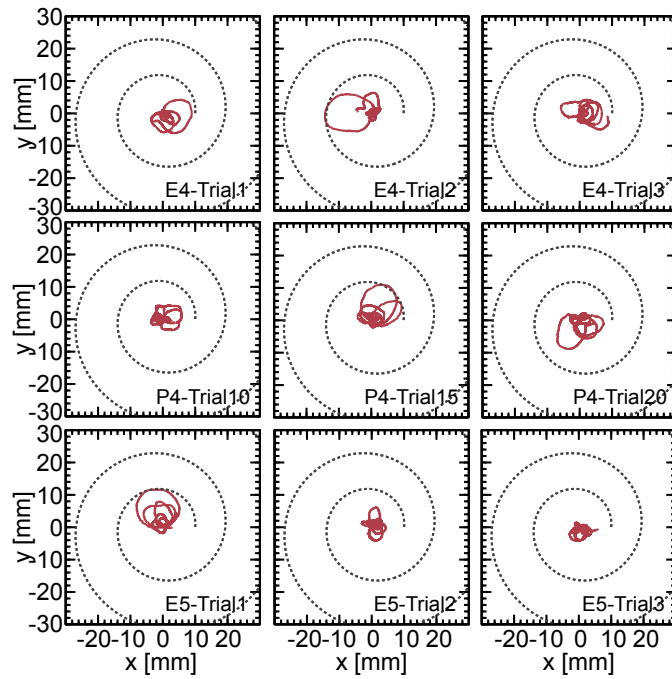


Fig. 5-25: One subject's aperiodic trajectories in E4, P4, and E5.

Chapter 6

Conclusions

This dissertation described the periodicity and aperiodicity for the separation, state control, disturbance compensation, and diagnosis. The basic concept was the periodic/apperiodic state composed of a periodic state and aperiodic state, where the lifted periodic and lifted aperiodic states were uniquely defined as low-frequency and high-frequency elements of the lifted periodic/apperiodic state, respectively. The proposals described by this dissertation are as follows.

- Periodic/apperiodic separation filter (PASF)
- Periodic/apperiodic state feedback control
- Separation principle for periodic/apperiodic state feedback control
- Periodic/apperiodic motion control including six types
- Periodic-disturbance observer (PDOB)
- Enhanced periodic-disturbance observer
- PASF-based haptic leak detection
- PASF-based proficiency diagnosis

Chapter 2 described the periodic/apperiodic separation. In Section 2.2, the periodic/apperiodic state, periodic state, and aperiodic state were defined by using the lifting technique. The periodic/apperiodic state was transformed using the lifting technique into the lifted periodic/apperiodic state, in which a constant

element was defined as the lifted perfect periodic state, and the low-frequency elements were defined as the lifted periodic state. Accordingly, the high-frequency elements were defined as the lifted aperiodic state. Based on the definitions, the lifted PASF that separates the lifted periodic/aperiodic state into the lifted periodic and aperiodic states was constructed, and the inverse lifting derived the PASF that separates the periodic/aperiodic state into the periodic and aperiodic states. In Section 2.3, the frequency estimator was constructed based on the adaptive notch filter as a supplementary method for estimating an unknown or varying frequency of the periodic/aperiodic state. The frequency estimator used a band-pass filter to extract a fundamental wave from the periodic/aperiodic state, and the adaptive notch filter estimates a fundamental frequency of the fundamental wave. Oscillation of the estimated fundamental wave was attenuated by a low-pass filter.

Chapter 3 described the periodic/aperiodic state control. In Section 3.2, the periodic/aperiodic state feedback control was constructed by using the PASF. Then, the separation principle for control, observation, and separation of the periodic/aperiodic state was proved. In Section 3.3, the periodic/aperiodic state feedback control was developed into the motion control framework. Then, the six periodic/aperiodic motion controls that assign position, force, and impedance controls to periodic motion and aperiodic motion were constructed.

Chapter 4 described the periodic/aperiodic disturbance compensation. In Section 4.2, the PDOB was constructed for periodic-disturbance compensation. Based on the model of a periodic disturbance, the Q-filter of the PDOB was designed to be able to eliminate the periodic disturbance. Moreover, the nominal stability analysis based on the characteristic equation showed that the delay of the PDOB does not affect the nominal stability. Furthermore, according to the comparison with classical DOBs, the improved periodic-disturbance suppression performance and robust stability in the tradeoff were confirmed using the sensitivity and complementary sensitivity functions. In Section 4.3, the PDOB was developed into the enhanced PDOB to enable to compensate for both the periodic and aperiodic disturbances. The enhanced PDOB was constructed by the combination design of the PDOB and DOB.

Chapter 5 described the periodic/aperiodic diagnosis. In Section 5.2, the PASF was applied to the food packing inspection as the PASF-based haptic leak-detection. The 10,000 packages inspection simulation, that was generated by randomly connecting the 388 experimental yank data, was conducted. The simulation validated that the PASF-based haptic leak-detection has the robustness against disturbances and achieves accurate anomaly detection. In Section 5.3, the PASF was applied to the motor proficiency evaluation for the drawing task of the minimum-angular-jerk logarithmic spiral. The PASF-based proficiency

diagnosis enabled to detect a small change of the drawing proficiency.

Therefore, my research has integrally designed the filter, controls, and diagnostic methods for the industry and humans on the basis of the periodicity and aperiodicity. The research might open up a new vista that facilitates the separated design and analysis for periodic/aperiodic phenomena in the field of the integrated design engineering.

Despite the novelty and improvements of the proposals, they still have limitations regarding interference between the estimated periodic and aperiodic states by the PASF. An ideal PASF is impossible to realize because the lifted periodic state was defined as low-frequency elements of the lifted periodic/aperiodic state. In other words, the ideal separation is impossible because an ideal low-pass filter cannot be causally constructed. Consequently, the interference occurs and affects the controls and diagnoses based on the PASF. However, the interference is not dominant and could be ignorable according to Subsection 2.2.2. Besides, my research has future works on consideration of continuous-time and sampled-data systems in addition to the discrete-time system. The works could expand the applicable range of the proposals.

The proposals are expected to have an impact on the society. The periodic/aperiodic motion control can realize periodic velocity and aperiodic impedance control, which is suitable for repetitive robot operations under sudden human contacts. The control enables a robot to achieve repetitive and precise operation and soft contact with humans. The enhanced PDOB based on the PDOB, which can suppress periodic and aperiodic disturbances, is significant for industrial applications. This is because most industrial machines work repetitively and induce periodic and aperiodic disturbances. Moreover, the PASF-based haptic leak detection has already demonstrated its usefulness to the industrial application. Finally, the PASF-based proficiency diagnosis, which has already performed the accurate motor proficiency evaluation for healthy young people, has the potential to evaluate also rehabilitation of stroke survivors accurately.

References

- [1] S. Chu and C. Burrus, "Multirate filter designs using comb filters," *IEEE Transactions on Circuits and Systems*, vol. 31, no. 11, pp. 913–924, Nov. 1984.
- [2] M. Niedźwiecki and M. Meller, "Generalized adaptive comb filters/smoother and their application to the identification of quasi-periodically varying systems and signals," *Automatica*, vol. 49, no. 6, pp. 1601–1613, Jun. 2013.
- [3] P. Zahradnik and M. Vlcek, "Analytical design method for optimal equiripple comb FIR filters," *IEEE Transactions on Circuits and Systems II: Express Briefs*, vol. 52, no. 2, pp. 112–115, Feb. 2005.
- [4] P. Zahradnik, M. Vlcek, and R. Unbehauen, "Design of optimal comb FIR filters-speed and robustness," *IEEE Signal Processing Letters*, vol. 16, no. 6, pp. 465–468, Jun. 2009.
- [5] S. F. George and A. S. Zamanakos, "Comb filters for pulsed radar use," in *Proceedings of the IRE*, vol. 42, no. 7, Jul. 1954, pp. 1159–1165.
- [6] G. Arndt, F. Stuber, and R. Panneton, "Video-signal improvement using comb filtering techniques," *IEEE Transactions on Communications*, vol. 21, no. 4, pp. 331–336, Apr. 1973.
- [7] R. Turner, "Some thoughts on using comb filters in the broadcast television transmitter and at the receiver," *IEEE Transactions on Consumer Electronics*, vol. CE-23, no. 3, pp. 248–257, Aug. 1977.
- [8] D. E. Veeneman and B. Mazor, "A fully adaptive comb filter for enhancing block-coded speech," *IEEE Transactions on Acoustics, Speech, and Signal Processing*, vol. 37, no. 6, pp. 955–957, Jun. 1989.
- [9] H. T. Hu, "Comb filtering of noisy speech using overlap-and-add approach," *Electronics Letters*, vol. 34, no. 1, pp. 16–18, Jan. 1998.

References

- [10] J. Liu and N. F. Declercq, “Pulsed ultrasonic comb filtering effect and its applications in the measurement of sound velocity and thickness of thin plates,” *Ultrasonics*, vol. 75, pp. 199–208, Mar. 2017.
- [11] G. J. Dolecek and M. Laddomada, “An economical class of droop-compensated generalized comb filters: Analysis and design,” *IEEE Transactions on Circuits and Systems II: Express Briefs*, vol. 57, no. 4, pp. 275–279, Apr. 2010.
- [12] G. J. Dolecek and A. Fernandez-Vazquez, “Trigonometrical approach to design a simple wideband comb compensator,” *AEU - International Journal of Electronics and Communications*, vol. 68, no. 5, pp. 437–441, May 2014.
- [13] M. Tahir and S. K. Mazumder, “Improving dynamic response of active harmonic compensator using digital comb filter,” *IEEE Journal of Emerging and Selected Topics in Power Electronics*, vol. 2, no. 4, pp. 994–1002, Dec. 2014.
- [14] B. Yegnanarayana, C. d’Alessandro, and V. Darsinos, “An iterative algorithm for decomposition of speech signals into periodic and aperiodic components,” *IEEE Transactions on Speech and Audio Processing*, vol. 6, no. 1, pp. 1–11, Jan. 1998.
- [15] P. Zubrycki and A. Petrovsky, “Accurate speech decomposition into periodic and aperiodic components based on discrete harmonic transform,” in *Proceedings of the 2007 15th European Signal Processing Conference*, Sep. 2007, pp. 2336–2340.
- [16] T. Fujimoto, T. Yoshimura, K. Hashimoto, K. Oura, Y. Nankaku, and K. Tokuda, “Speech synthesis using wavenet vocoder based on periodic/aperiodic decomposition,” in *Proceedings of the 2018 Asia-Pacific Signal and Information Processing Association Annual Summit and Conference*, Nov. 2018, pp. 644–648.
- [17] X. Serra and J. Smith, “Spectral modeling synthesis: A sound analysis/synthesis system based on a deterministic plus stochastic decomposition,” *Computer Music Journal*, vol. 14, no. 4, pp. 12–24, 1990.
- [18] Y. Stylianou, J. Laroche, and E. Moulines, “High-quality speech modification based on a harmonic+ noise model,” in *Proceedings of the Fourth European Conference on Speech Communication and Technology*, 1995, pp. 451–454.
- [19] A. Syrdal, Y. Stylianou, L. Garrison, A. Conkie, and J. Schroeter, “TD-PSOLA versus harmonic plus noise model in diphone based speech synthesis,” in *Proceedings of the 1998 IEEE International Conference on Acoustics, Speech and Signal Processing*, vol. 1, May 1998, pp. 273–276.

References

- [20] Y. Wang, F. Gao, and F. J. Doyle, “Survey on iterative learning control, repetitive control, and run-to-run control,” *Journal of Process Control*, vol. 19, no. 10, pp. 1589 – 1600, Dec. 2009.
- [21] D. A. Bristow, M. Tharayil, and A. G. Alleyne, “A survey of iterative learning control,” *IEEE Control Systems Magazine*, vol. 26, no. 3, pp. 96–114, Jun. 2006.
- [22] L. Cuiyan, Z. Dongchun, and Z. Xianyi, “A survey of repetitive control,” in *Proceedings of the 2004 IEEE/RSJ International Conference on Intelligent Robots and Systems*, vol. 2, Sep. 2004, pp. 1160–1166.
- [23] T. Inoue, M. Nakano, T. Kubo, S. Matsumoto, and H. Baba, “High accuracy control of a proton synchrotron magnet power supply,” in *Proceedings of the World Congress of the International Federation of Automatic Control*, vol. 20, Aug. 1981, pp. 216–221.
- [24] S. Hara, Y. Yamamoto, T. Omata, and M. Nakano, “Repetitive control system: a new type servo system for periodic exogenous signals,” *IEEE Transactions on Automatic Control*, vol. 33, no. 7, pp. 659–668, Jul. 1988.
- [25] H. Fujimoto, “RRO compensation of hard disk drives with multirate repetitive perfect tracking control,” *IEEE Transactions on Industrial Electronics*, vol. 56, no. 10, pp. 3825–3831, Oct. 2009.
- [26] H. Fujimoto and T. Takemura, “High-precision control of ball-screw-driven stage based on repetitive control using n -times learning filter,” *IEEE Transactions on Industrial Electronics*, vol. 61, no. 7, pp. 3694–3703, Jul. 2014.
- [27] B. Zhang, K. Zhou, and D. Wang, “Multirate repetitive control for PWM DC/AC converters,” *IEEE Transactions on Industrial Electronics*, vol. 61, no. 6, pp. 2883–2890, Jun. 2014.
- [28] Y. Yang, K. Zhou, and M. Cheng, “Phase compensation resonant controller for PWM converters,” *IEEE Transactions on Industrial Informatics*, vol. 9, no. 2, pp. 957–964, May 2013.
- [29] T. Liu and D. Wang, “Parallel structure fractional repetitive control for pwm inverters,” *IEEE Transactions on Industrial Electronics*, vol. 62, no. 8, pp. 5045–5054, Aug. 2015.
- [30] W. Rohouma, P. Zanchetta, P. W. Wheeler, and L. Empringham, “A four-leg matrix converter ground power unit with repetitive voltage control,” *IEEE Transactions on Industrial Electronics*, vol. 62, no. 4, pp. 2032–2040, Apr. 2015.
- [31] S. Yang, P. Wang, Y. Tang, and L. Zhang, “Explicit phase lead filter design in repetitive control for voltage harmonic mitigation of VSI-based islanded microgrids,” *IEEE Transactions on Industrial Electronics*, vol. 64, no. 1, pp. 817–826, Jan. 2017.

References

- [32] I. Houtzager, J. W. van Wingerden, and M. Verhaegen, “Rejection of periodic wind disturbances on a smart rotor test section using lifted repetitive control,” *IEEE Transactions on Control Systems Technology*, vol. 21, no. 2, pp. 347–359, Mar. 2013.
- [33] S. Bittanti and P. Bolzern, “Reachability and controllability of discrete-time linear periodic systems,” *IEEE Transactions on Automatic Control*, vol. 30, no. 4, pp. 399–401, Apr. 1985.
- [34] G. Guo, J. F. Qiao, and C. Z. Han, “Controllability of periodic systems: continuous and discrete,” *IEE Proceedings - Control Theory and Applications*, vol. 151, no. 4, pp. 488–490, Jul. 2004.
- [35] I. Markovskiy, J. Goos, K. Usevich, and R. Pintelon, “Realization and identification of autonomous linear periodically time-varying systems,” *Automatica*, vol. 50, no. 6, pp. 1632–1640, Jun. 2014.
- [36] B. A. Bamieh and J. B. Pearson, “A general framework for linear periodic systems with applications to H^∞ / sampled-data control,” *IEEE Transactions on Automatic Control*, vol. 37, no. 4, pp. 418–435, Apr. 1992.
- [37] S. Bittanti and P. Colaneri, “Invariant representations of discrete-time periodic systems,” *Automatica*, vol. 36, no. 12, pp. 1777–1793, Dec. 2000.
- [38] L. Paunonen, “Robust output regulation for continuous-time periodic systems,” *IEEE Transactions on Automatic Control*, vol. 62, no. 9, pp. 4363–4375, Sep. 2017.
- [39] M. Fardad, M. R. Jovanovic, and B. Bamieh, “Frequency analysis and norms of distributed spatially periodic systems,” *IEEE Transactions on Automatic Control*, vol. 53, no. 10, pp. 2266–2279, Nov. 2008.
- [40] P. Arcara, S. Bittanti, and M. Lovera, “Periodic control of helicopter rotors for attenuation of vibrations in forward flight,” *IEEE Transactions on Control Systems Technology*, vol. 8, no. 6, pp. 883–894, Nov. 2000.
- [41] L. Mirkin and Z. J. Palmor, “A new representation of the parameters of lifted systems,” *IEEE Transactions on Automatic Control*, vol. 44, no. 4, pp. 833–840, Apr. 1999.
- [42] Y. Ebihara, D. Peaucelle, and D. Arzelier, “Analysis of uncertain discrete-time linear periodic systems based on system lifting and LMIs,” *European Journal of Control*, vol. 16, no. 5, pp. 532–544, 2010.
- [43] Y. Yang, “An efficient lqr design for discrete-time linear periodic system based on a novel lifting method,” *Automatica*, vol. 87, pp. 383 – 388, Jan. 2018.

References

- [44] R. Marino and P. Tomei, “Adaptive notch filters are local adaptive observers,” *International Journal of Adaptive Control and Signal Processing*, vol. 30, no. 1, pp. 128–146, Jan. 2016.
- [45] M. Mojiri and A. R. Bakhshai, “An adaptive notch filter for frequency estimation of a periodic signal,” *IEEE Transactions on Automatic Control*, vol. 49, no. 2, pp. 314–318, Feb. 2004.
- [46] M. Mojiri and A. R. Bakhshai, “Estimation of n frequencies using adaptive notch filter,” *IEEE Transactions on Circuits and Systems—Part II: Analog and Digital Signal Processing*, vol. 54, no. 4, pp. 338–342, Apr. 2007.
- [47] Z. Cao and G. F. Ledwich, “Adaptive repetitive control to track variable periodic signals with fixed sampling rate,” *IEEE/ASME Transactions on Mechatronics*, vol. 7, no. 3, pp. 378–384, Sep. 2002.
- [48] B. Shahsavari, E. Keikha, F. Zhang, and R. Horowitz, “Adaptive repetitive control design with online secondary path modeling and application to bit-patterned media recording,” *IEEE/ASME Transactions on Mechatronics*, vol. 51, no. 4, pp. 1–8, Apr. 2015.
- [49] K. Ohnishi, M. Shibata, and T. Murakami, “Motion control for advanced mechatronics,” *IEEE/ASME Transactions on Mechatronics*, vol. 1, no. 1, pp. 56–67, Mar. 1996.
- [50] A. Sabanovic and K. Ohnishi, *Motion control systems*. John Wiley and Sons, 2011.
- [51] B. K. Kim and W. K. Chung, “Advanced disturbance observer design for mechanical positioning systems,” *IEEE Transactions on Industrial Electronics*, vol. 50, no. 6, pp. 1207–1216, Dec. 2003.
- [52] M. Iwasaki, K. Seki, and Y. Maeda, “High-precision motion control techniques: A promising approach to improving motion performance,” *IEEE Industrial Electronics Magazine*, vol. 6, no. 1, pp. 32–40, Mar. 2012.
- [53] T. Atsumi and W. C. Messner, “Compensating for ZOH-induced residual vibrations in head-positioning control of hard disk drives,” *IEEE/ASME Transactions on Mechatronics*, vol. 19, no. 1, pp. 258–268, Feb. 2014.
- [54] E. Sariyildiz and K. Ohnishi, “On the explicit robust force control via disturbance observer,” *IEEE Transactions on Industrial Electronics*, vol. 62, no. 3, pp. 1581–1589, Mar. 2015.
- [55] S. Oh and K. Kong, “High-precision robust force control of a series elastic actuator,” *IEEE/ASME Transactions on Mechatronics*, vol. 22, no. 1, pp. 71–80, Feb. 2017.
- [56] A. Calanca and P. Fiorini, “Understanding environment-adaptive force control of series elastic actuators,” *IEEE/ASME Transactions on Mechatronics*, vol. 23, no. 1, pp. 413–423, Feb. 2018.

References

- [57] N. Hogan, “Impedance control: An approach to manipulation: Part I–Theory. Part II–Implementation. Part III–Applications,” *Journal of Dynamic Systems, Measurement, and Control*, vol. 107, no. 1, pp. 1–24, Mar. 1985.
- [58] J. Koivumki and J. Mattila, “Stability-guaranteed impedance control of hydraulic robotic manipulators,” *IEEE/ASME Transactions on Mechatronics*, vol. 22, no. 2, pp. 601–612, Apr. 2017.
- [59] M. H. Raibert and J. J. Craig, “Hybrid position/force control of manipulators,” *Journal of Dynamic Systems, Measurement, and Control*, vol. 103, no. 2, pp. 126–133, Jun. 1981.
- [60] F. Jatta, G. Legnani, and A. Visioli, “Friction compensation in hybrid force/velocity control of industrial manipulators,” *IEEE Transactions on Industrial Electronics*, vol. 53, no. 2, pp. 604–613, Apr. 2006.
- [61] W. Iida and K. Ohnishi, “Reproducibility and operability in bilateral teleoperation,” in *Proceedings of the IEEE International Workshop on Advanced Motion Control*, Mar. 2004, pp. 217–222.
- [62] C. Mitsantisuk, K. Ohishi, and S. Katsura, “Estimation of action/reaction forces for the bilateral control using kalman filter,” *IEEE Transactions on Industrial Electronics*, vol. 59, no. 11, pp. 4383–4393, Nov. 2012.
- [63] T. Nozaki, T. Mizoguchi, and K. Ohnishi, “Decoupling strategy for position and force control based on modal space disturbance observer,” *IEEE Transactions on Industrial Electronics*, vol. 61, no. 2, pp. 1022–1032, Feb. 2014.
- [64] F. Logist, S. Sager, C. Kirches, and J. F. Van Impe, “Efficient multiple objective optimal control of dynamic systems with integer controls,” *Journal of Process Control*, vol. 20, no. 7, pp. 810–822, Aug. 2010.
- [65] A. A. Malikopoulos, “A multiobjective optimization framework for online stochastic optimal control in hybrid electric vehicles,” *IEEE Transactions on Control Systems Technology*, vol. 24, no. 2, pp. 440–450, Mar. 2016.
- [66] B. Pandurangan, R. Landers, and S. Balakrishnan, “Hierarchical optimal force-position control of a turning process,” *IEEE Transactions on Control Systems Technology*, vol. 13, no. 2, pp. 321–327, Mar. 2005.
- [67] Y. Yokokura, S. Katsura, and K. Ohishi, “Stability analysis and experimental validation of a motion-copying system,” *IEEE Transactions on Industrial Electronics*, vol. 56, no. 10, pp. 3906–3913, Oct. 2009.

References

- [68] K. Miura, A. Matsui, and S. Katsura, “Synthesis of motion-reproduction systems based on motion-copying system considering control stiffness,” *IEEE/ASME Transactions on Mechatronics*, vol. 21, no. 2, pp. 1015–1023, Apr. 2016.
- [69] H. Muramatsu and S. Katsura, “Repetitive motion-reproduction based on a motion-copying system for automation of human motions,” in *Proceedings of the 2017 56th Annual Conference of the Society of Instrument and Control Engineers of Japan*, Sep. 2017, pp. 1443–1446.
- [70] K. Ohishi, K. Ohnishi, and K. Miyachi, “Torque-speed regulation of DC motor based on load torque estimation method,” in *Proceedings of the IEEJ International Power Electronics Conference*, Apr. 1983, pp. 1209–1218.
- [71] W. H. Chen, J. Yang, L. Guo, and S. Li, “Disturbance-observer-based control and related methods—an overview,” *IEEE Transactions on Industrial Electronics*, vol. 63, no. 2, pp. 1083–1095, Feb. 2016.
- [72] E. Sariyildiz, R. Oboe, and K. Ohnishi, “Disturbance observer-based robust control and its applications: 35th anniversary overview,” *IEEE Transactions on Industrial Electronics*, vol. 67, no. 3, pp. 2042–2053, Mar. 2020.
- [73] E. Sariyildiz and K. Ohnishi, “Stability and robustness of disturbance-observer-based motion control systems,” *IEEE Transactions on Industrial Electronics*, vol. 62, no. 1, pp. 414–422, Jan. 2015.
- [74] J. Han, H. Kim, Y. Joo, N. H. Jo, and J. H. Seo, “A simple noise reduction disturbance observer and q-filter design for internal stability,” in *Proceedings of the 2013 13th International Conference on Control, Automation and Systems*, Oct. 2013, pp. 755–760.
- [75] J. Su, W.-H. Chen, and B. Li, “High order disturbance observer design for linear and nonlinear systems,” in *Proceedings of the 2015 IEEE International Conference on Information and Automation*, Aug. 2015, pp. 1893–1898.
- [76] H. Fujimoto, “Robust repetitive perfect tracking control of HDDs based on re-learning scheme,” *IEEJ Journal of Industry Applications*, vol. 2, no. 1, pp. 40–47, Jan. 2013.
- [77] W. Lu, K. Zhou, D. Wang, and M. Cheng, “A generic digital $nk \pm m$ -order harmonic repetitive control scheme for PWM converters,” *IEEE Transactions on Industrial Electronics*, vol. 61, no. 3, pp. 1516–1527, Mar. 2014.
- [78] W. Kim, D. Shin, D. Won, and C. C. Chung, “Disturbance-observer-based position tracking controller in the presence of biased sinusoidal disturbance for electrohydraulic actuators,” *IEEE Transactions on Control Systems Technology*, vol. 21, no. 6, pp. 2290–2298, Nov. 2013.

References

- [79] M. Ruderman, A. Ruderman, and T. Bertram, "Observer-based compensation of additive periodic torque disturbances in permanent magnet motors," *IEEE Transactions on Industrial Informatics*, vol. 9, no. 2, pp. 1130–1138, May 2013.
- [80] T. T. Phuong, R. Furusawa, C. Mitsantisuk, and K. Ohishi, "Force sensing considering periodic disturbance suppression based on high order disturbance observer and kalman-filter," in *Proceedings of the 2011 4th International Conference on Human System Interactions*, May 2011, pp. 336–341.
- [81] J. Karttunen, S. Kallio, P. Peltoniemi, and P. Silventoinen, "Current harmonic compensation in dual three-phase PMSMs using a disturbance observer," *IEEE Transactions on Industrial Electronics*, vol. 63, no. 1, pp. 583–594, Jan. 2016.
- [82] J. Na, R. Grino, R. Costa-Castello, X. Ren, and Q. Chen, "Repetitive controller for time-delay systems based on disturbance observer," *IET Control Theory Applications*, vol. 4, no. 11, pp. 2391–2404, Nov. 2010.
- [83] Y.-S. Lu, S.-M. Lin, M. Hauschild, and G. Hirzinger, "A torque-ripple compensation scheme for harmonic drive systems," *Electrical Engineering*, vol. 95, no. 4, pp. 357–365, Dec. 2013.
- [84] K. Cho, J. Kim, S. B. Choi, and S. Oh, "A high-precision motion control based on a periodic adaptive disturbance observer in a PMLSM," *IEEE/ASME Transactions on Mechatronics*, vol. 20, no. 5, pp. 2158–2171, Oct. 2015.
- [85] A. H. M. Sayem, Z. Cao, and Z. Man, "Model free ESO-based repetitive control for rejecting periodic and aperiodic disturbances," *IEEE Transactions on Industrial Electronics*, vol. 64, no. 4, pp. 3433–3441, Apr. 2017.
- [86] I. Takeuchi, N. Suzuki, A. Matsui, Y. Mizutani, and S. Katsura, "Development of a packing-leak tester by high-accuracy force detection," *Journal of the Japan Society for Precision Engineering*, vol. 81, no. 3, pp. 242–246, Mar. 2015.
- [87] Z. Shuangyang, "Fast inspection of food packing seals using machine vision," in *Proceedings of the 2010 International Conference on Digital Manufacturing Automation*, vol. 1, Dec. 2010, pp. 724–726.
- [88] S. Costello, M. P. Y. Desmulliez, and S. McCracken, "Review of test methods used for the measurement of hermeticity in packages containing small cavities," *IEEE Transactions on Components, Packaging and Manufacturing Technology*, vol. 2, no. 3, pp. 430–438, Mar. 2012.

References

- [89] V. Chandola, A. Banerjee, and V. Kumar, “Anomaly detection: A survey,” *ACM computing surveys*, vol. 41, no. 3, p. 15, Jul. 2009.
- [90] L. Fang and L. A. Menk, “On gas ingress of hermetic packages,” *IEEE Transactions on Components, Packaging and Manufacturing Technology*, vol. 9, no. 6, pp. 1038–1044, Jun. 2019.
- [91] E. J. Benjamin, S. S. Virani, C. W. Callaway, A. M. Chamberlain, A. R. Chang, S. Cheng, S. E. Chiuve, M. Cushman, F. N. Delling, R. Deo *et al.*, “Heart disease and stroke statistics-2018 update: a report from the american heart association,” *Circulation*, vol. 137, no. 12, pp. e67–e492, 2018.
- [92] N. Hogan, H. I. Krebs, J. Charnnarong, P. Srikrishna, and A. Sharon, “MIT-MANUS: a workstation for manual therapy and training. I,” in *Proceedings of the 1992 IEEE International Workshop on Robot and Human Communication*, 1992, pp. 161–165.
- [93] H. I. Krebs, N. Hogan, M. L. Aisen, and B. T. Volpe, “Robot-aided neurorehabilitation,” *IEEE Transactions on Rehabilitation Engineering*, vol. 6, no. 1, pp. 75–87, Mar. 1998.
- [94] A. Basteris, S. M. Nijenhuis, A. H. Stienen, J. H. Buurke, G. B. Prange, and F. Amirabdollahian, “Training modalities in robot-mediated upper limb rehabilitation in stroke: a framework for classification based on a systematic review,” *Journal of NeuroEngineering and Rehabilitation*, vol. 11, no. 1, p. 111, Jul. 2014.
- [95] H. Heuer and J. Luetgen, “Robot assistance of motor learning: A neuro-cognitive perspective,” *Neuroscience & Biobehavioral Reviews*, vol. 56, pp. 222–240, Sep. 2015.
- [96] R. Bertani, C. Melegari, M. C. De Cola, A. Bramanti, P. Bramanti, and R. S. Calabrò, “Effects of robot-assisted upper limb rehabilitation in stroke patients: a systematic review with meta-analysis,” *Neurological Sciences*, vol. 38, no. 9, pp. 1561–1569, Sep. 2017.
- [97] H. Muramatsu and S. Katsura, “Separated periodic/apperiodic state feedback control using periodic/apperiodic separation filter based on lifting,” *Automatica*, vol. 101, pp. 458–466, Mar. 2019.
- [98] H. Muramatsu and S. Katsura, “An adaptive periodic-disturbance observer for periodic-disturbance suppression,” *IEEE Transactions on Industrial Informatics*, vol. 14, no. 10, pp. 4446–4456, Oct. 2018.
- [99] H. Muramatsu and S. Katsura, “Periodic/apperiodic motion control using periodic/apperiodic separation filter,” *IEEE Transactions on Industrial Electronics*, 2020.
- [100] H. Muramatsu and S. Katsura, “Design of an infinite-order disturbance observer enhancing disturbance suppression performance,” *IEEJ Journal of Industry Applications*, vol. 6, no. 3, pp. 192–198, Mar. 2017.

References

- [101] H. Muramatsu and S. Katsura, “An enhanced periodic-disturbance observer for improving aperiodic-disturbance suppression performance,” *IEEJ Journal of Industry Applications*, vol. 8, no. 2, pp. 177–184, Mar. 2019.
- [102] T. Flash and N. Hogan, “The coordination of arm movements: an experimentally confirmed mathematical model,” *Journal of neuroscience*, vol. 5, no. 7, pp. 1688–1703, Jul. 1985.
- [103] S. Haykin, *Adaptive Filter Theory, 5th ed.* Prentice-Hall, 2014.
- [104] D. P. Kingma and M. Welling, “Auto-encoding variational bayes,” *arXiv:1312.6114*, Dec. 2013.
- [105] M. Soelch, J. Bayer, M. Ludersdorfer, and P. van der Smagt, “Variational inference for on-line anomaly detection in high-dimensional time series,” *arXiv:1602.07109*, Jun. 2016.
- [106] R. Chalapathy and S. Chawla, “Deep learning for anomaly detection: A survey,” *arXiv:1901.03407*, Jan. 2019.

List of Achievements

Journals (First author)

- [1] Hisayoshi Muramatsu and Seiichiro Katsura, “Periodic/Aperiodic Motion Control Using Periodic/Aperiodic Separation Filter,” *IEEE Transactions on Industrial Electronics*, 2020.
- [2] Hisayoshi Muramatsu and Seiichiro Katsura, “An Enhanced Periodic-Disturbance Observer for Improving Aperiodic-Disturbance Suppression Performance,” *IEEJ Journal of Industry Applications*, vol.8, no.2, pp. 177–184, May 2019.
- [3] Hisayoshi Muramatsu and Seiichiro Katsura, “Separated Periodic/Aperiodic State Feedback Control Using Periodic/Aperiodic Separation Filter Based on Lifting,” *Automatica*, vol. 101, pp. 458–466, Mar. 2019.
- [4] Hisayoshi Muramatsu and Seiichiro Katsura, “An Adaptive Periodic-Disturbance Observer for Periodic-Disturbance Suppression,” *IEEE Transactions on Industrial Informatics*, vol. 14, no. 10, pp. 4446–4456, Oct. 2018.
- [5] Hisayoshi Muramatsu and Seiichiro Katsura, “Design of an Infinite-Order Disturbance Observer Enhancing Disturbance Suppression Performance,” *IEEJ Journal of Industry Applications*, vol. 6, no. 3, pp. 192–198, May 2017.

International Conference (First author)

- [1] Hisayoshi Muramatsu, Yoshihiro Itaguchi, Chiharu Yamada, Hiroshi Yoshizawa, Kazuyoshi Fukuzawa, and Seiichiro Katsura, “Motor Learning with Four Types of Robot Controls,” *Neural Control of Movement, NCM 2019*, April 2019.
- [2] Hisayoshi Muramatsu and Seiichiro Katsura, “Frequency-Varying Periodic-Disturbance Compensation for Periodic Force Control,” *The 5th IEEJ international workshop on Sensing, Actuation, Motion Control, and Optimization, SAMCON 2019*, March 2019.

- [3] Hisayoshi Muramatsu and Seiichiro Katsura, “Design of A Skill-Learning System Based on Human-Motion Reproduction,” *The Annual IEEE Industrial Electronics Society’s 19th International Conference on Industrial Technology, ICIT 2018*, pp. 141–146, February 2018.
- [4] Hisayoshi Muramatsu and Seiichiro Katsura, “Repetitive Motion-Reproduction Based on a Motion-Copying System in Substitution for Human Motion,” *SICE Annual Conference 2017*, pp. 1443–1446, September 2017.
- [5] Hisayoshi Muramatsu and Seiichiro Katsura, “A Circle Disturbance Observer Based on Spatial Periodicity for Circle Systems,” *The Annual IEEE Industrial Electronics Society’s 18th International Conference on Industrial Technology, ICIT 2017*, pp. 648–653, March 2017.
- [6] Hisayoshi Muramatsu and Seiichiro Katsura, “Observation of Space Periodic Disturbance Based on Space-Based Disturbance Observer,” *SICE Annual Conference 2016*, September 2016.
- [7] Hisayoshi Muramatsu and Seiichiro Katsura, “Periodic Disturbance Suppression Based on Infinite-Order Disturbance Observer,” *The 2nd IEEJ International Workshop on Sensing, Actuation, Motion Control, and Optimization, SAMCON 2016*, March 2016.

International Conference (Co-author)

- [1] Xiao Feng, Hisayoshi Muramatsu, and Seiichiro Katsura, “Parameter Adjustment Based on Genetic Algorithm for Adaptive Periodic-Disturbance Observer,” *The 45th Annual Conference of the IEEE Industrial Electronics Society, IECON 2019*, Lisbon, Portugal, October 2019.
- [2] Takumi Karato, Hisayoshi Muramatsu, and Seiichiro Katsura, “Aperiodic Force Extraction Method Based on Variant Frequency Estimation and Normalization,” *The 5th IEEJ international workshop on Sensing, Actuation, Motion Control, and Optimization, SAMCON 2019*, Chiba, Japan, March 2019.
- [3] Takahiro Ebato, Hisayoshi Muramatsu, Yoshihiro Itaguchi, Eiji Yokota, Hiroshi Yoshizawa, Kazuyoshi Fukuzawa, and Seiichiro Katsura, “Hybrid Practice Scheduling of Motor Learning with Upper-Limb Rehabilitation Robot,” *The 5th IEEJ international workshop on Sensing, Actuation, Motion Control, and Optimization, SAMCON 2019*, Chiba, Japan, March 2019.
- [4] Akira Hirata, Hisayoshi Muramatsu, Yoshihiro Itaguchi, and Seiichiro Katsura, “Influence of Electrical Stimulation Patterns on Velocity of the Third-Finger Joints,” *Neuroscience 2018*, November 2018.

- [5] Taisei Araki, Hisayoshi Muramatsu, Yoshihiro Itaguchi, and Seiichiro Katsura, “Quantitative Stretch Reflex Measurement Using Motor System for the Elbow Joint,” *Neuroscience 2018*, November 2018.

Domestic Conference (First author)

- [1] Hisayoshi Muramatsu and Seiichiro Katsura, “Force Control Using Adaptive Periodic-Disturbance Observer,” *Proceedings of the 2019 IEEJ Annual Meeting*, March 2019 (in Japanese).
- [2] Hisayoshi Muramatsu and Seiichiro Katsura, “Combination Design of Periodic-Disturbance Observer Enhancing Aperiodic-Disturbance Suppression Performance,” *Proceedings of the 2019 IEEJ Industry Applications Society Conference, JIASC2019*, August 2018 (in Japanese).
- [3] Hisayoshi Muramatsu and Seiichiro Katsura, “Repetitive Movement Generation for Automation of Human Behavior,” *Proceedings of the 2018 IEEJ Annual Meeting*, March 2018 (in Japanese).
- [4] Hisayoshi Muramatsu and Seiichiro Katsura, “Multiplication Disturbance Suppression Based on Infinite-Order Disturbance Observer under Periodic Commands,” *Proceedings of the 2016 IEEJ Annual Meeting*, March 2016 (in Japanese).
- [5] Hisayoshi Muramatsu and Seiichiro Katsura, “Robust Motion Control with Probability,” *The IEEJ Tokyo Branch 6th Student Research Presentation*, August 2015 (in Japanese).

Domestic Conference (Co-author)

- [1] Issei Takeuchi, Akihito Beppu, Yukiko Osawa, Hisayoshi Muramatsu, and Seiichiro Katsura, “Force Visualization and Control Technology for Next-Generation Food Packaging,” *Proceedings of the 2017 IEEJ Annual Meeting*, March 2017 (in Japanese).

Awards

- [1] “IEEJ Excellent Presentation Award,” *Proceedings of the 2019 IEEJ Industry Applications Society Conference, JIASC2019*, August 2018
- [2] “SICE Annual Conference Young Author’s Award (YAA) finalist,” *SICE Annual Conference 2017*, September 2017.
- [3] “The Best Student Video Competition Award,” *The Annual IEEE Industrial Electronics Society’s 18th International Conference on Industrial Technology, ICIT*, March 2017.

- [4] “IES Student Paper Travel Assistance,” *The Annual IEEE Industrial Electronics Society’s 18th International Conference on Industrial Technology, ICIT*, March 2017.
- [5] “プリエレアイデアコンテスト 2016 作品賞,” 産総研フレキシブルエレクトロニクス研究センター, 2017年2月16日.
- [6] “プリエレアイデアコンテスト 2016 アイデア賞,” 産総研フレキシブルエレクトロニクス研究センター, 2017年2月16日.
- [7] “卒業研究優秀発表賞,” 慶應義塾大学理工学部システムデザイン工学科, 2016年3月23日.

Career

- [1] April 2018~March 2019
Research Associate
The Graduate School of Keio University
- [2] April 2019~
Research Fellow (DC2)
The Japan Society for the Promotion of Science